ENSO NONLINEARITY AND COMPLEXITY: FEATURES, MECHANISMS, IMPACTS AND PREDICTION

EDITED BY: Hong-Li Ren, Tao Lian, Michiya Hayashi, Ruihuang Xie and Wenjun Zhang

PUBLISHED IN: Frontiers in Earth Science and Frontiers in Climate

frontiers Research Topics

ISSN 1664-8714
ISBN 978-2-88976-725-0
DOI 10.3389/978-2-88976-725-0

About Frontiers

Frontiers is more than just an open-access publisher of scholarly articles: it is a pioneering approach to the world of academia, radically improving the way scholarly research is managed. The grand vision of Frontiers is a world where all people have an equal opportunity to seek, share and generate knowledge. Frontiers provides immediate and permanent online open access to all its publications, but this alone is not enough to realize our grand goals.

Frontiers Journal Series

The Frontiers Journal Series is a multi-tier and interdisciplinary set of open-access, online journals, promising a paradigm shift from the current review, selection and dissemination processes in academic publishing. All Frontiers journals are driven by researchers for researchers; therefore, they constitute a service to the scholarly community. At the same time, the Frontiers Journal Series operates on a revolutionary invention, the tiered publishing system, initially addressing specific communities of scholars, and gradually climbing up to broader public understanding, thus serving the interests of the lay society, too.

Dedication to Quality

Each Frontiers article is a landmark of the highest quality, thanks to genuinely collaborative interactions between authors and review editors, who include some of the world's best academicians. Research must be certified by peers before entering a stream of knowledge that may eventually reach the public - and shape society; therefore, Frontiers only applies the most rigorous and unbiased reviews.
Frontiers revolutionizes research publishing by freely delivering the most outstanding research, evaluated with no bias from both the academic and social point of view. By applying the most advanced information technologies, Frontiers is catapulting scholarly publishing into a new generation.

What are Frontiers Research Topics?

Frontiers Research Topics are very popular trademarks of the Frontiers Journals Series: they are collections of at least ten articles, all centered on a particular subject. With their unique mix of varied contributions from Original Research to Review Articles, Frontiers Research Topics unify the most influential researchers, the latest key findings and historical advances in a hot research area! Find out more on how to host your own Frontiers Research Topic or contribute to one as an author by contacting the Frontiers Editorial Office: frontiersin.org/about/contact

ENSO NONLINEARITY AND COMPLEXITY: FEATURES, MECHANISMS, IMPACTS AND PREDICTION

Topic Editors:
Hong-Li Ren, Chinese Academy of Meteorological Sciences, China
Tao Lian, Ministry of Natural Resources, China
Michiya Hayashi, National Institute for Environmental Studies (NIES), Japan
Ruihuang Xie, Ocean University of China, China
Wenjun Zhang, Nanjing University of Information Science and Technology, China

Citation: Ren, H.-L., Lian, T., Hayashi, M., Xie, R., Zhang, W., eds. (2022). ENSO Nonlinearity and Complexity: Features, Mechanisms, Impacts and Prediction. Lausanne: Frontiers Media SA. doi: 10.3389/978-2-88976-725-0

Table of Contents

frontiers | Frontiers in Earth Science

EDITORIAL
published: 11 July 2022
doi: 10.3389/feart.2022.967362

Editorial: ENSO Nonlinearity and Complexity: Features, Mechanisms, Impacts and Prediction

Hong-Li Ren[1,2]*, *Wenjun Zhang*[2], *Tao Lian*[3], *Ruihuang Xie*[4] and *Michiya Hayashi*[5]

[1]State Key Laboratory of Severe Weather, Chinese Academy of Meteorological Sciences, Beijing, China, [2]Collaborative Innovation Center on Forecast and Evaluation of Meteorological Disasters (CIC-FEMD), Nanjing University of Information Science and Technology, Nanjing, China, [3]State Key Laboratory of Satellite Ocean Environment Dynamics, Second Institute of Oceanography, Ministry of Natural Resources, Hangzhou, China, [4]Department of Marine Meteorology, College of Oceanic and Atmospheric Sciences, Ocean University of China, Qingdao, China, [5]Earth System Division, National Institute for Environmental Studies, Tsukuba, Japan

Keywords: El Niño-Southern Oscillation, ENSO complexity , ENSO nonlinearity, ENSO features, ENSO mechanisms, ENSO impacts, ENSO prediction

Editorial on the Research Topic

ENSO Nonlinearity and Complexity: Features, Mechanisms, Impacts and Prediction

El Niño-Southern Oscillation (ENSO) phenomenon is the most important tropical climate variability on the interannual timescale, but its impacts are not limited in the tropics, affecting weather and climate worldwide through far-field teleconnections. Over the past 4 decades, great progress has been made in understanding features, mechanisms, impacts, and prediction of ENSO (see reviews by McPhaden et al., 2020). However, with the increasing availability of observations, as well as the improvements of climate models, the ENSO complexity, which has received widespread attention in recent 2 decades because of the recognizing of ENSO spatial diversity, namely the distinction between the two main ENSO types, the eastern-Pacific (EP) and central-Pacific (CP) types, has become a hot topic and a challenge to the classical ENSO theory and dynamics (see reviews by Capotondi et al., 2015, 2020; Timmermann et al., 2018; Taschetto et al., 2020), e.g., the observed ENSO spatiotemporal diversity might be connected with a combination of two ENSO interannual modes (Timmermann et al., 2018; Wang and Ren 2020).

The ENSO complexity, essentially originating from the nonlinearity of ENSO itself and its interactions with other climate modes, makes it more difficult to do ENSO prediction and thus the prevention and mitigation of ENSO-related disasters. Better understanding towards the ENSO nonlinearity and complexity, as well as the development of corresponding predictability theory and prediction methodology of complex ENSO behaviors, is essential to enhance capabilities for the subseasonal-interannual climate prediction. Here, as one of the leading experts in the ENSO field, Jin summarized the recent active research on the dynamics of ENSO spatiotemporal pattern diversity (STPD) within a synthesized theoretical framework, and discussed challenges and outlooks for theoretical, diagnostic, and numerical modeling approaches to advance our understanding and modeling of ENSO, its STPD, and their broad impacts.

As a matter of fact, the observed key features of ENSO STPD are still inadequately captured by state-of-the-art climate models, though the physical process simulations and model resolutions are improving. Considering that hierarchical modeling approaches, comprising conceptual models, intermediate complexity models, and comprehensive climate models, are fundamental and constructive for ENSO-related research, the assessment and improvement of models are necessary for better simulating ENSO. Same in this Research Topic, Geng and Jin established a revised Cane-Zebiak (RCZ) model, which consists of revised model formulations and well-tuned

OPEN ACCESS

Edited and reviewed by:
Yuqing Wang,
University of Hawaii at Manoa,
United States

***Correspondence:**
Hong-Li Ren
renhl@cma.gov.cn

Specialty section:
This article was submitted to Atmospheric Science, a section of the journal Frontiers in Earth Science

Received: *12 June 2022*
Accepted: *21 June 2022*
Published: *11 July 2022*

Citation:
Ren H-L Zhang W, Lian T, Xie R and Hayashi M (2022) Editorial: ENSO Nonlinearity and Complexity: Features, Mechanisms, Impacts and Prediction. Front. Earth Sci. 10:967362. doi: 10.3389/feart.2022.967362

parameterization schemes. The simulated atmospheric and oceanic responses, as well as characteristics of ENSO in the RCZ model are much better than the original CZ model, making the RCZ model can be a useful tool in studying the dynamics of ENSO STPD. Ineson et al. explored the lack of ENSO amplitude asymmetry between El Niño and La Niña phases in HadGEM-GC3.1. They found that the underestimated subsurface zonal nonlinear dynamic warming due to the inadequate ocean circulation response to ENSO in the model probably be a major cause, which showed us a focus for future model development.

At present, accurately predicting the ENSO events at leads of 6–12 months is still a serious challenge, which is usually subject to the inherent spring predictability barrier of ENSO. The recent 2020/21 La Niña event was not well predicted by most climate models. Cao et al. detected that the predominance of anomalous southeasterly winds over the central equatorial Pacific in spring 2020 is critical for initiating this event by using a pattern clustering approach to compare the best and worst prediction members in an ENSO ensemble prediction system.

Meanwhile, a better simulated mean state in climate models is still an important factor for improving model simulations and predictions. Song et al. assessed the ENSO prediction skill of the recently updated seasonal prediction system FIO-CPS v2.0 from version 1.0 and found that FIO-CPS v2.0 had a better simulated mean state and thus had a higher skill for predicting ENSO compared with v1.0. In addition, due to the insufficient length of modern observational data, evaluating current models' performances in simulating past climate changes by using proxy datasets is a potential way to validate model simulations. Song and Chen examined tropical climate changes, including both basic state and interannual variability, using recently released Paleoclimate Model Inter-comparison Project phase 4 (PMIP4) outputs along with PMIP3 archives.

In the ENSO cycle, the warming and cooling of sea surface temperatures (SSTs) in the tropical Pacific are coupled with large-scale atmospheric circulation anomalies, interact with multiscale variability both within and outside the tropical Pacific. The diversity of ENSO triggers is an important factor for ENSO complexity (see reviews by Amaya, 2019; Cai et al., 2019; Wang 2019). Fu et al. revealed a significant leading role of Siberian High (SH) in the boreal winter on the ENSO development in the following year, and the evolution of the SH-associated response over the North Pacific plays a crucial role in linking SH with ENSO. Li et al. investigated that the reversal of winter surface air temperature anomalies over Central Asia between December and January is closely related to the SST anomalies over the central tropical Pacific. Gao et al. demonstrated that the medium-range predictability of western North Pacific subtropical high (WNPSH) mainly originates from ENSO, and its significant lagged effects on WNPSH well revealed in observation can be realistically reproduced by the National Centers for Environmental Prediction-Global Ensemble Forecast System within the effective prediction lengths. ENSO nonlinearity and complexity also lead to diverse impacts and teleconnections. Several La Niña events featuring relatively long duration and bimodal evolution recently have drawn much attention, showing different climate impacts and teleconnections compared with the canonical single-peak La Niña. Huang et al. systematically examined the multiyear La Niña and found that this type of La Niña could lead to long-lasting impacts on the precipitation in southern China alternately contributed by various mechanisms.

More than that, the global teleconnections of ENSO also have decadal changes, which might be modulated by interdecadal natural variabilities. Chen et al. suggested that the Pacific Decadal Oscillation (PDO) has a strong modulation on the linkage between the spring Arctic Oscillation (AO) and the following winter ENSO. Zhao et al. emphasized that the Atlantic Multidecadal Oscillation (AMO) modulates the relation of ENSO with the central-western Indian Ocean precipitation during the boreal winter.

Understanding broad aspects of ENSO nonlinearity and complexity gives rise to potential skills for seasonal predictions and future projections of ENSO and its global impacts, though properly simulating ENSO complexity in climate models remains a challenge. To provide better predictions and projections of worldwide climate, climate models need to be assessed and further improved from viewpoints of various components of ENSO complexity entangling with each other.

AUTHOR CONTRIBUTIONS

All authors listed have made a substantial, direct, and intellectual contribution to the work and approved it for publication.

FUNDING

This article was jointly supported by the National Natural Science Foundation of China (41975094, 42105067), the Basic Research and Operational Special Project of CAMS (2021Z007) and JSPS KAKENHI Grant Number JP21K13993.

REFERENCES

Amaya, D. J. (2019). The Pacific Meridional Mode and ENSO: a Review. *Curr. Clim. Change Rep.* 5, 296–307. doi:10.1007/s40641-019-00142-x

Cai, W., Wu, L., Lengaigne, M., Li, T., McGregor, S., Kug, J.-S., et al. (2019). Pantropical Climate Interactions. *Science* 363, eaav4236. doi:10.1126/science.aav4236

Capotondi, A., Wittenberg, A. T., Kug, J. S., Takahashi, K., and McPhaden, M. J. (2020). "ENSO Diversity," in *El Niño Southern Oscillation in a Changing Climate* (American Geophysical Union), 65–86. doi:10.1002/9781119548164.ch4

Capotondi, A., Wittenberg, A. T., Newman, M., Di Lorenzo, E., Yu, J.-Y., Braconnot, P., et al. (2015). Understanding ENSO Diversity. *Bull. Amer. Meteor. Soc.* 96, 921–938. doi:10.1175/BAMS-D-13-00117.1

McPhaden, M. J., Santoso, A., and Cai, W. (2020). *El Niño Southern Oscillation in a Changing Climate*. John Wiley & Sons.

Taschetto, A. S., Ummenhofer, C. C., Stuecker, M. F., Dommenget, D., Ashok, K., Rodrigues, R. R., et al. (2020). "ENSO Atmospheric Teleconnections," in *El*

Niño Southern Oscillation in a Changing Climate (American Geophysical Union), 309–335. doi:10.1002/9781119548164.ch14

Timmermann, A., An, S.-I., Kug, J.-S., Jin, F.-F., Cai, W., Capotondi, A., et al. (2018). El Niño-Southern Oscillation Complexity. *Nature* 559, 535–545. doi:10.1038/s41586-018-0252-6

Wang, C. (2019). Three-ocean Interactions and Climate Variability: a Review and Perspective. *Clim. Dyn.* 53, 5119–5136. doi:10.1007/s00382-019-04930-x

Wang, R., and Ren, H.-L. (2020). Understanding Key Roles of Two ENSO Modes in Spatiotemporal Diversity of ENSO. *J. Clim.* 33 (15), 6453–6469. doi:10.1175/JCLI-D-19-0770.1

Conflict of Interest: The authors declare that the research was conducted in the absence of any commercial or financial relationships that could be construed as a potential conflict of interest.

Publisher's Note: All claims expressed in this article are solely those of the authors and do not necessarily represent those of their affiliated organizations, or those of the publisher, the editors and the reviewers. Any product that may be evaluated in this article, or claim that may be made by its manufacturer, is not guaranteed or endorsed by the publisher.

frontiers in Climate

ORIGINAL RESEARCH
published: 20 December 2021
doi: 10.3389/fclim.2021.789869

ENSO Amplitude Asymmetry in Met Office Hadley Centre Climate Models

Sarah Ineson[1]*, *Nick J. Dunstone*[1], *Hong-Li Ren*[2], *Richard Renshaw*[1], *Malcolm J. Roberts*[1], *Adam A. Scaife*[1,3] *and Kuniko Yamazaki*[1]

[1] Met Office Hadley Centre, Met Office, Exeter, United Kingdom, [2] State Key Laboratory of Severe Weather, Institute of Tibetan Plateau and Polar Meteorology, Chinese Academy of Meteorological Sciences, Beijing, China, [3] College of Engineering, Mathematics and Physical Sciences, University of Exeter, Exeter, United Kingdom

Long climate simulations with the Met Office Hadley Centre General Circulation Model show weak El Niño-Southern Oscillation (ENSO) amplitude asymmetry between El Niño and La Niña phases compared with observations. This lack of asymmetry is explored through the framework of a perturbed parameter experiment. Two key hypotheses for the lack of asymmetry are tested. First, the possibility that westerly wind burst activity is biased is explored. It is found that the observed difference in wind burst activity during El Niño and La Niña tends to be underestimated by the model. Secondly, the warming due to subsurface non-linear advection is examined. While the model exhibits non-linear dynamic warming during both La Niña and El Niño, and thus a contribution to ENSO asymmetry, it is shown to be consistently underestimated in comparison with ocean reanalyses. The non-linear zonal advection term contributes most to the deficiency and the simulation of the anomalous zonal currents may be playing a key role in its underestimation. Compared with the ocean reanalyses, the anomalous zonal currents associated with ENSO are too weak in the vicinity of the equatorial undercurrent and the surface wind driven zonal currents extend too deep.

Keywords: El Niño-Southern Oscillation, asymmetry, non-linear dynamic warming, westerly wind burst, climate model

OPEN ACCESS

Edited by:
Swadhin Kumar Behera, Japan Agency for Marine-Earth Science and Technology (JAMSTEC), Japan

Reviewed by:
Han-Ching Chen, University of Hawaii at Manoa, United States
Tomomichi Ogata, Japan Agency for Marine-Earth Science and Technology (JAMSTEC), Japan
Agus Santoso, University of New South Wales, Australia

***Correspondence:**
Sarah Ineson
sarah.ineson@metoffice.gov.uk

Specialty section:
This article was submitted to Predictions and Projections, a section of the journal Frontiers in Climate

Received: *05 October 2021*
Accepted: *29 November 2021*
Published: *20 December 2021*

Citation:
Ineson S, Dunstone NJ, Ren H-L, Renshaw R, Roberts MJ, Scaife AA and Yamazaki K (2021) ENSO Amplitude Asymmetry in Met Office Hadley Centre Climate Models. Front. Clim. 3:789869. doi: 10.3389/fclim.2021.789869

INTRODUCTION

El Niño-Southern Oscillation (ENSO) is the strongest natural interannual climate signal in the tropics, with oscillations between warm El Niño and cold La Niña phases occurring every few years. ENSO events show considerable spatio-temporal complexity (Timmermann et al., 2018). In particular, the distribution of sea surface temperature (SST) variability in the Pacific is not Gaussian, in that the strongest El Niño events are stronger than the strongest La Niña events in the east Pacific (e.g., Burgers and Stephenson, 1999). This amplitude asymmetry in SSTs is associated with asymmetry of temperatures in the ocean subsurface (Jin et al., 2003; Zhang et al., 2009; Hayashi and Jin, 2017). There is also asymmetry in the duration of El Niño and La Niña events (Okumura and Deser, 2010), but here we focus on the amplitude asymmetry as it is an outstanding model error (Zhang and Sun, 2014).

ENSO amplitude asymmetry is generally underestimated in CMIP models (Sun et al., 2016; Hayashi et al., 2020; McKenna et al., 2020). Because the largest El Niño events are often associated with severe impacts (Hardiman et al., 2018; Anderson et al., 2019), this deficiency impacts on our ability to make long range predictions of the risk of extreme regional events. It has also been

suggested that future mean SST change in the east tropical Pacific may depend on a change in the asymmetry between the magnitudes of El Niño and La Niña SST anomalies under climate change (Ham, 2017; Kohyama and Hartmann, 2017). Better simulation of asymmetry may therefore also potentially improve future climate projections of ENSO (Hayashi et al., 2020; Cai et al., 2021).

While the reasons for ENSO amplitude asymmetry remain uncertain, a number of hypotheses have been put forward. For example, the westward shift of zonal wind stress anomalies during La Niña relative to El Niño may lead to relatively weak SST anomalies during La Niña (Kang and Kug, 2002; Im et al., 2015). A number of studies have also suggested an important role for westerly wind burst (WWB) events (Kessler and Kleeman, 2000; Eisenman et al., 2005; Chen et al., 2015; Levine et al., 2016; Hayashi and Watanabe, 2017). Ocean non-linear dynamic warming either in the mixed layer (Jin et al., 2003; An, 2009; Su et al., 2010) or ocean subsurface (Hayashi et al., 2020; Chen et al., 2021) is also thought to contribute. Similarly, another source of asymmetric heat convergence into the cold tongue region is associated with ocean tropical instability waves which occur preferentially in La Niña phases (Vialard et al., 2001; An, 2008). There is also asymmetry in the shortwave surface heat flux feedback (Lloyd et al., 2012; Bayr et al., 2018). For a recent review of these hypotheses see An et al. (2020), and references therein.

Here, we use the framework of a perturbed parameter experiment (PPE) of climate simulations (Yamazaki et al., 2021) to explore the reasons for the weak asymmetry simulated in the Met Office Hadley Centre model, HadGEM-GC3.1 (Williams et al., 2018). ENSO amplitude and periodicity have been shown to be sensitive to, for example, the specification of convection entrainment rate (Watanabe et al., 2011; Lu and Ren, 2016), and ENSO stability can be sensitive to the mean state (Kim et al., 2014). The parameter combinations in each member of the PPE used in this study have been shown to yield a range of plausible yet diverse climate model behaviors (Sexton et al., 2021; Yamazaki et al., 2021). This paper focuses on two of the key hypotheses relating to ENSO asymmetry; the role of westerly wind bursts, and the model representation of subsurface ocean warming due to non-linear advection.

METHODS

Skewness

The ENSO amplitude asymmetry is typically measured by skewness, which is a measure of the extent to which a distribution differs from a normal distribution:

$$\text{Skewness} = \frac{m_3}{(m_2)^{3/2}} \quad (1)$$

where m_k is the kth moment,

$$m_k = \sum_{i=1}^{N} \frac{(x_i - \overline{X})^k}{N}$$

where x_i is the ith observation, the overbar denotes the mean, and N the number of observations.

Here, skewness is calculated from monthly data.

Non-linear Advection

The ocean heat budget can be expressed as:

$$\frac{\partial T'}{\partial t} = -\left(u'\frac{\partial \overline{T}}{\partial x} + v'\frac{\partial \overline{T}x}{\partial y} + w'\frac{\partial \overline{T}}{\partial z} + \overline{u}\frac{\partial T'}{\partial x} + \overline{v}\frac{\partial T'}{\partial y} + \overline{w}\frac{\partial T'}{\partial z}\right) - \left(u'\frac{\partial T'}{\partial x} + v'\frac{\partial T'}{\partial y} + w'\frac{\partial T'}{\partial z}\right) + R' \quad (2)$$

Where T, u, v, and w are temperature, zonal, meridional, and vertical velocities, respectively. The overbar and prime denote climatological mean and anomalies, respectively. The first bracket represents the linear terms, the second bracket is the nonlinear terms and the residual term, R, denotes thermodynamic and subgrid-scale contributions. The heat budget terms are estimated from monthly mean anomalies with respect to the long-term monthly climatology.

Models

ENSO asymmetry is assessed in a number of long climate simulations of the Met Office Hadley Centre general circulation model HadGEM-GC3.1 (Williams et al., 2018) in three different resolutions: low (LL), medium (MM), and high (HH). LL and MM are CMIP6 preindustrial control simulations, at N96 (atmosphere midlatitude spacing of 135 km)/ORCA1 (1° ocean with enhanced meridional resolution near the equator) and N216 (60 km)/ORCA025 (1/4°) resolution, respectively (Menary et al., 2018). Each run length is 500 years. HH has a resolution of N512 (25 km)/ORCA12 (1/12°) and forcing representative of the year 1950 (Roberts et al., 2019). The run length is 150 years. All configurations have 85 levels in the atmosphere and 75 levels in the ocean. To investigate possible reasons for the weak asymmetry in these models, we use a PPE based on a similar model, HadGEM-GC3.05, at MM (N216/ORCA025) resolution. The objective of a PPE is to represent model uncertainty by perturbing model parameters within realistic ranges. There are 19 members, the "standard variant" (STD) unperturbed member (member 0) and 18 members with combinations of perturbations applied to atmosphere and land surface parameters. No perturbations are applied to the ocean. We use 200-year simulations with CMIP5 greenhouse gas and radiative forcing for the year 1900. Heat and fresh-water flux adjustments are derived for STD and applied to all PPE members. In addition, for the 18 perturbed members, a globally uniform, member specific, heat flux adjustment is applied (Yamazaki et al., 2021). The methodology behind the choice of the perturbed parameters and the values they take is described in detail by Sexton et al. (2021), and the identifier which links the ensemble members to the parameter perturbations is shown in brackets: 0 (00000), 1 (00090), 2 (00605), 3 (00834), 4 (01113), 5 (01554), 6 (01649), 7 (01843), 8 (01935), 9 (02089), 10 (02123), 11 (02242), 12 (02305), 13 (02335), 14 (02491), 15 (02753), 16 (02832), 17 (02868), 18 (02914).

WWB Index

WWBs are identified here as events where the daily 10 m zonal wind anomaly, averaged from 2.5°N-2.5°S, exceeds 3 ms^{-1} over a longitude range of at least 10° and lasts for at least 3 consecutive days in the equatorial Pacific (130°E-80°W). We define a WWB index as the sum of the maximum anomaly for each event over a given time period to give a measure of accumulated strength. In recent literature, a number of different criteria have been used for defining WWBs, leading to varying results in terms of numbers of WWBs identified (Santoso et al., 2017). The criteria used here gives an observed average WWB count of just over 12 per year which is within the range identified by other studies (e.g., Puy et al., 2016).

Verification Data

Model data are compared with monthly mean SST from HadISST1.1 for 1873 to 2020 (Rayner et al., 2003), monthly zonal wind stress from ERA5 for 1950 to 2020 (Hersbach et al., 2020), and monthly mean depth of the 20° isotherm estimated from the ocean temperature dataset, EN4, for 1950 to 2020 (Good et al., 2013). WWB activity is calculated using daily 10 m winds from the ERA-Interim reanalysis for 1980 to 2017 (Dee et al., 2011). Monthly mean ocean potential temperature and currents are from two products, the ocean reanalysis used in the GloSea5 seasonal forecast system (MacLachlan et al., 2015) and a recent ocean reanalysis based on the GO5 ocean model (Megann et al., 2014), both for the period 1993 to 2017. In the scatter diagrams, the time-period used for calculating HadISST skewness is chosen to be the same as that used for the corresponding reanalysis variable.

RESULTS

Skewness in Hadley Centre Models

Assessment of ENSO characteristics for HadGEM-GC3.1 at MM resolution shows that this model performs favorably with observations across a range of performance metrics (Williams et al., 2018) and in historical simulations, the PPE shows a range of plausible ENSO variability (Yamazaki et al., 2021). In this study, standard deviation for Nino3.4 (170-120°W, 5°N-5°S) across the PPE ranges from 0.51°C to 0.97°C. El Niño and La Niña composite SST anomaly patterns in HadGEM-GC3.1 are also reasonably realistic and similar at MM and HH resolutions, although for LL the ENSO pattern extends somewhat too far west (Menary et al., 2018; Roberts et al., 2019). However, compared with the observations, these El Niño and La Niña patterns are too symmetrical, reflecting a lack of extreme El Niño events in the models.

Amplitude asymmetry, measured here by SST skewness is weaker than in observations in all our model simulations and versions, irrespective of resolution, as shown in **Figure 1**. Because skewness in the more commonly used Niño3 region (150-90°W, 5°N-5°S) is weak in the PPE, we focus on a region in the far east Pacific (FEP) (110-80°W, 5°N-5°S) that maximizes skewness in the observations (Su et al., 2010; Santoso et al., 2017).

The spatial pattern of SST skewness for the most positively skewed (SK+), standard variant (STD), and least positively skewed (SK–) members of the 19-member PPE (**Figures 1A–C**) can be compared with the observations (**Figure 1D**). STD shows a similar pattern of skewness but is much weaker than observed, with an FEP skewness of 0.34 compared with 1.02 for observations. SK- shows weakly negative skewness along the equator with an FEP skewness of −0.11. For SK+, our most skewed simulation, the westward extent of the region of positive skewness is similar to that observed but again the SK+ member skewness for the FEP region is much weaker than observed, 0.65 compared with 1.02, and the pattern is more equatorially confined.

Skewness for the FEP region for all PPE members shows diversity across the ensemble in the mean, and also a variety of multidecadal variability (**Figure 1E**). However, no member has a mean skewness as high as observed, or indeed a maximum skewness in any 50-year period as high as the observed mean. We also show model data from different resolution HadGEM-GC3.1 models with lower (LL), the same (MM), and higher (HH) ocean and atmosphere resolution as the PPE. These all show similar characteristics to STD and lie within the PPE range, suggesting that lack of ENSO asymmetry is insensitive to resolution in HadGEM-GC3.1

Observations are most strongly positively skewed in the far east Pacific, decreasing to become weakly negatively skewed in the region near the dateline and in a horseshoe-like pattern in the west Pacific and extending somewhat into the South Pacific Convergence zone and the Intertropical Convergence zone. We note that PPE member SK+ has unrealistically high negative skewness in these regions and that in the PPE there is a tendency for the more positively skewed members to also have unrealistically high negative skewness in the west Pacific.

Mean State

In the tropical Pacific there is a close relationship between mean equatorial SST, zonal wind stress and thermocline depth in the mean state (Philander, 1990). As expected, the PPE reflects this, with significant correlations between these variables across individual member simulations.

The relationship between these key variables and skewness also shows significant correlations, with higher SST ($r = 0.54$, $p < 0.02$), weaker zonal wind stress ($r = 0.57$, $p < 0.02$) and shallower 20°C isotherm in the west pacific ($r = -0.44$, $p < 0.1$) all being related to higher skewness in the model (**Figure 2**). The PPE members with deeper thermocline in the western Pacific tend to have a somewhat shallower thermocline in the eastern Pacific (**Figure 2E**). Biases in the coupled model mean state can therefore clearly impact the model skewness and in principle could be responsible for the lack of ENSO asymmetry. However, as the observations lie well within the range of the modeled mean state for each of these assessed variables, the model mean state is not systematically biased in this respect. A realistic representation of these variables by the model does not in itself therefore necessarily lead to realistic asymmetry and we reject the hypothesis that these mean state errors are responsible for the lack of ENSO asymmetry.

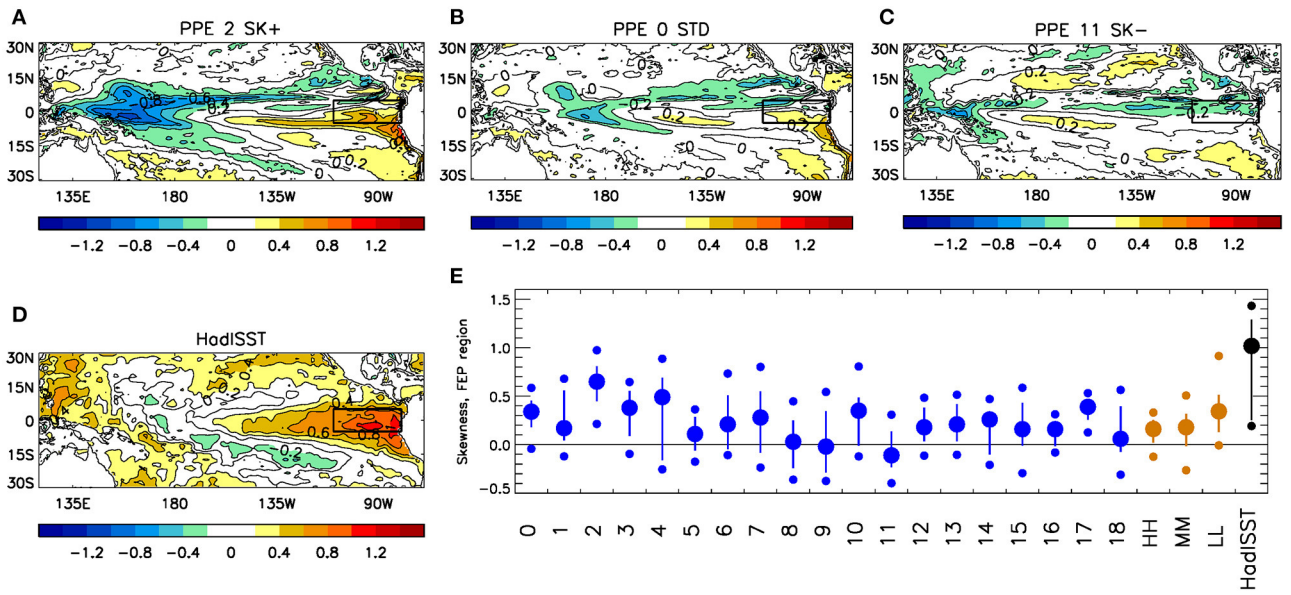

FIGURE 1 | Comparison of skewness in Met Office Hadley Centre models. Skewness in 3 PPE members **(A–C)** and observations (HadISST, 1873-2020) **(D)**. Rectangular box shows skewness in the far eastern Pacific region (FEP, 110-80°W, 5°N-5°S). Skewness in FEP for PPE members (blue), high, medium, and low resolution HadGEM-CG3.1 simulations (brown), and observations (black) **(E)**. Large circles show skewness over the full period of each model simulation, vertical bars show the 16th and 84th percentiles (corresponding to 1 standard deviation from the mean) and small circles are the maximum and minimum of skewness for 50-year sliding windows.

Westerly Wind Events

The relationship between WWBs and skewness is examined using a simple index as a measure of accumulated wind burst activity (WWB index, see section Methods) The index is calculated from daily 10 m zonal winds that have previously been filtered to remove timescales longer than a season (90 days).

We find there are large differences in the annual mean WWB index across our model versions, ranging from an average of 18.3 to 108.8 ms^{-1} per year (**Figure 3A**). However, there is only a weak (not significant) positive correlation ($r = 0.28$) between FEP skewness and WWB activity. We also note that although the two members with largest skewness have relatively high levels of WWB activity, we see that this is not a prerequisite for the PPE skewness. Indeed, the member with the lowest WWB index has similar moderate skewness to the member with the highest WWB index. Finally, we note that the WWB index for the reanalysis lies well within the range of the PPE simulations, suggesting that the model versions are not systematically biased with respect to annual mean WWB activity.

To test the importance of the modulation of wind burst activity by SST in the PPE we look at the difference in WWB activity between El Niño and La Niña events in the January to November period prior to ENSO events (**Figure 3B**). El Niño/La Niña events are defined here as DJF Niño3.4 anomalies exceeding a threshold of +/- 0.8°C. As has been previously demonstrated (e.g., Puy et al., 2016) there is a significant modulation of WWBs by ENSO, with more WWBs during El Niño. However, the majority of PPE members show only a weak difference, significantly underestimating the observed modulation. We also look at this relationship for two separate periods, during boreal spring, early in the ENSO growth cycle, and in boreal summer-autumn, when SST anomalies are established and growing in magnitude. We find a similar relationship for both periods (not shown), suggesting that the rather weak difference in WWB activity in the PPE may result in very large initial El Niño growth in the PPE being less likely than observed, and also, in the second part of the year, that the model may be underestimating the observed dependence of WWBs on SST. However, because of the lack of extreme El Niño events in the PPE this latter result may also simply reflect this lack of model skewness. While there is no relationship ($r = 0.2$) across the PPE with skewness, the difference between the model and observations suggests possible model error in HadGEM-GC3.1 in this respect.

Warming Due to Ocean Non-linear Advection

Equatorial non-linear advection for the combined ocean reanalysis product shows warming in the region of the thermocline and in the surface mixed layer, largely concentrated to the east of the dateline (**Figure 4A**). These features agree well with the analysis shown by Hayashi et al. (2020). Non-linear advection for the PPE, combined over all models, shows a similar pattern, but with muted warming in the ocean subsurface (**Figure 4B**).

Following Hayashi et al. (2020), area averages are calculated for the region (180-100°W, 1°S-1°N, 50–150 m), encompassing the maximum subsurface non-linear dynamic warming (NDW) in the reanalysis. There is a significant relationship ($r = 0.74$,

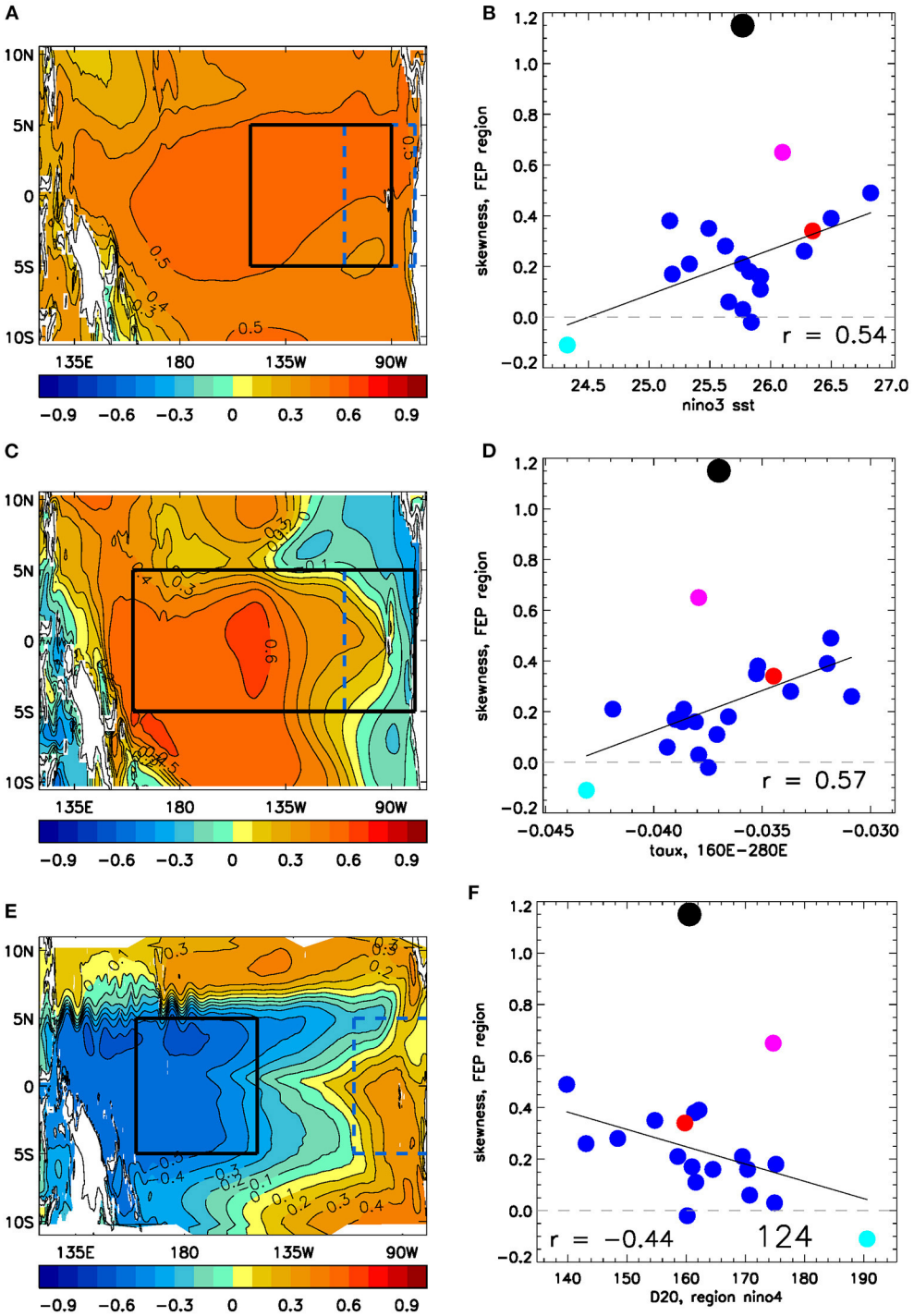

FIGURE 2 | Relationship between skewness and equatorial Pacific annual mean state. Spatial plot of grid point correlation of SST **(A)** zonal wind stress **(C)** and depth of 20° isotherm **(E)** with FEP skewness. Scatter diagram of FEP skewness against annual mean Niño3 SST **(B)**, central Pacific wind stress **(D)** and depth of 20° isotherm for region Niño4 **(F)** for PPE members (small blue circles, with SK+ magenta, STD red, SK- cyan) and reanalysis data (large black circle). Regions for FEP (110-80°W, 5°N-5°S), Niño3 (150-90°W, 5°N-5°S), central Pacific (160°E-80°W, 5°N-5°S) and Niño4 (160°E-150°W, 5N-5S) are shown by boxes in the left-hand panel.

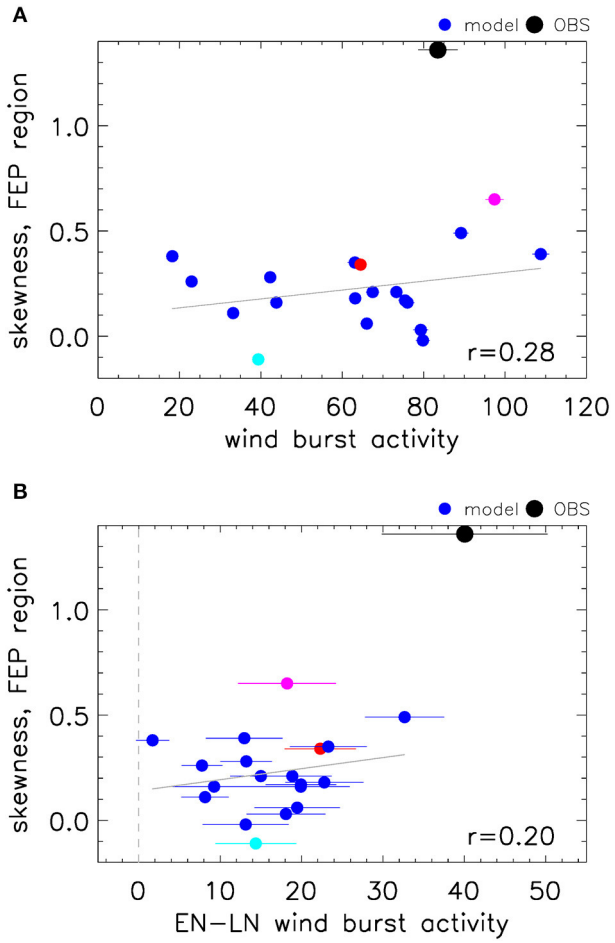

FIGURE 3 | Relationship between skewness and westerly wind burst activity. Scatter diagram of FEP SST skewness against annual mean wind burst activity **(A)** and against the El Niño minus La Niña difference in wind burst activity during the January to November period prior to ENSO events **(B)** for PPE members (small blue circles, with SK+ magenta, STD red, SK– cyan) and reanalysis data (large black circle). Horizontal bars show the standard error.

$p < 0.001$) between the FEP skewness and the NDW for the model simulations and ocean reanalyses (**Figure 4C**). The correlation over PPE members alone is also significant ($r = 0.41$, $p < 0.1$). Unlike our other hypothesized mechanisms for the underestimated ENSO asymmetry, there is a clear systematic model bias in the strength of the NDW and all of the PPE members underestimate the NDW relative to the ocean reanalysis. The NDW is therefore a strong candidate for the lack of asymmetry in the model, consistent with other studies on NDW (Hayashi et al., 2020; Chen et al., 2021).

To consider the contribution of NDW to the growth of ENSO, the NDW for the mean of April to November prior to the peak of ENSO is calculated for all El Niño and La Niña events. Overall, there is a positive contribution during *both* El Niño and La Niña for both the combined ocean reanalysis and the model members (**Figures 4D,E**) This acts to weaken cold (La Niña) events and strengthen warm (El Niño) events, contributing to amplitude asymmetry. However, the total warming in the reanalysis is over twice the magnitude of that in the model (see the right-hand bars in **Figures 4D,E**).

We now consider the three component terms of the NDW (Equation 2) to try to better understand the origin of the weak NDW in the model. The zonal non-linear warming term ($-u'\partial T'/\partial x$) and meridional term ($-v'\partial T'/\partial y$) both make a positive contribution to the warming, whereas the vertical ($-w'\partial T'/\partial z$) term is negative and acts to partially offset the horizontal terms. Comparing the PPE with the ocean analysis we see that it is the zonal component of non-linear advection which largely accounts for the difference in total magnitude (left hand bars in **Figures 4D,E**). It is noteworthy that there is also a significant relationship ($r = 0.48$, $p < 0.05$) between skewness and NDW for the zonal component across PPE members (not shown).

To further explore the reason for the difference in zonal NDW, we decomposed the zonal NDW for the observational reanalysis and the model (**Figures 5A,B**), into the zonal anomalous temperature gradient (**Figures 5C,D**) and anomalous zonal current (**Figures 5E,F**), although this separation is an approximation due to the correlation between the strength of T' and u' fluctuations. It can be seen that the anomalous eastward surface current anomalies extend too deep in the PPE compared with the reanalysis and in particular, that the anomalous westward currents in the region of the equatorial undercurrent are much weaker in the model (**Figures 5E,F**). This latter difference suggests that the ocean circulation response to ENSO is too weak in our model and provides a focus for future model development.

DISCUSSION

We have tested several hypotheses for the weak ENSO amplitude asymmetry in HadGEM-GC3.1, finding initially that mean state errors do not appear to be a factor limiting skewness in our model, at least in the large-scale areas examined here.

Overall, there is only a weak relationship between skewness and mean WWB activity and our model is not systematically biased in this respect. There is also no significant relationship between the state dependent WWB activity and skewness which is consistent with the recent study by Olson et al. (2021) who used an empirical stochastic model to suggest that state dependent noise does not play a role in El Niño asymmetry. However, in this case most of the PPE ensemble members do underestimate the difference in WWB activity between El Niño and La Niña, suggesting the likelihood of model error in this respect. This is consistent with Levine et al. (2016) who show that most CMIP5 models underestimate state-dependent noise forcing. Nevertheless, our simple diagnostic ignores the spatio-temporal diversity of westerly wind bursts (Hao et al., 2019) which could in principle affect the oceanic impact (Puy et al., 2016) and the SST response to WWBs may also depend on the oceanic background state, and hence be affected by ocean model bias (Puy et al., 2019)

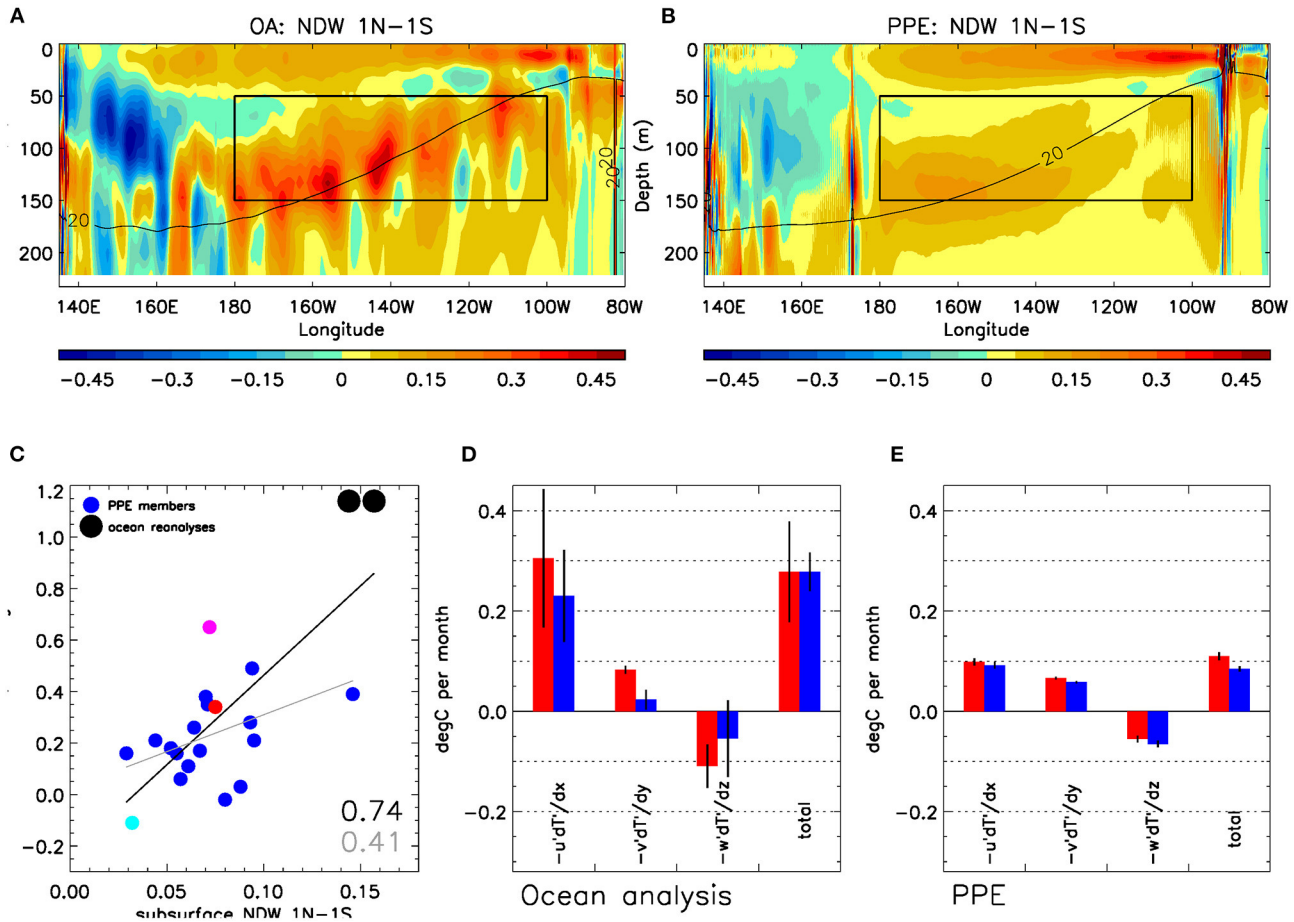

FIGURE 4 | Warming due to non-linear advection. Non-linear advection (K month^{-1}) for combined ocean analyses **(A)** and combined PPE members **(B)**. Box shows the averaging region for the non-linear advection. Scatter diagram of FEP skewness against non-linear advection for PPE ensemble members (small blue circles, with SK+ magenta, STD red, SK– cyan) and ocean reanalyses (large black circles) **(C)**. Non-linear advection terms during growth period of El Niño (red) and La Niña (blue) for combined ocean reanalyses **(D)** combined PPE **(E)**. Combined results are the average over the respective datasets.The growth period is defined here as the average of months April to November prior to the event, with the DJF El Niño/La Niña events identified using a ±0.8°C threshold. Data in **(C)** are area-averages taken over the box shown in the upper panels (180°-100°W,1°S-1°N, 50–150 m). The combined ocean analysis data **(A)** have been smoothed. Vertical bars in **(D,E)** show the 95% confidence interval.

so a more sophisticated analysis would be worthwhile to confirm our results.

In contrast, variation in subsurface NDW is significantly related to skewness and it is also underestimated in our model compared with observational ocean reanalyses. Our analysis suggests model bias in the subsurface zonal NDW, and particularly in anomalous zonal ocean currents which are too weak. These findings are in agreement with other recent analyses of CMIP5 and CMIP6 models (Hayashi et al., 2020; Chen et al., 2021).

The reasons for the weak ENSO response in the equatorial undercurrent variability are not fully understood, especially as the mean undercurrent strength is reasonably represented in the 0.25° ocean model. It's possible there may be a number of contributing factors. First, the mean ENSO amplitude in the combined PPE is slightly lower (by about 10%) than in the ocean reanalysis period, which would suggest slightly weaker amplitude ocean variability in the PPE. Secondly, and in common with other climate models, the dynamic coupling, usually measured by the regression on Niño4 zonal stress onto Niño3 SST, is underestimated (Planton et al., 2021). In the PPE the regression coefficient is from 15 to 55% lower than observed, indicating that the ENSO related momentum transfer to the ocean is too weak. In addition, the anomalous upper ocean currents extend somewhat too deep compared with the reanalysis, perhaps indicating that there is too much mixing of momentum in the upper ocean.

The mechanisms tested here do not rule out other explanations. However, at the 0.25° ocean model resolution used in our simulations, heat convergence associated with tropical instability waves is in reasonably good agreement with observational estimates (Graham, 2014), suggesting that tropical instability waves are unlikely to be the factor limiting

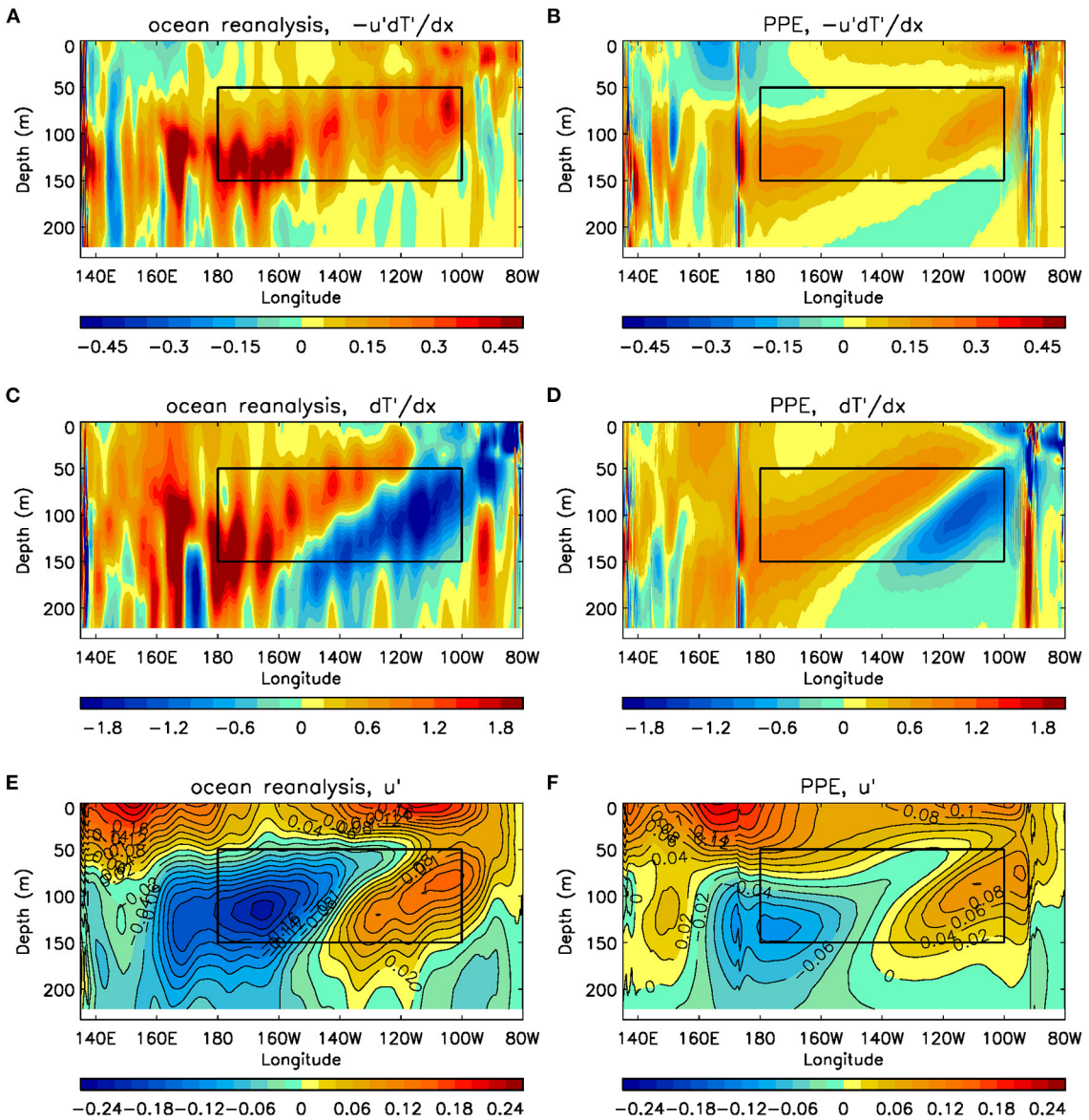

FIGURE 5 | Decomposition of zonal component of non-linear advection. Zonal component of non-linear advection (K month^{-1}) for combined ocean reanalysis **(A)** and combined PPE **(B)**, zonal gradient of temperature anomaly (K m^{-1}) for combined ocean reanalysis **(C)** and combined PPE **(D)**, and zonal current anomaly (ms^{-1}) for combined ocean reanalysis **(E)** and combined PPE **(F)**. Sections are for 1°N-1°S, for the growth period of ENSO, El Niño plus La Niña for **(A,B)** and El Niño minus La Niña for **(C–F)**. The combined ocean analysis data have been smoothed.

skewness in these models. In addition, we note that in our model there is no significant change in skewness across resolution. Other mechanisms have not been tested. We note that model members that have too cold mean SST in the east Pacific also tend to have lower skewness, which is consistent with Sun et al. (2016), who find that weak non-linear air–sea interaction due to cold tongue bias limits asymmetry. Similarly, Liang et al. (2017), find that the range of physical parameters for a system to fall into a regime with positive asymmetry may be rather narrow.

The Met Office Hadley Centre uses the same model in seasonal, decadal and climate prediction systems. While on seasonal timescales the initialized prediction realistically captures the amplitude of extreme El Niño events (Scaife et al., 2017), on longer timescales the predictions revert to the control behavior (Hermanson et al., 2018) with no asymmetry and too few, if any, extreme El Niño events. This may impact our ability to predict and evaluate the risk of extreme regional events associated with the most intense El Niños and highlights the importance of model assessment (e.g., Planton et al., 2021) and

further analysis of this important model error, with a view to future improvement.

DATA AVAILABILITY STATEMENT

The original contributions presented in the study are included in the article/supplementary material, further inquiries can be directed to the corresponding author.

AUTHOR CONTRIBUTIONS

KY, MR, and RR gave advice on, the PPE, HH, and ocean reanalysis data, respectively. SI carried out the analysis. AS, ND, and H-LR contributed to discussing the results and writing the paper. All authors commented on the manuscript.

FUNDING

This work, and contributors SI, ND, and AS, were supported by the UK-China Research & Innovation Partnership Fund through the Met Office Climate Science for Service Partnership (CSSP) China as part of the Newton Fund. H-LR was supported by China National Science Foundation (Grant No. 41975094) and the National Key Research and Development Program of China (Grant No.2018YFC1506000). KY was supported by Department for Business, Energy and Industrial Strategy. MR was supported by, and the HH model was performed as part of, the Horizon 2020 program PRIMAVERA project (Grant No. 641727). This study has been conducted using E.U. Copernicus Marine Service Information.

REFERENCES

An, S.-I., Tziperman, E., Okumura, Y., and Li, T. (2020). ENSO irregularity and asymmetry. *El Niño Southern Oscillation Chang. Clim. Geophys. Monogr.* 252, 153–172. doi: 10.1002/9781119548164.ch7

An, S. I. (2008). Interannual variations of the tropical ocean instability wave and ENSO. *J. Clim.* 21, 3680–3686. doi: 10.1175/2008JCLI1701.1

An, S. I. (2009). A review of interdecadal changes in the nonlinearity of the El Nino-Southern Oscillation. *Theor. Appl. Climatol.* 97, 29–40. doi: 10.1007/s00704-008-0071-z

Anderson, W. B., Seager, R., Baethgen, W., Cane, M., and You, L. (2019). Synchronous crop failures and climate-forced production variability. *Sci. Adv.* 5:eaaw1976. doi: 10.1126/sciadv.aaw1976

Bayr, T., Latif, M., Dommenget, D., Wengel, C., Harla,ß, J., and Park, W. (2018). Mean-state dependence of ENSO atmospheric feedbacks in climate models. *Clim. Dynam.* 50, 3171–3194. doi: 10.1007/s00382-017-3799-2

Burgers, G., and Stephenson, D. B. (1999). The "normality" of El Niño. *Geophys. Res. Lett.* 26, 1027–1039. doi: 10.1029/1999GL900161

Cai, W., Santoso, A., Collins, M., Dewitte, B., Karamperidou, C., Kug, J. S., et al. (2021). Changing El Niño–Southern oscillation in a warming climate. *Nat. Rev. Earth Environ.* 2, 628–644. doi: 10.1038/s43017-021-00199-z

Chen, D., Lian, T., Fu, C., Cane, M. A., Tang, Y., Murtugudde, R., et al. (2015). Strong influence of westerly wind bursts on El Niño diversity. *Nat. Geosci.* 8, 339–345. doi: 10.1038/ngeo2399

Chen, H. C., Jin, F. F., Zhao, S., Wittenberg, A. T., and Xie, S. (2021). ENSO dynamics in the E3SM-1-0, CESM2, and GFDL-CM4 climate models. *J. Clim.* 34, 9365–9384. doi: 10.1175/JCLI-D-21-0355.1

Dee, D. P., Uppala, S. M., Simmons, A. J., Berrisford, P., Poli, P., Kobayashi, S., et al. (2011). The ERA-Interim reanalysis: configuration and performance of the data assimilation system. *Q. J. R. Meteorol. Soc.* 137, 553–597. doi: 10.1002/qj.828

Eisenman, I., Yu, L., and Tziperman, E. (2005). Westerly wind bursts: ENSO's tail rather than the dog? *J. Clim.* 18, 5224–5238. doi: 10.1175/JCLI3588.1

Good, S. A., Martin, M. J., and Rayner, N. A. (2013). EN4: quality controlled ocean temperature and salinity profiles and monthly objective analyses with uncertainty estimates. *J. Geophys. Res. Oceans* 118, 6704–6716. doi: 10.1002/2013JC009067

Graham, T. (2014). The importance of eddy permitting model resolution for simulation of the heat budget of tropical instability waves. *Ocean Model.* 79, 21–32. doi: 10.1016/j.ocemod.2014.04.005

Ham, Y.-G. (2017). A reduction in the asymmetry of ENSO amplitude due to global warming: the role of atmospheric feedback. *Geophys. Res. Lett.* 44, 8576–8584. doi: 10.1002/2017GL074842

Hao, X., Ren, H. L., Zhang, W., Liu, M., and Wei, Y. (2019). Diagnosing the spatiotemporal diversity of westerly wind events in the tropical Pacific. *Dynam. Atm. Oceans* 86, 90–103. doi: 10.1016/j.dynatmoce.2019.03.004

Hardiman, S. C., Dunstone, N. J., Scaife, A. A., Bett, P. E., Li, C., Lu, B., et al. (2018). The asymmetric response of Yangtze river basin summer rainfall to El Niño/La Niña. *Environ. Res. Lett.* 13:024015. doi: 10.1088/1748-9326/aaa172

Hayashi, M., and Jin, F.-F. (2017). Subsurface nonlinear dynamical heating and ENSO asymmetry. *Geophys. Res. Lett.* 44, 12427–12435. doi: 10.1002/2017GL075771

Hayashi, M., Jin, F. F., and Stuecker, M. F. (2020). Dynamics for El Niño-La Niña asymmetry constrain equatorial-Pacific warming pattern. *Nat. Commun.* 11, 1–10. doi: 10.1038/s41467-020-17983-y

Hayashi, M., and Watanabe, M. (2017). ENSO complexity induced by state dependence of westerly wind events. *J. Clim.* 30, 3401–3420. doi: 10.1175/JCLI-D-16-0406.1

Hermanson, L., Ren, H. L., Vellinga, M., Dunstone, N. D., Hyder, P., Ineson, S., et al. (2018). Different types of drifts in two seasonal forecast systems and their dependence on ENSO. *Clim. Dynam.* 51, 1411–1426. doi: 10.1007/s00382-017-3962-9

Hersbach, H., Bell, B., Berrisford, P., Hirahara, S., Horányi, A., Muñoz-Sabater, J., et al. (2020). The ERA5 global reanalysis. *Q. J. R. Meteorol. Soc.* 146, 1999–2049. doi: 10.1002/qj.3803

Im, S. H., An, S. I., Kim, S. T., and Jin, F. F. (2015). Feedback processes responsible for El Niño-La Niña amplitude asymmetry. *Geophys. Res. Lett.* 42, 5556–5563. doi: 10.1002/2015GL064853

Jin, F. F., An, S. I., Timmermann, A., and Zhao, J. (2003). Strong El Niño events and nonlinear dynamical heating. *Geophys. Res. Lett.* 30, 20–21. doi: 10.1029/2002GL016356

Kang, I. S., and Kug, J. S. (2002). El Niño and La Niña sea surface temperature anomalies: asymmetry characteristics associated with their wind stress anomalies. *J. Geophys. Res. Atm.* 107:ACL-1. doi: 10.1029/2001JD000393

Kessler, W. S., and Kleeman, R. (2000). Rectification of the Madden–Julian oscillation into the ENSO cycle. *J. Clim.* 13, 3560–3575. doi: 10.1175/1520-0442(2000)013<3560:ROTMJO>2.0.CO;2

Kim, S. T., Cai, W., Jin, F. F., and Yu, J. Y. (2014). ENSO stability in coupled climate models and its association with mean state. *Clim. Dynam.* 42, 3313–3321. doi: 10.1007/s00382-013-1833-6

Kohyama, T., and Hartmann, D. L. (2017). Nonlinear ENSO warming suppression (NEWS). *J. Clim.* 30, 4227–4251. doi: 10.1175/JCLI-D-16-0541.1

Levine, A., Jin, F. F., and McPhaden, M. J. (2016). Extreme noise–extreme El Niño: how state-dependent noise forcing creates El Niño–La Niña asymmetry. *J. Clim.* 29, 5483–5499. doi: 10.1175/JCLI-D-16-0091.1

Liang, J., Yang, X. Q., and Sun, D. Z. (2017). Factors determining the asymmetry of ENSO. *J. Clim.* 30, 6097–6106. doi: 10.1175/JCLI-D-16-0923.1

Lloyd, J., Guilyardi, E., and Weller, H. (2012). The role of atmosphere feedbacks during ENSO in the CMIP3 models. Part III: the shortwave flux feedback. *J. Clim.* 25, 4275–4293. doi: 10.1175/JCLI-D-11-00178.1

Lu, B., and Ren, H. L. (2016). Improving ENSO periodicity simulation by adjusting cumulus entrainment in BCC_CSMs. *Dynam. Atm. Oceans* 76, 127–140. doi: 10.1016/j.dynatmoce.2016.10.005

MacLachlan, C., Arribas, A., Peterson, K. A., Maidens, A., Fereday, D., Scaife, A. A., et al. (2015). Global Seasonal forecast system version 5 (GloSea5): a high-resolution seasonal forecast system. *Q. J. R. Meteorol. Soc.* 141, 1072–1084. doi: 10.1002/qj.2396

McKenna, S., Santoso, A., Gupta, A. S., Taschetto, A. S., and Cai, W. (2020). Indian ocean dipole in CMIP5 and CMIP6: characteristics, biases, and links to ENSO. *Sci. Rep.* 10, 1–13. doi: 10.1038/s41598-020-68268-9

Megann, A., Storkey, D., Aksenov, Y., Alderson, S., Calvert, D., Graham, T., et al. (2014). GO5. 0: the joint NERC–Met Office NEMO global ocean model for use in coupled and forced applications. *Geosci. Model Dev.* 7, 1069–1092. doi: 10.5194/gmd-7-1069-2014

Menary, M. B., Kuhlbrodt, T., Ridley, J., Andrews, M. B., Dimdore-Miles, O. B., Deshayes, J., et al. (2018). Preindustrial control simulations with HadGEM3-GC3. 1 for CMIP6. *J. Adv. Model. Earth Syst.* 10, 3049–3075. doi: 10.1029/2018MS001495

Okumura, Y. M., and Deser, C. (2010). Asymmetry in the duration of El Niño and La Niña. *J. Clim.* 23, 5826–5843. doi: 10.1175/2010JCLI3592.1

Olson, R., An, S. I., Kim, S. K., and Fan, Y. (2021). A novel approach for discovering stochastic models behind data applied to El Niño–Southern Oscillation. *Sci. Rep.* 11, 1–12. doi: 10.1038/s41598-021-81162-2

Philander, S. G. H. (1990). *El Niño, La Niña, and the Southern Oscillation*. 293 p. San Diego, CA: Academic.

Planton, Y. Y., Guilyardi, E., Wittenberg, A. T., Lee, J., Gleckler, P. J., Bayr, T., et al. (2021). Evaluating climate models with the CLIVAR 2020 ENSO metrics package. *Bull. Am. Meteorol. Soc.* 102, E193–E217. doi: 10.1175/BAMS-D-19-0337.1

Puy, M., Vialard, J., Lengaigne, M., and Guilyardi, E. (2016). Modulation of equatorial Pacific westerly/easterly wind events by the Madden–Julian oscillation and convectively-coupled Rossby waves. *Clim. Dynam.* 46, 2155–2178. doi: 10.1007/s00382-015-2695-x

Puy, M., Vialard, J., Lengaigne, M., Guilyardi, E., Voldoire, A., and Madec, G. (2019). Modulation of equatorial Pacific sea surface temperature response to westerly wind events by the oceanic background state. *Clim. Dynam.* 52, 7267–7291. doi: 10.1007/s00382-016-3480-1

Rayner, N. A. A., Parker, D. E., Horton, E. B., Folland, C. K., Alexander, L. V., Rowell, D. P., et al. (2003). Global analyses of sea surface temperature, sea ice, and night marine air temperature since the late nineteenth century. *J. Geophys. Res. Atm.* 108:4407. doi: 10.1029/2002JD002670

Roberts, M. J., Baker, A., Blockley, E. W., Calvert, D., Coward, A., Hewitt, H. T., et al. (2019). Description of the resolution hierarchy of the global coupled HadGEM3-GC3.1 model as used in CMIP6 HighResMIP experiments. *Geosci. Model Dev.* 12, 4999–5028. doi: 10.5194/gmd-12-4999-2019

Santoso, A., Mcphaden, M. J., and Cai, W. (2017). The defining characteristics of ENSO extremes and the strong 2015/2016 El Niño. *Rev. Geophys.* 55, 1079–1129. doi: 10.1002/2017RG000560

Scaife, A. A., Comer, R., Dunstone, N., Fereday, D., Folland, C., Good, E., et al. (2017). Predictability of European winter 2015/2016. *Atmos. Sci. Lett.* 18, 38–44. doi: 10.1002/asl.721

Sexton, D. M., McSweeney, C. F., Rostron, J. W., Yamazaki, K., Booth, B. B., Murphy, J. M., et al. (2021). A perturbed parameter ensemble of HadGEM3-GC3.05 coupled model projections: part 1: selecting the parameter combinations. *Clim. Dynam.* 56, 3395–3436. doi: 10.1007/s00382-021-05709-9

Su, J., Zhang, R., Li, T., Rong, X., Kug, J. S., and Hong, C. C. (2010). Causes of the El Niño and La Niña amplitude asymmetry in the equatorial eastern Pacific. *J. Clim.* 23, 605–617. doi: 10.1175/2009JCLI2894.1

Sun, Y., Wang, F., and Sun, D. Z. (2016). Weak ENSO asymmetry due to weak nonlinear air–sea interaction in CMIP5 climate models. *Adv. Atm. Sci.* 33, 352–364. doi: 10.1007/s00376-015-5018-6

Timmermann, A., An, S. I., Kug, J. S., Jin, F. F., Cai, W., Capotondi, A., et al. (2018). El Niño–southern oscillation complexity. *Nature* 559, 535–545. doi: 10.1038/s41586-018-0252-6

Vialard, J., Menkes, C., Boulanger, J. P., Delecluse, P., Guilyardi, E., McPhaden, M. J., et al. (2001). A model study of oceanic mechanisms affecting equatorial Pacific sea surface temperature during the 1997–98 El Niño. *J. Phys. Oceanogr.* 31, 1649–1675. doi: 10.1175/1520-0485(2001)031<1649:AMSOOM>2.0.CO;2

Watanabe, M., Chikira, M., Imada, Y., and Kimoto, M. (2011). Convective control of ENSO simulated in MIROC. *J. Clim.* 24, 543–562. doi: 10.1175/2010JCLI3878.1

Williams, K. D., Copsey, D., Blockley, E. W., Bodas-Salcedo, A., Calvert, D., Comer, R., et al. (2018). The Met Office global coupled model 3.0 and 3.1 (GC3. 0 and GC3. 1) configurations. *J. Adv. Model. Earth Syst.* 10, 357–380. doi: 10.1002/2017MS001115

Yamazaki, K., Sexton, D. M., Rostron, J. W., McSweeney, C. F., Murphy, J. M., and Harris, G. R. (2021). A perturbed parameter ensemble of HadGEM3-GC3.05 coupled model projections: part 2: global performance and future changes. *Clim. Dynam.* 56, 3437–3471. doi: 10.1007/s00382-020-05608-5

Zhang, T., and Sun, D. Z. (2014). ENSO asymmetry in CMIP5 models. *J. Clim.* 27, 4070–4093. doi: 10.1175/JCLI-D-13-00454.1

Zhang, T., Sun, D. Z., Neale, R., and Rasch, P. J. (2009). An evaluation of ENSO asymmetry in the community climate system models: a view from the subsurface. *J. Clim.* 22, 5933–5961. doi: 10.1175/2009JCLI2933.1

Conflict of Interest: The authors declare that the research was conducted in the absence of any commercial or financial relationships that could be construed as a potential conflict of interest.

Publisher's Note: All claims expressed in this article are solely those of the authors and do not necessarily represent those of their affiliated organizations, or those of the publisher, the editors and the reviewers. Any product that may be evaluated in this article, or claim that may be made by its manufacturer, is not guaranteed or endorsed by the publisher.

frontiers in Earth Science

ORIGINAL RESEARCH
published: 03 February 2022
doi: 10.3389/feart.2021.810285

Interdecadal Modulation of the Pacific Decadal Oscillation on the Relationship Between Spring Arctic Oscillation and the Following Winter ENSO

Shangfeng Chen[1,2]*, *Wen Chen*[1,2], *Jun Ying*[3,4], *Yuqiong Zheng*[1,2] and *Xiaoqing Lan*[1]

[1]Center for Monsoon System Research, Institute of Atmospheric Physics, Chinese Academy of Sciences, Beijing, China, [2]College of Earth and Planetary Sciences, University of Chinese Academy of Sciences, Beijing, China, [3]State Key Laboratory of Satellite Ocean Environment Dynamics, Second Institute of Oceanography, Ministry of Natural Resources, Hangzhou, China, [4]Southern Marine Science and Engineering Guangdong Laboratory, Zhuhai, China

Previous studies indicated that Arctic Oscillation (AO) in boreal spring is an important extratropical trigger for the outbreak of El Niño and Southern Oscillation (ENSO) events in the succedent winter. This study reveals that the Pacific Decadal Oscillation (PDO) has a strong modulation on the linkage between the spring AO and the following winter ENSO. Particularly, impact of the spring AO on the succedent winter ENSO is strong during positive PDO phase (+PDO). By contrast, the spring AO-winter ENSO connection is weak during negative PDO phase (–PDO). During +PDO, positive spring AO induces a marked anomalous cyclone over the subtropical North Pacific *via* wave-mean flow interaction. The subtropical cyclonic anomaly leads to sea surface temperature (SST) warming and enhanced atmospheric heating there, which could further propagate southward to the tropical central Pacific *via* wind-evaporation-SST feedback mechanism and, thus, impact the following winter El Niño *via* the tropical process. During –PDO, the spring AO-generated SST, the atmospheric circulation, and the heating anomalies over the North Pacific are much weaker. As such, spring AO has weak impacts on the winter ENSO. The spring climatological storm track is stronger during +PDO than –PDO years due to an increase in the mean meridional temperature gradient over the North Pacific. Stronger storm track intensity during +PDO leads to stronger synoptic-scale eddy feedback to the mean flow, which results in stronger AO-related SST and atmospheric anomalies over the North Pacific and, thus, the stronger impact of the spring AO on the following winter ENSO.

Keywords: Arctic Oscillation, El Niño and Southern Oscillation (ENSO), Pacific decadal oscillation, storm track, air–sea interaction

OPEN ACCESS

Edited by:
Wenjun Zhang,
Nanjing University of Information Science and Technology, China

Reviewed by:
Lin Chen,
Nanjing University of Information Science and Technology, China
Xiaojing Jia,
Zhejiang University, China

***Correspondence:**
Shangfeng Chen
chenshangfeng@mail.iap.ac.cn

Specialty section:
This article was submitted to Atmospheric Science, a section of the journal Frontiers in Earth Science

Received: *06 November 2021*
Accepted: *15 December 2021*
Published: *03 February 2022*

Citation:
Chen S, Chen W, Ying J, Zheng Y and Lan X (2022) Interdecadal Modulation of the Pacific Decadal Oscillation on the Relationship Between Spring Arctic Oscillation and the Following Winter ENSO. Front. Earth Sci. 9:810285. doi: 10.3389/feart.2021.810285

INTRODUCTION

The El Niño and Southern Oscillation (ENSO) is the leading atmosphere–ocean coupling pattern over the tropical Pacific on the interannual timescale (Bjerknes, 1969; Philander, 1990; Neelin, 1998; Wang et al., 2000; Chen and Lian 2020; Fang and Xie 2020; Zhang et al., 2020; Hu et al., 2021). ENSO events could notably impact occurrences of extreme weather and climate events over many parts of

the world *via* modulating the tropical Walker circulation and triggering extratropical atmospheric teleconnections, and usually exert severe damages to the agriculture, terrestrial and marine ecosystems, and economic development (Zhang et al., 1996; Horel and Wallace, 1981; Zhang et al., 1997; Chen et al., 2000; Wang et al., 2000; Alexander et al., 2002; Huang et al., 2004; Yu and Zwiers, 2007; Zhou and Chan, 2007; Zhang et al., 2011, 2012; Cheung et al., 2012; Chen et al., 2013; Zhai et al., 2016; Chen et al., 2017; Song et al., 2017; Tang et al., 2018, Chen et al., 2019a, Chen et al., 2019b; Hu et al., 2020; Wei et al., 2020; Hu et al., 2021; Yang and Huang 2021, and references therein). Therefore, understanding the impact factors for the ENSO variability and improving the prediction skill of ENSO occurrence are of great importance.

In addition to the well-known positive atmosphere–ocean interaction and the oceanic processes within the tropical Pacific (Bjerknes, 1979; Philander, 1990; Schopf and Suares, 1988; Jin, 1997; Ren et el. 2016), more and more recent studies reported that the atmosphere–ocean forcings over extratropics also play considerable roles in modulating the onset, development, and phase transition of a specific ENSO event (Vimont et al., 2001, 2003; Alexander et al., 2010; Wang et al., 2011; Chang et al., 2007; Yu et al., 2012; Chen et al., 2014, Chen et al., 2020a, Chen et al., 2020b; Su et al., 2014; Yeh et al., 2015; Ding et al., 2015; Min et al., 2017; Zheng Y. Q. et al., 2021, Zheng Y et al, 2021; and references therein). For instance, Li et al. (1990) indicated that a stronger East Asian winter monsoon (EAWM) is more favorable for occurrence of an El Niño event in the following winter *via* triggering westerly wind bursts over the tropical western Pacific. The wintertime North Pacific Oscillation (NPO), the second Empirical Orthogonal Function (EOF) mode of sea level pressure (SLP) anomalies over extratropical North Pacific (Wallace and Gutzler 1981; Linkin and Nigam, 2008; Song et al., 2016; Chen and Wu, 2018), was suggested to exert a marked impact on the outbreak of ENSO events during the following winter *via* the seasonal footing mechanism (SFM) (Vimont et al., 2001, Vimont et al., 2003; Alexander et al., 2010). Wang et al. (2011) suggested that summertime sea surface temperature (SST) anomalies in the mid-latitude North Atlantic could trigger a Eurasian atmospheric teleconnection, which impacts the EAWM and the following winter ENSO occurrence. Studies also indicated that atmosphere–ocean systems over extratropics of Southern Hemisphere have a close relation with the following winter ENSO (e.g., Ding et al., 2015; Min et al., 2017).

The Arctic Oscillation [AO, also known as the Northern Annular Mode (NAM)] is the first EOF mode (EOF1) of atmospheric variability over extratropical Northern Hemisphere (Thompson and Wallace, 1998, Thompson and Wallace, 2000). Spatial structure of the AO is featured by an oscillation in the SLP and geopotential height anomalies between high- and mid-latitudes of Northern Hemisphere with a vertical barotropic structure (Thompson and Wallace, 1998, Thompson and Wallace, 2000). The wave-mean flow interaction is an important source in forming and maintaining the AO-related atmospheric circulation anomalies over mid-high-latitudes (Limpasuvan and Hartmann 1999; Lorenz and Hartmann 2003; Thompson et al., 2003). In addition to the significant impact of the AO on the weather and climate anomalies over extratropics (Thompson and Wallace, 1998, Thompson and Wallace, 2000), recent studies indicated that climate systems over tropics are also remarkably modulated by the AO (Nakamura te al. 2006; Gong et al., 2011; Choi et al., 2012; Chen et al., 2014). In particular, Nakamura et al. (2006) demonstrated that the boreal spring AO has a significant impact on the following winter ENSO outbreak *via* modulating the westerly wind anomalies over the tropical western Pacific. Chen et al. (2014) further analyzed the physical processes for the impact of the spring AO on the subsequent winter ENSO in detail. They demonstrated that the interaction between synoptic-scale eddy and low-frequency mean flow and related vorticity transportation play a key role in the generation of the atmospheric anomalies over the subtropical North Pacific and zonal wind anomalies over the equatorial western Pacific. The zonal wind anomalies over the equatorial western Pacific further impacts following winter ENSO outbreak *via* triggering eastward propagating and downwelling Kelvin waves (Barnett et al., 1989; Huang et al., 2001; Lengaigne et al., 2004; Nakamura et al., 2006; Chen et al., 2015). Chen et al. (2016a) revealed that the strong AO event in spring of 2015 plays an important role in the outbreak of the strong 2015–2016 EL Niño event *via* triggering strong westerly wind burst over the equatorial western Pacific.

However, the relationship between the spring AO and winter ENSO is unstable (Chen et al., 2015, Chen et al., 2020c). Specifically, Chen et al. (2015) reported that the spring AO–winter ENSO connection has undergone a pronounced interdecadal change around the 1970s. Spring AO-related atmospheric circulation anomalies over the North Pacific are much stronger after than before the 1970s (Chen et al., 2014), contributing to a stronger spring AO–winter ENSO connection after the interdecadal change. Moreover, studies have demonstrated that change in the connection between the spring AO and winter ENSO is essentially attributed to change in the climatology of the storm track intensity over North Pacific (Chen et al., 2015, Chen et al., 2017, Chen et al., 2020b). In particular, stronger springtime North Pacific storm track intensity could lead to a stronger feedback of the synoptic-scale eddy to mean flow (Chen et al., 2015, Chen et al., 2017). This leads to stronger atmospheric anomalies over North Pacific related to the spring AO, including the zonal wind anomalies over the equatorial western Pacific, and thus results in a stronger impact of the spring AO on the winter ENSO (Chen et al., 2015, Chen et al., 2017).

The Pacific Decadal Oscillation (PDO) is the leading EOF mode of SST anomalies in the North Pacific on the decadal time scale (Mantua et al., 1997). Studies have indicated that the PDO has a strong impact on the North Pacific storm track intensity and North Pacific atmosphere on the decadal time scale (Budikova 2005; Zhou et al., 2007; Wang et al., 2008; Lee et al., 2012; Ding et al., 2014; Kim et al., 2014). Hence, we speculate that the PDO may have an impact on the spring AO–winter ENSO connection *via* modulation of the North Pacific storm track intensity and *via* modulation of the spring AO-related atmospheric anomalies over

the North Pacific. In this analysis, we will present observational evidences to show that the PDO indeed has a marked modulation effect on the spring AO-winter ENSO connection. The physical processes for the modulation of the PDO are also examined.

The structure of the rest of this paper is organized as follows. The *Data and methodology* section describes the data and methods employed in this study. The *Spring AO–ENSO connection in different phases of PDO* section investigates the interdecadal modulation effect of the PDO on the spring AO–winter ENSO connection. The *Mechanisms for the modulation of the PDO* section examines the physical mechanisms for the modulation of the PDO on the spring AO–winter ENSO relation. The *Summary* section provides a summary.

DATA AND METHODOLOGY

This study employs the monthly average SST from the National Oceanic and Atmospheric Administration (NOAA) Extended Reconstructed SST version five dataset (ERSSTV5) (Huang et al., 2017; https://www.esrl.noaa.gov/psd/data/). ERSSTV5 SST data have a resolution of 2 × 2 and a span from 1854 to the present. Monthly and daily average SLP, geopotential height, winds, precipitation rate, and surface heat fluxes are extracted from the National Centers for Environmental Prediction and National Center for Atmospheric Research (NCEP-NCAR) reanalysis (Kalnay et al., 1996), with a horizontal resolution of 2.5 × 2.5 and available from 1948 to the present (https://psl.noaa.gov/data/gridded/data.ncep.reanalysis.html). The monthly average PDO index from 1900 to the present is obtained from the Joint Institute for the Study of the Atmosphere and Ocean (http://research.jisao.washington.edu/pdo/).

The Niño-3.4 SST index, defined by SST anomalies averaged over 5°S–5°N and 170°–120°W, is employed to represent the ENSO variability. An El Niño (a La Niña) event is identified when the 3-month running mean of the Niño-3.4 SST index are above 0.5°C (below −0.5°C) on five consecutive 3-month periods. The spring AO is defined as the first EOF mode of spring SLP anomalies north of 20°N. Correspondingly, the spring AO index is defined as the principal component (PC) time series of the first EOF mode. Positive (negative) spring AO years are selected when the normalized spring AO index are larger (less) than 0.5. Synoptic scale eddy activity (also called storm track) is calculated as the 2- to 8-day band-pass filtered daily geopotential height (Chang and Fu 2002; Lee et al., 2012; Chen et al., 2014). Positive (negative) PDO years are selected when the 9-year running mean PDO index is larger (less) than zero. Long-term trends and interdecadal components of all the variables, except PDO index, are removed by a 9-year high-pass Lanczos filter (Duchon, 1979). Significance levels of the linear regression and correlation are estimated based on the two-tailed Student's t-test. To ensure that the close connection between the spring AO and following winter ENSO is not due to the ENSO cycle, the preceding winter ENSO signal (represented by the Niño-3.4 SST index) has been linearly removed from the spring AO index and other variables. For example, the preceding winter ENSO signal was removed from the spring AO index as follows:

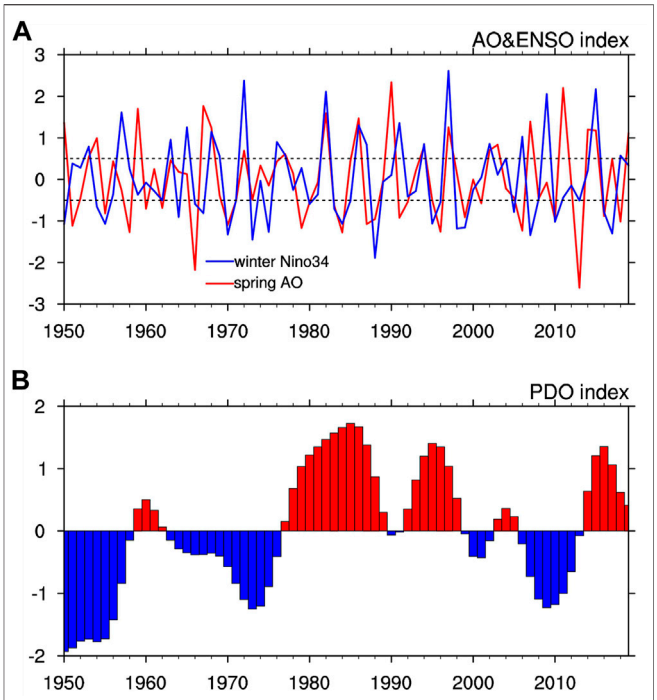

FIGURE 1 | (A) Standardized time series of the spring (MAM-average) Arctic Oscillation (AO) index and the following winter (DJF-average) Niño-3.4 sea surface temperature (SST) index over 1950–2019. **(B)** Nine-year running mean of the spring Pacific Decadal Oscillation (PDO) index over 1950–2019. Positive (negative) phase of the PDO (+PDO and −PDO) is defined when the PDO index is larger (less) than zero.

$AO_{res} = AO - Reg \times Niño\text{-}3.4$. Here, *AO* indicates the spring AO index, *Niño-3.4* indicates the preceding winter Niño-3.4 SST index. *Reg* is the regression coefficient between the preceding winter Niño-3.4 SST index and the spring AO index. AO_{res} is the part of the spring AO that ENSO signal has been linearly removed.

SPRING ARCTIC OSCILLATION–EL NIÑO AND SOUTHERN OSCILLATION CONNECTION IN DIFFERENT PHASES OF THE PACIFIC DECADAL OSCILLATION

Standardized time series of the spring [March–April–May, MAM(0)] AO index and subsequent winter [December–January–February, D(0)JF(1)] Niño-3.4 SST index are exhibited in **Figure 1A**. From **Figure 1A**, many positive spring AO years (i.e., 1953, 1963, 1968, 1972, 1977, 1982, 1994, 1997, 2002, 2009, 2014, and 2015) are followed by El Niño events in the following winter. In addition, a number of La Niña events are preceded by negative spring AO years (i.e., 1955, 1970, 1983, 1984, 1988, 1995, 1999, 2005, 2008, 2010, 2016). The correlation coefficient between the spring AO index and the following winter Niño-3.4 SST index is about 0.27 for the period of 1950–2016, significant at the 95% confidence level. Hence, this suggests that the spring AO has a close connection with the following winter ENSO, in concert with previous studies although according to

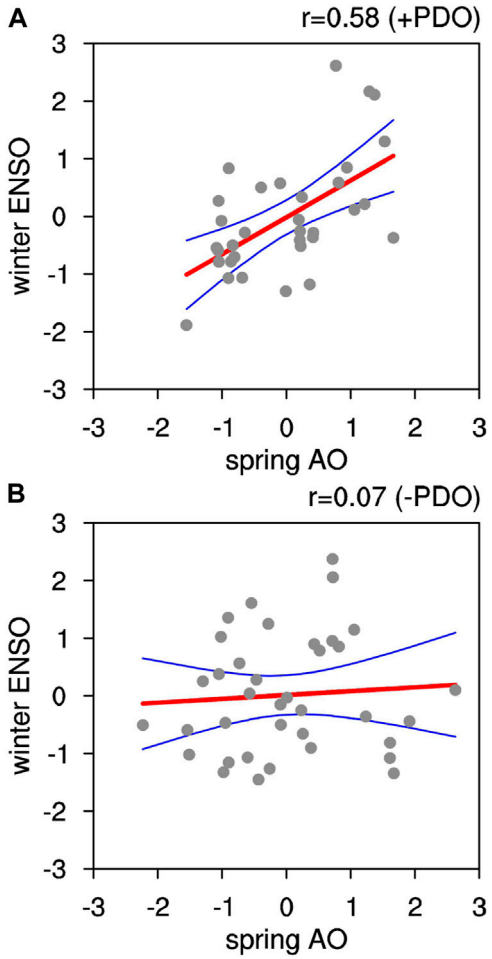

FIGURE 2 | Scatter plots of the spring AO index with the following winter Niño-3.4 SST index for the **(A)** +PDO and **(B)** −PDO years, respectively. Red lines indicate the best linear fit. Blue lines indicate the 95% confidence range of the linear regression.

different datasets and time periods (Nakamura et al., 2006; Chen et al., 2014, Chen et al., 2017).

According to **Figure 1A**, positive (negative) spring AO years are not always followed by an 1) El Niño (La Niña) event in the succedent winter. This indicates that the spring AO–winter ENSO connection is unstable. Chen et al. (2015) reported that the impact of the spring AO on the subsequent winter ENSO enhanced significantly after the 1970s, corresponding to transition of the PDO from its negative to positive phases (**Figure 1B**). Moreover, during the positive phase of the PDO (+PDO) (**Figure 1B**), the positive spring AO years in 1982, 1997, and 2015 are followed by strong El Niño events (**Figure 1A**). By contrast, during the negative phase of the PDO (−PDO), the positive spring AO years in 1959, 1967, 1990, and 2011 are not followed by El Niño events (**Figures 1A,B**). The correlation coefficient between the MAM(0) AO index and the D(0)JF(1) Niño-3.4 SST index reaches 0.58 for the +PDO years (33 years), significant at the 99.9% confidence level (**Figure 2A**). However, the relationship of the spring AO with the following winter Niño-3.4 SST index is very weak for the −PDO years (37 years), with a correlation coefficient of only 0.07 (**Figure 2B**). Particularly, difference in the correlation coefficient of the spring AO index with the Niño-3.4 SST index between +PDO and -PDO years are significant at the 99% confidence level according to Fisher's r-z transformation.

Therefore, above statistical analyses indicate that the PDO acts as an important modulator for the impact of the spring AO on the following winter ENSO. Under +PDO background, spring AO has a close connection with the following winter ENSO. In sharp contrast, impact of the spring AO on the following winter ENSO is very weak under −PDO background.

Mechanisms for the Modulation of the Pacific Decadal Oscillation

In this section, the plausible mechanisms for the modulation of the PDO on the spring AO-winter ENSO connection are examined. Evolutions of 850-winds, SST, and precipitation anomalies from simultaneous spring to the following winter regressed upon the spring AO index for the +PDO and −PDO years are shown in **Figures 3–5**, respectively. Evolutions of the winds, SST, and precipitation anomalies in association with the spring AO for the +PDO years are similar to those reported in previous studies (Chen et al., 2014, Chen et al., 2015, Chen et al., 2017), showing a marked impact of the spring AO on the following winter ENSO. For the +PDO years, positive spring AO years are related to a notable meridional dipole atmospheric anomaly pattern over North Pacific with a strong anticyclonic anomaly over mid-high-latitudes North Pacific (corresponding to the North Pacific component of the spring AO) and a marked cyclonic anomaly over subtropical North Pacific (**Figure 3A**). Note that spatial structures of the spring AO-related atmospheric anomalies at the 500-hPa and 200-hPa (not shown) are highly similar to those at the 850-hPa (**Figure 3A**), indicative of a barotropic vertical structure (Thompson and Wallace 1998, Thompson and Wallace 2000). As reported in previous studies (Chen et al., 2014, Chen et al., 2015, Chen et al., 2017), generation of the spring AO-related cyclonic anomaly over subtropical North Pacific is attributable to the interaction between synoptic-scale eddy activity and low frequency mean flow as well as the associated vorticity transportation. Specifically, the anticyclone anomaly over the mid-high-latitudes North Pacific is associated with strong easterly wind anomalies to its south side between 35°–45°N (**Figures 3A** and **6B**). These easterly wind anomalies are accompanied by significant decrease in the storm track activity (**Figures 6A–D**) (Chen et al., 2014). As has been demonstrated by previous studies (Lau 1988; Cai et al., 2007; Chen et al., 2014, Chen et al., 2015), the decrease in the storm track activity is immediately accompanied by cyclonic vorticity forcing to its south side and anticyclonic vorticity forcing to its north side. Therefore, the cyclonic vorticity forcing to the south side of the storm track explains the formation of the spring AO-related cyclonic anomaly over the subtropical North Pacific (Chen et al., 2014). In addition, the anticyclonic vorticity forcing to the north side of the storm track helps maintain the anticyclonic anomaly over mid-high-latitude North Pacific (i.e., North Pacific component of the spring

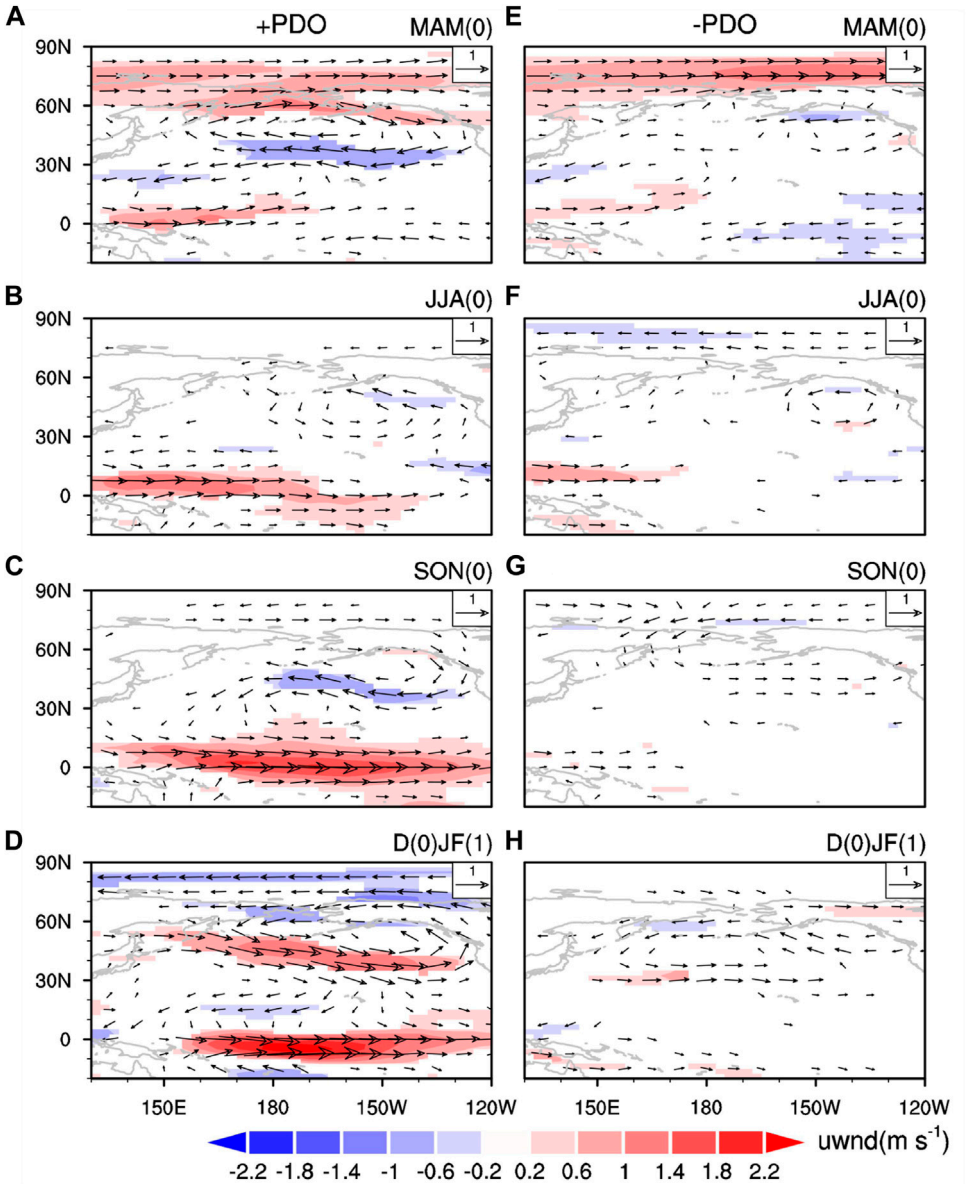

FIGURE 3 | Winds of 850-hPa (vectors, ms^{-1}) and 850-hPa zonal wind (shadings, ms^{-1}) anomalies in **(A,E)** spring [MAM(0)], **(B,F)** summer [JJA(0)], **(C,G)** autumn [SON(0)], and **(D,H)** winter [D(0)JF(1)] regressed upon the spring AO index for the (left column) +PDO and (right column) –PDO years. We only show the 850-hPa zonal wind anomalies that are significant at the 95% confidence level.

AO). Hence, the interaction between synoptic scale eddy and mean flow help maintain the spring AO-related atmospheric anomalies over North Pacific. This is consistent with the prevailing view that the wave-mean flow interaction plays an important role in the generation and maintenance of the AO-related atmospheric anomalies over extratropics (Limpasuvan and Hartmann 1999; Lorenz and Hartmann 2003).

The cyclonic anomaly over the subtropical North Pacific generated by the spring AO could directly lead to strong westerly wind anomalies over the tropical western Pacific (**Figure 3A**). These westerly wind anomalies over the tropical western Pacific could exert notable impacts on the occurrence of the following winter El Niño event (**Figures 4C,D**) *via* stimulating eastward propagating and downwelling warm equatorial Kelvin waves (Lengaigne et al., 2004; Chen et al., 2014, Chen et al., 2016b, Chen et al., 2016c). In addition, the spring cyclonic anomaly over the subtropical North Pacific would lead to SST warming over the subtropical central North Pacific (**Figure 4A**) *via* modulating surface heat flux (dominated by the surface latent heat flux). Specifically, the southwesterly wind anomalies over the subtropical central North Pacific oppose the mean northeasterly trade winds, reduce the total wind speed (**Figure 7C**), and upward surface latent heat (**Figure 7A**) and, thus, result in spring SST warming there

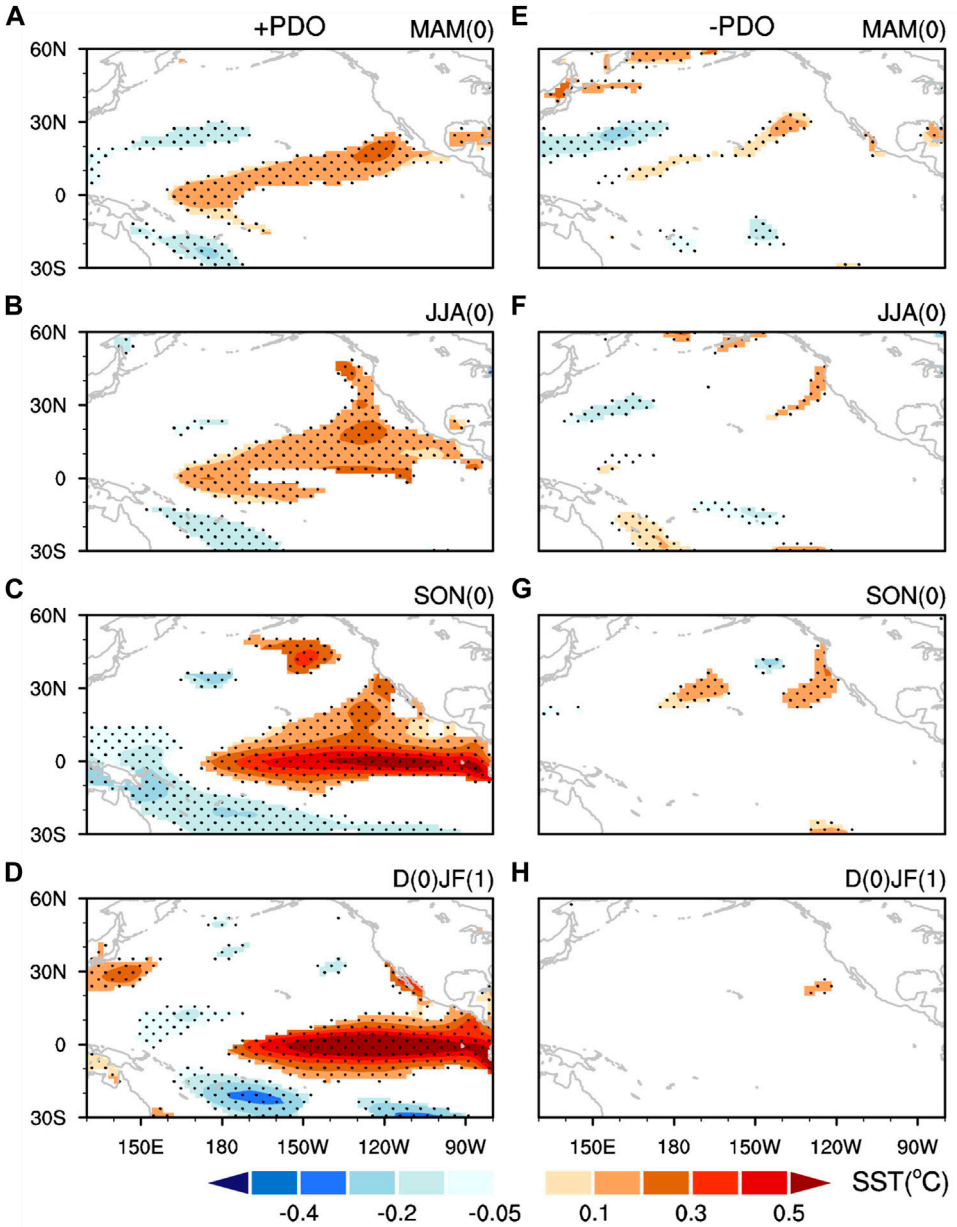

FIGURE 4 | SST anomalies (°C) in **(A,E)** spring [MAM(0)], **(B,F)** summer [JJA(0)]), **(C,G)** autumn [SON(0)], and **(D,H)** winter [D(0)JF(1)] regressed upon the spring AO index for the (left column) +PDO and (right column) –PDO years. We only show the SST anomalies that are significant at the 95% confidence level.

(**Figure 4A**), suggestive of the wind-evaporation-SST (WES) feedback (Xie and Philander 1994).

The spring AO-related SST anomalies in the subtropical North Pacific for the +PDO years bear a close resemblance to that related to the North Pacific Meridional Mode (PMM) (Chiang and Vimont 2004; Chang et al., 2007; Zheng et al., 2021), which is the dominant mode of air–sea coupling system over the subtropical Northeastern Pacific and is suggested to be an important channel in relaying impact of the extratropical forcings on the tropical ENSO events (Xie and Philander 1994; Chiang and Vimont 2004; Chang et al., 2007). This suggests that spring AO can exert impacts on the following winter ENSO *via* modulating the PMM for the +PDO years. In particular, the spring AO-generated SST warming in the subtropical central North Pacific leads to an increase in the atmospheric heating there (indicated by positive precipitation anomalies in **Figure 5A**). The enhanced atmospheric heating over the subtropical central North Pacific (**Figure 5A**) could maintain the spring AO-induced subtropical cyclonic anomaly (**Figure 3A**) *via* Gill-type atmospheric response, (Gill, 1980) which in turn maintains the SST warming in the subtropical central North Pacific (**Figure 4A**). The spring AO-related SST warming

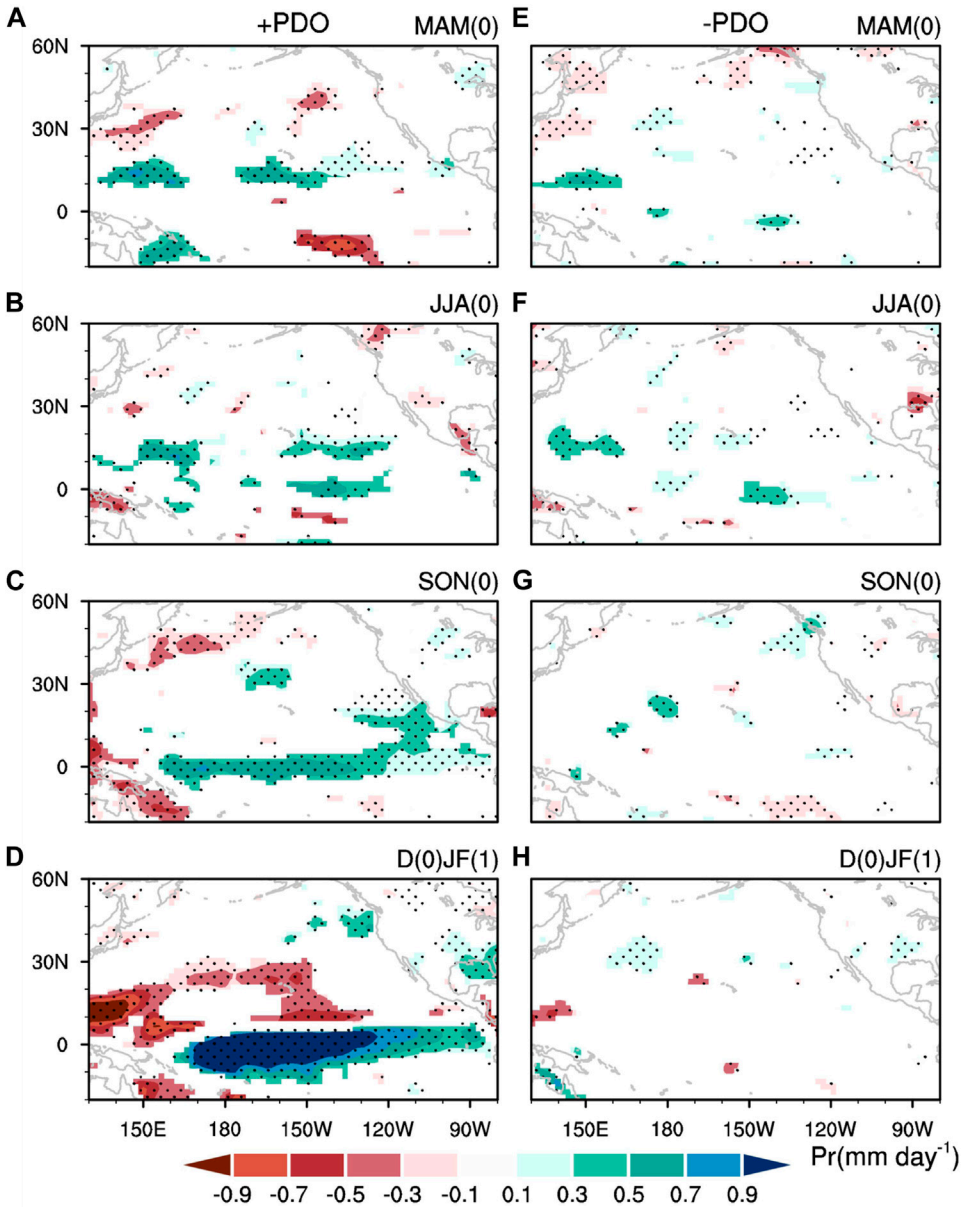

FIGURE 5 | As in **Figure 4**, but for precipitation anomalies (mm day^{-1}). Stippling regions indicate precipitation anomalies significant at the 95% confidence level.

maintains and further extends southward to the tropical central Pacific in the following summer *via* the WES feedback mechanism (**Figure 4B**). Then, the tropical SST warming can develop to an El Niño-like warming in the following winter *via* the Bjerknes-like positive air–sea interaction (**Figures 3B–D**, **Figures 4B–D**, and **Figures 5B–D**) (Bjerknes 1969).

In brief summary, during +PDO years, spring AO can induce a strong cyclonic anomaly over the subtropical North Pacific *via* wave-mean flow interaction. On one hand, this cyclonic anomaly could directly induce strong westerly wind anomalies over the tropical western Pacific and impact following winter ENSO occurrence *via* triggering eastward propagating warm equatorial Kelvin wave. On the other hand, the cyclonic anomaly generated by the spring AO could induce a PMM-like SST warming in the subtropical North Pacific, which further expand southward to the tropical central Pacific *via* the WES feedback mechanism and thus impact following winter ENSO *via* tropical positive air–sea interaction.

For the −PDO years, significant westerly wind anomalies in spring can be seen north of 60°N during positive phase of the spring AO (**Figure 3E**), similar to that for the +PDO years (**Figure 3A**). However, atmospheric anomalies over the North Pacific, especially the cyclonic anomalies over the subtropical North Pacific and westerly wind anomalies over the tropical western Pacific are very weak for the −PDO years. As such, the weak cyclonic anomalies (**Figure 3E**) could not induce clear

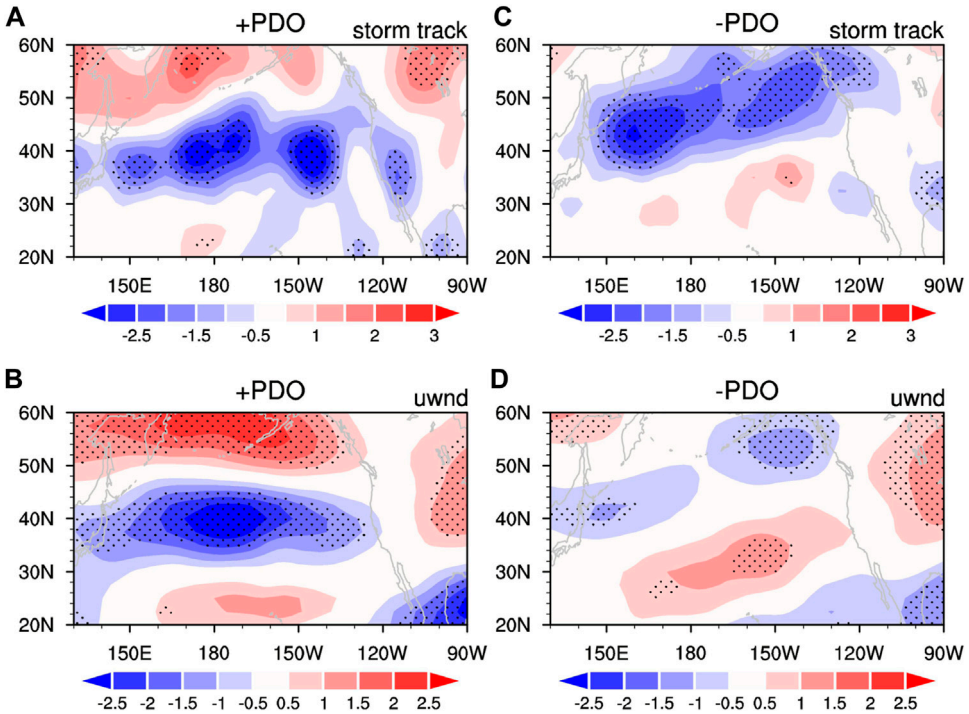

FIGURE 6 | Surface latent heat flux anomalies (W m^{-2}) in spring regressed upon the spring AO index for the **(A)** +PDO and **(B)** −PDO years, respectively. **(C,D)** are as in **(A,B)**, but for surface wind speed anomalies (m s^{-1}). We only show the values that are significant at the 95% confidence level.

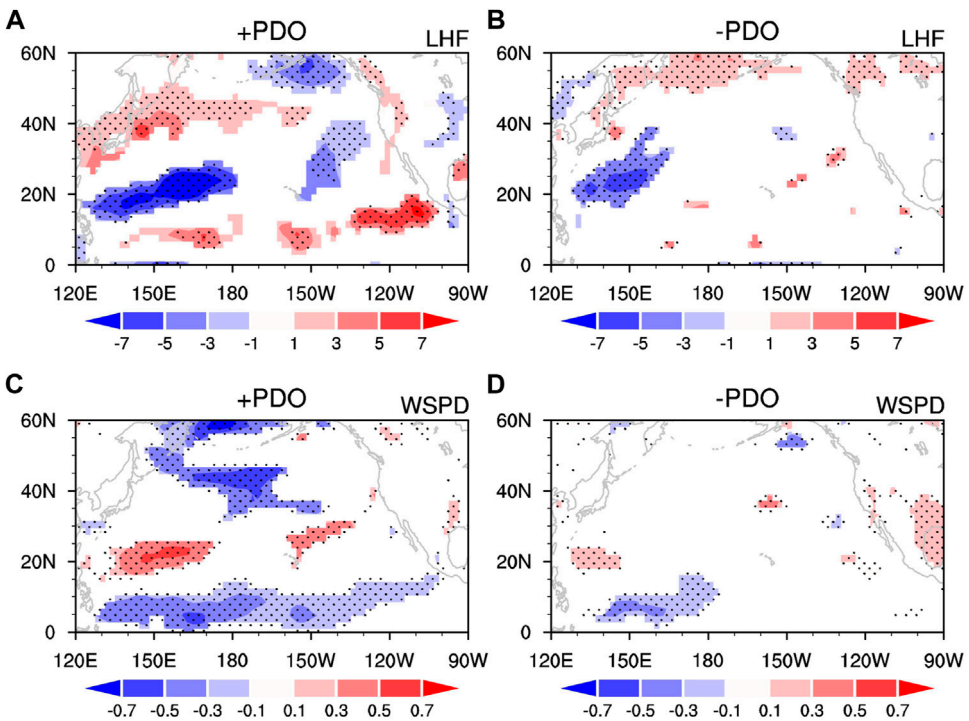

FIGURE 7 | Storm track anomalies (m) of 200 hPa in spring regressed upon the spring AO index for the **(A)** +PDO and **(B)** −PDO years, respectively. **(C,D)** are as in **(A,B)**, but for 200 hPa zonal wind anomalies (m s^{-1}).

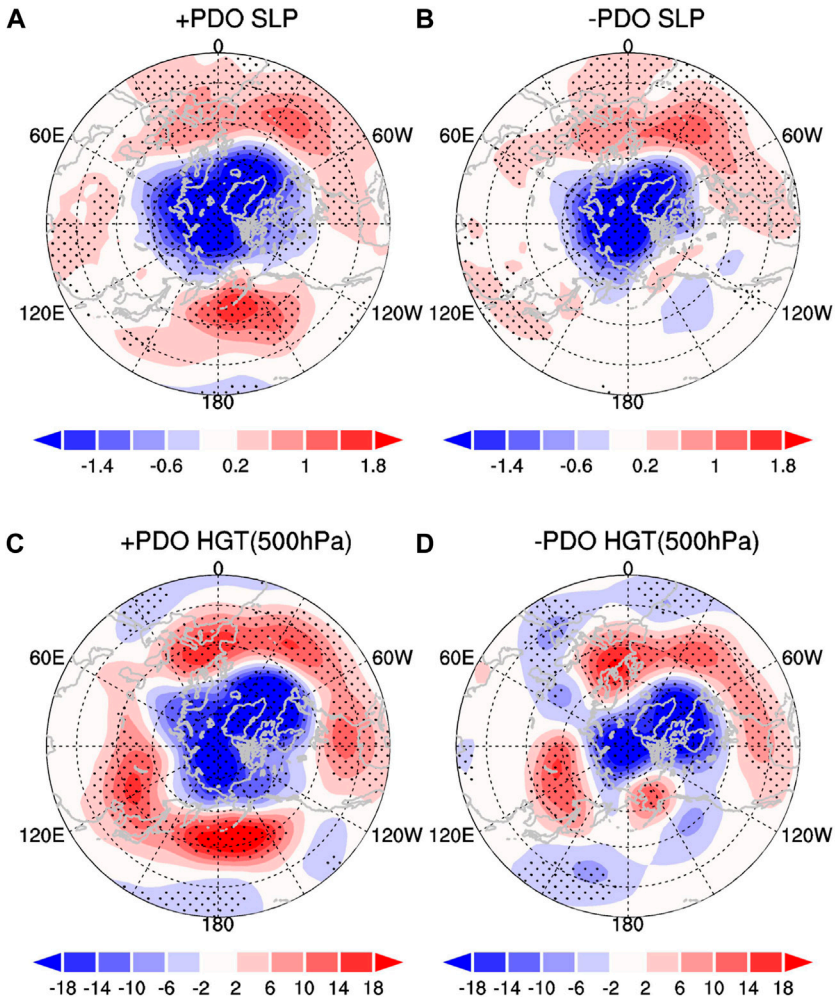

FIGURE 8 | Sea level pressure (SLP) anomalies (hPa) in spring regressed upon the spring AO index for the **(A)** +PDO and **(B)** −PDO years, respectively. **(C,D)** are as in **(A,B)**, but for 500 hPa geopotential height anomalies (m).

spring SST warming and atmospheric heating in the subtropical North Pacific (**Figures 4E** and **5E**) due to the weak surface wind speed and surface heat flux anomalies (**Figures 7B,D**). Therefore, the spring AO cannot exert clear impacts on the SST and atmospheric circulation over the tropical Pacific and, thus, have weak influences on the ENSO.

The above analysis indicates that the PDO has a notable influence on the spring AO-winter ENSO connection *via* changing the spring AO-related atmospheric anomalies over the North Pacific. In particular, the North Pacific component of the spring AO (i.e., the anticyclonic anomaly over the mid-high-latitudes North Pacific) and the generated cyclonic anomalies to its south side over the subtropical North Pacific are much weaker for the −PDO than the +PDO years, which can also be confirmed in **Figure 8** showing regressions of the spring SLP and 500-hPa geopotential height anomalies upon the spring AO index. For both +PDO and −PDO, significant positive SLP and geopotential height anomalies are apparent over the North Atlantic, and marked negative SLP and geopotential height anomalies appear over the Arctic (**Figure 8**). However, the positive SLP and geopotential height anomalies over mid-high-latitudes North Pacific are much stronger for the +PDO than −PDO years (**Figures 7A,B**).

Studies have indicated that the interaction between synoptic-scale eddy and low-frequency mean flow plays an important role for the formation and maintenance of the spring AO-related atmospheric anomalies over North Pacific (Lau 1988; Chen et al., 2014, Chen et al., 2015). The weaker atmospheric anomalies related to the spring AO over the North Pacific for the −PDO years imply a weaker wave-mean flow interaction and a weaker feedback of synoptic-scale eddy to mean flow compared with those for the +PDO years. Feedback strength of the synoptic scale eddy to mean flow has a close connection with the climatological intensity of the storm track as has been demonstrated by previous studies (Jin et al., 2006a, Jin et al., 2006b; Jin, 2010; Chen et al., 2015). In particular, if strength of the low-frequency mean flow is similar, feedback strength of the synoptic scale eddy activity to mean flow is much stronger during the periods with stronger

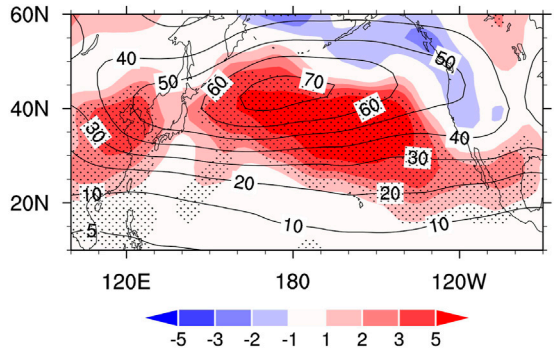

FIGURE 9 | Climatology of the spring 200-hPa storm track (contours, m) over 1950–2019. Shadings indicate differences in the climatology of spring storm track (shadings, m) between +PDO and –PDO years. Differences that are significantly different from zero at the 95% confidence level are stippled.

climatological storm track intensity, and vice versa (Chen et al., 2015, Chen et al., 2017). Climatology of the spring storm track activity over 1950–2019 (indicated by the contours) as well as the difference in the spring mean storm track between +PDO and −PDO years (indicated by the shadings) are shown in **Figure 9**. Maximum center of the climatology of spring storm track appears over mid-latitudes North Pacific around 45°N, 180°E (**Figure 9**). In addition, the difference map between + PDO and −PDO years shows significant positive storm track anomalies over North Pacific around 25°–45°N This indicates that the North Pacific storm track intensity in spring is much stronger and shifts southward during +PDO than -PDO. Therefore, according to the findings of previous studies (Jin et al., 2006a, Jin et al., 2006b; Jin, 2010; Chen et al., 2015), stronger climatological storm track over North Pacific during +PDO years would lead to stronger feedback of synoptic-scale eddy activities to low frequency mean flow. This explains the stronger atmospheric anomalies over North Pacific in association with the spring AO and, thus, the stronger impact of the spring AO on the following winter ENSO for the +PDO years than the −PDO years.

Then, how can the PDO modulate the intensity of the spring storm track over North Pacific? Studies have indicated that change in the storm track intensity is closely related to change in the mean meridional gradient of low-level temperature (Lindzen and Farrell 1980; Hoskins and Valdes 1990; Penny et al., 2010; Lee et al., 2012; Chen et al., 2015). Increase in the meridional gradient of low-level temperature is favorable for baroclinic growth of the synoptic scale eddy and lead to increase in the storm track (Lindzen and Farrell 1980; Hoskins and Valdes 1990; Penny et al., 2010; Chen et al., 2015). Differences in the spring mean SST and air temperature at 100-hPa between +PDO and −PDO years are shown in **Figures 10A**, B, respectively. Spatial structure of the SST difference is similar to that of the 1,000-hPa air temperature difference. Mean SST and 1,000-hPa air temperature is significantly stronger along west coast of North America with a southwestward extension to the tropical central-eastern Pacific and significantly weaker to the east of Japan around 30°–40°N (**Figure 10**). Hence, the mean meridional gradient of low-level temperature over the subtropical North Pacific is much larger for +PDO than −PDO years. This suggests that PDO could modulate spring storm track intensity *via* modulating the mean meridional temperature gradient.

SUMMARY

Previous studies indicated that the spring AO has a significant impact on the following winter ENSO, but such impact is unstable. In this study, we reveal that the PDO acts as one of the important factors in modulating the spring AO–winter ENSO connection. When PDO is in its positive phase, spring AO has a pronounced impact on the following winter ENSO. By contrast, during the negative PDO phase, the linkage between the spring AO and the following winter ENSO is not robust.

We further examine the factors for the notable modulation effect of the PDO on the spring AO-winter ENSO connection. During +PDO years, a significant anticyclonic circulation anomaly is seen over mid-high-latitudes North Pacific and a pronounced cyclonic circulation anomaly is found over subtropical North Pacific. This leads to significant westerly wind anomalies over the tropical western-central Pacific, which further impacts the following winter ENSO occurrence *via* triggering eastward propagating and downwelling Kelvin wave. In addition, the subtropical cyclonic anomaly induces SST warming in the subtropical central North

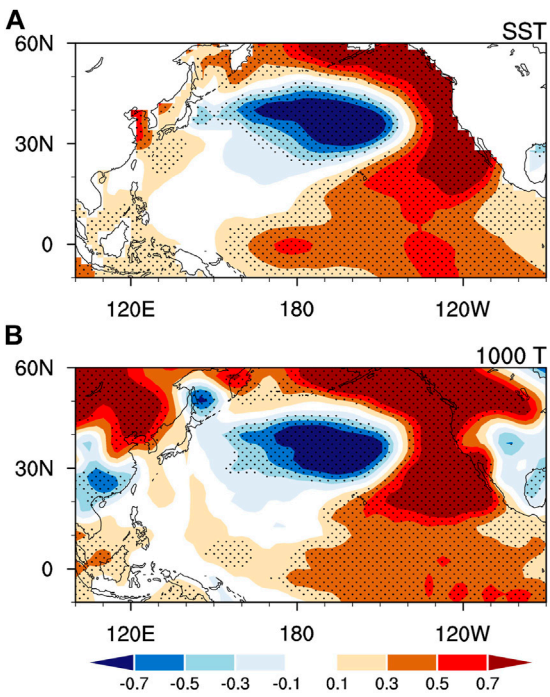

FIGURE 10 | Differences in the climatology of spring **(A)** SST (°C) and **(B)** air temperature at 1,000-hPa between +PDO and −PDO years. Differences that are significantly different from zero at the 95% confidence level are stippled.

Pacific, resembling the PMM pattern, *via* modulating surface latent heat flux. The subtropical PMM-like SST warming maintains and extends southward to the tropical central Pacific *via* WES feedback mechanism, which further impact following winter ENSO occurrence through the tropical air-sea interaction. However, for the −PDO years, the atmospheric anomalies over the North Pacific related to the spring AO are much weaker. Correspondingly, the SST warming and atmospheric heating anomalies over the North Pacific are weak. As such, the spring AO has a weak impact on the following winter ENSO.

Further analysis shows that the spring storm track activity over the North Pacific is much stronger during +PDO years than that during −PDO years. Stronger climatological spring storm track activity during +PDO leads to a stronger eddy feedback to low-frequency mean flow, which explains stronger atmospheric anomalies over the North Pacific in association with the AO. In addition, it is suggested that PDO could modulate the spring North Pacific storm track intensity *via* changing the mean meridional gradient of the low-level temperature, with much larger mean meridional temperature gradient during +PDO than −PDO years.

DATA AVAILABILITY STATEMENT

The original contributions presented in the study are included in the article/Supplementary Material. Further inquiries can be directed to the corresponding author.

AUTHOR CONTRIBUTIONS

SC designed the research, performed the analysis, and wrote the manuscript. All authors discussed the results and revised the manuscript.

FUNDING

This study is supported by the National Natural Science Foundation of China (Grant 42175039) and the Scientific Research Fund of the Second Institute of Oceanography, Ministry of Natural Resources (Grant QNYC 2001).

REFERENCES

Alexander, M. A., Bladé, I., Newman, M., Lanzante, J. R., Lau, N. C., and Scott, J. D. (2002). The Atmospheric Bridge: The Influence of ENSO Teleconnections on Air-Sea Interaction over the Global Oceans. *J. Clim.* 15, 2205–2231. doi:10.1175/1520-0442(2002)015<2205:tabtio>2.0.co;2

Alexander, M. A., Vimont, D. J., Chang, P., and Scott, J. D. (2010). The Impact of Extratropical Atmospheric Variability on ENSO: Testing the Seasonal Footprinting Mechanism Using Coupled Model Experiments. *J. Clim.* 23, 2885–2901. doi:10.1175/2010jcli3205.1

Barnett, T. P. (1983). Interaction of the Monsoon and Pacific Trade Wind System at Interannual Time Scales Part I: the Equatorial Zone. *Mon. Wea. Rev.* 111, 756–773. doi:10.1175/1520-0493(1983)111<0756:iotmap>2.0.co;2

Bjerknes, J. (1969). Atmospheric Teleconnections from the Equatorial Pacific1. *Mon. Wea. Rev.* 97, 163–172. doi:10.1175/1520-0493(1969)097<0163:atftep>2.3.co;2

Budikova, D. (2005). Impact of the Pacific Decadal Oscillation on Relationships between Temperature and the Arctic Oscillation in the USA in winter. *Clim. Res.* 29, 199–208. doi:10.3354/cr029199

Cai, M., Yang, S., Van Den Dool, H. M., and Kousky, V. E. (2007). Dynamical Implications of the Orientation of Atmospheric Eddies: a Local Energetics Perspective. *Tellus A: Dynamic Meteorology and Oceanography* 59, 127–140. doi:10.1111/j.1600-0870.2006.00213.x

Chang, E. K. M., and Fu, Y. (2002). Interdecadal Variations in Northern Hemisphere winter Storm Track Intensity. *J. Clim.* 15, 642–658. doi:10.1175/1520-0442(2002)015<0642:ivinhw>2.0.co;2

Chang, P., Zhang, L., Saravanan, R., Vimont, D. J., Chiang, J. C. H., Ji, L., et al. (2007). Pacific Meridional Mode and El Niño-Southern Oscillation. *Geophys. Res. Lett.* 34 (6), L16608. doi:10.1029/2007gl030302

Chen, D., and Lian, T. (2020). Frontier of El Niño-Southern Oscillation Research. *Chin. Sci. Bull.* 65, 4001–4003. doi:10.1360/tb-2020-1219

Chen, D., Lian, T., Fu, C., Cane, M. A., Tang, Y., Murtugudde, R., et al. (2015). Strong Influence of westerly Wind Bursts on El Niño Diversity. *Nat. Geosci* 8 (5), 339–345. doi:10.1038/ngeo2399

Chen, L., Li, T., Wang, B., and Wang, L. (2016b). Formation Mechanism for 2015/16 Super El Niño. *Sci. Rep.* 7, 2975. doi:10.1038/s41598-017-02926-3

Chen, L., Li, T., Yu, Y., and Behera, S. (2016a). A Possible Explanation for the Divergent Projection of ENSO Amplitude Change under Global Warming. *Clim. Dynam.* 49, 3799–3811.

Chen, L., Wang, L., Li, T., and Liu, J. (2019a). Drivers of Reduced ENSO Variability in Mid-holocene in a Coupled Model. *Clim. Dyn.* 52, 5999–6014. doi:10.1007/s00382-018-4496-5

Chen, L., Zheng, W., and Braconnot, P. (2019b). Towards Understanding the Suppressed ENSO Activity during Mid-holocene in PMIP2 and PMIP3 Simulations. *Clim. Dyn.* 53, 1095–1110. doi:10.1007/s00382-019-04637-z

Chen, S., Chen, W., and Wei, K. (2013). Recent Trends in winter Temperature Extremes in Eastern China and Their Relationship with the Arctic Oscillation and ENSO. *Adv. Atmos. Sci.* 30, 1712–1724. doi:10.1007/s00376-013-2296-8

Chen, S., Chen, W., Wu, R., Yu, B., and Graf, H.-F. (2020c). Potential Impact of Preceding Aleutian Low Variation on El Niño-Southern Oscillation during the Following Winter. *J. Clim.* 33, 3061–3077. doi:10.1175/jcli-d-19-0717.1

Chen, S., Chen, W., and Yu, B. (2017). The Influence of Boreal spring Arctic Oscillation on the Subsequent winter ENSO in CMIP5 Models. *Clim. Dyn.* 48, 2949–2965. doi:10.1007/s00382-016-3243-z

Chen, S. F., Wu, R., Chen, W., and Yu, B. (2020b). Influence of winter Arctic Sea Ice Concentration Change on the El Niño-Southern Oscillation in the Following winter. *Clim. Dynam.* 54 (1), 741–757. doi:10.1007/s00382-019-05027-1

Chen, S. F., Wu, R., Chen, W., and Yu, B. (2020a). Recent Weakening of the Linkage between the spring Arctic Oscillation and the Following winter El Niño-Southern Oscillation. *Clim. Dynam.* 54 (1), 53–67. doi:10.1007/s00382-019-04988-7

Chen, S., Wu, R., Chen, W., Yu, B., and Cao, X. (2016c). Genesis of westerly Wind Bursts over the Equatorial Western Pacific during the Onset of the strong 2015-2016 El Niño. *Atmos. Sci. Lett.* 17, 384–391. doi:10.1002/asl.669

Chen, S., and Wu, R. (2018). Impacts of winter NPO on Subsequent winter ENSO: Sensitivity to the Definition of NPO index. *Clim. Dyn.* 50, 375–389. doi:10.1007/s00382-017-3615-z

Chen, S., Yu, B., and Chen, W. (2014). An Analysis on the Physical Process of the Influence of AO on ENSO. *Clim. Dyn.* 42, 973–989. doi:10.1007/s00382-012-1654-z

Chen, S., Yu, B., and Chen, W. (2015). An Interdecadal Change in the Influence of the spring Arctic Oscillation on the Subsequent ENSO Around the Early 1970s. *Clim. Dyn.* 44, 1109–1126. doi:10.1007/s00382-014-2152-2

Chen, W., Graf, H. F., and Huang, R. H. (2000). The Interannual Variability of East Asian winter Monsoon and its Relation to the Summer Monsoon. *Adv. Atmos. Sci.* 17, 48–60.

Cheung, H. N., Zhou, W., Mok, H. Y., and Wu, M. C. (2012). Relationship between Ural-Siberian Blocking and the East Asian Winter Monsoon in Relation to the Arctic Oscillation and the El Niño-Southern Oscillation. *J. Clim.* 25, 4242–4257. doi:10.1175/jcli-d-11-00225.1

Chiang, J. C. H., and Vimont, D. J. (2004). Analogous Pacific and Atlantic Meridional Modes of Tropical Atmosphere-Ocean Variability*. *J. Clim.* 17, 4143–4158. doi:10.1175/jcli4953.1

Choi, K. S., Wu, C. C., and Byun, H. R. (2012). Possible Connection between Summer Tropical Cyclone Frequency and spring Arctic Oscillation over East Asia. *Clim. Dyn.* 38, 2613–2629. doi:10.1007/s00382-011-1088-z

Ding, R. Q., Li, J. P., and Tseng, Y. H. (2015). The Impact of South Pacific Extratropical Forcing on ENSO and Comparisons with the North Pacific. *Clim. Dynam.* 44, 2017–2034. doi:10.1007/s00382-014-2303-5

Ding, Y., Liu, Y., Liang, S., Ma, X., Zhang, Y., Si, D., et al. (2014). Interdecadal Variability of the East Asian winter Monsoon and its Possible Links to Global Climate Change. *J. Meteorol. Res.* 28, 693–713. doi:10.1007/s13351-014-4046-y

Duchon, C. E. (1979). Lanczos Filtering in One and Two Dimensions. *J. Appl. Meteorol.* 18, 1016–1022. doi:10.1175/1520-0450(1979)018<1016:lfioat>2.0.co;2

Fang, X., and Xie, R. (2020). A Brief Review of ENSO Theories and Prediction. *Sci. China Earth Sci.* 63 (4), 476–491. doi:10.1007/s11430-019-9539-0

Gill, A. E. (1980). Some Simple Solutions for Heat-Induced Tropical Circulation. *Q.J R. Met. Soc.* 106, 447–462. doi:10.1002/qj.49710644905

Gong, D. Y., Yang, J., Kim, S. J., Gao, Y., Guo, D., Zhou, T., et al. (2011). Spring Arctic Oscillation-East Asian Summer Monsoon Connection through Circulation Changes over the Western North Pacific. *Clim. Dyn.* 37, 2199–2216. doi:10.1007/s00382-011-1041-1

Horel, J. D., and Wallace, J. M. (1981). Planetary-scale Atmospheric Phenomena Associated with the Southern Oscillation. *Mon. Wea. Rev.* 109, 813–829. doi:10.1175/1520-0493(1981)109<0813:psapaw>2.0.co;2

Hoskins, B. J., and Valdes, P. J. (1990). On the Existence of Storm-Tracks. *J. Atmos. Sci.* 47, 1854–1864. doi:10.1175/1520-0469(1990)047<1854:oteost>2.0.co;2

Hu, K., Huang, G., Huang, P., Kosaka, Y., and Xie, S.-P. (2021). Intensification of El Niño-Induced Atmospheric Anomalies under Greenhouse Warming. *Nat. Geosci.* 14, 377–382. doi:10.1038/s41561-021-00730-3

Hu, P., Chen, W., Chen, S., Liu, Y., and Huang, R. (2020). Extremely Early Summer Monsoon Onset in the South China Sea in 2019 Following an El Niño Event. *Mon. Wea. Rev.* 148, 1877–1890. doi:10.1175/mwr-d-19-0317.1

Huang, B., Thorne, P. W., Banzon, V. F., Boyer, T., Chepurin, G., Lawrimore, J. H., et al. (2017). Extended Reconstructed Sea Surface Temperature, Version 5 (ERSSTv5): Upgrades, Validations, and Intercomparisons. *J. Clim.* 30 (20), 8179–8205. doi:10.1175/jcli-d-16-0836.1

Huang, R. H., Chen, W., Yang, B. L., and Zhang, R. H. (2004). Recent Advances in Studies of the Interaction between the East Asian winter and Summer Monsoons and ENSO Cycle. *Adv. Atmos. Sci.* 21, 407–424. doi:10.1007/bf02915679

Huang, R., Zhang, R., and Yan, B. (2001). Dynamical Effect of the Zonal Wind Anomalies over the Tropical Western Pacific on ENSO Cycles. *Sci. China Ser. D-earth Sci.* 44 (12), 1089–1098. doi:10.1007/bf02906865

Jin, F. F. (1997). An Equatorial Ocean Recharge Paradigm for ENSO. Part I: Conceptual Model. *J. Atmos. Sci.* 54, 811–829. doi:10.1175/1520-0469(1997)054<0811:aeorpf>2.0.co;2

Jin, F. F. (2010). Eddy-induced Instability for Low-Frequency Variability. *J. Atmos. Sci.* 67, 1947–1964. doi:10.1175/2009jas3185.1

Jin, F. F., Pan, L. L., and Watanabe, M. (2006a). Dynamics of Synoptic Eddy and Low-Frequency Flow Interaction. Part I: A Linear Closure. *J. Atmos. Sci.* 63, 1677–1694. doi:10.1175/jas3715.1

Jin, F. F., Pan, L. L., and Watanabe, M. (2006b). Dynamics of Synoptic Eddy and Low-Frequency Flow Interaction. Part II: A Theory for Low-Frequency Modes. *J. Atmos. Sci.* 63, 1695–1708. doi:10.1175/jas3716.1

Kalnay, E., Kanamitsu, M., Kistler, R., Collins, W., Deaven, D., Gandin, L., et al. (1996). The NCEP/NCAR 40-year Reanalysis Project. *Bull. Amer. Meteorol. Soc.* 77, 437–471. doi:10.1175/1520-0477(1996)077<0437:tnyrp>2.0.co;2

Kim, J. W., Yeh, S. W., and Chang, E. C. (2014). Combined Effect of El Niño-Southern Oscillation and Pacific Decadal Oscillation on the East Asian winter Monsoon. *Clim. Dyn.* 42, 957–971. doi:10.1007/s00382-013-1730-z

Lau, N. C. (1988). Variability of the Observed Midlatitude Storm Tracks in Relation to Low-Frequency Changes in the Circulation Pattern. *J. Atmos. Sci.* 45, 2718–2743. doi:10.1175/1520-0469(1988)045<2718:votoms>2.0.co;2

Lee, S. S., Lee, J. Y., Wang, B., Ha, K. J., Heo, K. Y., Jin, F. F., et al. (2012). Interdecadal Changes in the Storm Track Activity over the North Pacific and North Atlantic. *Clim. Dyn.* 39, 313–327. doi:10.1007/s00382-011-1188-9

Lengaigne, M., Guilyardi, E., Boulanger, J.-P., Menkes, C., Delecluse, P., Inness, P., et al. (2004). Triggering of El Ni**o** by westerly Wind Events in a Coupled General Circulation Model. *Clim. Dyn.* 23, 601–620. doi:10.1007/s00382-004-0457-2

Li, C. Y. (1990). Interaction between Anomalous winter Monsoon in East Asia and El Niño Events. *Adv. Atmos. Sci.* 7 (1), 36–46.

Limpasuvan, V., and Hartmann, D. L. (1999). Eddies and the Annular Modes of Climate Variability. *Geophys. Res. Lett.* 26, 3133–3136. doi:10.1029/1999gl010478

Lindzen, R. S., and Farrell, B. (1980). A Simple Approximate Result for the Maximum Growth Rate of Baroclinic Instabilities. *J. Atmos. Sci.* 37, 1648–1654. doi:10.1175/1520-0469(1980)037<1648:asarft>2.0.co;2

Linkin, M. E., and Nigam, S. (2008). The north pacific Oscillation-West Pacific Teleconnection Pattern: Mature-phase Structure and winter Impacts. *J. Clim.* 21, 1979–1997. doi:10.1175/2007jcli2048.1

Lorenz, D. J., and Hartmann, D. L. (2003). Eddy-zonal Flow Feedback in the Northern Hemisphere winter. *J. Clim.* 16, 1212–1227. doi:10.1175/1520-0442(2003)16<1212:effitn>2.0.co;2

Mantua, N. J., Hare, S. R., Zhang, Y., Wallace, J. M., and Francis, R. C. (1997). A Pacific Interdecadal Climate Oscillation with Impacts on salmon Production. *Bull. Amer. Meteorol. Soc.* 78, 1069–1079. doi:10.1175/1520-0477(1997)078<1069:apicow>2.0.co;2

Min, Q., Su, J., and Zhang, R. (2017). Impact of the South and North Pacific Meridional Modes on the El Niño-Southern Oscillation: Observational Analysis and Comparison. *J. Clim.* 30, 1705–1720. doi:10.1175/jcli-d-16-0063.1

Nakamura, T., Tachibana, Y., Honda, M., and Yamane, S. (2006). Influence of the Northern Hemisphere Annular Mode on ENSO by Modulating westerly Wind Bursts. *Geophys. Res. Lett.* 33, L07709. doi:10.1029/2005gl025432

Neelin, J. D., Battisti, D. S., Hirst, A. C., Jin, F.-F., Wakata, Y., Yamagata, T., et al. (1998). ENSO Theory. *J. Geophys. Res.* 103, 14261–14290. doi:10.1029/97jc03424

Penny, S., Roe, G. H., and Battisti, D. S. (2010). The Source of the Midwinter Suppression in Storminess over the North Pacific. *J. Clim.* 23, 634–648. doi:10.1175/2009jcli2904.1

Philander, S. G. (1990). *El Niño, La Niña, and the Southern Oscillation*, 46. London, UK: Academic Press, 289p.

Ren, H. L., Jin, F. F., Tian, B., and Scaife, A. A. (2016). Distinct Persistence Barriers in Two Types of ENSO. *Geophys. Res. Lett.* 43 (20), 10973–10979. doi:10.1002/2016gl071015

Schopf, P. S., and Suarez, M. J. (1988). Vacillations in a Coupled Ocean-Atmosphere Model. *J. Atmos. Sci.* 45, 549–566. doi:10.1175/1520-0469(1988)045<0549:viacom>2.0.co;2

Song, L., Chen, S., Chen, W., and Chen, X. (2017). Distinct Impacts of Two Types of La Niña Events on Australian Summer Rainfall. *Int. J. Climatol.* 37, 2532–2544. doi:10.1002/joc.4863

Song, L., Li, Y., and Duan, W. (2016). The Influence of Boreal winter Extratropical North Pacific Oscillation on Australian spring Rainfall. *Clim. Dyn.* 47, 1181–1196. doi:10.1007/s00382-015-2895-4

Su, J., Li, T., and Zhang, R. (2014). The Initiation and Developing Mechanisms of Central Pacific El Niños. *J. Clim.* 27 (12), 4473–4485. doi:10.1175/jcli-d-13-00640.1

Tang, Y., Zhang, R.-H., Liu, T., Duan, W., Yang, D., Zheng, F., et al. (2018). Progress in ENSO Prediction and Predictability Study. *Natl. Sci. Rev.* 5 (6), 826–839. doi:10.1093/nsr/nwy105

Thompson, D. W. J., Lee, S., and Baldwin, M. P. (2003). Atmospheric Processes Governing the Northern Hemisphere Annular Mode/North Atlantic Oscillation. *Geophys. Monogr. Am. Geophys. Union134*, 81–112. doi:10.1029/134gm05

Thompson, D. W. J., and Wallace, J. M. (2000). Annular Modes in the Extratropical Circulation. Part I: Month-To-Month Variability*. *J. Clim.* 13, 1000–1016. doi:10.1175/1520-0442(2000)013<1000:amitec>2.0.co;2

Thompson, D. W. J., and Wallace, J. M. (1998). The Arctic Oscillation Signature in the Wintertime Geopotential Height and Temperature fields. *Geophys. Res. Lett.* 25, 1297–1300. doi:10.1029/98gl00950

Vimont, D. J., Battisti, D. S., and Hirst, A. C. (2001). Footprinting: A Seasonal Connection between the Tropics and Mid-latitudes. *Geophys. Res. Lett.* 28, 3923–3926. doi:10.1029/2001gl013435

Vimont, D. J., Wallace, J. M., and Battisti, D. S. (2003). The Seasonal Footprinting Mechanism in the Pacific: Implications for ENSO*. *J. Clim.* 16, 2668–2675. doi:10.1175/1520-0442(2003)016<2668:tsfmit>2.0.co;2

Wallace, J. M., and Gutzler, D. S. (1981). Teleconnections in the Geopotential Height Field during the Northern Hemisphere winter. *Mon. Wea. Rev.* 109, 784–812. doi:10.1175/1520-0493(1981)109<0784:titghf>2.0.co;2

Wang, B., Wu, R., and Fu, X. (2000). Pacific-east Asian Teleconnection: How Does ENSO Affect East Asian Climate? *J. Clim.* 13, 1517–1536. doi:10.1175/1520-0442(2000)013<1517:peathd>2.0.co;2

Wang, L., Chen, W., and Huang, R. (2008). Interdecadal Modulation of PDO on the Impact of ENSO on the East Asian winter Monsoon. *Geophys. Res. Lett.* 35, L20702. doi:10.1029/2008gl035287

Wang, X., Wang, C., Zhou, W., Wang, D., and Song, J. (2011). Teleconnected Influence of North Atlantic Sea Surface Temperature on the El Niño Onset. *Clim. Dynam.* 37, 663–676. doi:10.1007/s00382-010-0833-z

Wei, K., Ouyang, C., Duan, H., Li, Y., Chen, M., Ma, J., et al. (2020). Reflections on the Catastrophic 2020 Yangtze River basin Flooding in Southern china. *The Innovation* 1. doi:10.1016/j.xinn.2020.100038

Xie, S. P., and Philander, S. G. H. (1994). A Coupled Ocean-Atmosphere Model of Relevance to the ITCZ in the Eastern Pacific. *Tellus Ser. A-dyn. Meteorol. Oceanol.* 46, 340–350. doi:10.1034/j.1600-0870.1994.t01-1-00001.x

Yang, X., and Huang, P. (2021). Restored Relationship between ENSO and Indian Summer Monsoon Rainfall Around 1999/2000. *The Innovation* 2, 100102. doi:10.1016/j.xinn.2021.100102

Yeh, S. W., Wang, X., Wang, C., and Dewitte, B. (2015). On the Relationship between the North Pacific Climate Variability and the central Pacific El Niño. *J. Clim.* 28 (2), 663–677. doi:10.1175/jcli-d-14-00137.1

Yu, B., and Zwiers, F. (2007). The Impact of Combined ENSO and PDO on the PNA Climate: a 1,000-year Climate Modeling Study. *Clim. Dynam.* 29, 837–851. doi:10.1007/s00382-007-0267-4

Yu, J. Y., Kim, S. T., and Lu, M. (2012). A Change in the Relationship between Tropical central Pacific SST Variability and the Extratropical Atmosphere Around 1990. *Environ. Res. Lett.* 7 (3), 034025. doi:10.1088/1748-9326/7/3/034025

Zhai, P. M., Rong, Y. U., Xuejuan, R., Yaqiang, W., Wenhui, X. U., Yanju, L., et al. (2016). The strong El Niño of 2015/16 and its Dominant Impacts on Global and China's Climate. *J. Meteorol. Res.* 30 (3), 283–297. doi:10.1007/s13351-016-6101-3

Zhang, R. H., Sumi, A., and Kimoto, M. (1996). Impact of El Niño on the East Asian Monsoon: A Diagnostic Study of the '86/87 and '91/92 Events. *J. Meteorol. Soc. Jpn.* 74 (1), 49–62. doi:10.2151/jmsj1965.74.1_49

Zhang, R. H., Yu, Y., Song, Z., Ren, H., Tang, Y., Qiao, F., et al. (2020). A Review of Progress in Coupled Ocean-Atmosphere Model Developments for ENSO Studies in China. *J. Ocean Limnology* 38 (4), 930–961. doi:10.1007/s00343-020-0157-8

Zhang, W. J., Jin, F. F., Li, J. P., and Ren, H. L. (2011). Contrasting Impacts of Two-type El Niño over the Western North Pacific during Boreal Autumn. *J. Meteorol. Soc. Jpn.* 89, 563–569. doi:10.2151/jmsj.2011-510

Zhang, W. J., Jin, F. F., Ren, H. L., Li, J. P., and Zhao, J. X. (2012). Differences in Teleconnection over the North Pacific and Rainfall Shift over the USA Associated with Two Types of El Niño during Boreal Autumn. *J. Meteorol. Soc. Jpn.* 90, 535–552. doi:10.2151/jmsj.2012-407

Zhang, Y., Wallace, J. M., and Battisti, D. S. (1997). ENSO-like Interdecadal Variability: 1900-93. *J. Clim.* 10, 1004–1020. doi:10.1175/1520-0442(1997)010<1004:eliv>2.0.co;2

Zheng, Y., Chen, S., Chen, W., and Yu, B. (2021). Diverse Influences of spring Arctic Oscillation on the Following winter El Niño-Southern Oscillation in CMIP5 Models. *Clim. Dynam.* 56, 275–297. doi:10.1007/s00382-020-05483-0

Zheng, Y. Q., Chen, W., and Chen, S. F. (2021). Intermodel Spread in the Impact of the Springtime Pacific Meridional Mode on Following-winter ENSO Tied to Simulation of the ITCZ in CMIP5/CMIP6. *Geophys. Res. Lett.* 48, e2021GL093945. doi:10.1029/2021gl093945

Zhou, W., and Chan, J. C. L. (2007). ENSO and South China Sea Summer Monsoon Onset. *Int. J. Climatol.* 27, 157–167. doi:10.1002/joc.1380

Zhou, W., Wang, X., Zhou, T. J., and Chan, J. C. L. (2007). Interdecadal Variability of the Relationship between the East Asian winter Monsoon and ENSO. *Meteorol. Atmos. Phys.* 98, 283–293. doi:10.1007/s00703-007-0263-6

Conflict of Interest: The authors declare that the research was conducted in the absence of any commercial or financial relationships that could be construed as a potential conflict of interest.

frontiers in Earth Science

ORIGINAL RESEARCH
published: 15 February 2022
doi: 10.3389/feart.2022.822854

Key Processes on Triggering the Moderate 2020/21 La Niña Event as Depicted by the Clustering Approach

Ting-Wei Cao[1,2], *Fei Zheng*[1]* *and Xiang-Hui Fang*[3]

[1]International Center for Climate and Environment Science (ICCES), Institute of Atmospheric Physics, Chinese Academy of Sciences, Beijing, China, [2]College of Earth and Planetary Sciences, University of Chinese Academy of Sciences, Beijing, China, [3]Department of Atmospheric and Oceanic Sciences and Institute of Atmospheric Sciences, Fudan University, Shanghai, China

The 2020/21 La Niña was not well predicted by most climate models when it started in early-mid 2020. This paper adopted an El Niño-Southern Oscillation (ENSO) ensemble prediction system to evaluate the key physical processes in the development of this cold event by performing a clustering analysis of 100 ensemble member predictions 1 year in advance. The abilities of two clustering approaches were first examined in regard to capturing the development of the 2020/21 La Niña event. One approach was index clustering, which adopted only the 12-month Niño3.4 indices in 2020 as an indicator, and the other was pattern clustering through contrasting the evolution of sea surface temperature (SST) anomalies over the tropical Pacific in 2020 for clustering. Pattern clustering surpasses index clustering in better describing the evolution over the off-equatorial and equatorial regions during the 2020/21 La Niña. Consequently, based on the pattern clustering approach, a comparison of the selected most (five best) and least (five worst) representative ensemble members illustrated that the predominance of anomalous southeasterly winds over the central equatorial Pacific in spring 2020 played a crucial role in initiating the moderate La Niña event in 2020/21, by preventing the development of westerly winds over the warm pool. Moreover, the inherent spring predictability barrier (SPB) was still a major challenge for improving the prediction skill of the 2020/21 La Niña event when the prediction occurred across the spring season.

Keywords: 2020/21 La Niña, clustering approach, southeasterly winds, SPB, off-equatorial processes

OPEN ACCESS

Edited by:
Hong-Li Ren,
Chinese Academy of Meteorological Sciences, China

Reviewed by:
Jieshun Zhu,
University of Maryland, United States
Xinghrong Chen,
National Marine Environmental Forecasting Center, China

***Correspondence:**
Fei Zheng
zhengfei@mail.iap.ac.cn

Specialty section:
This article was submitted to Atmospheric Science, a section of the journal Frontiers in Earth Science

Received: *26 November 2021*
Accepted: *04 January 2022*
Published: *15 February 2022*

Citation:
Cao TW, Zheng F and Fang XH (2022) Key Processes on Triggering the Moderate 2020/21 La Niña Event as Depicted by the Clustering Approach. Front. Earth Sci. 10:822854. doi: 10.3389/feart.2022.822854

INTRODUCTION

The El Niño-Southern Oscillation (ENSO), the largest interannual signal in the climate system, is a typical coupled atmosphere-ocean phenomenon with time scales of approximately 2–7 years (Ren et al., 2020). ENSO not only affects weather and climate anomalies in the equatorial Pacific but also affects other parts of the world through atmospheric teleconnections (Trenberth et al., 1998); therefore, successful prediction of ENSO has always been a hot topic (Luo et al., 2016; Song et al., 2021).

Since the 1960s, domestic and foreign scholars have established numerous theories regarding the onset and development of ENSO (Bjerknes, 1969; Wyrtki, 1975; Jin, 1997; Weisberg and Wang, 1997; Picaut et al., 1997); these theories offer much assistance in predicting and studying ENSO. With the increase in computing power and the introduction of techniques such as data assimilation (Evensen, 2004; Zheng and Zhu, 2010), current climate models can realize the effective prediction of El Niño

and La Niña events 6–12 months in advance (Jin et al., 2008; Barnston et al., 2012; Ludescher et al., 2013; Zhang and Gao, 2016; Zheng and Zhu, 2016; Ren et al., 2017; 2020; Zhang et al., 2020). However, there are also many problems in ENSO prediction, such as ENSO diversity (Xie et al., 2018; Ren et al., 2018) which indicates that various and complex forcing and feedback mechanisms exist throughout the entire process of ENSO onset and development (Kang et al., 2017), and this diversity still cannot be described well by current coupled models (Cai et al., 2018). Moreover, ENSO prediction skills were lower in the 2000s than in the 1980s or 1990s (Barnston et al., 2012; Zheng et al., 2016), even with an increase in ocean observations, especially in the equatorial tropical Pacific (Kumar et al., 2015). In addition, due to asymmetric ENSO features, the predictability between El Niño and La Niña events is distinctively different (Hu et al., 2019). First, the successful prediction of La Niña has not received the same attention as that of El Niño (Barnston et al., 2012). Feng et al. (2015) recognized that La Niña events are less predictable because of their weaker intensity and more features; Larson and Kirtman (2019) pointed out that El Niño events are more predictable from the aspect of the signal-to-noise ratio. Furthermore, most current models have a faster decline across the boreal spring in the prediction skill of La Niña events than for El Niño events (Lopez and Kirtman 2014).

The 2020/21 La Niña was not well predicted by most climate models when it started in early mid 2020 (IRI website at https://iri.columbia.edu/), which indicates that the onset and development of this event were complicated and that this event is worth exploring carefully. Furthermore, Zheng et al. (2021) pointed out that the 2020/21 La Niña event was responsible for the extremely cold winter in China, but they did not describe the key processes in this event and generally attributed them to atmospheric and oceanic processes. In this work, we utilized a clustering approach called pattern clustering because it is better and more reasonable for depicting the physical evolution of the tropical Pacific when compared with the traditional clustering approach called index clustering. This paper attempted to compare the information in an ENSO ensemble prediction system between the best and worst prediction members obtained by pattern clustering and found characteristics and key processes for this event. The paper is organized as follows: In **Section 2**, the selected model, data sources and methods are described. In **Section 3**, the comparison of the two clustering approaches is discussed. In **Section 4**, the main results through pattern clustering are reported. Finally, in **Section 5**, a conclusion and discussion are given.

MODEL, DATASETS AND METHODS

Model

This paper adopted the ENSO ensemble prediction system (EPS) developed at the Institute of Atmospheric Physics (IAP), Chinese Academy of Sciences (Zheng et al., 2006; Zheng et al., 2009; Zheng and Zhu, 2016), to evaluate the key processes of the 2020/21 La Niña event. This system utilizes the ensemble Kalman filter (EnKF) data assimilation method (Zheng and Zhu, 2010), which is based on an intermediate coupled model, and establishes ENSO real-time prediction (Zheng and Zhu, 2015) by taking the initial uncertainty and the uncertainty in the prediction process into account (Zheng et al., 2009). The implementation of a 20-year retrospective 12-month ensemble forecast experiment proved that the EPS can successfully predict the possibility of ENSO events 1 year in advance (Zheng and Zhu, 2016).

Datasets

Based on this model using the same initial conditions but different stochastic model error perturbations, we obtained 100 ensemble members that predict a 12-month lead from January 2020. The prediction results contained monthly data of physical quantities such as the sea surface temperature anomaly (SSTA), 20°C isotherm depth anomaly (Z20), zonal wind stress anomaly (Tauxa), and meridional wind stress anomaly (Tauya). This dataset has a longitude interval of 2° and an unequal latitude interval of 0.5°. The SSTA in the observation data was derived from the monthly extended reconstruction of SST data (ERSST v5) (Huang et al., 2017), with a horizontal resolution of 2°, and the monthly wind stress data were from the NECP–DOE (National Centers for Environmental Prediction–Department of Energy) Reanalysis II (Kanamitsu et al., 2002), with a global T62 Gaussian grid (192 × 94).

Methods

Clustering analysis, a statistical approach, is widely used in ENSO research and related studies. Cassou and Terray (2001) pointed out the asymmetrical role of El Niño and La Niña in influencing the winter atmospheric variability of the North Atlantic/Europe using K-means clustering. Singh and Delcroix (2013) indicated that the EP El Niño (maximum anomalous warm center in the equatorial eastern Pacific) and CP El Niño (same as EP El Niño but in the equatorial central Pacific) have different recharge and discharge processes through hierarchical clustering analysis. Zhao et al. (2020), using clustering analysis, demonstrated that the Pacific meridional mode (PMM) has two types, which have different characteristics on the impact of ENSO. As a classification method in machine learning, clustering usually includes K-nearest neighbor (KNN) clustering, K-means clustering and hierarchical clustering. In this paper, the principle of the KNN clustering algorithm was adopted; that is, we selected the k-training samples nearest to the input sample in the feature space, and we could also select abnormal values compared with the input sample. Therefore, this paper aims to find the closest and farthest prediction members to the observations. The distance between the prediction members and observation sample is calculated based on the Euclidean distance. The calculation formula is as follows:

$$d_{ij} = \sqrt{\sum_{k=1}^{p} (x_{ik} - x_{jk})^2} \quad (1)$$

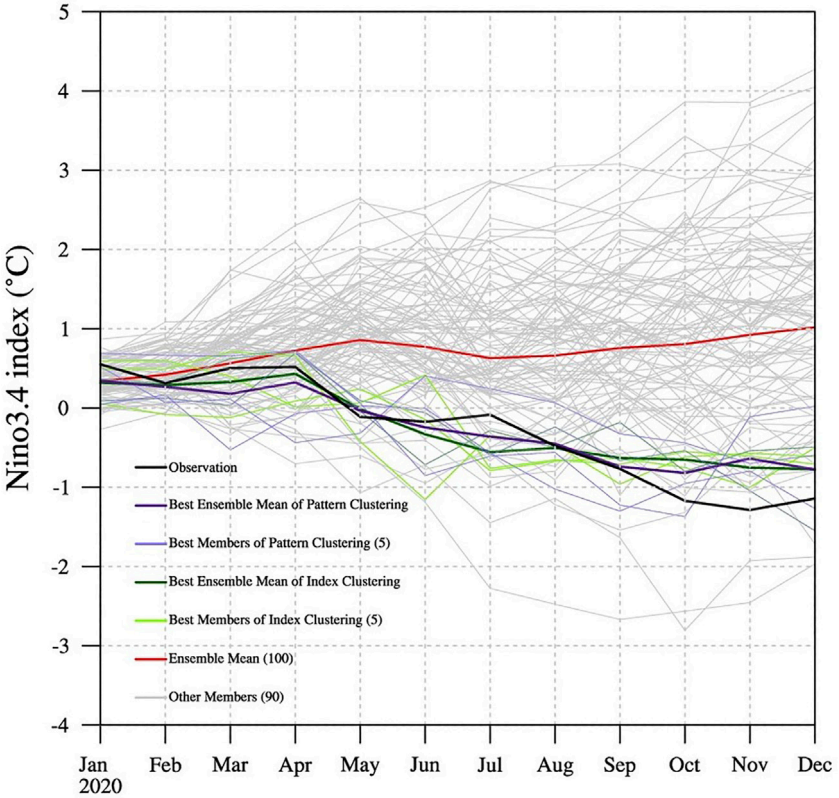

FIGURE 1 | The temporal variation in the Niño3.4 index in 2020 of the observations (black line) and of the best prediction members selected by the two clustering methods. The red line represents the ensemble mean from all 100 ensemble members. The green lines represent the best five ensemble members (light) with the ensemble-mean forecast (dark) selected by index clustering, the purple lines represent the best five ensemble members (light) with the ensemble-mean forecast (dark) selected by pattern clustering, and other gray lines are other residual ensemble members.

In this formula, i and j represent two different samples, which can be regarded as the prediction and observation, respectively, k represents the corresponding elements between the two samples, and p is the total number of samples.

To obtain members closer to the observations from the ensemble members, two different clustering approaches were adopted, namely, index clustering and pattern clustering. The former was based on 12-month Niño3.4 (170°W-120°W, 5°S-5°N) indices for clustering to obtain different degrees of similarity in the actual evolution of the Niño3.4 index among ensemble members and only utilized the SSTA-based index for clustering, called as index clustering. The latter realized clustering by using the 12-month Pacific anomalous SST (120°E-80°W, 30°S-30°N) evolution, and it is referred to pattern clustering. At the same time, this paper adopted principal component analysis (PCA) which is an unsupervised machine learning method commonly used in dimensionality reduction, to reduce the amount of calculation of pattern clustering. In this work, we regarded the 12-month Pacific SSTA field as a whole, which was the input of the PCA, and extracted an explanation variance of 90% to represent the evolution of the 12-month Pacific SSTA. Finally, the output of PCA was performed for clustering analysis.

THE ABILITY OF INDEX CLUSTERING AND PATTERN CLUSTERING TO REPRESENT LA NIÑA'S DEVELOPMENT IN 2020/21

As indicated by Zheng et al. (2021), the moderate 2020/21 La Niña event originated from the cold SSTA of the equatorial eastern Pacific in May 2020, gaining strength and spreading westward under the easterly wind anomaly in the autumn, and since October 2020, the Niño3.4 index exceeded −1.0°C and reached its peak in the boreal winter.

To find ensemble members that were closer to the development of the 2020/21 La Niña event, this paper utilized two clustering approaches (index clustering and pattern clustering) to obtain the top five best ensemble members, which were mostly similar to the observations, called the best prediction members (**Figure 1**). On the one hand, the ensemble mean of the model indicated that the equatorial Pacific developed into an El Niño event in 2020, while in reality it developed into a La Niña event, which was completely opposite of the observations, illustrating that the model starting from January also failed to predict the 2020/21 La Niña event. On the other hand, the best members selected by the two clustering approaches had temporal variations in the Niño3.4 index similar to the

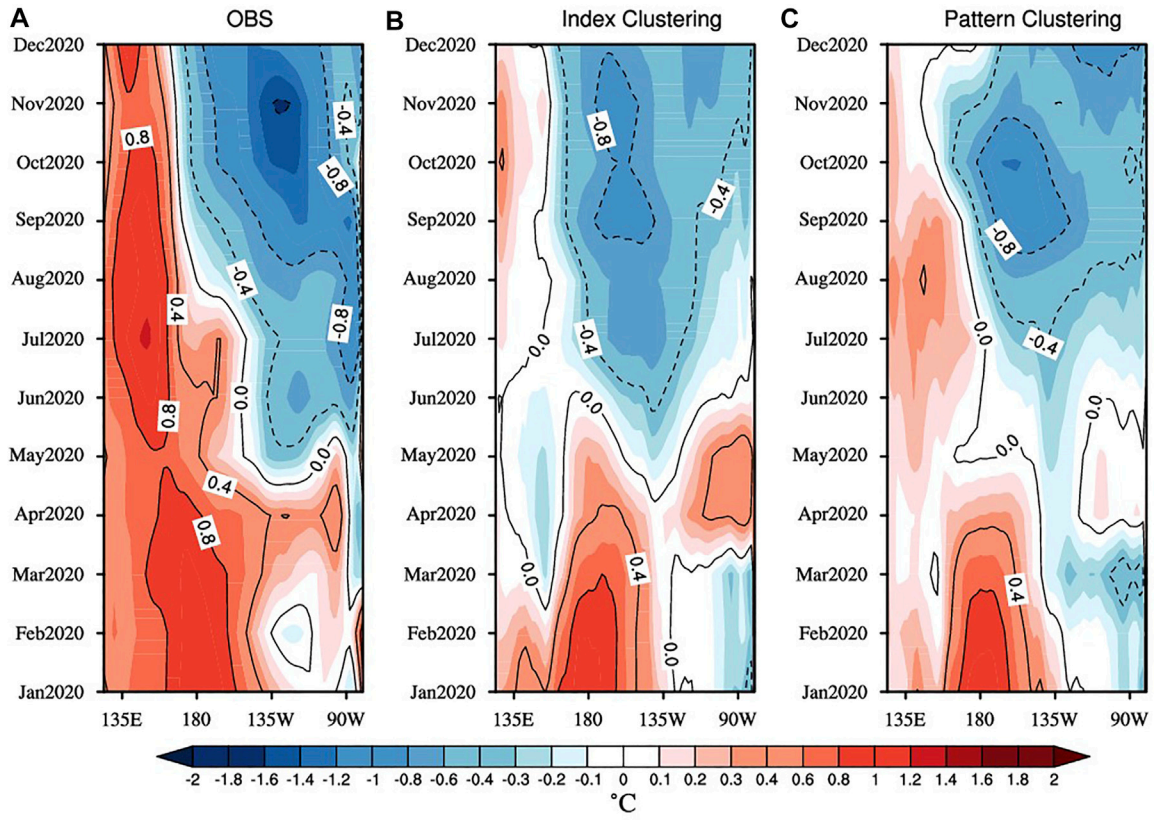

FIGURE 2 | Temporal evolution of the SSTA along the equatorial Pacific (averaged between 5°S and 5°N) in 2020 for **(A)** observations, **(B)** the ensemble mean of the best prediction members by index clustering, and **(C)** the ensemble mean of the best prediction members by pattern clustering. The contour interval is 0.4°C.

observations, and there were few obvious differences in index evolution between the two methods. Furthermore, it was necessary to find a better method, such as the evolution of sea surface temperature or the wind field, to distinguish these two approaches.

The SSTA distributions obtained by the two clustering approaches were further explored, and we not only paid attention to the evolution of the SSTA within the equator (**Figure 2**) but also showed the evolutionary characteristics of the SSTA outside the equator (**Figure 3**). The onset time of this La Niña event was May 2020 based on observations of the anomalous development of the cold SSTA of this La Niña event within the equator as mentioned in previous work (Zheng et al., 2021). The cold SSTA gradually spread westward over time, reaching La Niña status (i.e., the Niño 3.4 index exceeded -0.5°C) in August, and approached its peak in November 2020, forming a moderate La Niña event (**Figure 1**). The cold anomaly center was located near 135°W, and the entire equatorial western Pacific always had a warm SSTA. Both clustering approaches could show the cold SSTA in the equatorial central and eastern Pacific in the boreal winter of 2020, but only pattern clustering could describe westward propagation of the cold SSTA, which was closer to the realistic 2020/21 La Niña evolution, while the variation in the cold SSTA in index clustering tended to be locally generated in the central equatorial Pacific. In addition, when describing the anomalous sea temperature in the western equatorial Pacific, index clustering from March to June obviously had a cold SSTA, which was somewhat different from the actual situation.

Furthermore, from the evolution of the SSTA outside the equator, we also found that there were apparent differences between the two clustering approaches (**Figure 3**). First, in observing the evolutionary characteristics of the SSTA south and north of the equator (**Figures 3A,D**), we found that the cold SSTA south of the equator began to spread westward from June, which corresponded to the time when the cold SSTA in the equator began to develop. For the two clustering approaches, index clustering compared with pattern clustering had two propagation paths of a cold SSTA south of the equator (**Figures 3B,E**) and eastward propagation of a cold SSTA north of the equator (**Figures 3C,F**), which were both inconsistent with the observational facts. Therefore, the best members selected by pattern clustering were closer to the observations regardless of observing the variation in the SSTA within or outside the equator.

To further examine the differences between the two clustering approaches from another perspective, we focused on the evolution of the anomalous wind field. Since the cold SSTA south of the equator mentioned above was closely related to this La Niña event, the variation in the anomalous wind field

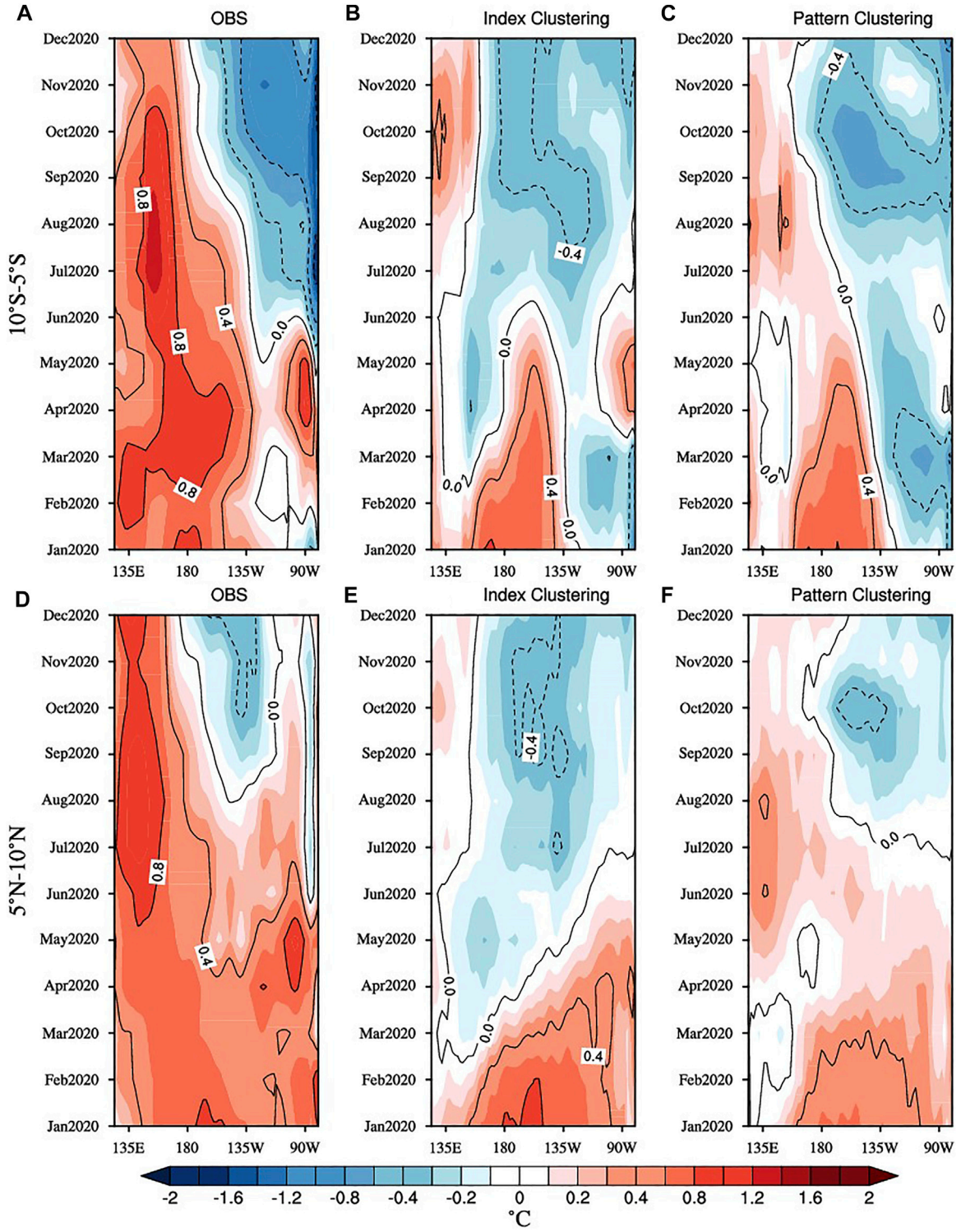

FIGURE 3 | Temporal evolution of the SSTA along the off-equatorial Pacific (averaged between 10°S and 5°S and between 5°N and 10°N) in 2020 for **(A,D)** observations, **(B,E)** the ensemble mean of the best prediction members by index clustering, and **(C,F)** the ensemble mean of the best prediction members by pattern clustering. The contour interval is 0.4°C.

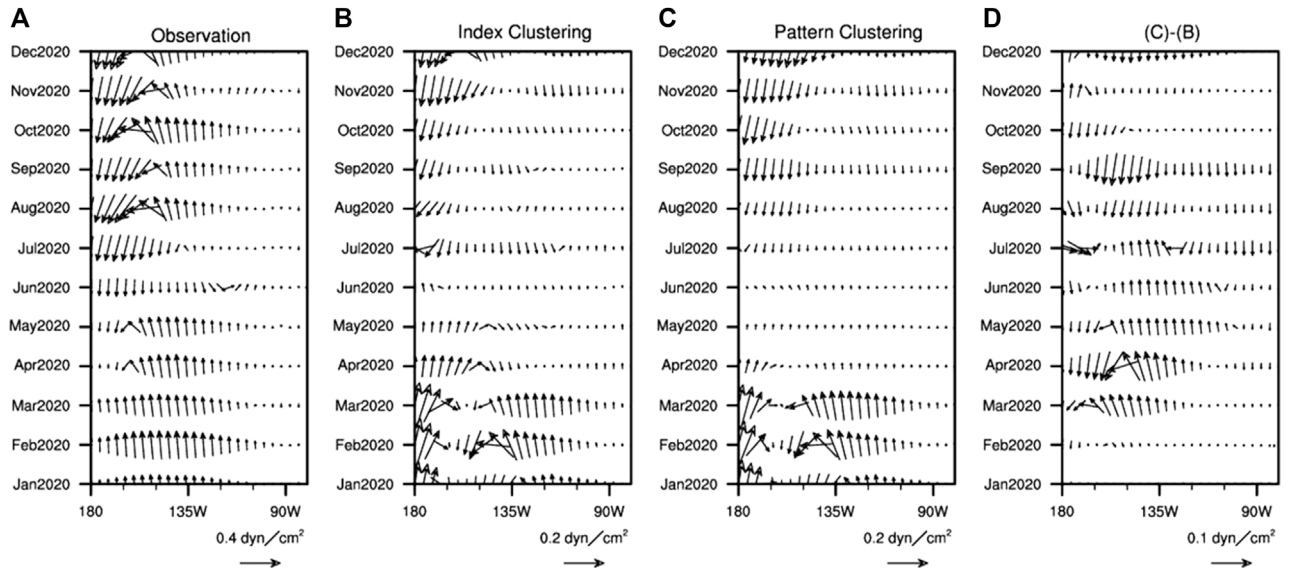

FIGURE 4 | Temporal evolution of wind stress anomalies along the equatorial Pacific (averaged between 10°S and EQ) in 2020 for **(A)** observations, **(B)** the ensemble mean of the best prediction members by index clustering, **(C)** the ensemble mean of the best prediction members by pattern clustering, and **(D)** ensemble mean of the best prediction members by pattern clustering minus ensemble mean of the best prediction members by index clustering (i.e., **(C)**–**(B)**).

south of the equator was mainly considered (**Figure 4**). The mean wind anomalies in **Figures 4B,C** were obtained by the ensemble mean of the best prediction members in index clustering and pattern clustering based on SSTA differences, respectively. From observations, it could be found that the eastern Pacific in the Southern Hemisphere basically maintained a state of southerly wind anomaly, which was conducive to transporting cold water south of the equator to the equator. For the two clustering approaches, even though the prediction results of wind stress were weaker than the observations (Zheng and Zhu, 2016), from the difference map (pattern clustering minus index clustering), it could be determined that the best prediction members selected by pattern clustering could better reflect the southerly wind anomaly, especially in the area near 135°W. In summary, regardless of the evolution of the SSTA or of the anomalous wind field, pattern clustering was more in line with the observational facts and was more conducive to discussing the developmental characteristics of this event.

KEY PROCESSES OF THE 2020/21 LA NIÑA EVENT REVEALED BY PATTERN CLUSTERING

Based on the above comparison, this paper utilized pattern clustering to select the best and worst prediction members, and the evolution of the Niño3.4 index of the two sets is shown in **Figure 5**. Through the comparison of the best and worst prediction members, we could analyze which key process could trigger this La Niña event. First, the prediction results of the evolution of the SSTA and anomalous wind field from January to May for the best and worst prediction members are displayed in **Figure 6**. From the observations, the entire equatorial Pacific was warm in the west and cold in the east in January, and it was one of the structures most likely to produce the "spring predictability barrier" (SPB) (Webster and Yang, 1992; Yu et al., 2009), a phenomenon in which most ENSO prediction models suffer a sharp decrease in prediction skill across the spring season (Latif et al., 1994). Currently, the SPB is still a major challenge in ENSO prediction (Zheng and Yu, 2017). When we focused on the variation in the Niño 3.4 index of the ensemble mean and observations (**Figure 1**), apparent discrepancies appeared after spring, which displayed an obvious SPB phenomenon in the 2020/21 La Niña event. Second, even under the action of an easterly wind anomaly in the eastern equatorial Pacific, the development of the cold SSTA in this area was interrupted from January to March, mainly because the strength of the coupled ocean-atmosphere system is weak in boreal spring, which is one of the possible reasons for the SPB phenomenon (Zebiak and Cane, 1987; Webster, 1995). Therefore, it is difficult to have good coordination between the wind field and sea temperature. After spring, the cold SSTA developed again and was accompanied by the transportation of cold water south of the equator. In summary, this event actually exhibited a characteristic: the uncoordinated ocean-atmosphere configuration structure formed by the large-scale warm SSTA in the western equatorial Pacific and the general easterly wind anomaly in the equatorial region. This uncoordinated ocean-atmosphere coupled structure appeared in spring and was superimposed on the weak coupled strength of the ocean-atmosphere, which further increased the difficulty of prediction starting at this time, and it may be one of the reasons why many models starting in spring failed to predict the 2020/2021 La Niña event. From the perspective of the best and worst prediction members, there were two completely

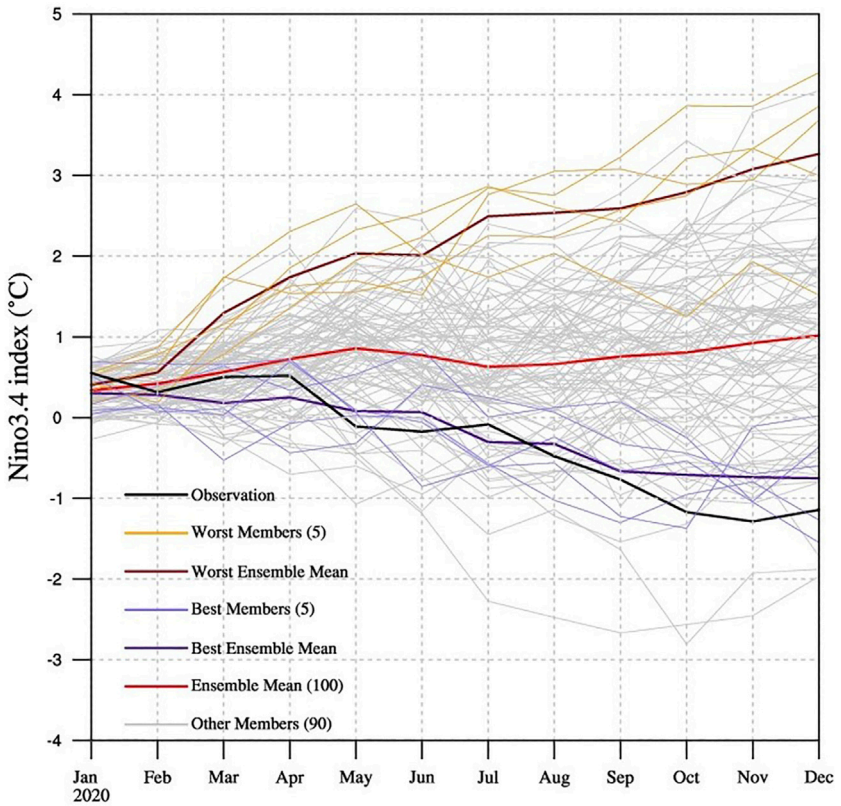

FIGURE 5 | The temporal variation in the Niño3.4 index in 2020 of observations (black line) and of the best and worst prediction members selected by pattern clustering. The red line represents the ensemble mean from all 100 ensemble members. The purple lines represent the best five ensemble members (light) with the best ensemble-mean forecast (dark), the orange lines represent the worst five ensemble members with the worst ensemble-mean forecast (dark red line), and the gray lines represent other ensemble members.

opposite development situations, that is, the best (worst) prediction members showed the gradual weakening (strengthening) of the westerly wind anomaly in the western equatorial Pacific, and correspondingly showed that this anamaly was beneficial to the development of the cold (warm) SSTA in the equatorial eastern Pacific; therefore, the different variation of the Niño3.4 index between the best and worst prediction members formed two totally opposite events (**Figure 5**).

We further explored the reason for the opposite development of the best prediction members and the worst prediction members using pattern clustering. **Figure 6** shows that in January, the ocean-atmosphere configuration (wide range of warm SSTA in the tropical Pacific and westerly wind anomaly in the western Pacific) of the best and worst prediction members can easily develop into the state of El Niño, and the cold SSTA in the eastern equatorial Pacific was relatively weak compared with the large-scale warm SSTA; however, the configuration developed into the La Niña event in the best prediction members. One possible reason for this development may be that its cold SSTA in the eastern equatorial Pacific was obviously stronger than the worst prediction members in January 2020 (**Figure 6**). Furthermore, we analyzed the Hovmoller diagrams (**Figure 7**), which are profile diagrams first proposed by Hovmöller in 1949 to reflect the temporal variation of atmospheric variables (Hovmöller, 1949) and are now widely used in the analysis of zonal or meridional variation characteristics of ENSO events (Feng et al., 2015; Lian et al., 2017; Lian and Chen, 2021; Hu et al., 2019; Zheng et al., 2021). At the starting time of the forecast (January 2020), the most obvious differences between the worst prediction members and the best prediction members in the four variables (Taux, Tauy, SSTA, and Z20) were the cold SSTA located in the southeast Pacific. Even though there were southerly wind anomalies in this region, the cold SSTA of the worst prediction members was weaker than that of the best prediction members. It was easier for the cold SSTA of the best prediction members to occupy the equatorial region, thereby establishing the Bjerknes feedback (Bjerknes, 1969), leading to the westward development of cold SSTA in the eastern equatorial region, weakening the westerly wind anomaly, and thus establishing the easterly wind anomaly. Therefore, the best prediction members successfully predicted that the cold SSTA in the southeast Pacific explained why the best and worst prediction members had completely opposite development directions.

Moreover, the discrepancies between the best and worst prediction members deserve further discussion to determine the specific time and sequence of apparent differences in variables (Taux, Tauy, SSTA, and Z20) and to further find the different roles of the atmosphere and ocean in the development of this La Niña event. Therefore, the difference diagrams along the equatorial Pacific (from 5°S to 5°N) between the best prediction members and the worst prediction

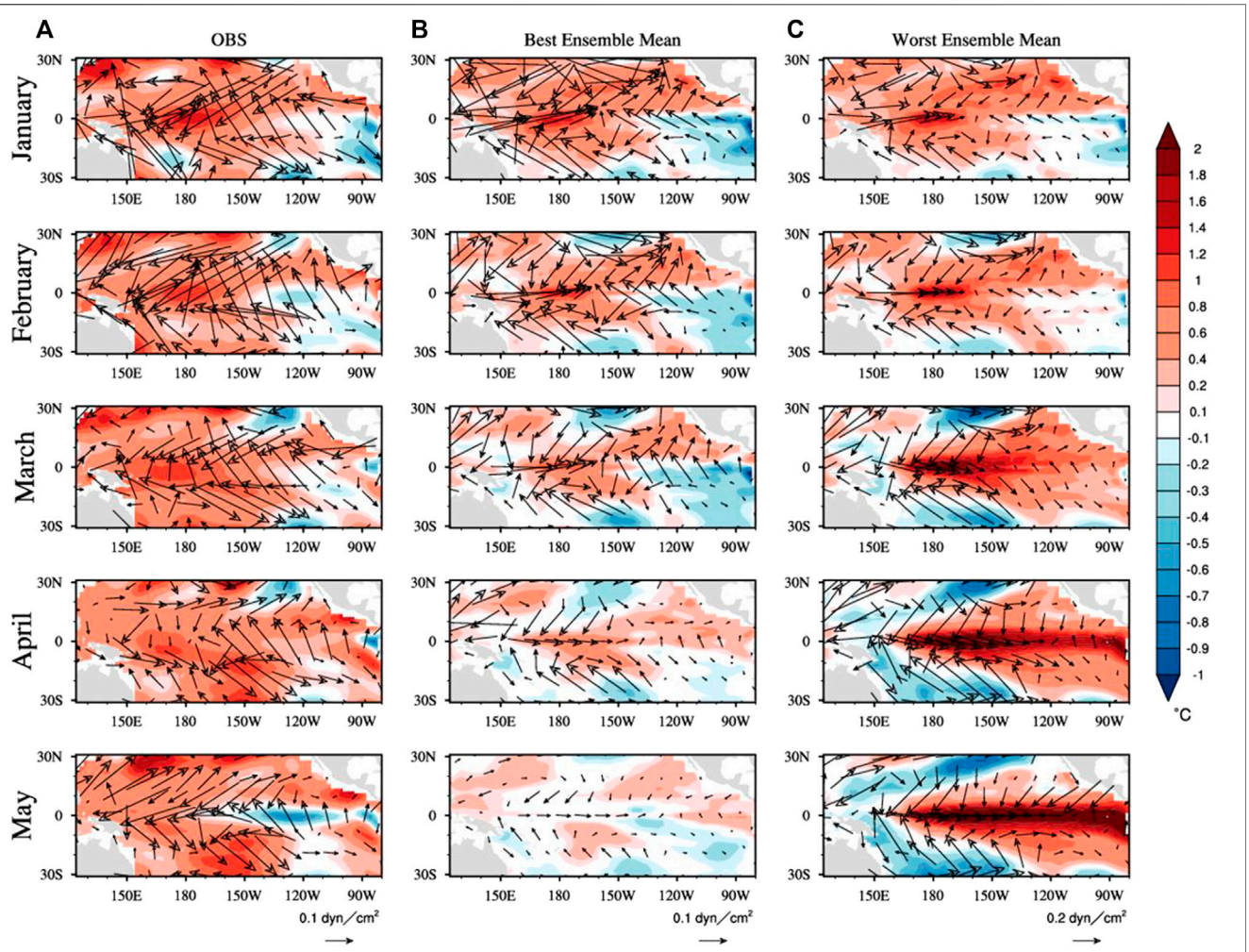

FIGURE 6 | Temporal evolution of wind stress anomalies (vectors) and SSTA (shading) (30°S-30°N, 120°E-80°W) from January to May 2020 [**(A)**: observations; **(B)**: the ensemble mean of the best prediction members by pattern clustering; and **(C)**: the ensemble mean of the worst prediction members by pattern clustering].

members are shown in **Figure 8** (ensemble mean of the best prediction members minus ensemble mean of the worst prediction members). Based on the discussion above, the anomalous cold water from the best prediction members in the southeast Pacific flowed into the equatorial region under the impact of the southerly wind anomaly, and by February, there were differences in SSTA compared with the worst prediction members. The atmosphere responded quickly to the differences; **Figure 8** shows the negative and positive values of the anomalous zonal wind and meridional wind, respectively, and the most obvious areas of the differences were near the date line. Therefore, for the best prediction members, it manifested as the strengthening of a southeasterly wind anomaly near the date line, and it was this anomalous wind field condition that was conducive to the appearance of the cold SSTA in the central and eastern equatorial Pacific and the northward transportation of cold water south of the equator. Correspondingly, apparent differences in the thermocline depth anomaly appeared after spring. The discrepancies between the best and worst prediction members emerged in the spring season. On the one hand, this was the result of the cold SSTA in the Southern Hemisphere under the influence of the southerly wind anomaly, and on the other hand, it actually reflected the SPB phenomenon of this model in this cold event. Furthermore, the differences between the best and worst prediction members also emphasized the dominant role of surface signals in the development of the moderate 2020/21 La Niña event.

DISCUSSION AND CONCLUSION

Clustering using traditional index types could not accurately describe the evolution of the entire event, and clustering analysis using the evolution of the anomalous sea temperature field (120°E-80°W, 30°S-30°N) better fit the physical changes of the actual event; for such a coupled system, both the SSTA field and the anomalous wind field

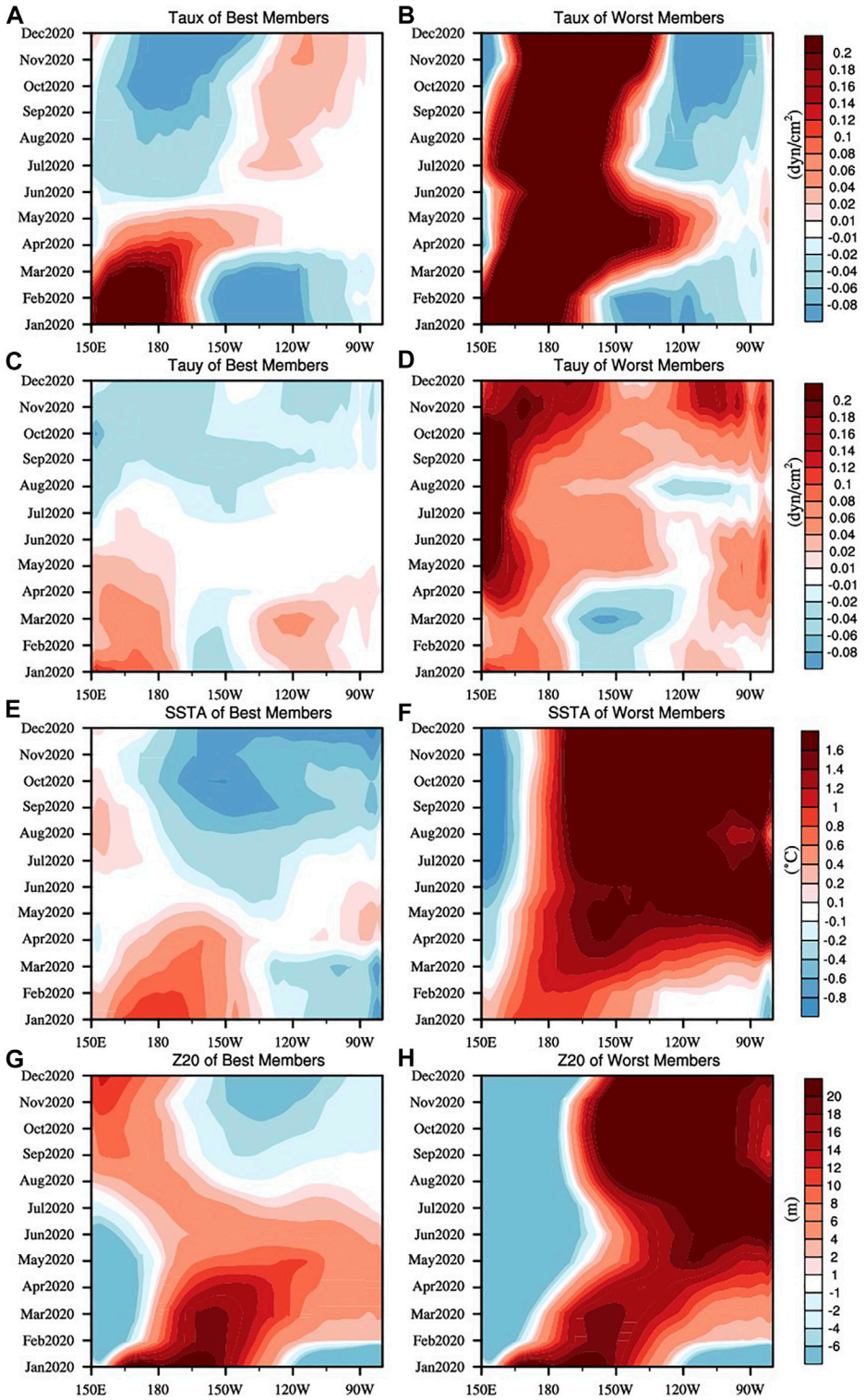

FIGURE 7 | Temporal variation of Taux, Tauy, SSTA, and Z20 of the ensemble mean of the best prediction members (i.e., **(A,C,E,G)**) and the worst prediction members by pattern clustering (i.e. **(B,D,F,H)**) along the 10°S to the equator.

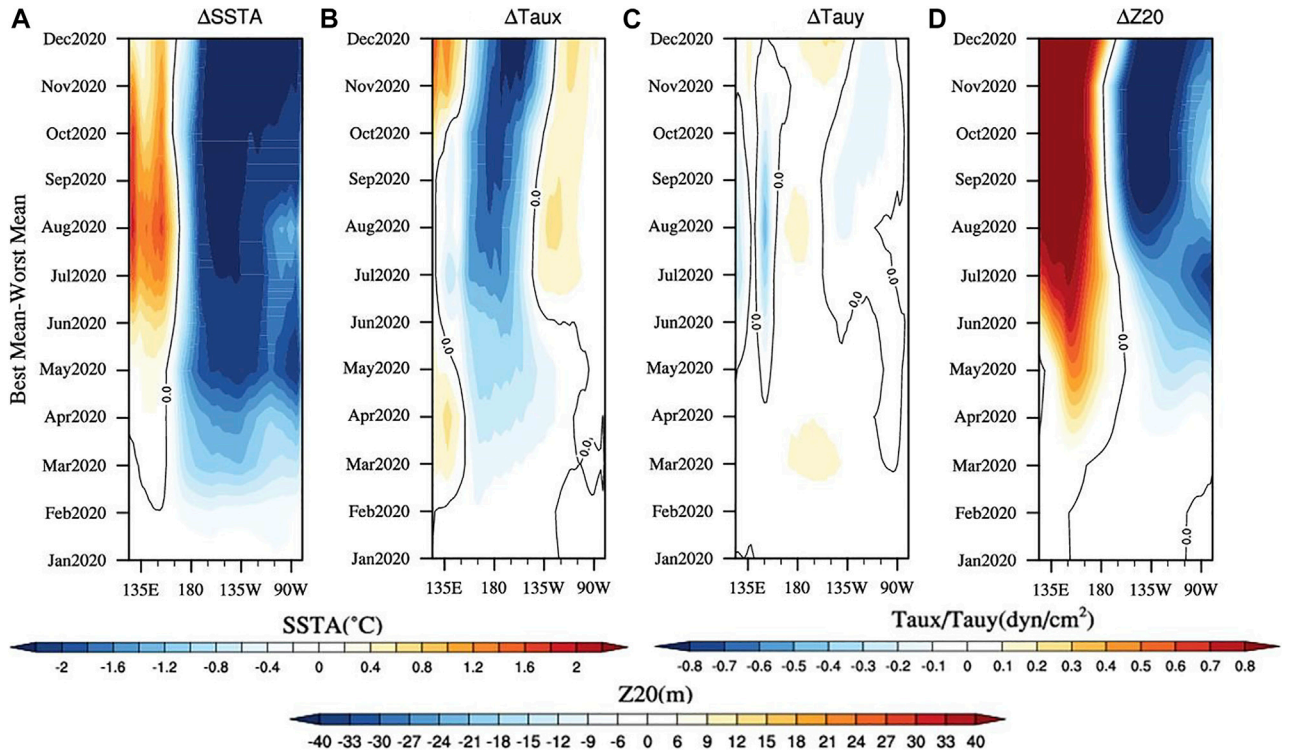

FIGURE 8 | Temporal evolution of the differences (ensemble mean of the best prediction members minus ensemble mean of the worst prediction members) of four variables along the equatorial Pacific (averaged between 5°S and 5°N) in 2020 for **(A)** ΔSSTA, **(B)** ΔTaux, **(C)** ΔTauy, and **(D)** ΔZ20.

showed a better fit with the observation. The development of the 2020/21 La Niña event had an obvious SPB. In spring, there was an obvious inconsistency in ocean-atmosphere coordination, and the strength of the coupled ocean-atmosphere system was weak; therefore, the cold SSTA in the equatorial eastern Pacific in spring did not develop even under the action of an easterly wind anomaly, leading to the occurrence of cold-warm-cold variation in the SSTA in the equatorial eastern Pacific. This uncoordinated coupled ocean-atmosphere structure explains the failure of many models starting in the spring of 2020 to predict the event and indicates its complexity. The best members predicted by pattern clustering were closer to the actual observations, indicating that the development of this event was closely related to the cold SSTA south of the equator and the southeasterly wind anomaly in this region, which were the key processes of the 2020/21 La Niña event and the reason for opposite development between the best prediction members and the worst prediction members. Previous works (Min et al., 2017; Hua and Su, 2020) demonstrated that the important role of the southeast Pacific in the prediction of the ENSO event, and the failure to predict the cold SSTA in the southeast Pacific among the worst prediction members may be the reason for the obvious SPB phenomenon in this model. Moreover, this event also showed the dominant role of the surface signals.

A very obvious difference between the ensemble mean and the observation after spring (**Figure 1**) is the apparent performance of the SPB of this model, that is, the prediction skills suffer a sharp decline after the spring season, and at the same time, as mentioned in previous discussions, the atmosphere-ocean configuration of the equatorial Pacific in early 2020 was uncoordinated, which made it more difficult to determine the development direction of this event. Therefore, the prediction results starting in January are worthwhile for analyzing the specific performance and role of the SPB phenomenon in this event. From the discussion of the best and worst prediction members, it was found that successful predictions for the cold SSTA in the southeast Pacific would be extremely beneficial in overcoming the SPB phenomenon, thereby significantly improving prediction skills across the spring season, though only for this cold event.

In this work, we highlighted the importance of the SPB in predicting the 2020/21 La Niña event and the primary role of surface signals in the development of this event. However, this paper only explained the key processes of this event from a qualitative perspective, and the specific role of the wind field needs further study. At the same time, when comparing the best and worst prediction members by pattern clustering, apparent differences appeared in the spring season, and the relationship between this and the SPB and whether all of the obvious differences in each prediction of the ensemble prediction system appeared in spring are worthy of further exploration.

DATA AVAILABILITY STATEMENT

Publicly available datasets were analyzed in this study. This data can be found here: https://psl.noaa.gov/data/gridded/data.noaa.ersst.v5.html; and https://psl.noaa.gov/data/gridded/data.ncep.reanalysis2.gaussian.html.

AUTHOR CONTRIBUTIONS

W-TC is mainly responsible for the drawing of the paper graphics and article writing, and FZ is mainly responsible for the supply of data, the construction and revision of the paper, furthermore, H-XF is responsible for the revision and comment of the paper.

FUNDING

This work was supported by the Key Research Program of Frontier Sciences, CAS (Grant No. ZDBS-LY-DQC010), the National Natural Science Foundation of China (Grant Nos. 41876012; 42175045), and the Strategic Priority Research Program of the Chinese Academy of Sciences (Grant No. XDB42000000).

REFERENCES

Barnston, A. G., Tippett, M. K., L'Heureux, M. L., Li, S., and DeWitt, D. G. (2012). Skill of Real-Time Seasonal ENSO Model Predictions during 2002-11: Is Our Capability Increasing. *Bull. Amer. Meteorol. Soc.* 93 (5), 631–651. doi:10.1175/BAMS-D-11-00111.1

Bjerknes, J. (1969). Atmospheric Teleconnections from the Equatorial Pacific. *Mon. Wea. Rev.* 97 (3), 163–172. doi:10.1175/1520-0493(1969)097<0163:atftep>2.3.co;2

Cai, W., Wang, G., Dewitte, B., Wu, L., Santoso, A., Takahashi, K., et al. (2018). Increased Variability of Eastern Pacific El Niño under Greenhouse Warming. *Nature* 564 (7735), 201–206. doi:10.1038/s41586-018-0776-9

Cassou, C., and Terray, L. (2001). Dual Influence of Atlantic and Pacific SST Anomalies on the North Atlantic/Europe winter Climate. *Geophys. Res. Lett.* 28 (16), 3195–3198. doi:10.1029/2000GL012510

Evensen, G. (2004). Sampling Strategies and Square Root Analysis Schemes for the EnKF. *Ocean Dyn.* 54 (6), 539–560. doi:10.1007/s10236-004-0099-2

Feng, L., Zheng, F., Zhu, J., and Liu, H. (2015). The Role of Stochastic Model Error Perturbations in Predicting the 2011/12 Double-Dip La Niña. *SOLA* 11, 65–69. doi:10.2151/sola.2015-014

Hovmöller, E. (1949). The Trough-And-Ridge Diagram. *Tellus* 1 (2), 62–66. doi:10.1111/j.2153-3490.1949.tb01260.x

Hu, J., Duan, W., and Zhou, Q. (2019). Season-dependent Predictability and Error Growth Dynamics for La Niña Predictions. *Clim. Dyn.* 53, 1063–1076. doi:10.1007/s00382-019-04631-5

Hua, L.-J., and Su, J.-Z. (2020). Southeastern Pacific Error Leads to Failed El Niño Forecasts. *Geophy. Res. Lett.* 47 (17). doi:10.1029/2020GL008764

Huang, B., Thorne, P. W., Banzon, V. F., Boyer, T., Chepurin, G., Lawrimore, J. H., et al. (2017). Extended Reconstructed Sea Surface Temperature, Version 5 (ERSSTv5): Upgrades, Validations, and Intercomparisons. *J. Clim.* 30 (20), 8179–8205. doi:10.1175/JCLI-D-16-0836.1

Jin, E. K., Kinter, J. L., Wang, B., Park, C.-K., Kang, I.-S., Kirtman, B. P., et al. (2008). Current Status of ENSO Prediction Skill in Coupled Ocean-Atmosphere Models. *Clim. Dyn.* 31 (6), 647–664. doi:10.1007/s00382-008-0397-3

Jin, F.-F. (1997). An Equatorial Ocean Recharge Paradigm for ENSO. Part I: Conceptual Model. *J. Atmos. Sci.* 54 (7), 811–829. doi:10.1175/1520-0469(1997)054<0811:AEORPF>2.0.CO;2

Kanamitsu, M., Ebisuzaki, W., Woollen, J., Yang, S.-K., Hnilo, J. J., Fiorino, M., et al. (2002). NCEP-DOE AMIP-II Reanalysis (R-2). *Bull. Amer. Meteorol. Soc.* 83 (11), 1631–1644. doi:10.1175/BAMS-83-11-1631

Kang, X., Zhang, R.-H., Gao, C., and Zhu, J. (2017). An Improved ENSO Simulation by Representing Chlorophyll-Induced Climate Feedback in the NCAR Community Earth System Model. *Sci. Rep.* 7 (1), 17123. doi:10.1038/s41598-017-17390-2

Kumar, A., Chen, M., Xue, Y., and Behringer, D. (2015). An Analysis of the Temporal Evolution of ENSO Prediction Skill in the Context of the Equatorial Pacific Ocean Observing System. *Mon. Wea. Rev.* 143 (8), 3204–3213. doi:10.1175/MWR-D-15-0035.1

Larson, S. M., and Kirtman, B. P. (2019). Linking Preconditioning to Extreme ENSO Events and Reduced Ensemble Spread. *Clim. Dyn.* 52, 7417–7433. doi:10.1007/s00382-017-3791-x

Latif, M., Barnett, T. P., Cane, M. A., Flügel, M., Graham, N. E., von Storch, H., et al. (1994). A Review of ENSO Prediction Studies. *Clim. Dyn.* 9 (4-5), 167–179. doi:10.1007/bf00208250

Lian, T., and Chen, D. (2021). The Essential Role of Early-spring westerly Wind Burst in Generating the Centennial Extreme 1997/98 El Niño. *J. Clim.* 34 (20), 1–38. doi:10.1175/JCLI-D-21-0010.1

Lian, T., Tang, Y., Zhou, L., Islam, S. U., Zhang, C., Li, X., et al. (2017). Westerly Wind Bursts Simulated in CAM4 and CCSM4. *Clim. Dyn.* 50 (3-4), 1353–1371. doi:10.1007/s00382-017-3689-7

Lopez, H., and Kirtman, B. P. (2014). WWBs, ENSO Predictability, the spring Barrier and Extreme Events. *J. Geophys. Res. Atmos.* 119 (17), 114–210. doi:10.1002/2014JD021908

Ludescher, J., Gozolchiani, A., Bogachev, M. I., Bunde, A., Havlin, S., and Schellnhuber, H. J. (2013). Improved El Nino Forecasting by Cooperativity Detection. *Proc. Natl. Acad. Sci.* 110 (29), 11742–11745. doi:10.1073/PNAS.1309353110

Luo, J.-J., Yuan, C., Sasaki, W., Behera, S. K., Masumoto, Y., Yamagata, T., et al. (2016). Current Status of Intraseasonal–Seasonal-To-Interannual Prediction of The Indo-Pacific Climate. *Indo-Pacific Clim. Variability Predictability,World Scientific Ser. Asia-Pacific Weather Clim.* 7, 63–107. doi:10.1142/9789814696623_0003

Min, Q., Su, J., and Zhang, R. (2017). Impact of the South and North Pacific Meridional Modes on the El Niño-Southern Oscillation: Observational Analysis and Comparison. *J. Clim.* 30 (5), 1705–1720. doi:10.1175/JCLI-D-16-0063.1

Picaut, J., Masia, F., and du Penhoat, Y. (1997). An Advective-Reflective Conceptual Model for the Oscillatory Nature of the ENSO. *Science* 277 (5326), 663–666. doi:10.1126/science.277.5326.663

Ren, H.-L., Jin, F.-F., Song, L., Lu, B., Tian, B., Zuo, J., et al. (2017). Prediction of Primary Climate Variability Modes at the Beijing Climate Center. *J. Meteorol. Res.* 31 (1), 204–223. doi:10.1007/s13351-017-6097-3

Ren, H.-L., Scaife, A. A., Dunstone, N., Tian, B., Liu, Y., Ineson, S., et al. (2018). Seasonal Predictability of winter ENSO Types in Operational Dynamical Model Predictions. *Clim. Dyn.* 52, 3869–3890. doi:10.1007/s00382-018-4366-1

Ren, H.-L., Zheng, F., Luo, J.-J., Wang, R., Liu, M., Zhang, W., et al. (2020). A Review of Research on Tropical Air-Sea Interaction, ENSO Dynamics, and ENSO Prediction in China. *J. Meteorol. Res.* 34 (1), 43–62. doi:10.1007/s13351-020-9155-1

Singh, A., and Delcroix, T. (2013). Eastern and central Pacific ENSO and Their Relationships to the Recharge/discharge Oscillator Paradigm. *Deep Sea Res. Oceanographic Res. Pap.* 82, 32–43. doi:10.1016/J.DSR.2013.08.002

Song, Y., Shu, Q., Bao, Y., Yang, X., and Song, Z. (2021). The Short-Term Climate Prediction System FIO-CPS v2.0 and its Prediction Skill in ENSO. *Front. Earth Sci.* 9. doi:10.3389/feart.2021.759339

Trenberth, K. E., Branstator, G. W., Karoly, D., Kumar, A., Lau, N.-C., and Ropelewski, C. (1998). Progress during TOGA in Understanding and Modeling Global Teleconnections Associated with Tropical Sea Surface Temperatures. *J. Geophys. Res.* 103 (C7), 14291–14324. doi:10.1029/97JC01444

Webster, P. J. (1995). The Annual Cycle and the Predictability of the Tropical Coupled Ocean-Atmosphere System. *Meteorl. Atmos. Phys.* 56 (1-2), 33–55. doi:10.1007/BF01022520

Webster, P. J., and Yang, S. (1992). Monsoon and ENSO: Selectively Interactive Systems. *Q.J R. Met. Soc.* 118 (507), 877–926. doi:10.1002/QJ.49711850705

Weisberg, R. H., and Wang, C. (1997). A Western Pacific Oscillator Paradigm for the El Niño-Southern Oscillation. *Geophys. Res. Lett.* 24 (7), 779–782. doi:10.1029/97GL00689

Wyrtki, K. (1975). El Niño-The Dynamic Response of the Equatorial Pacific Oceanto Atmospheric Forcing. *J. Phys. Oceanogr.* 5 (4), 572–584. doi:10.1175/1520-0485(1975)005<0572:ENTDRO>2.0.CO;2

Xie, S.-P., Peng, Q., Kamae, Y., Zheng, X.-T., Tokinaga, H., and Wang, D. (2018). Eastern Pacific ITCZ Dipole and ENSO Diversity. *J. Clim.* 31 (11), 4449–4462. doi:10.1175/JCLI-D-17-0905.1

Yu, Y., Duan, W., Xu, H., and Mu, M. (2009). Dynamics of Nonlinear Error Growth and Season-dependent Predictability of El Niño Events in the Zebiak-Cane Model. *Q.J.R. Meteorol. Soc.* 135 (645), 2146–2160. doi:10.1002/QJ.526

Zebiak, S. E., and Cane, M. A. (1987). A Model El Niñ-Southern Oscillation. *Mon. Wea. Rev.* 115 (10), 2262–2278. doi:10.1175/1520-0493(1987)115<2262:AMENO>2.0.CO;2

Zhang, R.-H., and Gao, C. (2016). The IOCAS Intermediate Coupled Model (IOCAS ICM) and its Real-Time Predictions of the 2015-2016 El Niño Event. *Sci. Bull.* 61 (13), 1061–1070. doi:10.1007/s11434-016-1064-4

Zhang, R.-H., Yu, Y., Song, Z., Ren, H.-L., Tang, Y., Qiao, F., et al. (2020). A Review of Progress in Coupled Ocean-Atmosphere Model Developments for ENSO Studies in China. *J. Ocean. Limnol.* 38 (4), 930–961. doi:10.1007/s00343-020-0157-8

Zhao, J., Kug, J.-S., Park, J.-H., and An, S.-I. (2020). Diversity of Pacific Meridional Mode and its Distinct Impacts on El Niño-Southern Oscillation. *Geophys. Res. Lett.* 47 (19), doi:10.1029/2020gl088993

Zheng, F., Fang, X. H., Zhu, J., Yu, J. Y., and Li, X. C. (2016). Modulation of Bjerknes Feedback on the Decadal Variations in ENSO Predictability. *Geophys. Res. Lett.* 43 (24), 12560–12568. doi:10.1002/2016GL071636

Zheng, F., and Yu, J.-Y. (2017). Contrasting the Skills and Biases of Deterministic Predictions for the Two Types of El Niño. *Adv. Atmos. Sci.* 34 (12), 1395–1403. doi:10.1007/s00376-017-6324-y

Zheng, F., Yuan, Y., Ding, Y., Li, K., Fang, X., Zhao, Y., et al. (2021). Extreme Cold Events from East Asia to North America in Winter 2020/21. *Adv. Atmos. Sci.*. doi:10.1007/s00376-021-1033-y

Zheng, F., and Zhu, J. (2010). Coupled Assimilation for an Intermediated Coupled ENSO Prediction Model. *Ocean Dyn.* 60 (5), 1061–1073. doi:10.1007/s10236-010-0307-1

Zheng, F., and Zhu, J. (2016). Improved Ensemble-Mean Forecasting of ENSO Events by a Zero-Mean Stochastic Error Model of an Intermediate Coupled Model. *Clim. Dyn.* 47 (12), 3901–3915. doi:10.1007/s00382-016-3048-0

Zheng, F., and Zhu, J. (2015). Roles of Initial Ocean Surface and Subsurface States on Successfully Predicting 2006-2007 El Niño with an Intermediate Coupled Model. *Ocean Sci.* 11 (1), 187–194. doi:10.5194/os-11-187-2015

Zheng, F., Zhu, J., Wang, H., and Zhang, R.-H. (2009). Ensemble Hindcasts of ENSO Events over the Past 120 Years Using a Large Number of Ensembles. *Adv. Atmos. Sci.* 26 (2), 359–372. doi:10.1007/s00376-009-0359-7

Zheng, F., Zhu, J., Zhang, R.-H., and Zhou, G.-Q. (2006). Ensemble Hindcasts of SST Anomalies in the Tropical Pacific Using an Intermediate Coupled Model. *Geophys. Res. Lett.* 33 (19), L19604. doi:10.1029/2006GL026994

Conflict of Interest: The authors declare that the research was conducted in the absence of any commercial or financial relationships that could be construed as a potential conflict of interest.

Publisher's Note: All claims expressed in this article are solely those of the authors and do not necessarily represent those of their affiliated organizations, or those of the publisher, the editors and the reviewers. Any product that may be evaluated in this article, or claim that may be made by its manufacturer, is not guaranteed or endorsed by the publisher.

frontiers in Earth Science

ORIGINAL RESEARCH
published: 21 February 2022
doi: 10.3389/feart.2022.862989

Medium-Range Predictability of Boreal Summer Western North Pacific Subtropical High and Its ENSO Modulation

Li Gao[1]*, *Pengfei Ren*[2] *and Jiawen Zheng*[3]

[1]CMA Earth System Modeling and Prediction Centre (CEMC), National Meteorological Center, and State Key Laboratory of Severe Weather, Beijing, China, [2]Guangdong Meteorological Observatory, Guangdong Meteorological Bureau, Guangzhou, China, [3]Guangzhou Meteorological Service, Guangdong Meteorological Bureau, Guangzhou, China

OPEN ACCESS

Edited by:
Ruihuang Xie,
Ocean University of China, China

Reviewed by:
Chao He,
Jinan University, China
Yang Li,
Chengdu University of Information Technology, China

***Correspondence:**
Li Gao
gaol@cma.gov.cn

Specialty section:
This article was submitted to Atmospheric Science, a section of the journal Frontiers in Earth Science

Received: 26 January 2022
Accepted: 07 February 2022
Published: 21 February 2022

Citation:
Gao L, Ren P and Zheng J (2022) Medium-Range Predictability of Boreal Summer Western North Pacific Subtropical High and Its ENSO Modulation. Front. Earth Sci. 10:862989. doi: 10.3389/feart.2022.862989

In boreal summer, variations of intensity and location of the western North Pacific subtropical high (WNPSH) have significant impacts on weather and climate in East Asia. In this study, the medium-range prediction of WNPSH is comprehensively evaluated with various scores based on reforecast data of the National Centers for Environmental Prediction - Global Ensemble Forecast System, and the predictability source of the WNPSH medium-range forecasting is further analyzed by examining how well the model can reproduce the modulation of El Niño-Southern Oscillation (ENSO) on WNPSH as observed. The results show that this system has a systematic bias in the WNPSH forecasts, mainly manifested by the weak strength and the southeastward shifted position, and such a bias further increases with lead time. Effective prediction skills of WNPSH are 10–11 days for its intensity and area, 7 days for its ridge line, but only 1–3 days for its western boundary ridge point in terms of different scores, respectively, which can be improved through developing a bias correction method of prediction. It is demonstrated that the medium-range predictability of WNPSH is mainly originated from ENSO and its significant lagged effects on WNPSH well revealed in observation can be realistically reproduced by this system within the effective prediction lengths. A strong ENSO modulation of the WNPSH prediction skills has been clearly found in terms of the different indices, which depends on the ENSO's developing and decaying phases. The intensity and area of WNPSH are usually highly predictable due to the ENSO effect being reproduced by the system well while the location indices of WNPSH have relatively low predictability, which are mainly affected by internal variability and difficultly captured by the model. Predictability analysis of WNPSH as modulated by ENSO shows good potential for medium-range forecasting with high skills.

Keywords: medium-range predictability, western north Pacific subtropical high, enso, NCEP-GEFS, ensemble reforecasts

1 INTRODUCTION

In the subtropics of the northern and southern hemispheres, there exist the subtropical high-pressure belts. Due to the land-sea distributions, such belts often break into several high-pressure monomers, collectively referred to as subtropical highs. The western North Pacific subtropical high (WNPSH) is well known over the East Asia area as a permanent high-pressure circulation system, usually represented by the 5880-gpm line surrounded area in the 500-hPa geopotential height field west of 180°E (Liu et al., 2012). In previous studies, various indices for representing the WNPSH activities have been defined (Yang and Sun, 2003; Huang et al., 2015; Huang and Li, 2015; Yang et al., 2017; He et al., 2018). The WNPSH's area, intensity and position movements have been confirmed to have significant influences on summer precipitation and typhoon activity in the East Asia (Huang, 1963; Zhu et al., 1992; Tao and Wei, 2006; Matsumura et al., 2015; Wen et al., 2015). Given that WNPSH has high impacts on the East-Asian weather/climate, the medium- and long-term prediction as well as predictability regarding its intensity and location variations are of particular importance.

WNPSH has significant signals on various time scales as regulated by diverse factors. Many studies have shown a close relationship between the El Niño-Southern Oscillation (ENSO) and WNPSH (Ying and Sun 2000; Cai et al., 2003; Wang and Zou 2004; Li et al., 2017; Zhang et al., 2017). Ying and Sun (2000) examined the response of WNPSH to anomalous tropical sea surface temperature (SST) and revealed that SST anomalies in the eastern equatorial Pacific could enhance the strength of WNPSH through the so-called anomalous "quasi-walker circulation". Cai et al. (2003) explored the relationship between the summer WNPSH and previous SST and found that the formation of the ENSO event was ahead of the transition of WNPSH intensity for about half a year. Wang and Zou (2004) proposed a possible mechanism for explaining the interannual variation of WNPSH calculating the correlation between WNPSH and ENSO. Zhang et al. (2017) reviewed the effects of El Niño on WNPSH and the mechanism of WNPSH formation and further pointed out the asymmetric effects of El Niño and La Niña. Although understanding of ENSO affecting WNPSH is relatively mature, there are few systematic studies on the different ENSO stages, especially the La Niña's influence on WNPSH characteristics such as intensity, area, western ridge point, and ridge line due to the asymmetry of ENSO. It is worthy of a deep study of how such influences can be predicted in dynamical operational models.

There have been many studies aiming to illustrate the predictability source of WNPSH on the climate timescale. Some of them suggested that ENSO is the major source of seasonal predictability of summer circulation patterns including WNPSH in East Asia (Wu et al., 2003; Wang et al., 2009; Zhou et al., 2020). Others have emphasized on the importance of the teleconnection associated with the tropical Indian Ocean in generating the anticyclone over the western North Pacific (Yang et al., 2007; Li et al., 2008; Xie et al., 2009; Wu et al., 2010; Zhang et al., 2012; Song and Zhou, 2014; He et al., 2019). However, it should be noted that the tropical Indian Ocean SST comes from the Indo-West Pacific capacitor (Xie et al., 2009), which is closely related to ENSO. And a paucity of attention has been paid to the forecast verification and predictability analysis of WNPSH on the weather timescale. In recent, Gao et al. (2020) verified the medium-range (1–15 days) forecasts of the WNPSH intensity, area, western boundary point and ridgeline using 2-year real-time operational forecasts in China. Further investigations for the WNPSH weather forecast verification and predictability analysis would be needed by using long enough datasets.

In this study, we will focus on the medium-range forecasts of WNPSH for comprehensively verifying its indices of different properties and investigating its modulation by ENSO through employing a multi-decade reforecast dataset from the National Centers for Environmental Prediction (NCEP) of the National Oceanic and Atmospheric Administration (NOAA). This dataset has been widely employed in forecast research by providing us with an opportunity to evaluate the model's ability to predict certain phenomena over the medium-to-long term (Hamill et al., 2013). The remainder of this paper is organized as follows: The data and methods are given in **Section 2**. The forecasting skill of WNPSH in the model is evaluated in **Section 3**. **Section 4** shows the model's ability to reproduce the ENSO modulation on WNPSH. Predictability source of WNPSH is illustrated in **Section 5**. Summary and discussions are presented in **Section 6**.

2 DATA AND METHODS

2.1 Observational and Forecasting Data

The model reforecast dataset used in this study was previously generated from the Global Ensemble Forecast System (GEFS) version 10 of NCEP/NOAA, covering the period of 1985–2019, with the horizontal resolution of $1^\circ \times 1^\circ$ and vertical resolution of 42 levels, the reforecast data have 11 ensemble members, and each member has a forecast out to 16 days. The initial condition of NCEP-GEFS was generated from the climate forecast system reanalysis (CFSR), using the ensemble transforms with rescaling (ETR) to form the perturbed initial condition, and the stochastic total tendency perturbation (STTP) scheme to represent the effect of model uncertainties. More details on NCEP-GEFS can be obtained from Hamill et al. (2013).

The verification data used in this study include: 1) National Centers for Environmental Prediction/Department of Energy (NCEP/DOE) Reanalysis 2 (Kanamitsu et al., 2002) covering the period from 1 January 1951 to 31 December 2019, including wind and geopotential height; 2) The Niño 3.4 SST anomaly index is downloaded from the website of National Climate Center of China Meteorological Administration, https://cmdp.ncc-cma.net/cn/index.htm; 3) monthly SST data are from Climate Prediction Center (CPC), https://www.cpc.ncep.noaa.gov.

For easy comparison, the verification and reforecast data are interpolated to a uniform resolution of 1° longitude × 1° latitude, and our results do not depend on such a resolution. In this study, we only examine WNPSH in boreal summer (June to August, JJA).

2.2 Methods

2.2.1 Definition of the WNPSH Indices

Here, we use a series of WNPSH indices defined by Liu et al. (2012), including the WNPSH intensity, area, western boundary

point, and ridge line, which can well reflect the impact of WNPSH on summer rainfall in East Asia. The four indices can be used to quantify the strength and relative position of WNPSH, thereby more intuitively representing its basic characteristics. Referring to Liu et al. (2012), the daily WNPSH indices are defined as follows:

1) Area and intensity: the area index is defined by the area surrounded by the grids, which are not less than 5,880°gpm in the range of 110–180°E and north of 10°N at 500-hPa. Correspondingly, the difference between the height over these grids and 5,870°gpm is multiplied by the area defined above and then accumulated, and the result is defined as the intensity index.
2) Ridge line: the average latitude of the characteristic line, featured by a zonal wind $u = 0$, $\frac{\partial u}{\partial y} > 0$, and located within the range enclosed by 5880-gpm contour. If the 5880-gpm contour does not exist, the standard can be gradually lowered to 5,840 gpm. If there is not the 5840-gpm contour, the historical minimum is substituted.
3) Western boundary ridge point (ridge point for short): the longitude at the westernmost boundary of the 5,880 gpm grid in the range of 90°–180°E. If it is west of 90°E, it will be counted as 90°E. If the 5,880°gpm contour is not present, it is replaced by the historical maximum.

2.2.2 Verification and Evaluation Methods

Various verification statistics are calculated to evaluate the forecasting skill of the WNPSH intensity and location by the reforecast. Mean error (*ME*), normalized root mean square error (*NRMSE*) and correlation coefficient (*R*) are used to measure the deviation, amplitude error and consistency between observation and model reforecasts, respectively. The agreement between the predicted and observed time series is represented by the values of *ME* and *NRMSE* close to 0, and that of *R* close to 1. The effective skills of the WNPSH forecasts by this forecasting system can be determined as $R \geq 0.6$ and $NRMSE < 1$ as usual. Their definitions are as follows:

$$ME = \frac{1}{n}\sum_{i=1}^{n} F_i - O_i, \tag{1}$$

$$NRMSE = \frac{\sqrt{\frac{1}{n}\sum_{i=1}^{n}(F_i - O_i)^2}}{\sqrt{\frac{1}{n-1}\sum_{i=1}^{n}(O_i - \bar{O})^2}}, \tag{2}$$

$$R = \frac{\sum_{i=1}^{n}(F_i - \bar{F})(O_i - \bar{O})}{\sqrt{(F_i - \bar{F})^2 (O_i - \bar{O})^2}} \tag{3}$$

and an additional performance score (*PS*) that can consider both similarity and magnitude error (Chen et al., 2013),

$$PS = \frac{(1+R)^2}{\left(SDR + \frac{1}{SDR}\right)^2}, \tag{4}$$

Here, F_i and O_i are the ith values in the forecast and observational time series, respectively. n is the sample size. $\bar{F}$ and $\bar{O}$ represent time mean of the forecasts and observations, respectively. Especially, *R* in **Eq. 4** denotes the pattern correlation between observation and model forecast and the *SDR* is the ratio of the spatial standard deviation of the forecast against observation.

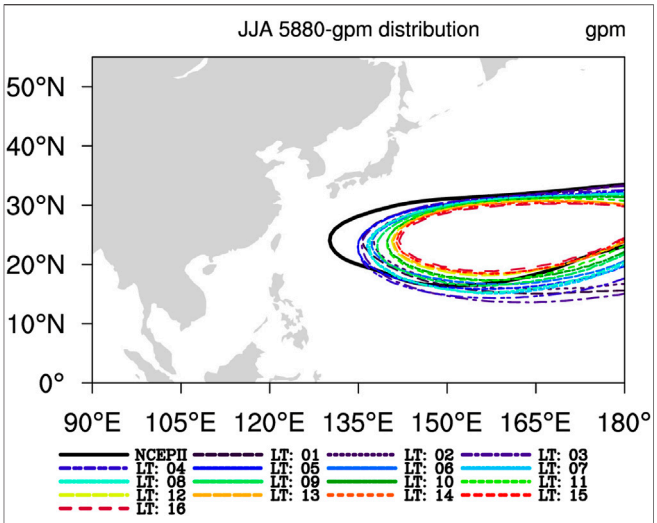

FIGURE 1 | Summer-averaged 5880-gpm lines of the NCEP/DOE Reanalysis (black line) and NCEP-GEFS reforecasts (color lines) at different lead times (LT, unit: day).

3 MEDIUM-RANGE FORECASTING OF WNPSH IN NCEP-GEFS REFORECAST

As a primary circulation pattern in East Asia, WNPSH is usually characterized by the area surrounded by the 5880-gpm line in 500-hPa height field. **Figure 1** shows the distribution of the 5880-gpm lines in the summer-mean height in terms of different lead days. It is clearly found there are systematic biases in the WNPSH forecasts, such as a smaller area, eastward and southward shift of location. Such biases further increase with the extension of the forecast time. Interestingly, the southward shift of WNPSH in the reforecasts is different from most CMIP3 and CMIP5 AGCM models, which reproduce the northward shift bias of WNPSH (Song and Zhou, 2014).

The forecasting skill of the WNPSH indices by the NCEP-GEFS reforecasts is shown in **Figure 2**. For *ME*, the reforecasts reproduce a weaker WNPSH with a smaller area and a southeastward shifted position, consistent with **Figure 1**. Compared with the corresponding threshold, days with the effective skills of the intensity, area, ridge point, and ridge line in terms of the *NRMSE* score are 10, 9, 0, and 7 days, respectively. In terms of the *R* score, the most commonly used in verifying forecast, days with the effective skills of the intensity, area, ridge point, and ridge line can reach 11, 10, 3, and 7 days, respectively. These verification results indicate that the forecasting skill of the ridge point is the worst in NCEP-GEFS because the position of WNPSH shifts too east in the model compared to observation. Similar results were also found in other models (Niu and Zhai, 2013), which mean that state-of-art models still have biases in

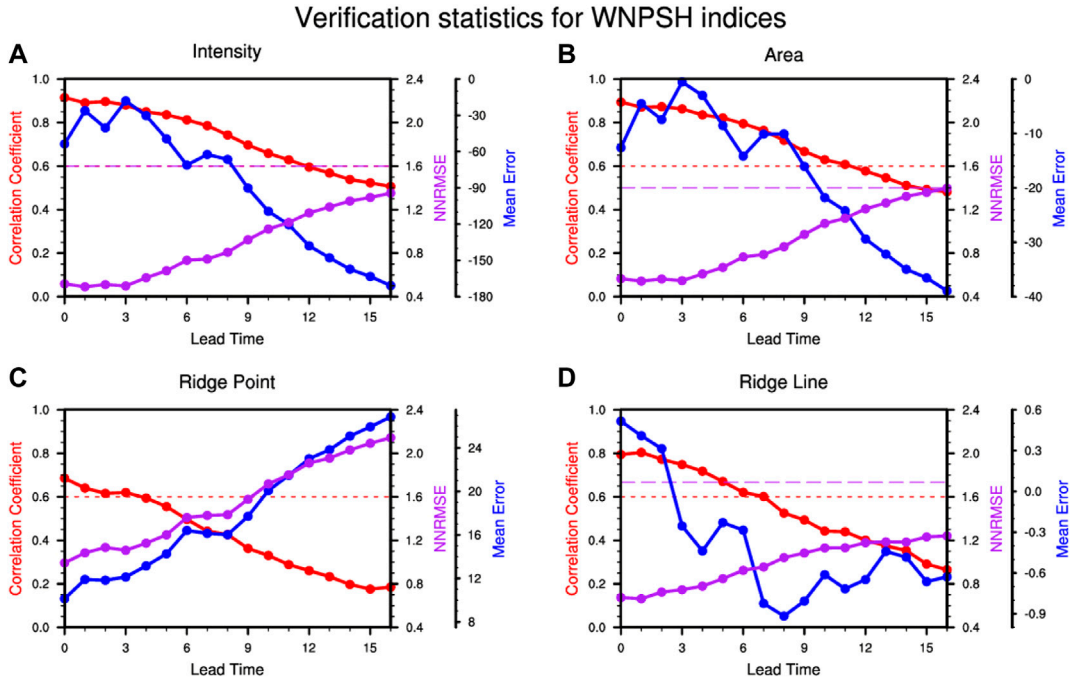

FIGURE 2 | Verification statistics as a function of lead time (days), where red lines represent correlation coefficient (*R*), purple lines do normalized root mean square error (*NRMSE*) and blue lines do mean error (*ME*) for verifying the WNPSH indices of **(A)** intensity, **(B)** area, **(C)** western boundary ridge point and **(D)** ridgeline by the NCEP-GEFS reforecasts. The red and purple dash lines represent the corresponding thresholds of *R* and *NRMSE*, respectively.

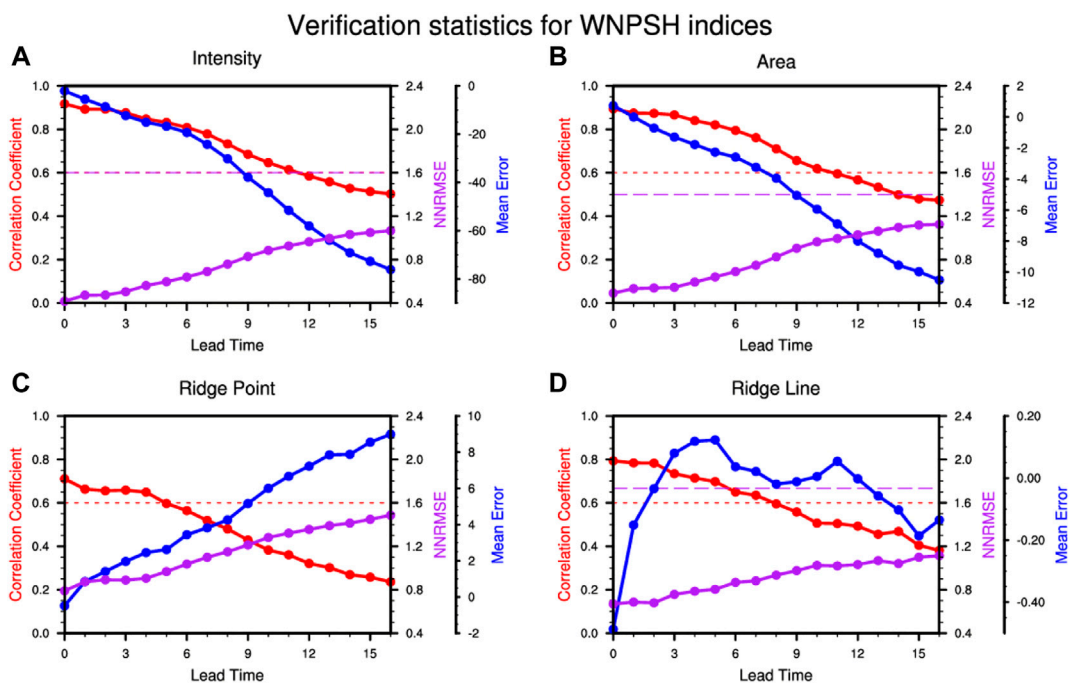

FIGURE 3 | Same as **Figure 2**, but for reforecasts after the bias correction in terms of **Eq. 5**.

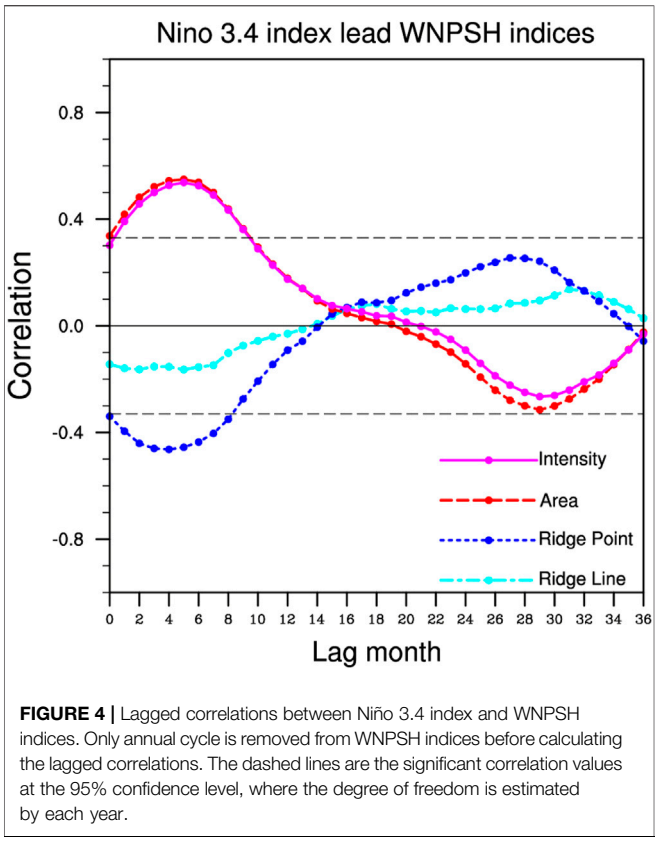

FIGURE 4 | Lagged correlations between Niño 3.4 index and WNPSH indices. Only annual cycle is removed from WNPSH indices before calculating the lagged correlations. The dashed lines are the significant correlation values at the 95% confidence level, where the degree of freedom is estimated by each year.

predicting the longitudinal motion of WNPSH. In addition, the model's ability to predict the ridge line of WNPSH is also quite limited (~7 days). Given that the location of WNPSH is closely related to summer rainfall distributions in China (Liu et al., 2012), the model's medium-term forecasting of WNPSH is still challenging.

As shown in **Figure 1**, the predictions of WNPSH of NCEP GEFS have a systematic bias. Here, we develop a bias correction method as derived in **Eq. 5**. The climatic states of observations and reforecasts can be obtained at different leads.

$$H_{mc} = \overline{H_{obs}} - \overline{H_m} + H_m, \tag{5}$$

where, $\overline{H_{obs}}$ and $\overline{H_m}$ represent summer mean of observation and reforecasts at different leads; H_m and H_{mc} represent the values before and after the correction by **Eq. 5**, respectively.

After the correction, as seen in **Figure 3**, the *R*-score only shows a slight improvement with the effective skills of 11, 11 5, and 8°days for intensity, area, ridge point, and ridge line, respectively. However, it is clear that not only the average errors of the four WNPSH indices are decreased, but also their effective skills in terms of the *NRMSE* score are increased to 13, 11, 5, and 9°days, respectively. Especially, for the ridge point, the *NRMSE* of the corrected forecasts has been increased by more than one pentad. These results indicate that the predictive capability of the WNPSH index in the model system can be greatly improved by developing a bias correction method which idea has been widely adopted in climate predictions. This is quite meaningful with highly predictable WNPSH signals for rainfall forecasts in China due to the significant positive correlations of the forecasting skill between WNPSH and precipitation (Song and Zhou, 2014).

4 REPRODUCTION OF ENSO MODULATION ON WNPSH IN REFORECASTS

Many previous studies have proven the lag effect of ENSO on WNPSH. The significant lag correlations between the Niño3.4 index and the WNPSH indices, as shown in **Figure 4**, indicate the effect of the SST anomalies in the tropical Pacific on WNPSH after 4 months of the ENSO peak. It is worth noting that similar results can also be obtained using the Niño3 and Niño4 indices. This means that ENSO does have a significant impact on the WNPSH's intensity, area, and ridge point, except for the ridge line due to its relatively lower correlation. Previous experiences tell that ENSO in different phases usually has quite different modulation effects on WNPSH. To examine such modulation of WNPSH by ENSO at different phases, the approach of Chou et al. (2003) is applied to classification the ENSO phases (see **Table 1**).

Considering the availability of the reforecast data, only the impact of ENSO on the boreal summer WNPSH from 1985 to 2019 can be examined here. Composite patterns in terms of the ENSO phases in **Figure 5** show a significant modulation on the WNPSH behaviors in observation. In the developing phase of El Niño (**Figure 5B**), anomalous westerly winds in the equatorial central and western Pacific act to weaken the easterlies in the south of WNPSH, making the WNPSH weaker, smaller, and westward shifted. As a contrast, in the El Niño decaying phase, anomalous easterly winds in the equatorial western Pacific make the WNPSH stronger, larger, and eastward shifted, compared with the climatology (**Figure 5C**), which has been demonstrated as the indirect responses of ENSO through the air-sea teleconnection (Wang et al., 1999) and the Indian Ocean capacitor effect (Xie et al., 2009). La Niña's two phases show generally opposite situations of the WNPSH's intensity, area, and positions, compared to El Niño phases (**Figures 5D,E**).

The observed modulation of the different ENSO phases on WNPSH can be well reproduced by the model system at different leads whether the prediction results have been corrected or not, as clearly seen in **Figure 5**. This means that NCEP-GEFS can accurately catch the impact of ENSO on the WNPSH properties such as intensity and position, which vary little with lead, illustrating the potentials for the medium-range prediction of WNPSH. The clearer modulation of ENSO on WNPSH can be directly seen in **Figure 6**, which shows the variations of the WNPSH indices with the ENSO phases. Generally, the model system can capture well the evolutions of the different WNPSH indices throughout the four ENSO phases; i.e., WNPSH is stronger (weaker) and more westward (eastward) in the EDy (EDp) and LDp (LDy) summers. Indeed, the

TABLE 1 | Classification of the summers during 1951–2019 into the five ENSO phases.

ENSO phases	Numbers	Years
El Niño developing (EDp)	12	1957,1963,1965,1968,1972,1982,1986,1991,1994,1997,2009,2015
El Niño decaying (EDy)	13	1958,1964,1966,1969,1973,1983,1987,1992,1995,1998,2003,2010,2016
La Niña developing (LDp)	11	1955,1970,1973,1975,1984,1988,1995,1998,2007,2010,2017
La Niña decaying (LDy)	11	1956,1971,1974,1976,1985,1989,1996,2000,2008,2011,2018
Non-ENSO	25	1951–1954,1959–1962,1967,1977–1981,1990,1993,2001–2002, 2004–2006,2012–2014,2019

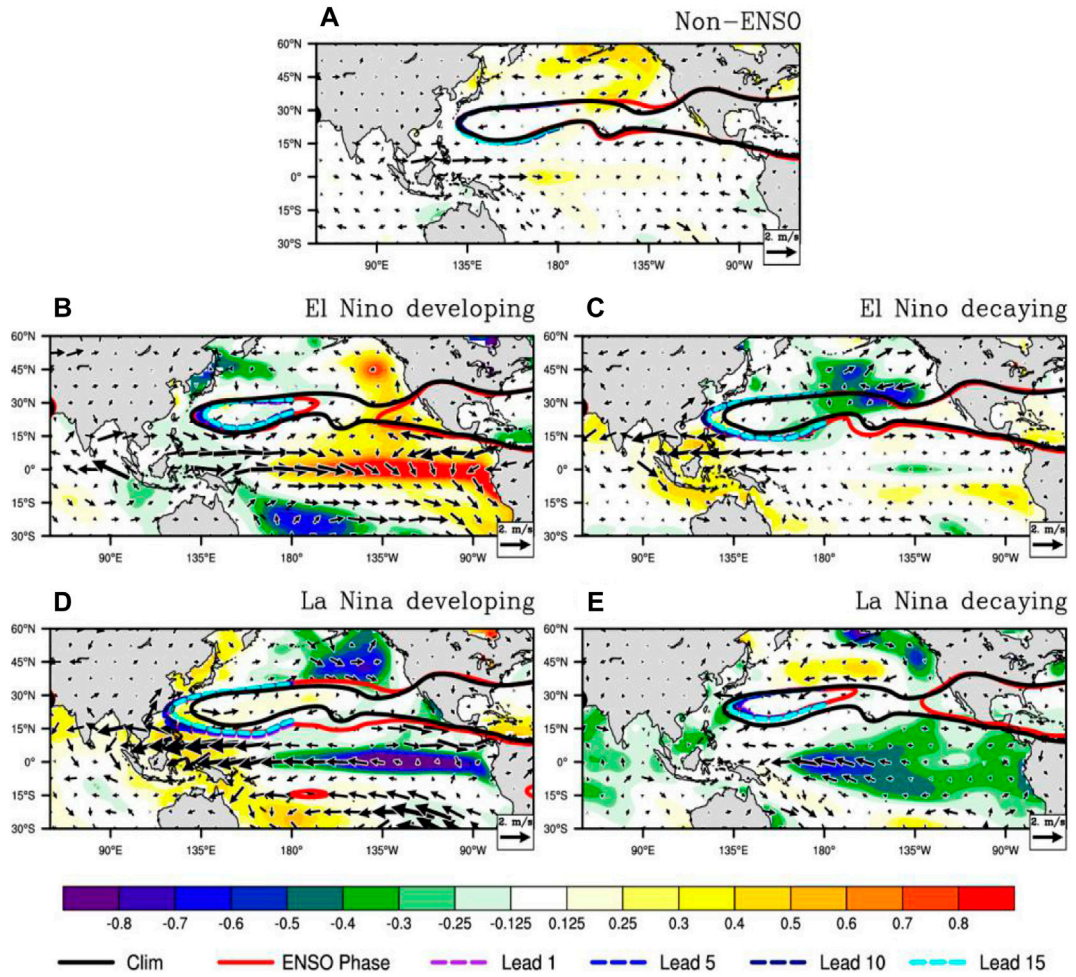

FIGURE 5 | Composites for 5880-gpm over 500-hPa height field [contours, black line represent all years during 1985–2019 and color lines are for a specific phase of ENSO in observation (red) and the model at different lead days], SST (shading, units: °C) and 850-hPa wind anomalies (vector, m s^{-1}) during the non-ENSO **(A)**, El Niño developing **(B)**, El Niño decaying **(C)**, La Niña developing **(D)** and La Niña decaying **(E)** summers.

predictions have certain systematic biases regardless of the indices and the biases tend to become larger as the lead time increases. For example, the magnitudes of the WNPSH intensity and area have been clearly underestimated (overestimated) in the EDp and EDy (LDy) summers. Interestingly, for the LDp, the model also produces a varying strength bias and even changes signs of the bias with lead time increases. Similar modulation was found for the ridge point, which has an eastward shift in the model predictions in the EDp and EDy summers, but a westward shift in the LDy summers. In particular, in the LDp summers, the WNPSH ridge point predicted by the model shifts westward and gradually becomes an eastward shift as the lead time increases. The modulation of ENSO to the ridge line is not as significant as the other three indices (see **Figure 4**) and thus the WNPSH ridge line predicted by the model varies weakly with the ENSO phase changing.

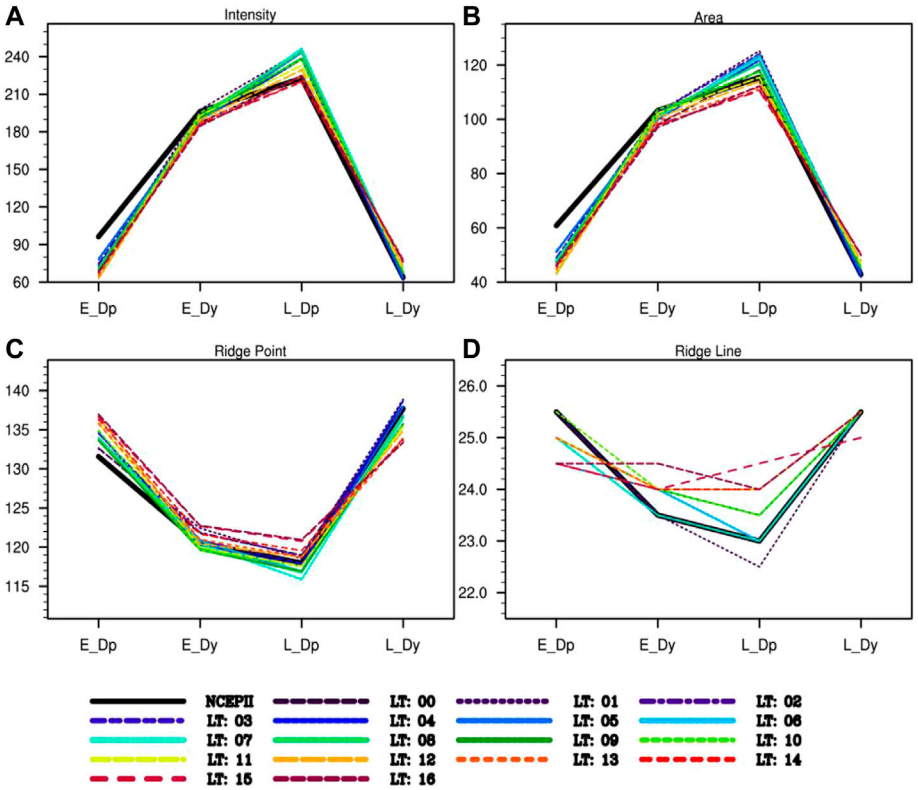

FIGURE 6 | Forecasts of the WNPSH indices in NCEP-GEFS for **(A)** Intensity, **(B)** Area, **(C)** ridge point and **(D)** ridge line during the different phases of ENSO (E_Dp, E_Dy, L_Dp and L_Dy represent the El Niño developing, El Niño decaying, La Niña developing, and La Niña decaying summers, respectively) at the different lead time (0–16 days).

5 MEDIUM-RANGE PREDICTABILITY ANALYSIS OF THE WNPSH INDICES

From **Section 4**, we have seen that ENSO has a significant modulation on WNPSH and it has been reasonably reproduced by NCEP-GEFS at different leads. Then, one natural question here is whether ENSO or any other factor plays a role in regulating medium-range predictability as well as prediction skills for WNPSH? To answer this question, we will reveal the predictability source of WNPSH at the medium range, which can provide indications for relevant weather forecasts. **Figure 7** first shows the yearly prediction skills of the WNPSH indices at different leads. Clearly, prediction skills of the four indices decrease as the lead time increases and also show interannual variability. Overall, the peaks and valleys of skill fluctuations are well consistent with each other among different lead times, which implies that initial states of the model system largely determine the quality of forecasts. Although the skill variations of the intensity and area indices are relatively consistent, they are still significantly different from those of the ridge point and ridge line. This suggests that the factors affecting the prediction skill for the WNPSH intensity and position may be different. In the following, we work to study the influence factors that contribute to the prediction skill of the intensity and position of WNPSH.

Figure 8 shows the averaged skills from all the different leads in **Figure 7**. It is seen that the prediction skill not only has strong interannual variations, but also an interdecadal change around 2000. That is, the prediction skill after 2000 suddenly becomes much higher than before, which reason is still unclear. Although the WNPSH intensity is significantly affected by ENSO (**Figure 6**), and its prediction skills vary greatly from year to year (**Figure 7**), we do not find a clear relationship between prediction skills and the ENSO phases. For example, the 3 years with the highest skills are 2003, 2006, and 2009, which correspond to the EDy, weak EDp, and EDp years, respectively. In contrast, the 3 years with the lowest skills are 1985, 1992, and 1994, corresponding to the LDy, EDy, and non-ENSO years, respectively.

To further reveal what dynamical processes may contribute to the prediction skill of intensity, **Figure 9A** shows correlations between the prediction skills in **Figure 8** and the 500-hPa geopotential height and SST anomalies. There are mainly three highly correlated height anomalies, one in the WNP and two in the northeastern and southeastern tropical Pacific. The positive height anomaly corresponds to the positive SST anomaly over the WNP region, indicating the atmospheric forcing on the ocean there. Clearly, the maximum correlations with SST are located over the TIO, which are dynamically connected with the maximum correlations of the WNP height, constituting a

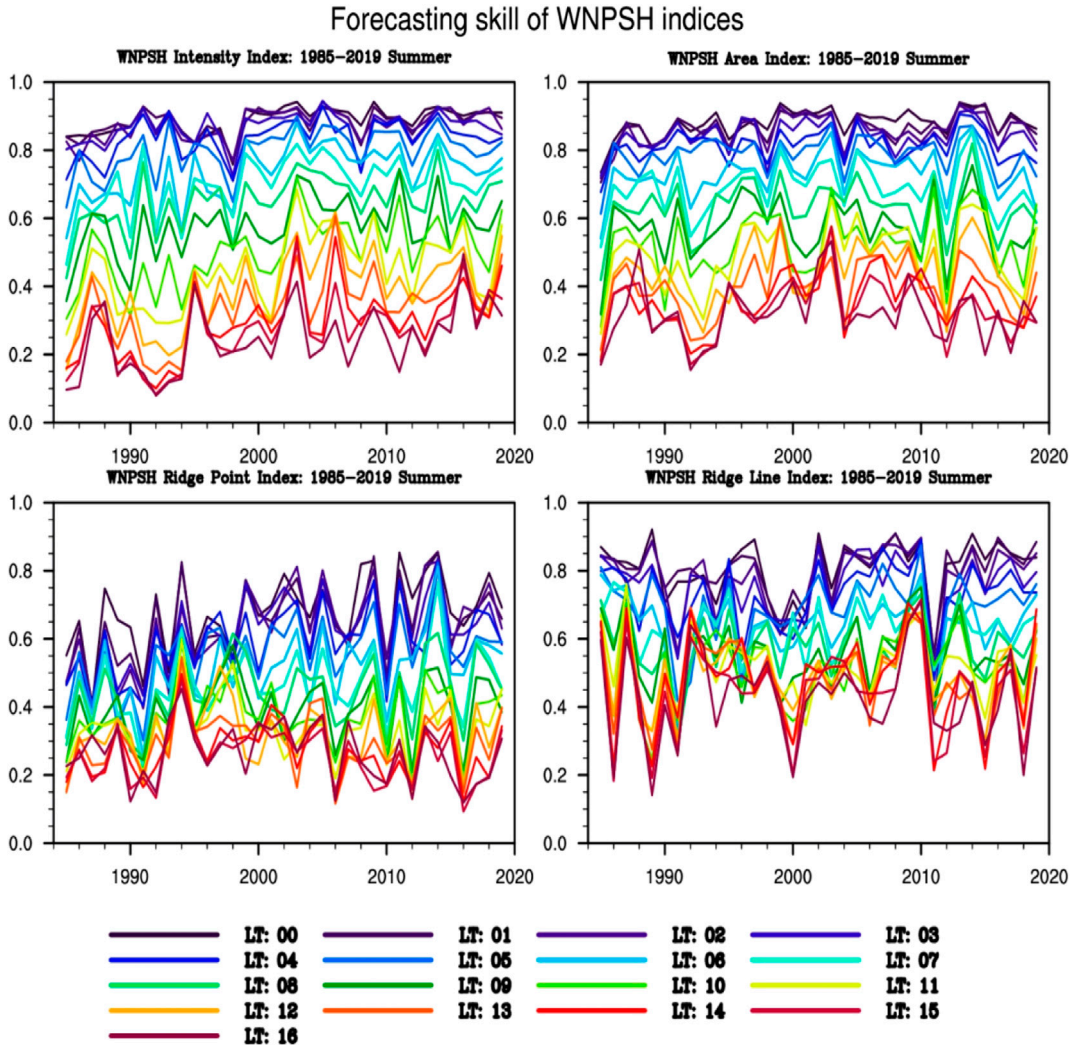

FIGURE 7 | Yearly variations in prediction skills of the summer WNPSH indices **(A–D)** represent intensity, area, ridge point, and ridge line, respectively.

TIO-WNP teleconnection (Yang et al., 2007; Li et al., 2008; Xie et al., 2009; Wu et al., 2010; Zhang et al., 2012; He et al., 2019). In **Figures 9A,B** significant correlation of 0.81 is found between the box-average-defined indices of the SST anomalies in TIO and the 500-hPa height anomalies in WNP, meaning that the former can explain a variance greater than 60% of the latter. Previous studies figured out that a successful reproduction of the interannual East-Asian summer Monsoon (EASM) pattern highly depends on the TIO-WNP teleconnection (Zhang et al., 2012; Song and Zhou 2014). Our results clearly suggest that the TIO-WNP teleconnection is also crucial for the medium-range predictability of the WNPSH intensity, i.e., a stronger teleconnection contributing to higher prediction skills. The TIO SST and WNP anomalies have significant correlations of 0.64 and 0.58 with prediction skills of the WNPSH intensity, respectively, and also show clear upward trends (**Figure 9B**). This may be the reason for the observed interdecadal change of the intensity skills around 2000 (**Figure 8**). In other words, the warming of TIO since 2000 has enhanced WNPSH through the TIO-WNP teleconnection and then led to a significant increase in the intensity skills. ENSO may have an indirect effect on prediction skills of the WNPSH intensity due to the significant modulation as shown in **Figure 6A** though their direct connection is not yet found. Moreover, a similar conclusion has also been found for the WNPSH area index (not shown).

For ridge point (**Figure 10A**), the years with higher prediction skills are 1994 (EDp), 2005 (non-ENSO), 2009 (EDp), and 2014 (non-ENSO), and the years with lower skills are 1985 (LDy), 1987 (EDy), and 1991 (EDp). For ridge line (**Figure 10B**), the years with prediction skills greater than 1 standard deviation are 1985 (LDy), 1987 (EDy), and 2010 (EDy and LDp), and the years with skills less than 1 standard deviation are 1991 (EDp), 1999 (persisting La Niña), 2000 (LDy), and 2011 (LDy). However, we cannot find a close relationship between prediction skills of the WNPSH position and ENSO or other common factors, which may be the main reason that their prediction skills are relatively

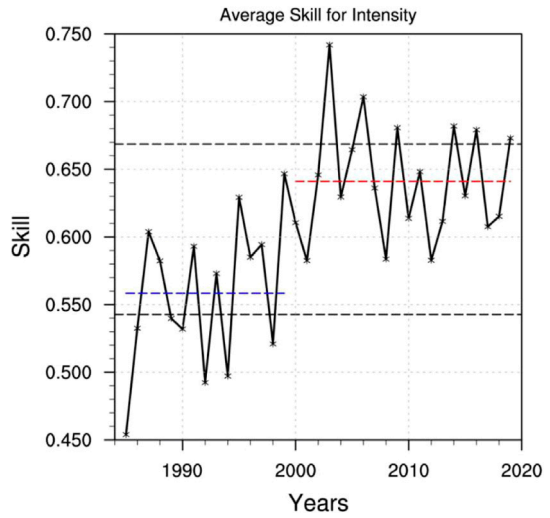

FIGURE 8 | The average prediction skills of the WNPSH intensity index of different lead times as shown in **Figure 7**. The two black dotted lines represent that the all-year mean pluses or minuses one standard deviation. The blue dashed line represents the average skill during 1985–1999 and the red one does during 2000–2019.

lower compared to the WNPSH intensity and area (**Figures 2**, **3**). We compared prediction skills of the two position indices with their standard deviations and found that these skills may be mainly contributed from their variability. As seen in **Figure 10A**, the fluctuation in prediction skills of the ridge point and its variability corresponds well with a significant correlation of 0.36 at the 95% confidence level and 0.55 at the 99.9% confidence level after detrending. This confirms prediction performance of the ridge point can be largely affected by its variability. That is when the east-west movement of ridge point is more (less) frequent, the prediction skills tend to be higher (lower). In contrast, the variability of the ridge line has only a weakly negative correlation (about -0.2) with its prediction skill.

Although it is difficult to directly determine which process is related to the prediction skill of the ridge point, we could find out the factor that determines the variability of ridge point and thus those processes may indirectly affect prediction skill. Correlations of the ridge point skill with the 500-hPa height anomalies show the significant regions in the tropics (**Figure 11A**). It is worth noting that the significant negative correlations are not caused by climate trends that have been removed before the correlation calculating. **Figure 11B** shows standard deviations of the ridge point and the height anomaly indices averaged over the entire tropical region. A significant correlation can be found between them in boreal summer and even spring height anomalies are also highly correlated with the ridge point in terms of their standard deviations, which indicates that the height anomalies over tropics in spring may have implications for predicting the summer WNPSH. The correlations between the standard deviations of ridge point and height anomalies are −0.55 and −0.64 in spring

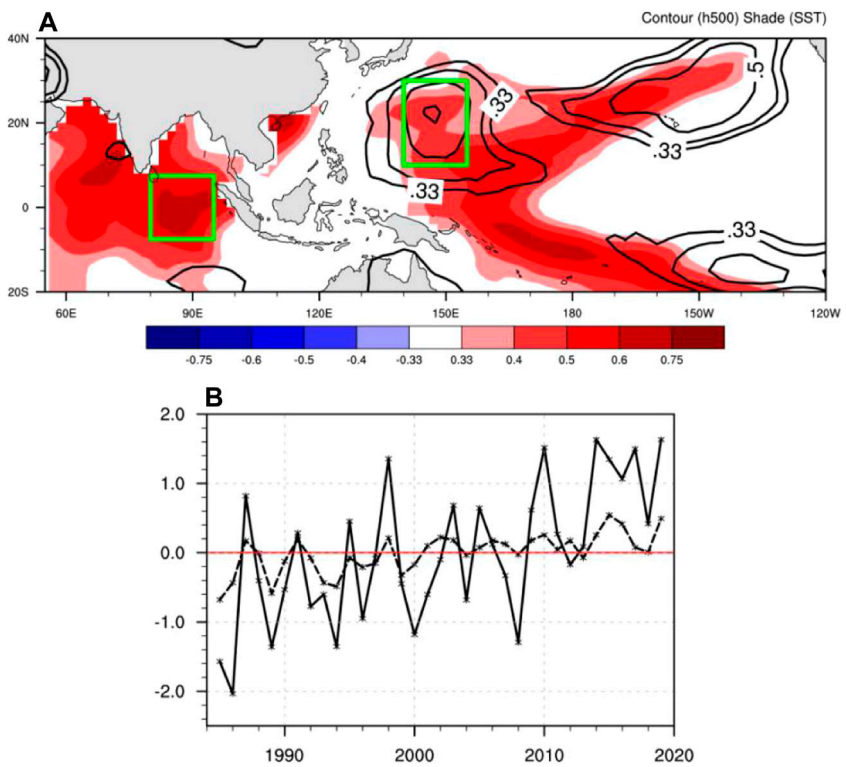

FIGURE 9 | (A) Correlation coefficients between 500-hPa height (contours), SST anomaly (shade) and the prediction skills of the WNPSH intensity in **Figure 8**, only show the values that pass the 95% confidence *t*-test. **(B)** The standardized domain-averaged indices of the SST anomaly (dashed line) in the tropical Indian Ocean and 500-hPa height anomaly (solid line) in the western North Pacific, where the two domains are defined by the boxes in (a).

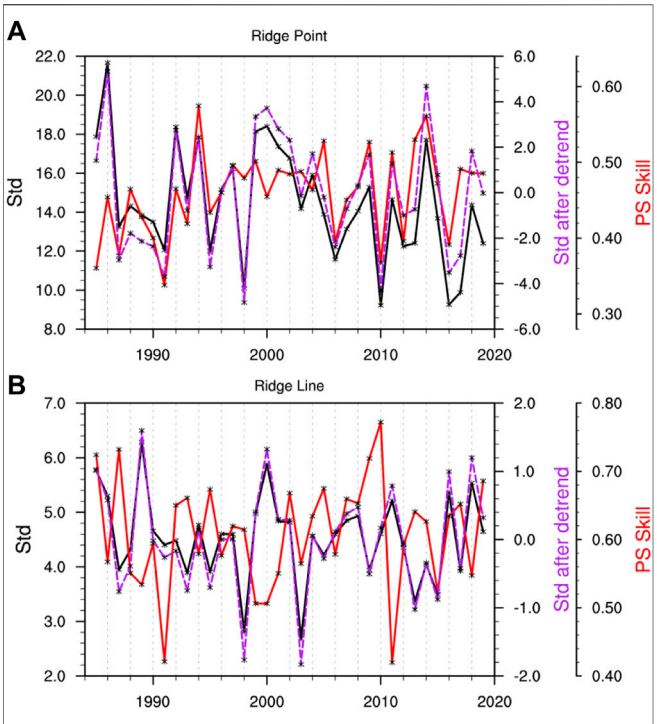

FIGURE 10 | Average prediction skills of the WNPSH **(A)** ridge point and **(B)** ridge line indices of different lead times in **Figure 7**. The red lines represent PS skills, the black lines do standard deviation, and the purple lines do standard deviation after detrending.

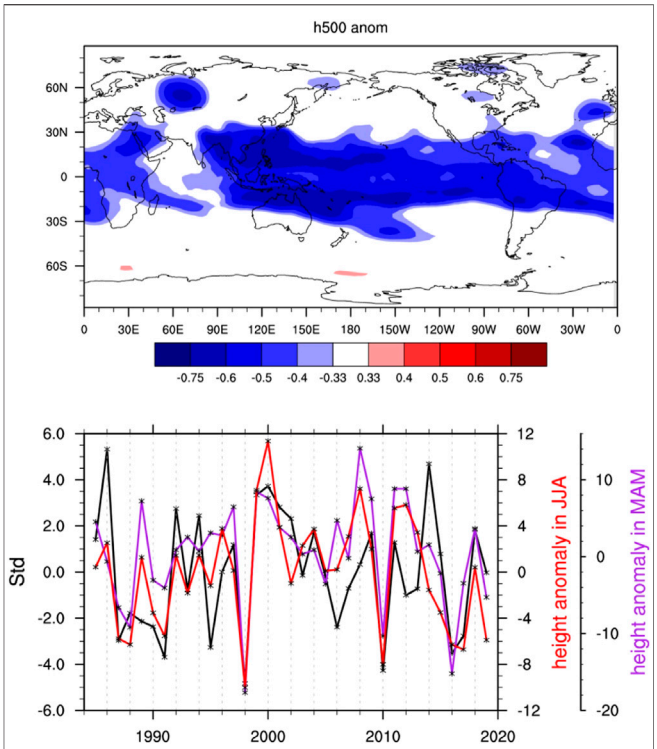

FIGURE 11 | (A) Correlation coefficients between the detrended 500-hPa height anomaly and the ridge point prediction skills in **Figure 10A**, only show the values passing the 95% confidence *t*-test. **(B)** Standard deviations of the WNPSH ridge point index (black line), the 500-hPa height anomaly indices during summer (red line) and spring (purple line) averaged over the tropical region (30°S–30°N, 0–360°E). Here, the height anomalies have been multiplied by -1.

and summer, respectively, which are statistically significant at the 99.9% confidence level. This means that the east-west movement of WNPSH will be more frequent when the height anomalies in the tropics are negative. Note that the prediction skill of the ridge point tends to be higher when the WNPSH has more frequent east-west movement (**Figure 10A**). Therefore, the height anomalies in the tropics may indirectly affect the performance of the ridge point prediction.

6 SUMMARY AND DISCUSSIONS

Variations of the WNPSH intensity and location are closely related to weather and climate in East Asia. Research on their prediction evaluation and predictability analysis has been a crucial issue. However, less attention is paid to the medium-range forecasting and its predictability source though many prior studies have paid much attention to the seasonal forecasting of WNPSH and its predictability. In this study, a few scores were used to comprehensively evaluate the performance of NCEP-GEFS in medium-ranged forecasting WNPSH. In addition, given the significant ENSO modulation of WNPSH, the capability of the model system in reproducing such modulation and the predictability sources of the WNPSH medium-range forecasting were also investigated.

NCEP-GEFS has a systematic bias in the WNPSH forecasts, mainly manifested by the weak strength, eastward and southward shift of location, and such a bias can further increase with the extension of forecast length. The three skill scores (called *ME*, *NRMSE*, and *R*), measuring the amplitude error, normalized deviation, and consistency between the forecasts and observations, respectively, have been used to evaluate the prediction skills of the WNPSH indices. The results show that the skillful prediction lengths of WNPSH intensity, area, ridge point and ridge line are 10 (11), 9 (10), 0 (3), 7 7) days in terms of *NRMSE* (*R*), respectively, which can be improved to 13 (11), 11 (11), 5 (5), and 9 8) days through introducing the correction method of systematic bias.

The Niño 3.4 index of representing ENSO is significantly correlated with the intensity, area, and ridge point of WNPSH, with the peak correlations at 4-months lag, showing the significant modulation of the WNPSH by ENSO. Further results show that the WNPSH intensity and area tend to be stronger (weaker) during the EDy (EDp) and LDp (LDy) summers, and the ridge point is also accompanied by westward extension during the EDy and LDp summers and eastward withdrawal during the EDp and LDy summers. Such a modulation can be well reproduced by the NCEP GEFS which thus has given realistic forecasts to some degree. This means that the medium-range weather forecasting system (not climate

prediction system) can also capture the seasonal anomalies of WNPSH associated with ENSO on the interannual time scale.

The predictability source of the medium-range forecasting of the WNPSH indices was further analyzed. Our results showed that the prediction skill of the intensity could be modulated by the TIO-WNP teleconnection, i.e., the stronger latter is, the higher skills of the form are. However, the prediction skill of the WNPSH location indices is less affected by external forcing, but more by internal variability. For the ridge point, its prediction skill is positively proportional to its variability that has a significantly negative correlation with the geopotential height anomalies in the tropics, implying that the latter may indirectly affect the prediction skill of ridge point.

This study showed that the capability of NCEP-GEFS to accurately reproduce the TIO-WNP teleconnection strength and the height anomalies in the tropics is the key for the model system to give accurate medium-range forecasts of WNPSH. However, the results have been based on one model only. In the next steps, more models that own the medium-range reforecasts need to be introduced to validate our results. In addition, we have only examined the predictability source of interannual variations in the prediction skills of WNPSH. Future research will be needed to investigate issues in the sub-seasonal variations of the prediction skills and their predictability Gao et al., 2019.

DATA AVAILABILITY STATEMENT

The original contributions presented in the study are included in the article/Supplementary Material, further inquiries can be directed to the corresponding author.

AUTHOR CONTRIBUTIONS

LG provided the idea and wrote the paper, PR carried out the analysis. JZ contributed to discussing the results and writing the paper. All authors commented on the manuscript.

FUNDING

This work was jointly supported by the National Natural Science Foundation of China (41875138 and 42175015) and the National Key Research and Development Program of China (2018YFF0300103).

REFERENCES

Cai, X. Z., Wen, Z. Z., and Wu, B. (2003). Relationship between West Pacific Subtropical High and ENSO and its Influence on Rainfall Distribution of Rainy Season in Fujian. *J. Trop. Meteorology* 19 (1), 36–42. (in Chinese). doi:10.3969/j.issn.1006-8775.2003.01.007

Chen, L., Yu, Y., and Sun, D.-Z. (2013). Cloud and Water Vapor Feedbacks to the El Niño Warming: Are They Still Biased in CMIP5 Models? *J. Clim.* 26, 4947–4961. doi:10.1175/jcli-d-12-00575.1

Chou, C., Tu, J.-Y., and Yu, J.-Y. (2003). Interannual Variability of the Western North Pacific Summer Monsoon: Differences between ENSO and Non-ENSO Years. *J. Clim.* 16, 2275–2287. doi:10.1175/2761.1

Gao, L., Ren, H.-L., Zheng, J., and Chen, Q. (2019). Diagnosing Features of Extreme Temperature Variations in China Based on the NCEP-GEFS Reforecasts. *Trans. Atmos. Sci.* 42 (1), 58–67. (in Chinese). doi:10.13878/j.cnki.dqkxxb.20180911001

Gao, L., Ren, P., Zhou, F., Zheng, J., and Ren, H. (2020). Evaluations and Ensemble Approaches of Western-Pacific Subtropical High and South-Asian High Ensemble Forecasting in GRAPES-GEPS. *Adv. Earth Sci.* 35 (7), 715–730. (in Chinese). doi:10.11867/j.issn.1001-8166.2020.060

Hamill, T. M., Bates, G. T., Whitaker, J. S., Murray, D. R., Fiorino, M., Galarneau, T. J., Jr., et al. (2013). NOAA's Second-Generation Global Medium-Range Ensemble Reforecast Dataset. *Bull. Amer. Meteorol. Soc.* 94, 1553–1565. doi:10.1175/bams-d-12-00014.1

He, C., Lin, A., Gu, D., Li, C., Zheng, B., Wu, B., et al. (2018). Using Eddy Geopotential Height to Measure the Western North Pacific Subtropical High in a Warming Climate. *Theor. Appl. Climatol.* 131, 681–691. doi:10.1007/s00704-016-2001-9

He, C., Zhou, T., and Li, T. (2019). Weakened Anomalous Western North Pacific Anticyclone during an El Niño–Decaying Summer under a Warmer Climate: Dominant Role of the Weakened Impact of the Tropical Indian Ocean on the Atmosphere. *J. Clim.* 32, 213–230. doi:10.1175/jcli-d-18-0033.1

Huang, S. S. (1963). A Study of the Longitudinal of Movement and its Forecasting of Subtropical Anticyclones. *Acta Meteorologica Sinica* (in Chinese) 33 (3), 320–332. doi:10.11676/qxxb1963.030

Huang, Y., and Li, X. (2015). The Interdecadal Variation of the Western Pacific Subtropical High as Measured by 500 hPa Eddy Geopotential Height. *Atmos. Oceanic Sci. Lett.* 8 (6), 371–375. doi:10.3878/AOSL20150038

Huang, Y., Wang, H., Fan, K., and Gao, Y. (2015). The Western Pacific Subtropical High after the 1970s: Westward or Eastward Shift? *Clim. Dyn.* 44, 2035–2047. doi:10.1007/s00382-014-2194-5

Kanamitsu, M., Ebisuzaki, W., Woollen, J., Yang, S.-K., Hnilo, J. J., Fiorino, M., et al. (2002). NCEP-DOE AMIP-II Reanalysis (R-2). *Bull. Amer. Meteorol. Soc.* 83 (11), 1631–1644. doi:10.1175/bams-83-11-1631

Li, S., Lu, J., Huang, G., and Hu, K. (2008). Tropical Indian Ocean basin Warming and East Asian Summer Monsoon: A Multiple AGCM Study. *J. Clim.* 21, 6080–6088. doi:10.1175/2008jcli2433.1

Li, T., Wang, B., Wu, B., Zhou, T., Chang, C.-P., and Zhang, R. (2017). Theories on Formation of an Anomalous Anticyclone in Western North Pacific during El Niño: A Review. *J. Meteorol. Res.* 31, 987–1006. doi:10.1007/s13351-017-7147-6

Liu, Y., Li, W., Ai, W., and Li, Q. (2012). Reconstruction and Application of the Monthly Western Pacific Subtropical High Indices. *J. Appl. Meteorol. Sci.* (in Chinese) 23 (4), 414–423.

Matsumura, S., Sugimoto, S., and Sato, T. (2015). Recent Intensification of the Western pacific Subtropical High Associated with the East Asian Summer Monsoon. *J. Clim.* 28 (7), 2873–2883. doi:10.1175/jcli-d-14-00569.1

Niu, R., and Zhai, P. (2013). Synoptic Verification of Medium-Extended-Range Forecasts of the Northwest pacific Subtropical High and South Asian High Based on Multi-center TIGGE Data. *Acta Meteorol. Sin* 27 (5), 725–741. doi:10.1007/s13351-013-0513-0

Song, F., and Zhou, T. (2014). Interannual Variability of East Asian Summer Monsoon Simulated by CMIP3 and CMIP5 AGCMs: Skill Dependence on Indian Ocean-Western Pacific Anticyclone Teleconnection. *J. Clim.* 27 (4), 1679–1697. doi:10.1175/jcli-d-13-00248.1

Tao, S., and Wei, J. (2006). The Westward, Northward Advance of the Subtropical High over the West Pacific in Summer. *J. Appl. Meteorol. Sci.* (in Chinese) 17 (5), 513–525. doi:10.11898/1001-7313.20060509

Wang, C., Weisberg, R., and Virmani, J. (1999). Western Pacific interannual variability associated with the El Niño-Southern Oscillation. *J. Geophys. Res.* 104(C3), 5131–5149. doi:10.1029/1998JC900090

Wang, B., Lee, J.-Y., Kang, I.-S., Shukla, J., Park, C.-K., Kumar, A., et al. (2009). Advance and Prospectus of Seasonal Prediction: Assessment of the APCC/

CliPAS 14-model Ensemble Retrospective Seasonal Prediction (1980-2004). *Clim. Dyn.* 33, 93–117. doi:10.1007/s00382-008-0460-0

Wang, C., and Zou, L. (2004). West Pacific Subtropical High's Interannual Variability and Relativity to ENSO. *J. Trop. Meteorology* (in Chinese) 20 (2), 137–144. doi:10.3969/j.issn.1004-4965.2004.02.004

Wen, N., Liu, Z., and Liu, Y. (2015). Direct Impact of El Niño on East Asian Summer Precipitation in the Observation. *Clim. Dyn.* 44, 2979–2987. doi:10.1007/s00382-015-2605-2

Wu, R., Hu, Z.-Z., and Kirtman, B. P. (2003). Evolution of ENSO-Related Rainfall Anomalies in East Asia. *J. Clim.* 16, 3742–3758. doi:10.1175/1520-0442(2003)016<3742:eoerai>2.0.co;2

Wu, B., Li, T., and Zhou, T. (2010). Relative Contributions of the Indian Ocean and Local SST Anomalies to the Maintenance of the Western North Pacific Anomalous Anticyclone during the El Niño Decaying Summer*. *J. Clim.* 23, 2974–2986. doi:10.1175/2010JCLI3300.1

Xie, S.-P., Hu, K., Hafner, J., Tokinaga, H., Du, Y., Huang, G., et al. (2009). Indian Ocean Capacitor Effect on Indo-Western Pacific Climate during the Summer Following El Niño. *J. Clim.* 22, 730–747. doi:10.1175/2008jcli2544.1

Yang, H., and Sun, S. Q. (2003). Longitudinal Displacement of the Subtropical High in the Western Pacific in Summer and its Influence. *Adv. Atmos. Sci.* 20, 921–933. doi:10.1007/BF02915515

Yang, J., Liu, Q., Xie, S.-P., Liu, Z., and Wu, L. (2007). Impact of the Indian Ocean SST basin Mode on the Asian Summer Monsoon. *Geophys. Res. Lett.* 34, L02708. doi:10.1029/2006GL028571

Yang, R., Xie, Z., and Cao, J. (2017). A Dynamic index for the Westward ridge point Variability of the Western Pacific Subtropical High during Summer. *J. Clim.* 30, 3325–3341. doi:10.1175/jcli-d-16-0434.1

Ying, M., and Sun, S. (2000). A Study on the Response of Subtropical High over the Western Pacific on the SST Anomaly. *Chin. J. Atmos. Sci.* (in Chinese) 24, 193–206. doi:10.1007/s10011-000-0335-3

Zhang, M., Li, S., Lu, J., and Wu, R. (2012). Comparison of the Northwestern Pacific Summer Climate Simulated by AMIP II AGCMs. *J. Clim.* 25, 6036–6056. doi:10.1175/JCLI-D-11-00322.1

Zhang, R., Min, Q., and Su, J. (2017). Impact of El Niño on Atmospheric Circulations over East Asia and Rainfall in China: Role of the Anomalous Western North Pacific Anticyclone. *Sci. China Earth Sci.* 60, 1124–1132. doi:10.1007/s11430-016-9026-x

Zhou, F., Ren, H. L., Hu, Z. Z., Liu, M. H., Wu, J., Liu, C. Z., and Tang, D. (2020). Seasonal Predictability of Primary East Asian Summer Circulation Patterns by Three Operational Climate Prediction Models. *QJR Meteorol. Soc.* 146, 629–646. doi:10.1002/qj.3697

Zhu, Q., Lin, J., Shou, S., et al. (1992). *Principles and Methods of Synoptic Meteorology*. Beijing: China Meteorological Press, pp677. (in Chinese).

Conflict of Interest: The authors declare that the research was conducted in the absence of any commercial or financial relationships that could be construed as a potential conflict of interest.

Publisher's Note: All claims expressed in this article are solely those of the authors and do not necessarily represent those of their affiliated organizations, or those of the publisher, the editors and the reviewers. Any product that may be evaluated in this article, or claim that may be made by its manufacturer, is not guaranteed or endorsed by the publisher.

frontiers in Earth Science

ORIGINAL RESEARCH
published: 07 March 2022
doi: 10.3389/feart.2022.853577

Responses of Tropical Background State and ENSO Behaviors to Mid-Holocene Forcing Simulated by PMIP3 and PMIP4 Models

*Meng-Er Song and Lin Chen**

Key Laboratory of Meteorological Disaster, Ministry of Education (KLME), Joint International Research Laboratory of Climate and Environmental Change (ILCEC), Collaborative Innovation Center on Forecast and Evaluation of Meteorological Disasters (CIC-FEMD), Nanjing University of Information Science and Technology, Nanjing, China

The mid-Holocene (MH), a period about 6,000 years ago, provides an opportunity to understand climate change in response to orbital forcing change. Numerical model simulation is an effective tool through which we can study the climate change in the MH, although the climate in the MH can be partly inferred from proxy data. As the Paleoclimate Model Inter-comparison Project phase 4 (PMIP4) recently released the latest simulations for different past climate scenarios, we investigated tropical climate changes, including both the basic state and interannual variability, and tried to find out whether the PMIP phase 3 (PMIP3) and PMIP4 results can be reconciled. Almost all the modelling results show that the inter-hemisphere contrast was enhanced over the tropical Pacific, with warmer and wetter condition on the northern side of the equator and an intensified cross-equatorial flow in the MH than at present, and the annual cycle of the sea-surface temperature (SST) during the MH was reduced. Such background mean state changes arose from the seasonal changes of the solar incident radiation in the MH. In addition to the consistent changes in background mean state changes, some El Niño-Southern Oscillation (ENSO) features, such as the seasonal phase locking feature and periodicity, show consistent changes across the PMIP3 and PMIP4 models, that is, both suites of models exhibit no marked difference in the MH with respect to present-day simulations. In contrast, the modeling results show only agreement on the sign of the ENSO amplitude change (i.e., decrease in the ENSO amplitude in the MH), while the range of reduction varied with model and region. Additionally, the occurrence probability of central Pacific El Niño events increases in the MH, whereas the significance is quite marginal. The modeled changes in the mean state and ENSO serve as a test bed for studying tropical climate system's response to natural warming, which may provide some insights into understanding climate changes in response to the current anthropogenic warming.

Keywords: mid-Holocene, PMIP, tropical pacific background states, multi-model consistency, ENSO (El Niño-Southern Oscillation) prediction

OPEN ACCESS

Edited by:
Ruihuang Xie,
Ocean University of China, China

Reviewed by:
Eduardo Zorita,
Helmholtz Centre for Materials and Coastal Research (HZG), Germany
Youichi Kamae,
University of Tsukuba, Japan

****Correspondence:***
Lin Chen
chenlin@nuist.edu.cn

Specialty section:
This article was submitted to Atmospheric Science, a section of the journal Frontiers in Earth Science

Received: *12 January 2022*
Accepted: *07 February 2022*
Published: *07 March 2022*

Citation:
Song M-E and Chen L (2022) Responses of Tropical Background State and ENSO Behaviors to Mid-Holocene Forcing Simulated by PMIP3 and PMIP4 Models. Front. Earth Sci. 10:853577. doi: 10.3389/feart.2022.853577

INTRODUCTION

In the mid-Holocene (MH) of ~6,000 years before present, the climate system differed greatly with respect to the present-day climate. It is accepted that the root cause leading to the distinctive MH climate that differed from the present-day climate lies in different orbital parameters in the MH epoch (e.g., Kutzbach and Otto-Bliesner 1982; Kutzbach and Liu 1997; Zheng and Braconnot 2013; Zheng and Yu 2013). Understanding the paleoclimate changes, especially the change in the typical warming period—MH period, has profound meaning.

During the MH, the climate in the Earth system experienced obvious changes. For instance, the insolation at high latitudes in the boreal summer was greater in the MH than in present-day climate; hence, a lot of ice sheets in the Northern Hemisphere (NH) melted (Gong et al., 2015; Gierz et al., 2020). The global monsoon areas and precipitation in the MH were enlarged compared with the present-day based on the evidence from pollen data and model simulations (Kohfeld and Harrison 2000; Jiang et al., 2015). Moreover, the tropical Pacific region also witnessed the orbital-induced climate changes in the MH. Previous studies have shown that the mean state, annual cycle and dominant interannual variability in the tropical Pacific, which is called the El Niño-Southern Oscillation (ENSO), exhibited great changes in response to the orbital forcing alteration in the MH. However, these studies also underscored uncertainty regarding the climate changes in the tropical Pacific region in the MH.

Based on the evidence of fossil corals, Gagan (1998) indicated that parts of the tropics were warmer during the MH than at present-day. In contrast, through measuring $\delta^{18}O$ from proxy data, Koutavas et al. (2006) and Carre et al. (2014) found that the mean sea-surface temperature (SST) during the MH was cooler than that at present-day by about 0.5°–3°C. In addition to the mean state, ENSO variability in the MH also had some differences from the present-day. A number of proxy records, such as corals, fossil mollusk shells and ice cores, provide evidence for a weakening ENSO variability during the MH, but the magnitude of this weakening varies in a range of 29–80% (e.g., Tudhope et al., 2001; Koutavas et al., 2006; Koutavas and Joanides 2012; Carre et al., 2014; Emile-Geay et al., 2016). However, an interesting study conducted by Cobb (2013) argued that the fossil coral sequences may be too short to reveal the ENSO activity change for a long period of time, and they even argued that one may not easily obtain the conclusion that a significant reduction of ENSO variability is found in the MH. To summarize, there is no consensus on the magnitude of ENSO variability reduction based on the proxy data. This promotes the paleoclimate community to turn to the model simulation's help.

During the past several decades, more and more efforts have been devoted to paleoclimate simulations, e.g., the continuous Paleoclimate Model Inter-comparison Project phase (PMIP) projects. They found that the mean SST in the tropical Pacific was around 1°C cooler than the present-day, especially in the tropical Pacific cold tongue region (e.g., Otto-Bliesner 1999; Liu et al., 2000; Otto-Bliesner et al., 2003; Brown et al., 2006), which supports part of the proxy

TABLE 1 | Information describing the model resolutions and simulation length.

Model		Resolution		Length (years)	
		Atmos	Ocean	PI (0 ka)	MH (6 ka)
PMIP3 models	BCC-CDM1-1	128 × 64 L26	360 × 320 L40	500	100
	CCSM4	288 × 192 L26	320 × 384 L60	500	300
	CNRM-CM5	256 × 128 L31	362 × 292 L42	850	200
	CSIRO-MK3-6	192 × 96 L18	192 × 192 L31	500	100
	CSIRO-MK3-1-2	64 × 56 L18	128 × 112 L21	1,000	500
	FGOALS-g2	128 × 60 L26	360 × 180 L30	700	680
	FGOALS-s2	128 × 64 L26	360 × 196 L30	500	100
	GISS-E2-R	144 × 90 L40	288 × 180 L32	500	100
	HadGEM2-ES	192 × 145 L60	360 × 216 L40	475	100
	IPSL-CM5A-LR	96 × 95 L39	182 × 149 L31	1,000	100
	MIROC-ESM	128 × 64 L80	256 × 192 L40	500	100
	MPI-ESM-P	196 × 98 L47	256 × 220 L40	1,000	100
	MRI-CGCM3	320 × 160 L48	364 × 368 L51	500	100
PMIP4 Models	CESM2	288 × 192 L32	320 × 384 L60	1,051	100
	EC-Earth3-LR	512 × 256 L91	362 × 292 L75	201	201
	FGOALS-f3-L	Cube96 L32	360 × 218 L30	561	500
	FGOALS-g3	180 × 90 L26	360 × 218 L30	700	500
	GISS-E2-1-G	144 × 90 L40	360 × 180 L32	851	100
	INM-CM4-8	180 × 120 L21	360 × 318 L40	531	200
	IPSL-CM6A-LR	144 × 143 L79	362 × 332 L75	1,200	550
	MPI-ESM1-2-LR	192 × 96 L47	256 × 220 L40	1,000	500
	MRI-ESM2-0	320 × 160 L80	360 × 364 L61	701	200
	NESM3	192 × 96 L47	384 × 362 L46	100	100
	NorESM1-F	144 × 96 L26	360 × 384 L70	200	200
	NorESM2-LM	144 × 96 L32	360 × 384 L70	391	100

TABLE 2 | Model boundary conditions.

	PI (0 ka)	PMIP3 MH (6 ka)	PMIP4 MH (6 ka)
Trace gases	CO_2 = 280 ppm	CO_2 = 280 ppm	CO_2 = 264.4 ppm
	CH_4 = 760 ppb	CH_4 = 650 ppb	CH_4 = 597 ppb
	N_2O = 270 ppb	N_2O = 270 ppb	N_2O = 262 ppb
Orbital parameters	ecc = 0.016724	ecc = 0.018682	ecc = 0.018994
	obl = 23.446°	obl = 24.105°	obl = 24.105°
	peri - 180° = 102.04°	peri - 180° = 0.87°	peri - 180° = 0.87°
Aerosols	Average from 1850 to 2014	Same as in CMIP5 PI	Same as in CMIP6 PI
Solar constant	1,365 W/m2	Same as in CMIP5 PI	Same as in CMIP6 PI
Ice-sheets	Present day	Same as in CMIP5 PI	Same as in CMIP6 PI

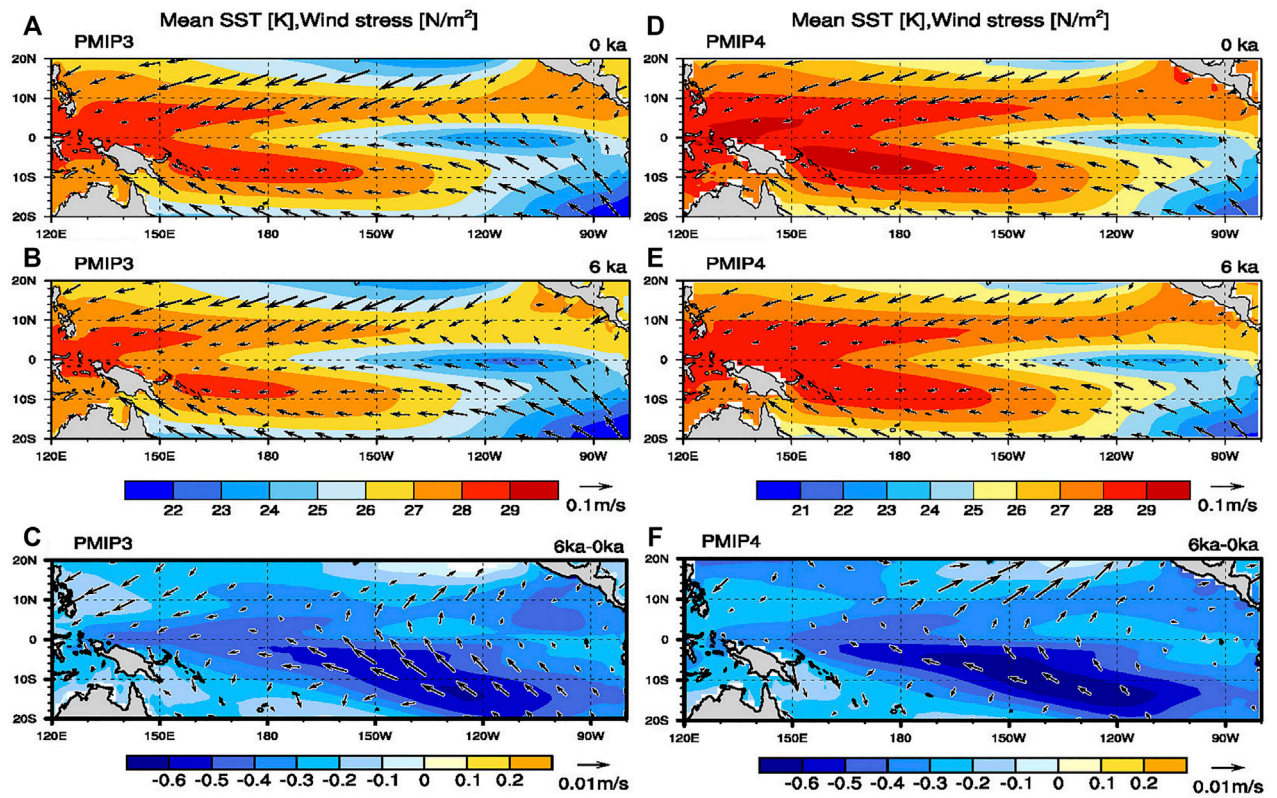

FIGURE 1 | Plots for MME of mean SST and surface wind stress derived from PMIP3 (left column) and PMIP4 (right column) models. **(A)** and **(D)** are PI simulations; **(B)** and **(E)** are MH simulations; and **(C)** and **(F)** are their differences (MH minus PI). Shading and vector in **(C)** and **(F)** indicate the difference between MH and PI is significant at the 95% level by Student's *t*-test.

records. Same as proxy records, plenty of modeling studies showed that the ENSO activity in the MH was reduced, but the magnitude of the reduction varied from 5 to 80% (Otto Bliesner et al., 2003; Zheng et al., 2008; Zheng and Yu 2013; Tian et al., 2017; Chen et al., 2019a; Chen et al., 2019b; Brown et al., 2020). Although most modeling studies show an agreement on the sign of ENSO amplitude change during the MH, there are still large uncertainty regarding the specific magnitude of ENSO amplitude change among these modelling studies.

Recently, the PMIP phase 4 (hereafter PMIP4) simulation results were released (Kageyama et al., 2018), it is necessary to find out whether the PMIP phase 3 (hereafter PMIP3) and PMIP4 results can be reconciled. Here we focused on the mean state, annual cycle and ENSO activity reconstructed by the PMIP4 models over the tropical Pacific during the MH. The simulations of the PMIP3 models were used to be compared with those of the PMIP4 models, and the discrepancies of simulation results between PMIP3 and PMIP4 models were analyzed. The data used in this study is introduced in **Section 2**. The simulation results of mean state and annual cycle are shown in **Section 3**, and the ENSO variability is examined in **Section 4**. We summarize this study in **Section 5**.

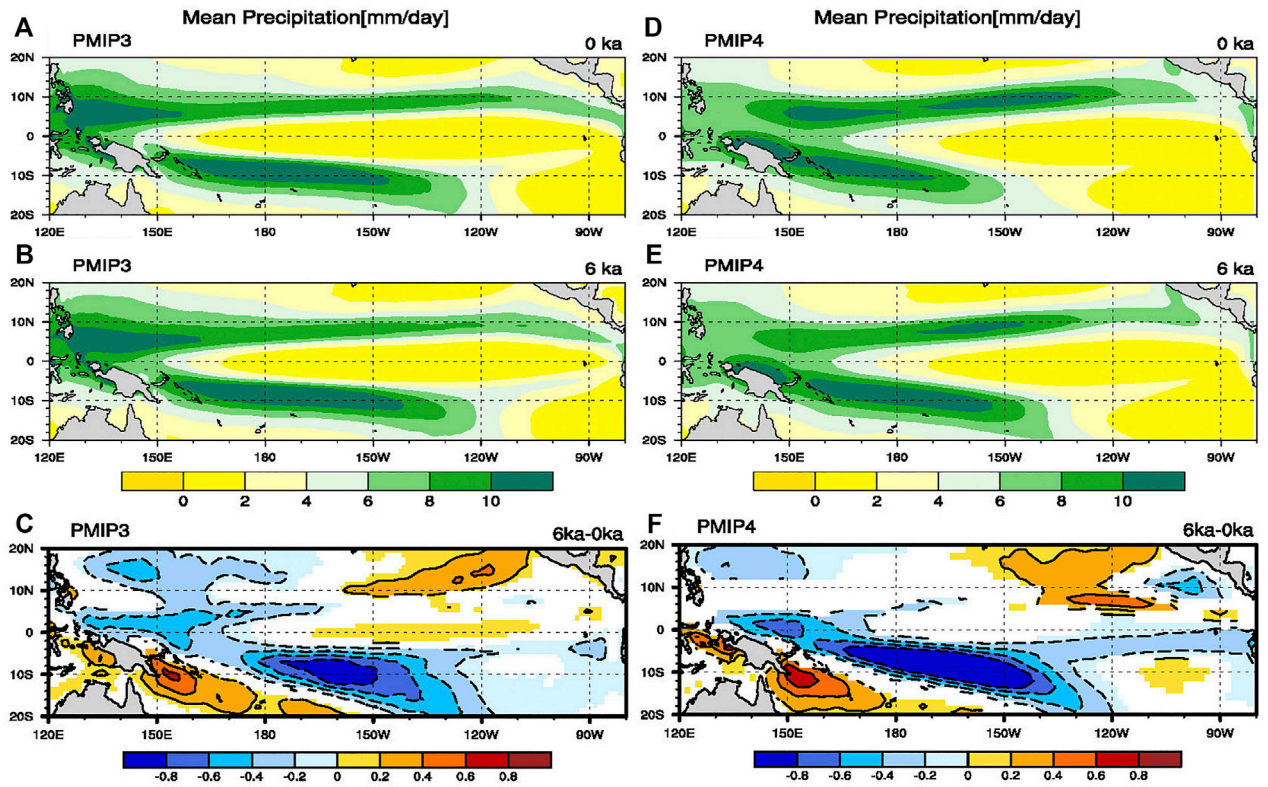

FIGURE 2 | Plots for MME of mean precipitation derived from PMIP3 (left column) and PMIP4 (right column) models. **(A)** and **(D)** are PI simulations; **(B)** and **(E)** are MH simulations; and **(C)** and **(F)** are their differences (MH minus PI). Shading and vector in **(C)** and **(F)** indicate the difference between MH and PI is significant at the 95% level by Student's *t*-test.

DATA

The simulation for the MH climate period is one of the important experiments in the PMIP, which is also part of Coupled Model Intercomparison Project (CMIP). According to the data ability, 13 PMIP3 models and 12 PMIP4 models were used in this study. The basic information of the 25 models are presented in **Table 1**, and the boundary conditions for the MH simulation in both PMIP3 and PMIP4 are shown in **Table 2**. The primary difference between the PMIP3 and the PMIP4 experiments boundary conditions lies in greenhouse gases (GHG) concentration, and the other boundary conditions such as ice-sheets, aerosols and solar constant are identical. The variables used in this study include SST, precipitation, surface wind stress, sea water potential temperature and top of the atmosphere incident shortwave radiation. Due to the different model horizontal resolutions, all data were interpolated onto a regular $1^{\circ} \times 1^{\circ}$ (latitude x longitude) grid.

TROPICAL BACKGROUND STATE

Mean States

The tropical climate states of SST and wind stress during the PI and MH of 13 PMIP3 models and 12 PMIP4 models and their differences in terms of multi-model ensemble mean (MME) are shown in **Figure 1**. In the present-day climate simulations (**Figures 1A,D**) and MH simulations (**Figures 1B,E**), both PMIP3 and PMIP4 models show similar large-scale distribution features, including the cold tongue in the eastern equatorial Pacific, the warm pool in the western Pacific, and the surface winds converging toward the warm surface temperature region. In general, the trade wind and mean SST appear approximately symmetric with respect to the equator over the western tropical Pacific, while the mean SST exhibits asymmetric distribution with respect to the equator over the eastern tropical Pacific (i.e., warm SST in the northeastern part but cold SST in the southeastern part), matching the cross-equatorial southerly over the eastern Pacific, especially the southerly near the coast of Peru. The difference maps (**Figures 1C,F**) show the mean SST cooling to various extent over the entire tropical Pacific in the MH compared to that in the PI. In the MMEs of both PMIP3 and PMIP4 models, the magnitude of the cooling in the tropical Pacific reached about 0.1°–0.6°C in the MH. In general, the decrease in the mean SST in the MH is greater in the western equatorial Pacific than in the eastern equatorial Pacific, indicating a slightly westward extension of the cold tongue. The obvious feature from the difference maps (**Figures 1C,F**) lies in the inter-hemisphere contrast, that is, the mean

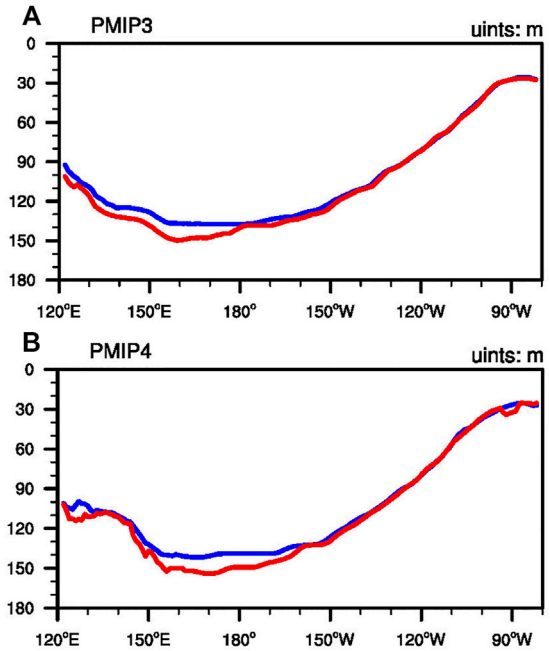

FIGURE 3 | Plots for MME of mean thermocline depth alone the equator (averaged between 5°S and 5°N) derived from **(A)** PMIP3 and **(B)** PMIP4 models. The depth of the mean thermocline is calculated from the location at the maximum vertical gradient of the mean temperature. Blue and red lines indicate PI and MH simulations, respectively.

SST cooling over the tropical Pacific is more obvious in the Southern Hemisphere (SH) than in the NH, consistent with the cross-equatorial southerly. Previous studies (e.g., Luan et al., 2012; Zhao and Harrison 2012) suggested that such inter-hemisphere contrast may result from the strengthened monsoon precipitation in the NH and weakened monsoon precipitation in the SH, which fundamentally stems from orbital forcing change, that is, the enhanced summer insolation in the NH and reduced summer insolation in the SH. It is noted that such inter-hemisphere contrast is slightly stronger in the MME of the PMIP4 models than of the PMP3 models.

Figure 2 shows the spatial distribution of mean precipitation in the PI and MH simulations, as well as their differences. The simulated mean precipitation in the PI simulations resembles that in the observation (not shown), except for the excessive eastward extension of the South Pacific convergence zone (SPCZ), which is associated with the notorious double-intertropical convergence zone (ITCZ) bias—a prevalent bias in coupled models. It is worth mentioning that such double-ITCZ bias is slightly alleviated in the PI simulations of the PMIP4 models compared to the counterpart in the PMIP3. Next, we analyze the difference of tropical mean precipitation in the MH with respect to the PI. As shown in **Figures 2C,F**, the difference in mean precipitation in the MH also exhibits marked inter-hemisphere contrast, that is, more precipitation in the NH than in the SH. Such asymmetric mean precipitation difference distribution is consistent with the aforementioned inter-hemisphere contrast of the mean SST and surface wind. Again, the magnitude of the difference in the mean precipitation is slightly larger in the PMIP4 than in the PMIP3.

Figure 3 shows the equatorial profile of the mean thermocline depth for the MME results from the PI and MH simulations. We can see that the difference in the equatorial mean thermocline during the MH and PI is negligible; this feature is also true for the individual models (not shown). This may be due to the fact that surface flow changes are insignificant for the zonal wind at the equator during the MH, although the southerly wind difference is obvious. The insignificant difference in surface zonal wind may be responsible for the similar equatorial mean thermocline profiles in the two periods.

Annual Cycle

In this subsection, we examine the annual cycle of SST in the equatorial (5°S–5°N) Pacific derived from the MMEs of the PMIP3 and PMIP4 models. The annual cycle is characterized by the climatological monthly average after removing the long-term annual mean. As shown in **Figures 4A,D**, the PI simulations in both PMIP3 and PMIP4 models show an obvious annual cycle of SST in the eastern equatorial Pacific, close to that in the observation (not shown). When comparing the annual cycle result in the PI simulations with the MH simulations, we find that the annual cycle in the eastern equatorial Pacific is weaker in the MH simulations (**Figures 4B,E**). Additionally, the peak interval time of the annual cycle in the MH shows a slight difference from that in the PI simulations, that is, the annual cycle of SST in the eastern Pacific reached its positive peak in april and negative peak in August in the PI simulations, whereas the positive peak was slightly shifted toward May and the negative peak, shifted toward July in the MH simulations.

Two factors are responsible for the obvious weakening in the annual cycle of SST in the MH. Following Xie (1994) and An and Choi (2013); An and Choi (2014), the physical reason for the reduced annual cycle amplitude can be explained by the following equation that describes the annual cycle amplitude of SST,

$$\frac{\partial\langle MLT_{AC}^2\rangle}{\partial t} = -(\bar{u}_0 - c)\frac{\partial\langle MLT_{AC}^2\rangle}{\partial x} + \frac{4}{\rho C_p h}\langle SW \cdot MLT_{AC}\rangle - (1+\beta)\frac{4\overline{LH}}{\rho C_p h}\frac{\bar{v}}{|\bar{u}|^2}\langle v_{AC} \cdot MLT_{AC}\rangle - 2\varepsilon\langle MLT_{AC}^2\rangle \quad (1)$$

where MLT indicates mixed layer temperature, subscript AC indicates the annual cycle after removing the annual mean, c is the phase speed associated with air-sea interaction, h represents mixed layer depth, $\bar{u}_0$ indicates mixed layer-averaged mean zonal current, and β denotes the vertical mixing effect on the latent heat flux. $\bar{u}$ and $\bar{v}$ indicate the mean zonal and meridional winds, respectively. ε denotes the Newtonian cooling coefficient. LH and SW are the mean latent heat flux and the

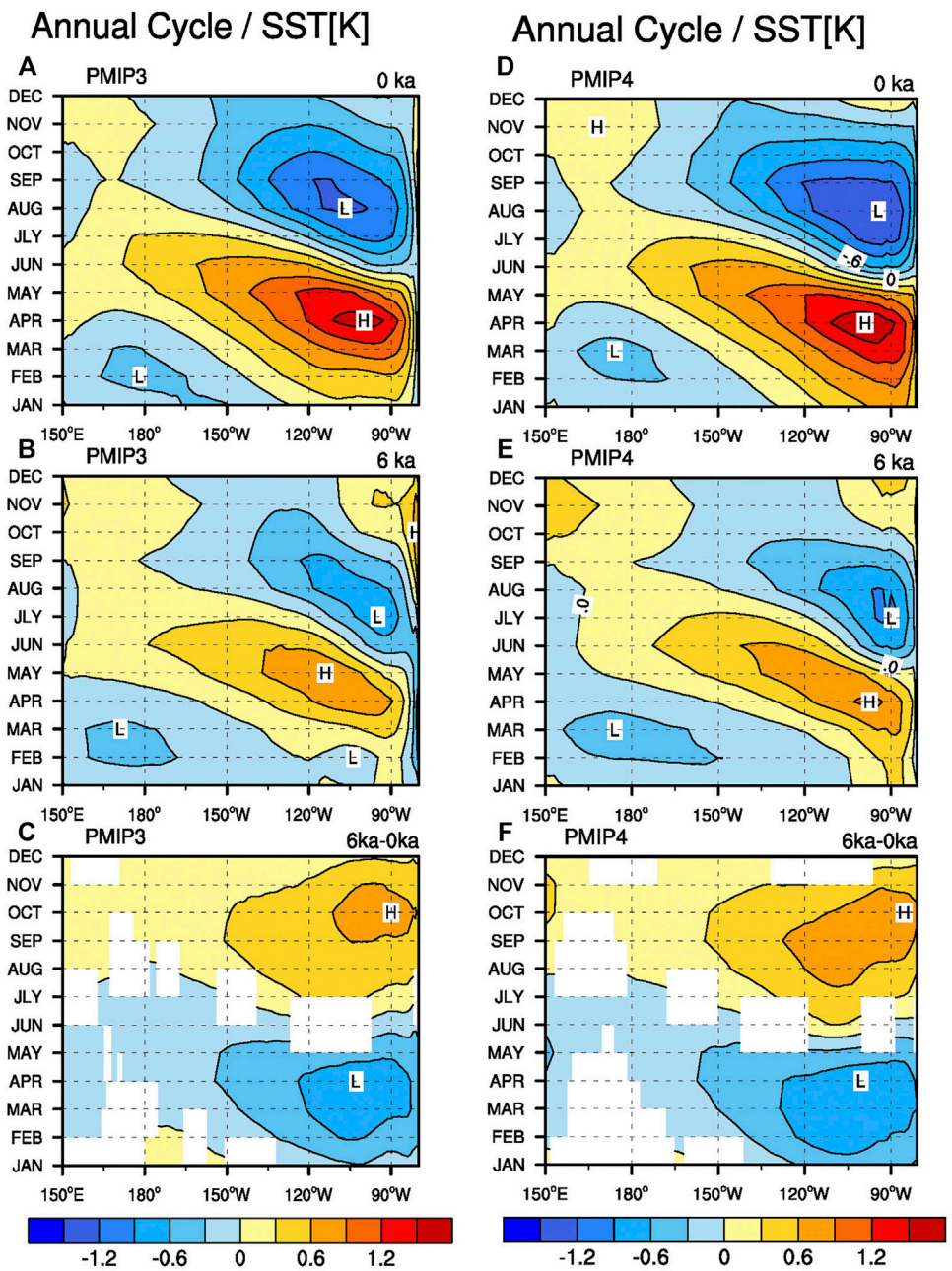

FIGURE 4 | Plots for MME of SST annual cycle over the equatorial Pacific (averaged between 5°S and 5°N) derived from PMIP3 (left column) and PMIP4 (right column) models. **(A)** and **(D)** are PI simulations; **(B)** and **(E)** are MH simulations; and **(C)** and **(F)** are their differences (MH minus PI). Letters H and L represent the positive and negative centers, respectively. Shading in **(C)** and **(F)** indicate the difference between MH and PI is significant at the 95% level by Student's *t*-test.

perturbed solar radiation, respectively. It is worth noting that the amplitude of SST annual cycle is directly defined as the difference between the maximum and the minimum (e.g., Chen and Jin 2018), which means that the amplitude of SST annual cycle is closely related to the seasonal evolution of the corresponding SST tendency. Considering that the positive SST tendency will be offset by the negative SST tendency in a calendar year, a mathematical treatment is conducted through multiplying both sides of the original mixed layer temperature (MLT) tendency equation by MLT_{AC}. In this way, we obtained **Equation 1** and the term $\frac{\partial \langle MLT_{AC}^2 \rangle}{\partial t}$ in the left-hand side of **Equation 1** is proportional to the overall SST (or MLT) tendency that determines the annual cycle magnitude. Previous studies (e.g., An and Choi 2013, 2014) pointed out that the annual cycle amplitude of SST is largely determined by the second and third terms on the right-hand side of the

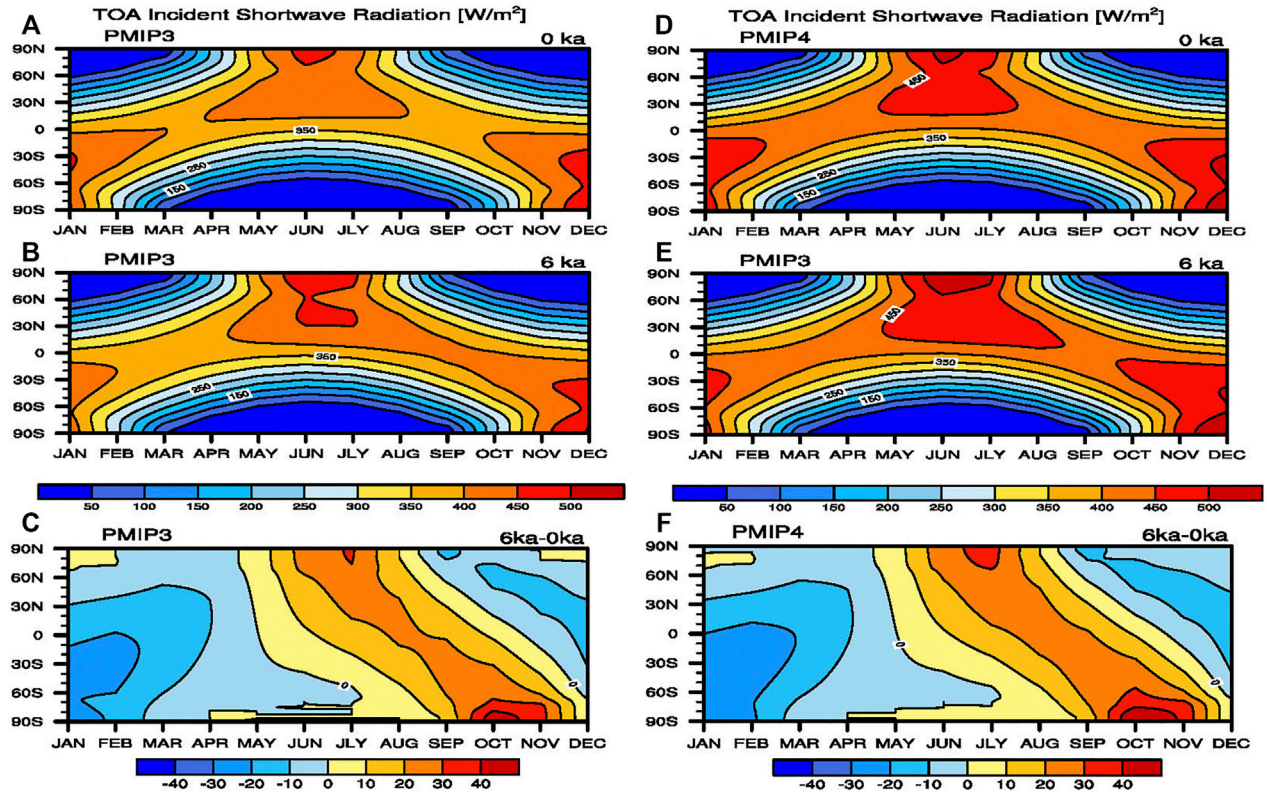

FIGURE 5 | MME of mean insolation at the top of the atmosphere over the tropical Pacific (averaged between 120°E and 160°E) from PMIP3 (left column) and PMIP4 (right column) models. **(A)** and **(D)** are PI simulations; **(C)** and **(B)** are MH simulations; and **(C)** and **(E)** are their difference (MH minus PI).

equation, that is, by the factors associated with the solar radiation and latent heat flux.

The change in the annual cycle of SST during the MH can be traced back to the orbital parameter change (Clement et al., 2000; Braconnot et al., 2012a), that is, the insolation at the top of the atmosphere, which varies between spring and fall, as a result of the orbital-induced alteration during the MH (Berger 1978). As shown in **Figure 5**, the incoming solar radiation is less in early calendar months (especially February) but more in the boreal summer (especially August) in the equatorial region. According to the second term on the right-hand side of **Eq. 1**, such change in the incoming solar radiation can cause a weakened annual cycle of SST in the MH. Consequently, the annual cycle of SST shows a decrease in the MH simulations compared to that in the *p*I. Moreover, the slightly intensified cross-equatorial wind may lead to a slight deepening in the ocean mixed layer (not shown) due to the strengthened stirring effect. The second and third terms on the right-hand side of **Eq. 1** indicate that the annual cycle amplitude is inversely proportional to the mixed layer depth *h*; thus, the slightly deepened mixed layer can cause the increase in the thermal inertia and the reduction of the annual cycle amplitude of SST.

Note that the shading in **Figures 1C,F**, **Figures 2C,F**, **Figures 4C,F** indicates the difference between the MH and PI simulations is significant based on Student's *t*-test. To summarize, the modelled tropical Pacific mean states during the MH show an agreement across the PMIP3 and PMIP4 models, including the mean SST cooling in the tropical Pacific with severely cooling in the SH, mean precipitation decrease in the SH but slight increase in the NH, insignificant difference in the mean thermocline depth in the equatorial Pacific, and remarkable weakening in the annual cycle of SST in the eastern equatorial Pacific.

EL NINO-SOUTHERN OSCILLATION

In this section, we focus on whether there were some obvious differences in the dominant interannual mode of the ENSO during the MH. The ENSO activity is commonly described by the standard deviation (STD) of SST anomalies. **Figure 6** shows the STDs of monthly SST anomalies averaged in the central-eastern equatorial Pacific in each of the PMIP3 and PMIP4 models. First, the majority of the models show that the mature phase of ENSO is phase-locked to the boreal winter (November–January) in the PI simulations, although a few models fail to show such phase-locking feature. When comparing the seasonal phase-locking feature between the PI and MH simulations, we can clearly see that there are nearly no differences in ENSO phase-locking feature.

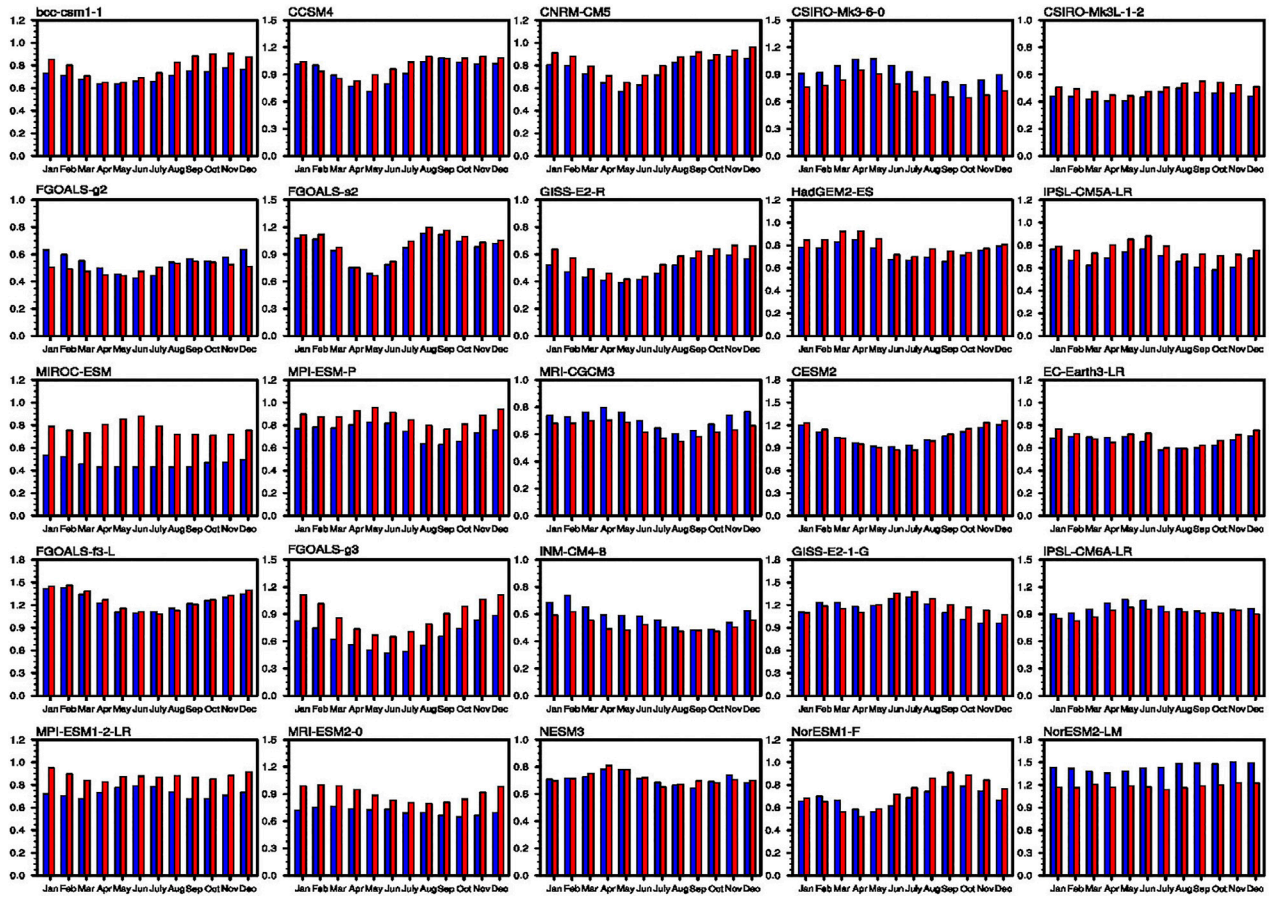

FIGURE 6 | Monthly STD of SST anomalies in the equatorial Pacific (160°E–90°W, 5°S–5°N) for the PI (blue bar) and MH (red bar) simulations from PMIP3 and PMIP4 models. Unit is K.

Figure 7 shows the spatial distribution of the STD of SST anomalies averaged over the boreal winter (November–January) for the MMEs of PMIP3 and PMIP4 models. The difference plots between MH and PI simulations (**Figures 7C,F**) show an obvious decrease in the interannual variation of SST anomalies over the central-eastern equatorial Pacific, indicating a reduced ENSO activities during the MH. Additionally, the extent of the reduction is more obvious in the PMIP4 MME than in the PMIP3 MME. Note that in both PMIP3 and PMIP4 models, the stippling denotes that the majority of the models (i.e., exceeding two thirds) show an agreement with the change sign, indicating the majority show suppressed ENSO variability.

To show the spread of ENSO variability changes across the models, we plot the box and whisker chart. As shown in **Figure 8**, there is large uncertainty regarding the changes in ENSO-related SST anomalies during the MH. For one thing, the spread among the models is somewhat large. Moreover, the magnitude of reduction in MME is small, although the overall variation of SST anomalies shows decreases in different regions, including the Niño3, Niño4, and Niño3.4 regions. For instance, the STDs of the Niño3.4 index are 0.86 and 1.15 for the MMEs of PMIP3 and PMIP4 PI simulations, respectively; and the counterpart in the MH simulations are only 0.81 and 1.05 for the MMEs of the PMIP3 and PMIP4, showing a reduction of about 5.8% and 8.7%, respectively. Recall the relatively large spread among the models, such minor reduction may cause a loss of certainty regarding the modeled changes in ENSO variability. For the Niño1+2 region, a core region for the ENSO, the difference in the variation of SST anomalies between the MH and PI is negligible (**Figure 8D**). Since the reductions in the variation of SST anomalies are somewhat small in the MMEs of the PMIP3 and PMIP4 models, we use **Figure 9** to clearly show these small changes. Nearly all the scatters that represent the STDs of the SST anomalies over the Niño1+2 region for the PI and MH simulations are located along the diagonal line (**Figure 9A**), indicating little change regarding the variation of SST anomalies in the Niño1+2 region. For the regions to the west (Niño3, Niño3.4, and Niño4), the number of the models that show weaker STDs of SST anomalies in the MH than in the PI increases. Such increase may be partly due to the fact that most of the coupled

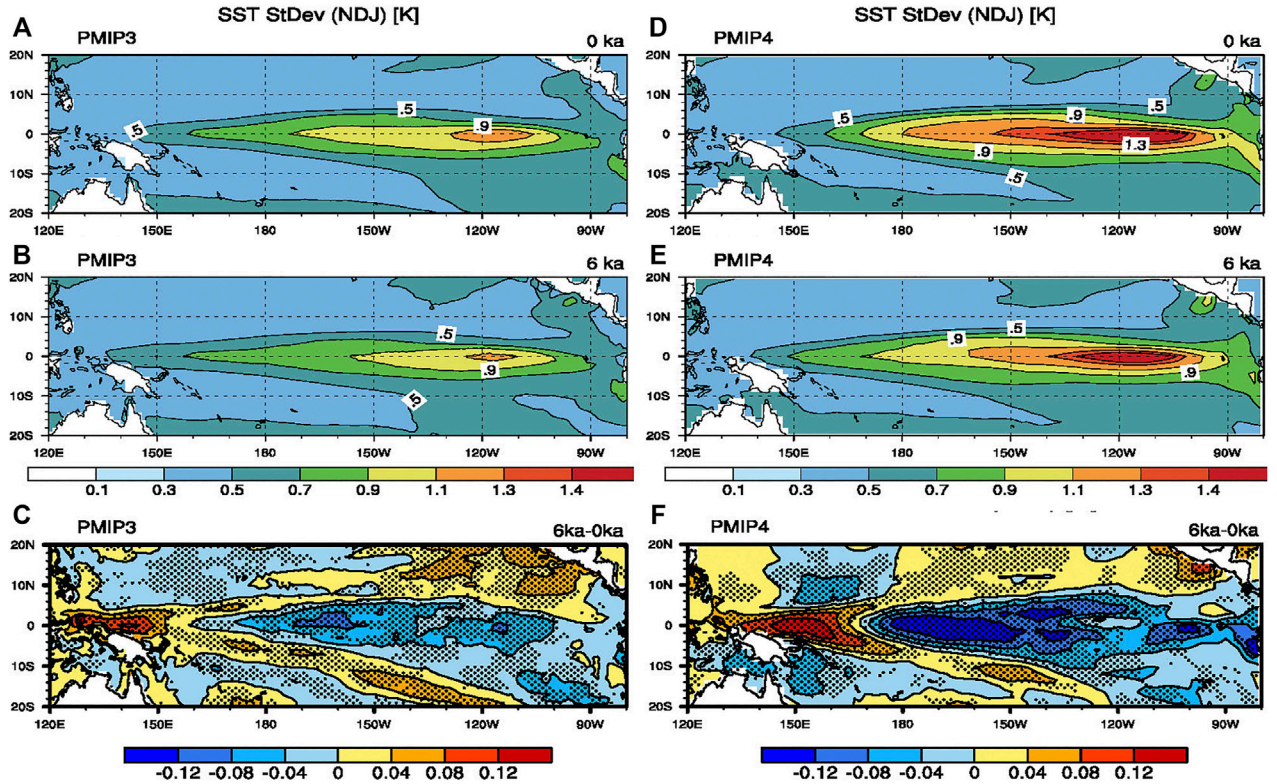

FIGURE 7 | Standard deviation of SST anomalies in boreal winter (November–January) obtained from PMIP3 (left column) and PMIP4 (right column) models. **(A)** and **(D)** are PI simulations; **(B)** and **(E)** are MH simulations; and **(C)** and **(F)** are their differences. Stippling in **(C)** and **(F)** indicates the model consistency exceeds two thirds of the total model's count.

models exhibit westward shifting bias in simulating ENSO-related SST anomalies (Fang and Xie 2020; Ge and Chen 2020; Zhang et al., 2020). As a result, the changes in the Niño4 and Niño3 regions are more dominant.

To summarize the changes of ENSO-related SST anomalies, we present the violin plots for all the PMIP3 and PMIP4 models. **Figure 10** shows the probability density of each relevant index. The results are consistent with the aforementioned results building on the PMIP3 or PMIP4 models only, that is, the ENSO-related SST anomalies in the Niño4, Niño3.4, and Niño3 regions exhibit a weakening to some extent in the MH compared to the PI, where the uncertainty remains large.

So far, various mechanisms have been put forward to account for the suppressed ENSO amplitude in the MH. For instance, Clement et al. (2000) indicated the reduced ENSO variance is regarded as a response to the orbital-induced change of the tropical annual cycle. Liu et al. (2000) suggested the deepened mean equatorial thermocline and the strengthened Asian summer monsoon may lead the suppression of ENSO intensity in MH. Moreover, Zheng et al. (2008) pointed out that the reduction of ENSO intensity is interpreted as the influence of strengthened easterly trade wind in tropic Pacific. Chen et al. (2019a); Chen et al. (2019b) suggested that the changes in the mean Pacific subtropical cell (STC) is the key factor responsible for the reduced ENSO intensity in the MH. In a word, the real physical reason for the inhibition of ENSO activity in the MH period is complex, which still needs some more in-depth investigation in the future.

Next, we examine whether there is any change in terms of ENSO periodicity. **Figure 11** suggests almost no change regarding the spectrum, for either PMIP3 or PMIP4 MME. Such results indicate that the ENSO period is not sensitive to the orbital forcing change in the MH, at least in the current climate models.

In addition to ENSO amplitude and periodicity, we also investigate the change in ENSO diversity in response to the orbital forcing. Several studies uncovered a new flavor of El Niño events in recent years, which is characterized by warm SST anomalies in the central Pacific (CP) and usually called the CP El Niño, El Niño Modoki, warm pool El Niño, or dateline El Niño (Larkin and Harrison 2005; Ashok et al., 2007; Kug et al., 2009; Yu and Kao 2009; Chen et al., 2018). Based on the criteria proposed by Kug et al. (2009), we first compare the SST anomalies in the boreal winter averaged in the Niño3 region with that in the Niño4 region for certain El Niño event, and then label this event as the eastern Pacific (EP) El Niño (CP El Niño), if the Niño3 index is greater (less)

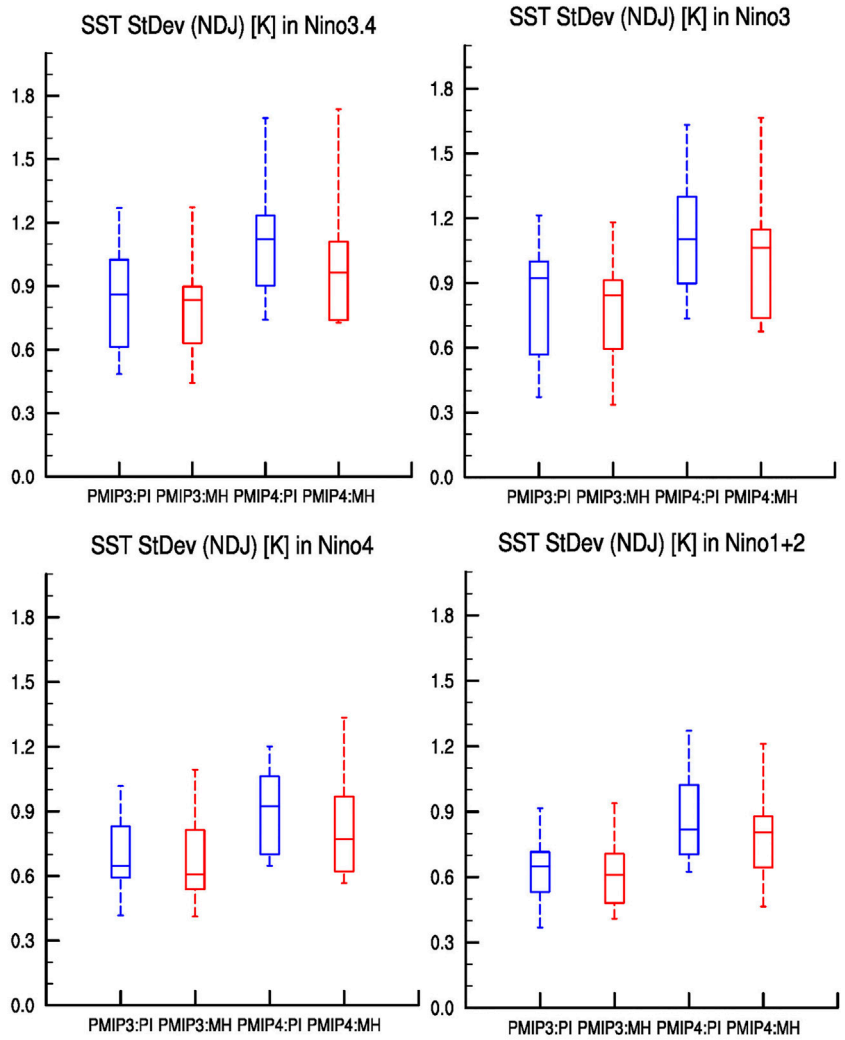

FIGURE 8 | Boxplots for standard deviation of various ENSO indices for PMIP3 and PMIP4 models. Blue boxes indicate the PI simulations, and red boxes indicate the MH simulations. The upper and lower bounds of each box represent 25th and 75th percentiles, respectively; the solid line in the middle of each box is the median; and whiskers are the maximum or minimum, respectively. Definitions for each area: Niño1+2 (90°–80°W, 0°–10°S). Niño3 (150°–90°W, 5°S–5°N), Niño3.4 (170°–120°W, 5°S–5°N), and Niño4 (160°E–150°W, 5°S–5°N).

than the Niño4 index. **Figure 12** shows the ratio of the CP El Niño number to the EP El Niño number for each model and its corresponding MME. Clearly, a divergent performance in simulating the change of the ratio exist across the models. Half of the PMIP3 models (six out of the 13 models) show the ratio of the incidence of CP El Niño events to the EP El Niño events in the MH outstrips the that in the PI, and five among them exhibit a significant increase in the occurrence of CP El Niño during the MH at the 95% confidence level. For the PMIP4 models, eight out of the 12 models record more incidence of CP El Niño events during the MH, and five among them have enhanced ratios exceeding the 95% confidence level. Then, we obtain the MMEs for the PMIP3 and PMIP4 models (the rightmost columns of **Figures 12A,B**). The increase of CP El Niño events during the MH is minor and insignificant for the PMIP4 MME. Although the increase of CP El Niño events during the MH is relatively large for the PMIP3 MME, it is also not statistically significant at the 95% significant level. Overall, the model results show a larger occurrence of CP El Niño in the MH than in the PI, though the significance is quite marginal.

SUMMARY

Increasing attention has been given to understand tropical climate change, especially in terms of ENSO behaviors, in response to global warming; however, some puzzles remain

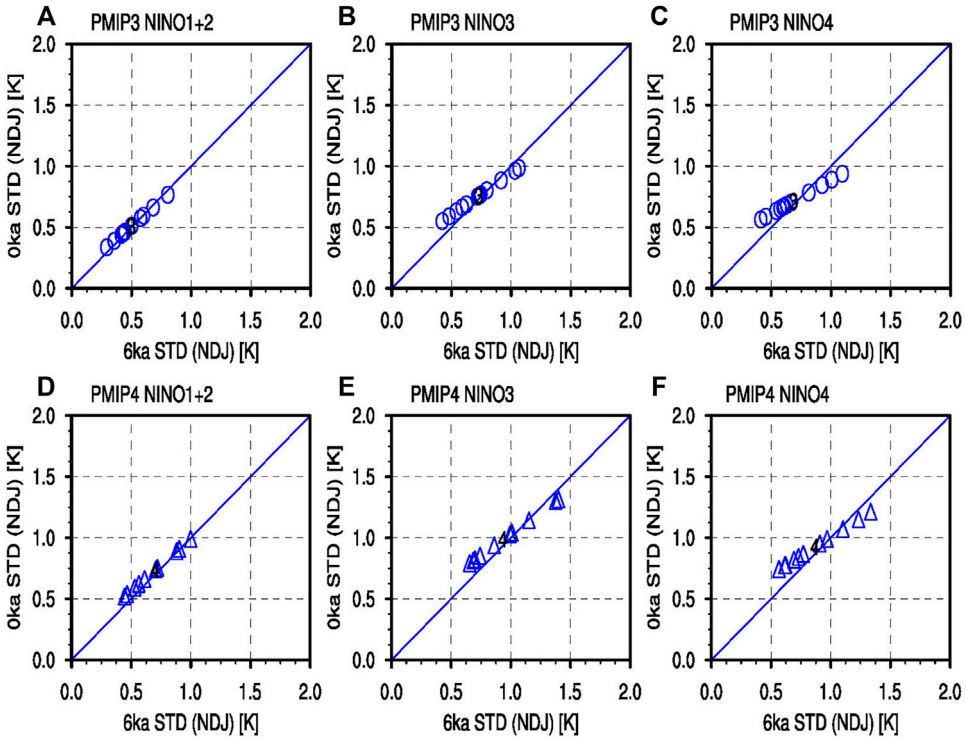

FIGURE 9 | Scatter plots for the STD of the ENSO indices in boreal winter (November–January) derived from PMIP3 and PMIP4 models. The MMEs of PMIP3 and PMIP4 models are marked by 3 and 4, respectively. **(A)** and **(D)** for Niño1+2 (90°–80°W, 0°–10°S) indices, **(B)** and **(E)** for Niño3 (150°–90°W, 5°S–5°N) indices, and **(C)** and **(F)** for Niño4 (160°E–150°W, 5°S–5°N) indices.

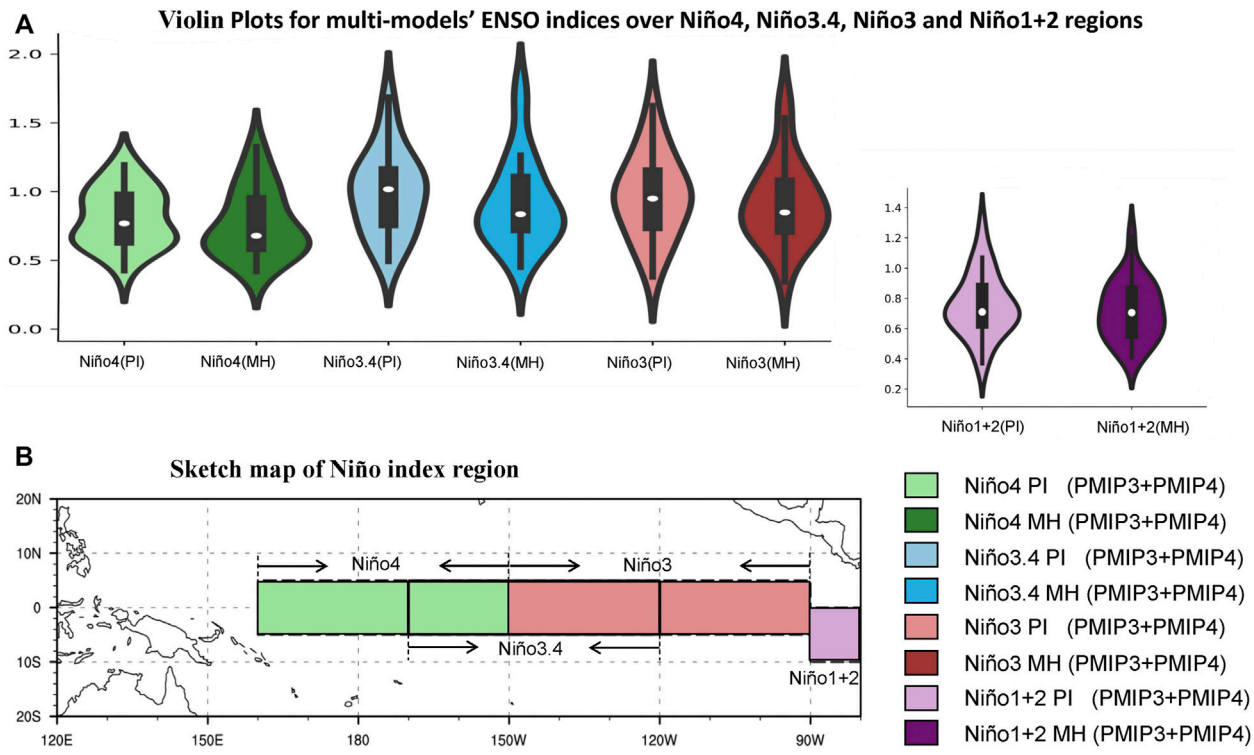

FIGURE 10 | Violin plots **(A)** for STD of winter (November–January) El Niño indices based on PMIP3 and PMIP4 models during the PI (light color) and MH (dark color). Unit is K. The black outline is the probability density of each index's STD. The solid black boxes are the interquartile range, and the white circle in the black box is the median value. **(B)** is the schematic plot of ENSO index distribution region.

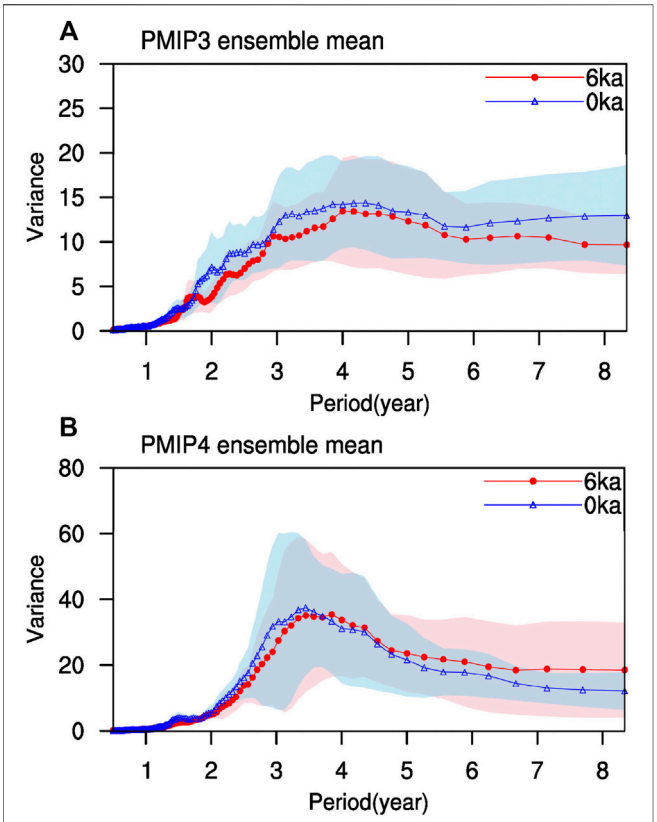

FIGURE 11 | MME of power spectrum derived from **(A)** PMIP3 and **(B)** PMIP4 models. Blue and red colors indicate the PI and MH simulations, respectively.

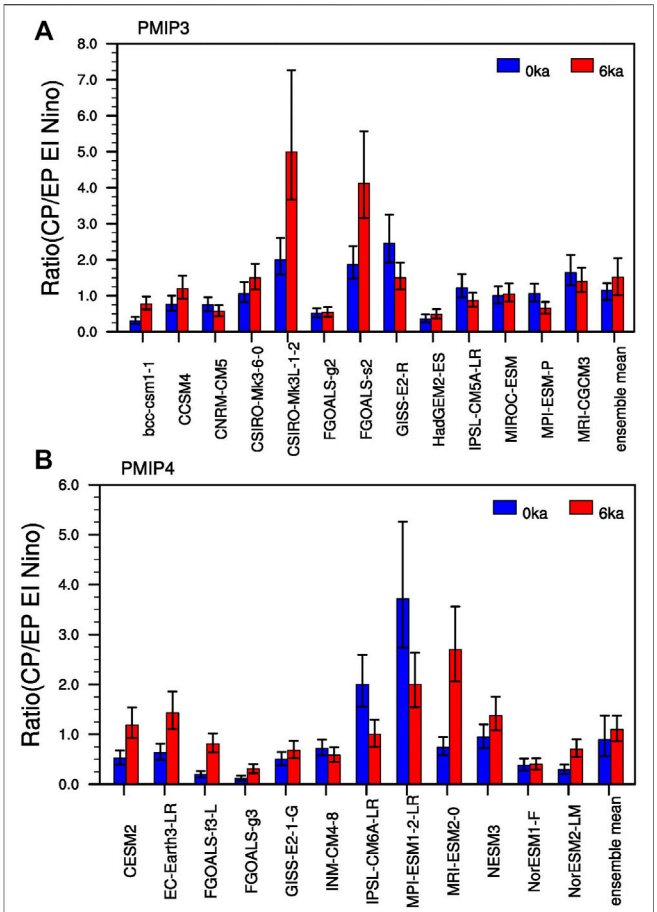

FIGURE 12 | Rates of different types of El Niño obtained from **(A)** PMIP3 and **(B)** PMIP4 models. Blue and red bars represent PI and MH simulations, respectively. The error bars represent the upper and lower limits of varying range in the occurrence ratio at the 95% confidence level by using the bootstrap method.

(e.g., Collins et al., 2010; Chen et al., 2015; Chen et al., 2017). One way to gain confidence in future projections is to evaluate current models' performances in simulating past climate changes (Braconnot et al., 2012a; Braconnot et al., 2012b), because some proxy datasets can be used as reference. Here, we investigated the response of tropical Pacific climate to the orbital forcing in the MH, an epoch about 6,000 years ago, by analyzing model results. Although the climate in MH can be partly inferred from proxy data, model simulation is an effective tool through which we can study the climate change in the MH.

Using recently released PMIP4 outputs along with PMIP3 archives, we examined tropical climate changes, including both basic state and interannual variability; we then attempted to find out whether there is any aspect that can be reconciled for the PMIP3 and PMIP4 model results. The main conclusions are summarized here.

1) All the PMIP3 and PMIP4 models show the enhancement of the inter-hemisphere contrast over the tropical Pacific, including the warmer and wetter condition north of the equator and an intensified cross-equatorial flow in the MH than at present. This difference can be attributed to the change in the orbital forcing, or more straightforwardly, the change in the solar incident radiation.
2) Most models show a weakening in the annual cycle of SST during the MH. The relevant air-sea processes may be more complicated, although such background mean state changes can also be linked to the orbital forcing change in the MH. Specifically, the weakened annual cycle amplitude of SST primarily arises from the seasonal change in the incoming solar radiation during the MH, and the slight shoaling in the mixed layer depth plays a secondary role.
3) The majority of the PMIP3 and PMIP4 models show that ENSO amplitude was suppressed during the MH, while the range of reduction varies with model and region. When synthesizing the overall probability distribution of the changes in ENSO indices, we found that the results remain large uncertainty, which varies with space and pattern. Additionally, the occurrence probability of CP El Niño events increased in the MH, whereas the significance is quite marginal. Interestingly, the other ENSO behaviors, such as the seasonal phase-locking feature and periodicity, exhibit no obvious differences between the MH and PI simulations.

DATA AVAILABILITY STATEMENT

Publicly available datasets were analyzed in this study. This data can be found here: https://esgf-node.llnl.gov/search/cmip6/, https://esgf-node.llnl.gov/search/cmip5/.

AUTHOR CONTRIBUTIONS

M-ES contributed to data analysis and paper writing, LC designed this study and paper writing.

FUNDING

This work was jointly supported by the National Key Research and Development Program on Monitoring, Early Warning and Prevention of Major Natural Disaster (2019YFC1510004), the Natural Science Foundation of Jiangsu (BK20190781), the National Natural Science Foundation of China (No. 42005020), the General Program of Natural Science Foundation of Jiangsu Higher Education Institutions (19KJB170019), and the Open Fund of State Key Laboratory of Loess and Quaternary Geology (SKLLQG 1802).

REFERENCES

An, S.-I., and Choi, J. (2013). Inverse Relationship between the Equatorial Eastern Pacific Annual-Cycle and ENSO Amplitudes in a Coupled General Circulation Model. *Clim. Dyn.* 40, 663–675. doi:10.1007/s00382-012-1403-3

An, S.-I., and Choi, J. (2014). Mid-Holocene Tropical Pacific Climate State, Annual Cycle, and ENSO in PMIP2 and PMIP3. *Clim. Dyn.* 43, 957–970. doi:10.1007/s00382-013-1880-z

Ashok, K., Behera, S. K., Rao, S. A., Weng, H., and Yamagata, T. (2007). El Niño Modoki and its Possible Teleconnection. *J. Geophys. Res.* 112, C1107. doi:10.1029/2006jc003798

Berger, A. (1978). Long-Term Variations of Daily Insolation and Quaternary Climatic Changes. *J. Atmos. Sci.* 35, 2362–2367. doi:10.1175/1520-0469(1978)035<2362:ltvodi>2.0.co;2

Braconnot, P., Harrison, S. P., Kageyama, M., Bartlein, P. J., Masson-Delmotte, V., Abe-Ouchi, A., et al. (2012a). Evaluation of Climate Models Using Palaeoclimatic Data. *Nat. Clim Change* 2, 417–424. doi:10.1038/nclimate1456

Braconnot, P., Luan, Y., Brewer, S., and Zheng, W. (2012b). Impact of Earth's Orbit and Freshwater Fluxes on Holocene Climate Mean Seasonal Cycle and ENSO Characteristics. *Clim. Dyn.* 38, 1081–1092. doi:10.1007/s00382-011-1029-x

Brown, J., Collins, M., and Tudhope, A. (2006). Coupled Model Simulations of Mid-holocene ENSO and Comparisons with Coral Oxygen Isotope Records. *Adv. Geosci.* 6, 29–33. doi:10.5194/adgeo-6-29-2006

Brown, J. R., Brierley, C. M., An, S.-I., Guarino, M.-V., Stevenson, S., Williams, C. J. R., et al. (2020). Comparison of Past and Future Simulations of ENSO in CMIP5/PMIP3 and CMIP6/PMIP4 Models. *Clim. Past* 16, 1777–1805. doi:10.5194/cp-16-1777-2020

Carré, M., Sachs, J. P., Purca, S., Schauer, A. J., Braconnot, P., Falcón, R. A., et al. (2014). Holocene History of ENSO Variance and Asymmetry in the Eastern Tropical Pacific. *Science* 345, 1045–1048. doi:10.1126/science.1252220

Chen, L., Li, T., and Yu, Y. (2015). Causes of Strengthening and Weakening of ENSO Amplitude under Global Warming in Four CMIP5 Models*. *J. Clim.* 28, 3250–3274. doi:10.1175/jcli-d-14-00439.1

Chen, L., Li, T., Yu, Y., and Behera, S. K. (2017). A Possible Explanation for the Divergent Projection of ENSO Amplitude Change under Global Warming. *Clim. Dyn.* 49, 3799–3811. doi:10.1007/s00382-017-3544-x

Chen, L., Wang, L., Li, T., and Sun, D.-Z. (2018). Contrasting Cloud Radiative Feedbacks during Warm Pool and Cold Tongue El Niños. *Sola* 14, 126–131. doi:10.2151/sola.2018-022

Chen, L., Wang, L., Li, T., and Liu, J. (2019a). Drivers of Reduced ENSO Variability in Mid-holocene in a Coupled Model. *Clim. Dyn.* 52, 5999–6014. doi:10.1007/s00382-018-4496-5

Chen, L., Zheng, W., and Braconnot, P. (2019b). Towards Understanding the Suppressed ENSO Activity during Mid-holocene in PMIP2 and PMIP3 Simulations. *Clim. Dyn.* 53, 1095–1110. doi:10.1007/s00382-019-04637-z

Chen, Y.-Y., and Jin, F.-F. (2018). Dynamical Diagnostics of the SST Annual Cycle in the Eastern Equatorial Pacific: Part I a Linear Coupled Framework. *Clim. Dyn.* 50, 1841–1862. doi:10.1007/s00382-017-3725-7

Clement, A. C., Seager, R., and Cane, M. A. (2000). Suppression of El Niño during the Mid-holocene by Changes in the Earth's Orbit. *Paleoceanography* 15, 731–737. doi:10.1029/1999pa000466

Cobb, K. M., Westphal, N., Sayani, H. R., Watson, J. T., Di Lorenzo, E., Cheng, H., et al. (2013). Highly Variable El Niño-Southern Oscillation throughout the Holocene. *Science* 339, 67–70. doi:10.1126/science.1228246

Collins, M., An, S.-I., Cai, W., Ganachaud, A., Guilyardi, E., Jin, F.-F., et al. (2010). The Impact of Global Warming on the Tropical Pacific Ocean and El Niño. *Nat. Geosci* 3, 391–397. doi:10.1038/ngeo868

Emile-Geay, J., Cobb, K. M., Carré, M., Braconnot, P., Leloup, J., Zhou, Y., et al. (2016). Links between Tropical Pacific Seasonal, Interannual and Orbital Variability during the Holocene. *Nat. Geosci* 9, 168–173. doi:10.1038/ngeo2608

Fang, X., and Xie, R. (2020). A Brief Review of ENSO Theories and Prediction. *Sci. China Earth Sci.* 63, 476–491. doi:10.1007/s11430-019-9539-0

Gagan, M. K., Ayliffe, L. K., Hopley, D., Cali, J. A., Mortimer, G. E., Chappell, J., et al. (1998). Temperature and Surface-Ocean Water Balance of the Mid-holocene Tropical Western Pacific. *Science* 279, 1014–1018. doi:10.1126/science.279.5353.1014

Ge, Z.-A., and Chen, L. (2020). Preliminary Analysis of the Zonal Distribution of ENSO-Related SSTA in Three CMIP5 Coupled Models. *Atmos. Oceanic Sci. Lett.* 13, 443–451. doi:10.1080/16742834.2020.1775475

Gierz, P., Ackermann, L., Rodehacke, C. B., Krebs-Kanzow, U., Stepanek, C., Barbi, D., et al. (2020). *Simulating Interactive Ice Sheets in the Multi-Resolution AWI-ESM 1.2: A Case Study Using SCOPE 1.0*. Geoscientific Model Development Discussions, 1–32.

Gong, X., Zhang, X., Lohmann, G., Wei, W., Zhang, X., and Pfeiffer, M. (2015). Higher Laurentide and Greenland Ice Sheets Strengthen the North Atlantic Ocean Circulation. *Clim. Dyn.* 45, 139–150. doi:10.1007/s00382-015-2502-8

Jiang, D., Tian, Z., and Lang, X. (2015). Mid-Holocene Global Monsoon Area and Precipitation from PMIP Simulations. *Clim. Dyn.* 44, 2493–2512. doi:10.1007/s00382-014-2175-8

Kageyama, M., Braconnot, P., Harrison, S. P., Haywood, A. M., Jungclaus, J. H., Otto-Bliesner, B. L., et al. (2018). The PMIP4 Contribution to CMIP6 - Part 1: Overview and Over-arching Analysis Plan. *Geosci. Model. Dev.* 11, 1033–1057. doi:10.5194/gmd-11-1033-2018

Kohfeld, K. E., and Harrison, S. P. (2000). How Well Can We Simulate Past Climates? Evaluating the Models Using Global Palaeoenvironmental Datasets. *Quat. Sci. Rev.* 19, 321–346. doi:10.1016/s0277-3791(99)00068-2

Koutavas, A., Demenocal, P. B., Olive, G. C., and Lynch-Stieglitz, J. (2006). Mid-Holocene El Niño-Southern Oscillation (ENSO) Attenuation Revealed by Individual Foraminifera in Eastern Tropical Pacific Sediments. *Geol* 34, 993–996. doi:10.1130/g22810a.1

Koutavas, A., and Joanides, S. (2012). El Niño-Southern Oscillation Extrema in the Holocene and Last Glacial Maximum. *Paleoceanography* 27, PA4208. doi:10.1029/2012pa002378

Kug, J.-S., Jin, F.-F., and An, S.-I. (2009). Two Types of El Niño Events: Cold Tongue El Niño and Warm Pool El Niño. *J. Clim.* 22, 1499–1515. doi:10.1175/2008jcli2624.1

Kutzbach, J. E., and Liu, Z. (1997). Response of the African Monsoon to Orbital Forcing and Ocean Feedbacks in the Middle Holocene. *Science* 278, 440–443. doi:10.1126/science.278.5337.440

Kutzbach, J. E., and Otto-Bliesner, B. L. (1982). The Sensitivity of the African-Asian Monsoonal Climate to Orbital Parameter Changes for 9000 Years B.P. In a Low-Resolution General Circulation Model. *J. Atmos. Sci.* 39, 1177–1188. doi:10.1175/1520-0469(1982)039<1177:tsotaa>2.0.co;2

Larkin, N. K., and Harrison, D. E. (2005). Global Seasonal Temperature and Precipitation Anomalies during El Niño Autumn and winter. *Geophys. Res. Lett.* 32, L16705. doi:10.1029/2005gl022860

Liu, Z., Kutzbach, J., and Wu, L. (2000). Modeling Climate Shift of El Nino Variability in the Holocene. *Geophys. Res. Lett.* 27, 2265–2268. doi:10.1029/2000gl011452

Luan, Y., Braconnot, P., Yu, Y., Zheng, W., and Marti, O. (2012). Early and Mid-holocene Climate in the Tropical Pacific: Seasonal Cycle and Interannual Variability Induced by Insolation Changes. *Clim. Past* 8, 1093–1108. doi:10.5194/cp-8-1093-2012

Otto-Bliesner, B. L., Brady, E. C., Shin, S.-I., Liu, Z., and Shields, C. (2003). Modeling El Niño and its Tropical Teleconnections during the Last Glacial-Interglacial Cycle. *Geophys. Res. Lett.* 30, 2198–2202. doi:10.1029/2003gl018553

Otto-Bliesner, B. L. (1999). El Niño/La Niña and Sahel Precipitation during the Middle Holocene. *Geophys. Res. Lett.* 26, 87–90. doi:10.1029/1998gl900236

Tian, Z., Li, T., Jiang, D., and Chen, L. (2017). Causes of ENSO Weakening during the Mid-holocene. *J. Clim.* 30, 7049–7070. doi:10.1175/jcli-d-16-0899.1

Tudhope, A. W., Chilcott, C. P., Mcculloch, M. T., Cook, E. R., Chappell, J., Ellam, R. M., et al. (2001). Variability in the El Niño-Southern Oscillation through a Glacial-Interglacial Cycle. *Science* 291, 1511–1517. doi:10.1126/science.1057969

Xie, S.-P. (1994). On the Genesis of the Equatorial Annual Cycle. *J. Clim.* 7, 2008–2013. doi:10.1175/1520-0442(1994)007<2008:otgote>2.0.co;2

Yu, J.-Y., and Kao, H.-Y. (2009). Contrasting Eastern-Pacific and Central-Pacific Types of ENSO. *J. Clim.* 22, 615–632. doi:10.1175/2008jcli2706.1

Zhang, R.-H., Yu, Y., Song, Z., Ren, H.-L., Tang, Y., Qiao, F., et al. (2020). A Review of Progress in Coupled Ocean-Atmosphere Model Developments for ENSO Studies in China. *J. Ocean. Limnol.* 38, 930–961. doi:10.1007/s00343-020-0157-8

Zhao, Y., and Harrison, S. P. (2012). Mid-Holocene Monsoons: a Multi-Model Analysis of the Inter-hemispheric Differences in the Responses to Orbital Forcing and Ocean Feedbacks. *Clim. Dyn.* 39, 1457–1487. doi:10.1007/s00382-011-1193-z

Zheng, W., and Braconnot, P. (2013). Characterization of Model Spread in PMIP2 Mid-holocene Simulations of the African Monsoon. *J. Clim.* 26, 1192–1210. doi:10.1175/jcli-d-12-00071.1

Zheng, W., Braconnot, P., Guilyardi, E., Merkel, U., and Yu, Y. (2008). ENSO at 6ka and 21ka from Ocean-Atmosphere Coupled Model Simulations. *Clim. Dyn.* 30, 745–762. doi:10.1007/s00382-007-0320-3

Zheng, W., and Yu, Y. (2013). Paleoclimate Simulations of the Mid-holocene and Last Glacial Maximum by FGOALS. *Adv. Atmos. Sci.* 30, 684–698. doi:10.1007/s00376-012-2177-6

Conflict of Interest: The authors declare that the research was conducted in the absence of any commercial or financial relationships that could be construed as a potential conflict of interest.

Publisher's Note: All claims expressed in this article are solely those of the authors and do not necessarily represent those of their affiliated organizations, or those of the publisher, the editors, and the reviewers. Any product that may be evaluated in this article, or claim that may be made by its manufacturer, is not guaranteed or endorsed by the publisher.

frontiers in Earth Science

ORIGINAL RESEARCH
published: 25 October 2021
doi: 10.3389/feart.2021.759339

The Short-Term Climate Prediction System FIO-CPS v2.0 and its Prediction Skill in ENSO

Yajuan Song[1,2,3], *Qi Shu*[1,2,3], *Ying Bao*[1,2,3], *Xiaodan Yang*[1,2,3] *and Zhenya Song*[1,2,3]*

[1]Key Laboratory of Marine Science and Numerical Modeling, First Institute of Oceanography, Ministry of Natural Resources, Qingdao, China, [2]Laboratory for Regional Oceanography and Numerical Modeling, Pilot National Laboratory for Marine Science and Technology, Qingdao, China, [3]Shandong Key Laboratory of Marine Science and Numerical Modeling, Qingdao, China

The climate model is an important tool for simulating and predicting the mean state and variability of the climate system. The First Institute of Oceanography-Climate Prediction System (FIO-CPS), built on a climate model with the oceanic observation initialization, has been updated from version 1.0 to 2.0, with a finer resolution and more reasonable physical processes. Previous assessments show that the mean state was well simulated in version 2.0, and its influence on the prediction was further analyzed in this study. Hindcast experiments were conducted using FIO-CPS v1.0 and v2.0, and their prediction abilities based on 27 years (1993–2019) experiment data were analyzed. The results show that the sea surface temperature (SST) biases over the eastern Pacific and the Southern Ocean are improved in the initial condition of FIO-CPS v2.0. Moreover, this new system has a higher skill for predicting El Niño-Southern Oscillation (ENSO). The prediction skill represented by the anomaly correlation coefficient (ACC) of the Niño3.4 index is greater than 0.78 at the 6-month lead time, which increases by 11.09% compared to the value of 0.70 in FIO-CPS v1.0. The root mean square error (RMSE) decreases by 0.20, which accounts for 28.59% of the FIO-CPS v1.0 result. Furthermore, the improvement of the prediction skill changes seasonally, featured by the ACC significantly increasing in the boreal winter and early spring. The improvement in the annual mean SST prediction over the Equatorial Pacific mainly contributes to the enhanced ENSO prediction skill in FIO-CPS v2.0. These results indicate that a state-of-the-art climate model with a well-simulated mean state is critical in improving the prediction skill on the seasonal time scale.

Keywords: short-term climate prediction system, seasonal prediction, ENSO, climate model, sea surface temperature, FIO-CPS

OPEN ACCESS

Edited by:
Ruihuang Xie,
Ocean University of China, China

Reviewed by:
Fei Zheng,
Institute of Atmospheric Physics, Chinese Academy of Sciences (CAS), China
Libin Ma,
Chinese Academy of Meteorological Sciences, China

***Correspondence:**
Zhenya Song
songroy@fio.org.cn

Specialty section:
This article was submitted to Atmospheric Science, a section of the journal Frontiers in Earth Science

Received: *16 August 2021*
Accepted: *29 September 2021*
Published: *25 October 2021*

Citation:
Song Y, Shu Q, Bao Y, Yang X and Song Z (2021) The Short-Term Climate Prediction System FIO-CPS v2.0 and its Prediction Skill in ENSO. Front. Earth Sci. 9:759339. doi: 10.3389/feart.2021.759339

INTRODUCTION

The climate model, also known as the coupled general circulation model, is an important tool for simulating the processes and interactions among the atmosphere, ocean, land, and other components (Dai et al., 2014; Zhou et al., 2020). Furthermore, it is one of the most important methods of future climate prediction and has been widely used in operational prediction from seasonal to decadal time scales (Ren et al., 2019; Barnston et al., 2019).

Accurate seasonal predictions based on state-of-the-art climate models can prevent and mitigate climate-related disasters in the coming season and have aroused wide concern by international climate researchers and society (Jin et al., 2008; Barnston et al., 2012; Luo et al., 2016). Over the past

thirty years, seasonal prediction skills have improved due to the availability of more reasonable initial conditions, increased ensembles and the rapid development of climate models (Wyrtki, 1975; Cane et al., 1986; Drosdowsky, 2006, Zheng et al., 2006; Zheng et al., 2007). Meanwhile, the changes of climate mean state and variability raise new challenges to the seasonal prediction (Zheng and Yu, 2017). Based on the increasing amount of available observations, sophisticated data assimilation techniques can incorporate more observations into the climate models and provide optimal initial conditions for seasonal predictions (Zheng and Zhu, 2010; Zhao et al., 2019; Zhang et al., 2020). Furthermore, the development of climate models on account of the deeper understanding of air-sea interactions also contributes to improving the prediction skill (Chen et al., 2004; Hu et al., 2013; Zheng and Zhu, 2016). Previous studies show that the mean state in coupled model has significant influence on seasonal prediction capability. However, the mean state, used for calculating the anomalies, still has systematic errors in coupled prediction system, hence the simulated bias of climate variability is identified by the differences between predicted physical fields and the unreal mean state. Zheng and Yu (2017) show that the errors characterized by a warm bias in the eastern Pacific and a cold bias in the central part of the basin indicate a stronger spring prediction barrier for the central Pacific El Niño. Moreover, The climatological cold bias of SST in the upper tropical Pacific Ocean influences the predictive capability of the climate model in predicting the amplitude of El Niño-Southern Oscillation (ENSO) (Kim et al., 2017). Zhu et al. (2017) demonstrated that improving the mean state simulation by amending the physical parameterization scheme in model is helpful to enhance the seasonal prediction skill. Therefore, improving the mean state in the climate model can ameliorate the simulation of variability, it might further improve prediction capability.

The First Institute of Oceanography-Climate Prediction System (FIO-CPS) is a seasonal prediction system, based on an atmosphere-wave-ocean-sea ice-land surface coupled climate model and an oceanic assimilation module. In version 1.0, the role of the ocean surface waves in the climate system was considered by incorporating the non-breaking surface wave-induced mixing effect (Qiao et al., 2004; Qiao et al., 2010). We had assessed the seasonal prediction of the SST based on the hindcast results of FIO-CPS v1.0 in the North Pacific. The wave-induced vertical mixing plays a key role in the seasonal prediction of the SST. The results show that the prediction error is significantly reduced at high latitudes in the North Pacific when the effects of the surface waves were considered (Zhao et al., 2019; Song et al., 2020). In addition, FIO-CPS v1.0 was also employed to predict the El Niño evolution in 2015/16. The predicted strength more than 2.0°C is comparable to the observations (Song et al., 2015). The new version of FIO-CPS (v2.0) was developed based on the First Institute of Oceanography-Earth System Model version 2.0 (FIO-ESM v2.0), which participates in phase 6 of the Coupled Model Intercomparison Project (CMIP6). Each new version component has been updated by including more reasonable physical processes and improved horizontal and vertical resolutions. In addition, more physical processes related to air-sea interactions were considered in FIO-ESM v2.0 (**Figure 1**). FIO-ESM v2.0 can capture the major features of the observed climatology in the historical period. In particular, the results based on historical experiments show that the new model has fairly good skill in simulating the climatological state of the atmosphere and ocean (Bao et al., 2020). The influence of the improved mean state on the prediction ability requires further analysis.

In this study, the prediction skill of FIO-CPS v2.0 in predicting the ENSO was evaluated and compared with that of FIO-CPS v1.0 based on two hindcast experiments. The paper is organized as follows. The details of the climate model, initialization method, experiments, and datasets are described in *Model and Datasets*. *Results* presents the initiation conditions and prediction results for FIO-CPS v1.0 and v2.0. Finally, the conclusions and discussion are presented in *Conclusion*.

MODEL AND DATASETS

Climate Prediction System and Experiments

The seasonal prediction systems FIO-CPS, developed by the First Institute of Oceanography, Ministry of Natural Resources of China, was built on the FIO-ESM and an oceanic assimilation

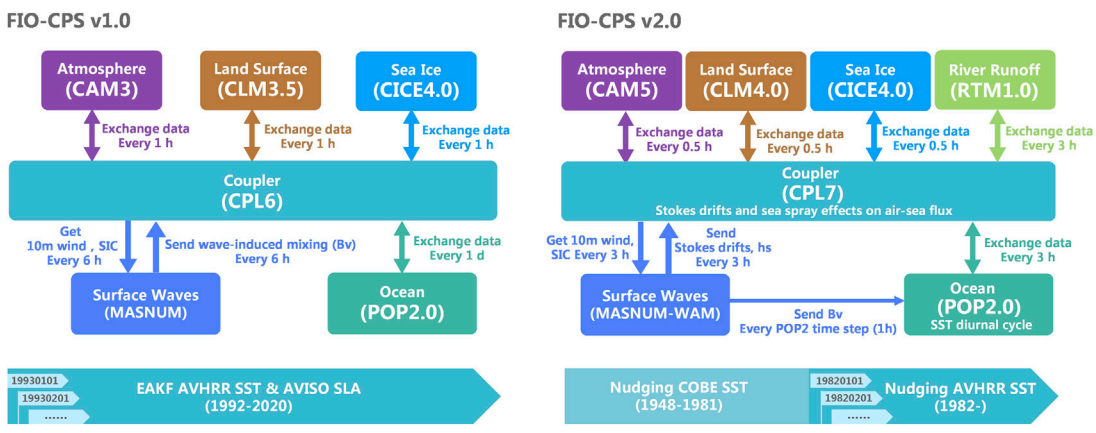

FIGURE 1 | Flowcharts for FIO-CPS v1.0 and FIO-CPS v2.0.

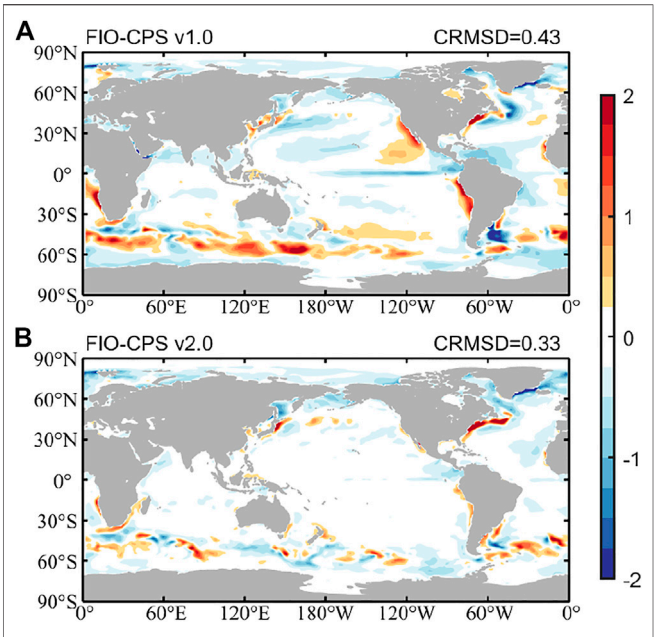

FIGURE 2 | Climatological SST differences (units: °C) between the initial conditions and COBE SST: **(A)** FIO-CPS v1.0 and **(B)** FIO-CPS v2.0. The CRMSD is listed in the top right corners.

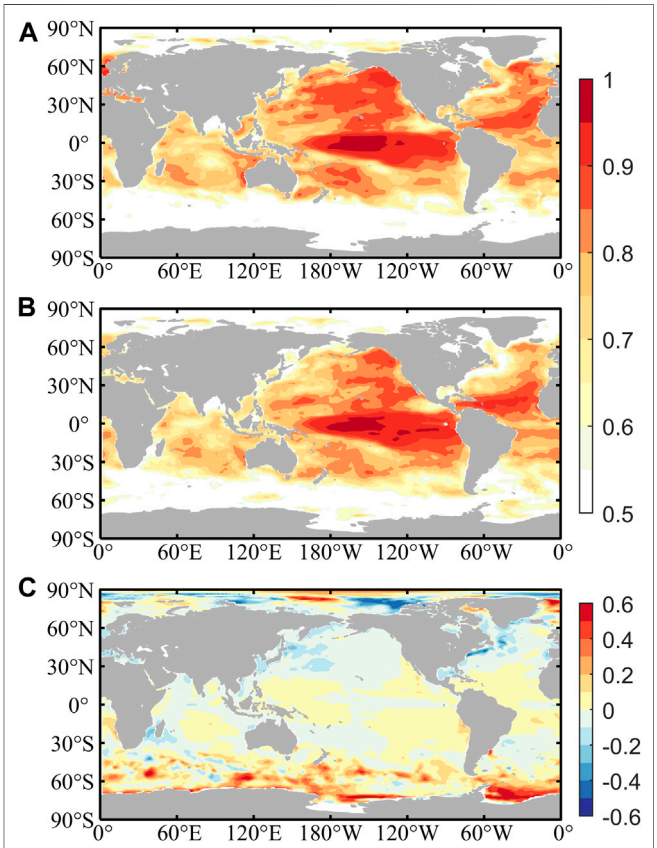

FIGURE 3 | The SSTA ACC between the COBE SST and the initial conditions. **(A)** FIO-CPS v1.0; **(B)** FIO-CPS v2.0; and **(C)** FIO-CPS v2.0–FIO-CPS v1.0.

module. FIO-ESM includes the physical model and a biogeochemical module. The FIO-CPS was developed based on the physical model of FIO-ESM, while the biogeochemical processes were not considered. The FIO-CPS v1.0 was based on the First Institute of Oceanography-Earth System Model version 1.0 (FIO-ESM v1.0), which had participated in phase 5 of the Coupled Model Intercomparison Project (CMIP5) and conducted the required experiments. The numerical simulations show that the basic patterns and variability of the ocean and atmosphere, including the ENSO, are well simulated during the historical period (Qiao et al., 2013). An ocean surface wave model named Marine Science and Numerical Modeling (MASNUM) was incorporated into the system. So FIO-CPS v1.0 consists of five component models: the atmospheric general circulation model, the land surface model, the oceanic general circulation model, the sea ice model, and the ocean surface wave model.

Now the FIO-CPS has been updated from version 1.0 to 2.0, accompanied by higher horizontal-vertical resolution and improved physical processes. The atmospheric model component was updated from the Community Atmosphere Model Version 3.0 (CAM 3.0) to CAM 5.0. In the atmospheric component, the Eulerian dynamical core in CAM3 is replaced by a finite-volume dynamical core in CAM 5.0. The resolution was also improved. Specifically, the horizontal resolution in CAM 3.0 is T42 (about 2.875° in latitude and longitude), with 26 vertical layers. In CAM 5.0, the horizontal resolution is f09 (1.25° in longitude and 0.9° in latitude), with 30 vertical layers. In addition, the Parallel Ocean Program 2 (POP2), an oceanic general circulation model, also has a refined resolution, with the vertical layers increased from 40 to 61. The land surface model was updated from Community Land Model version 3.5 (CLM3.5) to CLM4.0, and the sea ice model component is the Los Alamos sea ice model version 4 (CICE4) with the same horizontal resolution as POP2. All the components are connected by the coupler. The coupler receives data from each component to calculate the flux, then returns the flux and related physical state to respective components. For example, in FIO-CPS v1.0, the coupler receives the hourly atmospheric data and daily oceanic data, then calculates and returns the flux to each component. More details can be found in Bao et al. (2020).

In addition to the effect of the wave-induced vertical mixing, three other distinctive physical processes related to air-sea interactions, including the effect of the Stokes drift, the sea spray, and the SST diurnal cycle, were included in FIO-ESM v2.0 (Bao et al., 2020). The horizontal residual velocity caused by the Stokes drift motion can influence relative surface speed when calculating heat and momentum fluxes. Sea spray also has significant effects on the air-sea heat transport when water droplets are emitted into the air by broken ocean surface waves. In addition, the difference between the day and night temperatures at the ocean surface, represented by the SST diurnal cycle parameterization, was considered to modulate the heat and gas fluxes. All these physical processes play important roles in the heat and mass transport at the air-sea interface.

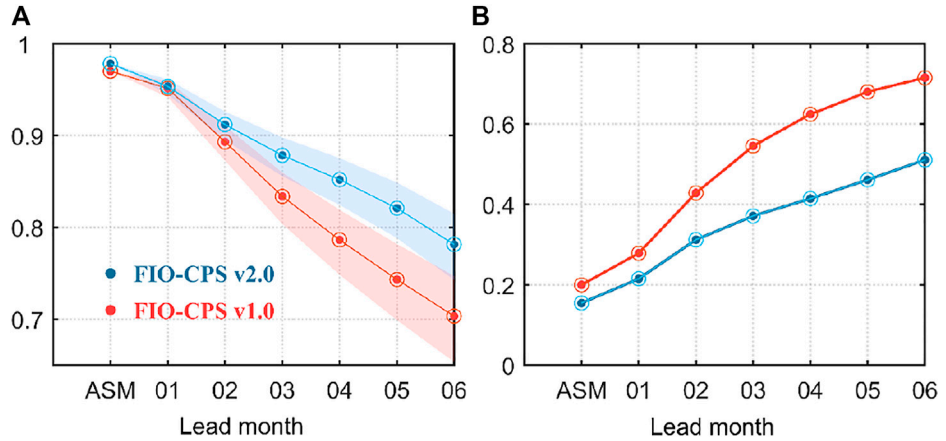

FIGURE 4 | (A) ACC and **(B)** RMSE of the Niño 3.4 index between the OISST v2.1 and the simulation for 1993–2019. The red and blue lines represent the assimilated and predicted results of FIO-CPS v1.0 and FIO-CPS v2.0 for 1-month to 6-month lead times, and the shaded area in **(A)** indicates the 95% confidence interval.

The initial oceanic condition is also crucial in the seasonal prediction. FIO-CPS v1.0 uses the ensemble adjustment Kalman filter (EAKF) method to assimilate the daily SST and sea level anomaly for the initialization (Chen et al., 2015). The key variables in the upper ocean, such as the ocean temperature, salinity, and velocity, are harmonious during the assimilation and prediction. The assimilation experiment was conducted from 1992 to 2019, and the EAKF data assimilation included ten ensembles under the three-dimensional ocean temperature perturbation method with a magnitude of 10^{-3}°C (Song et al., 2020). Then, the seasonal hindcast experiment for 1993–2019 was started on the first day of each month. In FIO-CPS v2.0, the assimilation experiment was started from 1948 to acquire more stable results. With one ensemble simulation, the nudging approach was utilized to consider the ocean satellite observations in the initial conditions. The upper ocean temperature in the mixed layer was assimilated to the observation. The assimilation window is 30 days. Here, a threshold method with the temperature criterion (the temperature is less than 1°C relative to SST) was chosen to determine the mixed layer depth (MLD). Meanwhile, a factor representing the nudging degree is multiplied, changing linearly from 1 at sea surface to 0 at the bottom of the mixed layer. In the polar region, there is no assimilation in the ocean where covered by sea ice. Ten ensembles were produced in the hindcasts using the three-dimensional ocean temperature perturbation method mentioned above. In FIO-CPS v1.0, each hindcast runs for 6 month, and the prediction time extends to 13 month in FIO-CPS v2.0. The information of the prediction system and experiments are shown in **Figure 1**. The experimental results for the common years from 1993 to 2019 with 6 months hindcast results were analyzed in this study.

Datasets and Method

In FIO-CPS v1.0, the daily Optimum Interpolation Sea Surface Temperature (OISST v2) based on the Advanced Very High Resolution Radiometer (AVHRR) satellite data from the National Oceanic and Atmospheric Administration (NOAA) National Climate Data Center (NCDC), and sea level anomaly from the Archiving, Validation, and Interpretation of Satellite Data (AVISO) were assimilated using the EAKF assimilation method (Ducet et al., 2000; Reynolds et al., 2007). The horizontal resolution of both datasets is 0.25° in a uniform grid. In FIO-CPS v2.0, the daily Sea Surface Analysis for Climate Monitoring and Prediction (COBE) with a resolution of 1° × 1° were incorporated using the nudging method from 1948 to 1981 (Hirahara et al., 2014), and then, the 1/4° daily SST from improved estimation OISST v2.1 were nudged since 1982 (Banzon et al., 2020). The initial condition was compared with COBE SST from 1993 to 2019, and the predicted result was compared with OISST v2.1. To evaluate the subsurface ocean temperature, the National Centers for Environmental Prediction (NCEP) Global Ocean Assimilation System (GODAS) datasets was analyzed (Behringer et al., 1998). All the observations and simulations were linearly interpolated to a 1° grid before the validation. The monthly anomalies for each experiment and the observations were defined by concerning their own climatology for the same period. To measure the relationship between the predicted and observed anomalies, several statistical indicators, including the anomaly correlation coefficient (ACC), the root mean square error (RMSE), the centered root mean square difference (CRMSD, calculated as the RMSE of the predication and observation after subtracting their own mean value), and the absolute average errors (AAE, calculated as the absolute mean value of differences between prediction and observation time series), were used to evaluate the performances of those prediction systems.

RESULTS

Initial State

The monthly mean initial results based on FIO-CPS v1.0 and FIO-CPS v2.0 were analyzed for 1993–2019 by comparing the differences in the annual mean SST of the simulation and OISST

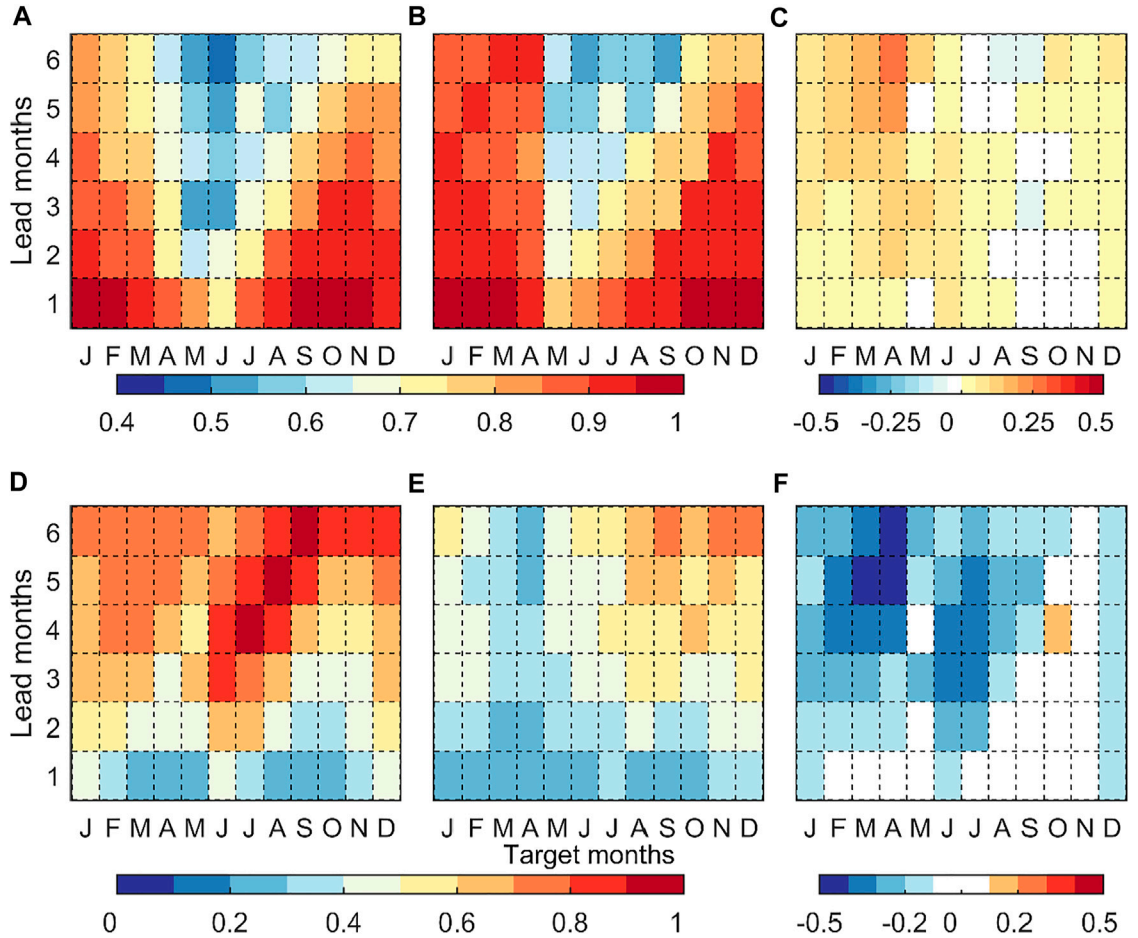

FIGURE 5 | ACC and RMSE of the Niño 3.4 SSTA as a function of the target month and lead month obtained using the **(A, D)** FIO-CPS v1.0; **(B, E)** FIO-CPS v2.0; **(C, F)** the differences between FIO-CPS v2.0 and FIO-CPS v1.0.

v2.1. As shown in **Figure 2**, the bias of FIO-CPS v2.0 is generally smaller than that of FIO-CPS v1.0. There are negative biases in the equatorial Pacific, the western boundary current region in the North Pacific and Atlantic, and several areas in the Southern Ocean, indicating that the simulated SST in these areas is lower than the observations. In addition, the SST differences for FIO-CPS v1.0 exhibit a large warm bias in the eastern boundary of the Pacific and the Southern Ocean. In FIO-CPS v2.0, these biases are obviously improved. Both the spatial correlation coefficients in FIO-CPS v1.0 and v2.0 are greater than 0.99, and the bias represented by the CRMSD decreases from 0.43 to 0.33. The annual mean results reveal that the initial values simulated using FIO-CPS v2.0 are more consistent with the observations.

Figures 3A,B shows the ACC of the sea surface temperature anomaly (SSTA) between the OISST v2.1 and the assimilation results. It is found that the model that assimilates the observations captures the SSTA pattern reasonably well in the tropical eastern Pacific, with the highest ACC distribution in both models' results. Generally, the ACC in the tropics is higher than it in the subtropics and at high-latitudes. In the zonal direction, the initiation conditions in the Atlantic and Pacific are more consistent with the observations than those in the Indian Ocean. The difference of ACC between FIO-CPS v2.0 and v1.0 is shown in **Figure 3C**. The assimilation results of FIO-CPS v2.0 are improved compared with those of FIO-CPS v1.0, especially in the Southern Ocean and the tropical region. The ACC of FIO-CPS v1.0 is less than 0.6 in most Southern Ocean, where the ACC in FIO-CPS v2.0 exhibits a increase. Generally, the improvement is more significant in the Southern Hemisphere than the Northern Hemisphere.

Seasonal Prediction

The ENSO is the dominant natural variability in the equatorial Pacific on seasonal to interannual timescales. Here, we examined the predictive skills of the two versions of the system in predicting the ENSO state indicated by the Niño3.4 index, which is calculated by the area-averaged SSTA with a 3-month running mean (**Figure 4**). The seasonal predictions of the ensemble mean

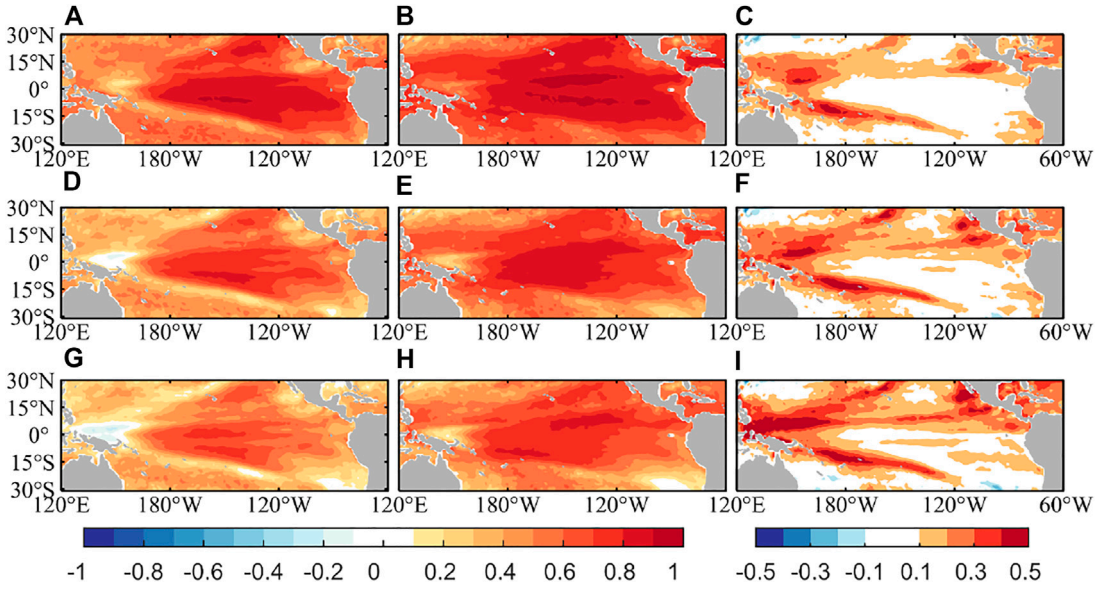

FIGURE 6 | Spatial distribution of the SSTA ACC in the tropical Pacific for different lead months, **(A, D, G)** FIO-CPS v1.0 results, **(B, E, H)** FIO-CPS v2.0 results, and **(C, F, I)** the difference between FIO-CPS v2.0 and FIO-CPS v1.0. The result for **(A–C)** 2-month lead time, **(D–F)** 4-month lead time, and **(G–I)** 6-month lead time.

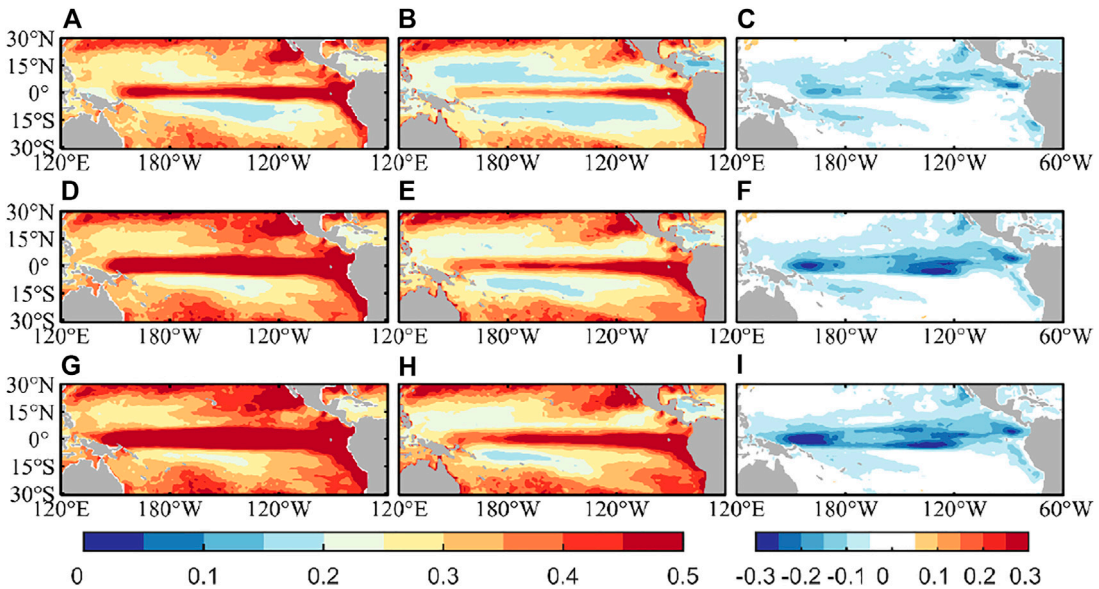

FIGURE 7 | Spatial distribution of the absolute average error (AAE, units: °C) of the SSTA between the predictions and OISST v2.1, **(A, D, G)** FIO-CPS v1.0 results, **(B, E, H)** FIO-CPS v2.0 results, and **(C, F, I)** the difference between FIO-CPS v2.0 and FIO-CPS v1.0. **(A–C)** 2-month lead time, **(D–F)** 4-month lead time, and **(G–I)** 6-month lead time.

results based on FIO-CPS v1.0 and v2.0 were evaluated by calculating the respective metrics (i.e., the ACC and RMSE). The horizontal axis represents the initial conditions and the prediction month for 1-month to 6-month lead times. As shown in **Figure 4A**, considering the assimilated results, the ACC between the FIO-CPS v2.0's simulation and the observations is higher than that for the FIO-CPS v1.0. This result is consistent with the spatial distribution of the ACC (**Figure 3**). The ACC of FIO-CPS v2.0 is higher than that of FIO-CPS v1.0, indicating that FIO-CPS v2.0 is more skillful than FIO-CPS v1.0 in predicting the Niño3.4 index. As the predicted month increases, the difference between the two models increases. At a 6-month lead time, the ACC of FIO-CPS v2.0 is 0.78, which increases by 11.09% compared with the value of

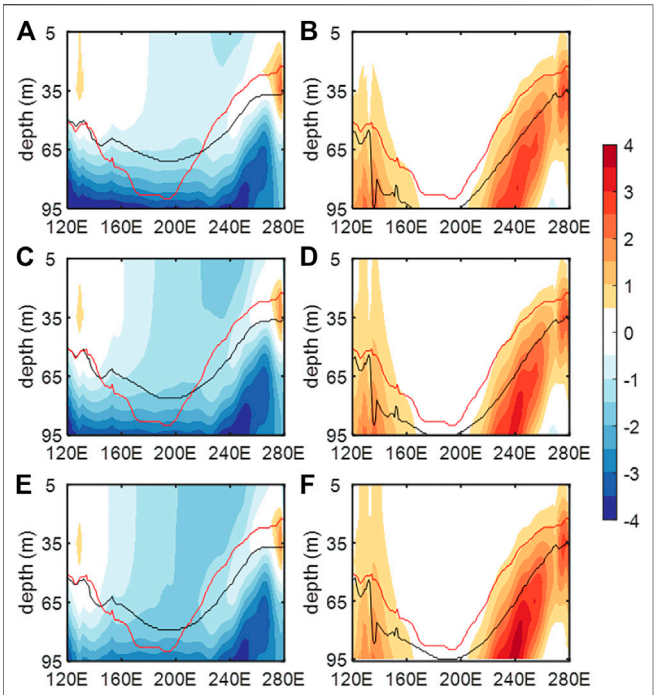

FIGURE 8 | Vertical profile of subsurface ocean temperature along the equator (averaged between 5°S and 5°N) between prediction and GODAS, (A, C, E) FIO-CPS v1.0 and (B, D, F) FIO-CPS v2.0 results for the period 1993–2019, (A, B) 2-month lead time, (C, D) 4-month lead time, and (E, F) 6-month lead time. The red and black line represent the MLD based on observation and prediction.

0.70 in FIO-CPS v1.0. In addition, the RMSEs of the two models are compared in **Figure 4B**. The RMSE of FIO-CPS v1.0 increases rapidly from the 2-month lead time. In contrast, FIO-CPS v2.0, with its smaller RMSE in the initial conditions, exhibits a slower error growth during the prediction. From lead-4 to lead-6 month, the RMSE decreases by more than 0.20 that accounts for about 30% of the result of FIO-CPS v1.0. In addition, we also found that the ability of the model to predict strong ENSO events has a great impact on the average skill. For example, if the strong ENSO event index in 2015/16 and the next few years are removed from the time series, the ACC is 0.85 for a 6-month lead time predicted using FIO-CPS v2.0, and the value is 0.75 based on the FIO-CPS v1.0 (not shown).

Figure 5 shows the ACC and RMSE of the Niño 3.4 SSTA of FIO-CPS v1.0 and v2.0 as a function of the predicted target month and lead time. The ACC distributions of the two systems generally exhibit similar patterns. Both predictions indicate a spring predictability barrier in the ENSO, with relatively lower prediction skills in the boreal spring and extending to later seasons for longer lead times. Generally, the FIO-CPS v2.0 has a higher correlation skill in contrast to FIO-CPS v1.0, especially in boreal winter and spring. The significant positive difference in the ACC as the target month ranging from February to May demonstrates that the predictability in winter has been improved in FIO-CPS v2.0. Furthermore, we found that the most significant improvement in the skill was for 3- to 6-month lead times in spring. Both the well initial conditions and the improved climate model provide more skillful predictions for a longer lead time. In addition, the RMSE of FIO-CPS v1.0 increases significantly in the boreal summer from 2-month lead times, while the RMSE of FIO-CPS v2.0 is obvious smaller than that of v1.0. In boreal winter and early spring, the RMSE decreases by 0.5 for 5-month to 6-month lead times, and it decreases by more than 0.3 in boreal summer for 3-month to 5-month lead times. Overall, based on the ACC and RMSE indicators, the predicted ENSO is dramatically improved in the boreal winter and summer. Besides, the spring predictability barrier is still obvious in FIO-CPS v2.0, but there is a clear improvement of this problem and its persistence.

To explore the improvement in the ENSO prediction in more detail, the spatial distributions of the SSTA ACC for 2-, 4-, and 6-month lead times are shown in **Figure 6**. The ACC is higher in the central and eastern tropical Pacific but is lower in the western tropical Pacific and subtropical Pacific. The spatial patterns for the different lead times are similar, but the magnitude differs for the different lead months. FIO-CPS v2.0 exhibits an improved skill in terms of the SSTA prediction in the tropical Pacific. As previously discussed, the skill of FIO-CPS v2.0 in predicting the Niño3.4 index is improved (**Figure 4A**). However, the most obvious improvement is not in the equatorial Pacific. The SSTA in the western Pacific and subtropical eastern Pacific are predicted considerably better than the SSTA in the equatorial Pacific. As shown by the differences in the ACC of SSTA, there is a positive value in the western Pacific and the extra-equatorial area.

The annual mean AAE of SSTA calculated using the absolute value of the differences between the predictions and OISST v2.0 reflects the model's ability to predict the mean state of the SSTA. As shown in **Figure 7**, a large AAE exists in the equatorial Pacific, with a maximum larger than 0.5°C for FIO-CPS v1.0. As the prediction time increases, the error persists in the equator Pacific and even increases. A clear improvement, with a reduced AAE, in the equatorial Pacific is seen for FIO-CPS v2.0 over the whole range of lead times. The difference in the AAE is negative along the equator, and the improvement is more obvious in the northern tropical Pacific. It is found that the negative difference of less than 0.3°C is distributed in the northern tropical Pacific for 2- and 4-month lead times.

The vertical profile of upper ocean temperature differences averaged between 5°S and 5°N between the prediction and GODAS datasets is shown in **Figure 8**. The solid line represents the mixed layer depth (determined by the criteria: a temperature change from the ocean surface of 0.5°C) of GODAS (red line) and prediction results (black line). There are cold biases below the mixed layer in FIO-CPS v1.0, while the FIO-CPS v2.0 presents warm bias, especially in the eastern Pacific. The bias gradually magnifies with the increase of lead month. Moreover, the predicted MLD is deeper as compared with the GOADS result in FIO-CPS v2.0. The ENSO variability is closely related to the MLD variation. In the mixed layer, the FIO-CPS v1.0 has an obvious cold bias in the Niño region, which tents to produce the La Niña event more frequently, however, the temperature bias in the FIO-CPS v2.0 is dramatically improved. Generally, the FIO-CPS v2.0 tends to predict a more reasonable vertical structure of upper ocean temperature.

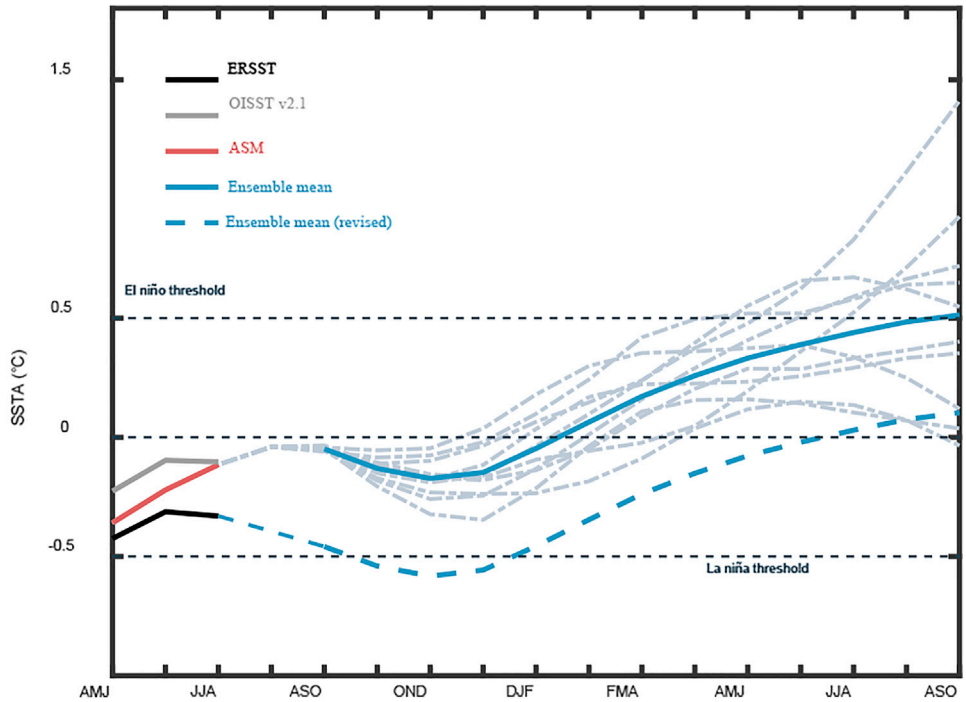

FIGURE 9 | The Niño 3.4 index with respect to the 1982–2020 climatology based on the prediction starting from 1 September 2021. The black, grey and red lines are the index of ERSST, OISST v2.1 and the initial state. The blue solid and dashed lines show the prediction of ensemble mean and revised index, and the dashed light blue line represents each ensemble.

Figure 9 shows the prediction of the Niño3.4 index starting from 1 September 2021, here the SSTA is respect to the 1982–2020 climatology. The ensemble mean of the Niño3.4 index is close to zero in September and will decrease in winter, but the Niño3.4 index doesn't surpass a threshold of -0.5°C. It indicates that ENSO will be in a neutral state during the winter time. Then, the Niño3.4 SSTA will increase from January in 2022. Specifically, the Niño3.4 index of five ensembles will increase with anomalies of up to 0.5°C in early summer in 2022. It is found that there is significant differences between different observational data. The index derived from OISST v2.1 is higher than the ERSST result. In FIO-CPS v2.0, the daily OISST v2.1 is assimilated, thus the nudging OISST v2.1 provides a warmer initial condition for the prediction. A neutral ENSO condition with negative Niño3.4 index are favored through the winter of 2021 based on the ensemble mean prediction of FIO-CPS v2.0. However, if the prediction is revised according to the ERSST, a transition from ENSO-neutral to La Niña is favored in the winter 2021–22.

CONCLUSION

The seasonal prediction system FIO-CPS v2.0 was recently developed, and its prediction ability indicated by Niño index and SSTA in the tropical Pacific Ocean was evaluated based on the hindcast results from 1993 to 2019. Compared with FIO-CPS v1.0, FIO-CPS v2.0 has an improved skill in predicting ENSO based on the indicators of ACC and RMSE. The increases in the spatial and temporal correlations between the simulation and the observations reveal that the initial state of FIO-CPS v2.0 is well simulated. The improved initialization and physical model result in a more skillful seasonal prediction. Specifically, the ENSO prediction skill, represented by the ACC, is 0.78 for a 6-month lead time, which is 11.09% better than that of FIO-CPS v1.0. And the RMSE decreases by 0.20 that represents 28.59% of the FIO-CPS v1.0 result. The prediction errors of the Niño 3.4 SSTA exhibit a seasonally dependent evolution, with the lowest ACC in the boreal spring and early summer. A spring predictability barrier exists in FIO-CPS v1.0 and v2.0, but this problem is less pronounced in FIO-CPS v2.0. Moreover, the prediction skill significantly increases in boreal winter and spring for 3- to 6-month lead times, and in summer for 1- to 2-month lead times in FIO-CPS v2.0.

It seems that the well-predicted mean state of the SSTA mainly contributes to the improvement of the ENSO prediction. In FIO-CPS v2.0, all model components are improved, with a more reasonable parameterization scheme and higher horizontal and vertical resolutions. Bao et al. (2020) and Liao et al. (2021) pointed out that FIO-ESM v2.0 can simulate the strength and period of the ENSO fairly well compared with observation. The improvement in the model's performance at simulating ENSO plays a crucial role in enhancing its prediction ability. In this

study, the prediction errors of the mean state were evaluated. In the equatorial Pacific, the mean state of the SSTA is more consistent with the observations. However, the change in the ACC, representing the variability of the SSTA, did not exhibit a comparable improvement. This further illustrates the importance of the model's ability in accurately simulating and predicting the mean states in the tropical Pacific.

As shown by Barnston et al. (2019), the correlation skill of the North American multi-model ensemble prediction plume's results is greater than 0.6 for 11- to 12-month lead times. However, the error growth of the Niño3.4 SSTA is accelerated for a greater than 8-month lead time in FIO-CPS v2.0, and the prediction skill is reduced to 0.5 for a 12-month lead time. In FIO-CPS v2.0, only the fine resolution SST is considered in the initial field using the nudging method, which can only modulate the ocean temperature in the mixed layer. This implies that the simple assimilation technique and neglecting the observations in the subsurface ocean may lead to the growth of the SSTA error during the prediction. To continually improve the prediction skill of FIO-CPS v2.0, more observation datasets and reasonable assimilation methods are needed to reduce the growth of the prediction error.

DATA AVAILABILITY STATEMENT

The original contributions presented in the study are publicly available. The prediction datasets based on FIO-CPS v1.0 and v2.0 have been uploaded to Figshare at https://doi.org/10.6084/m9.figshare.15171366 and https://doi.org/10.6084/m9.figshare.15171369, respectively.

AUTHOR CONTRIBUTIONS

ZS initially designed and organized analysis. YS conducted the hindcast experiments, made some figures and wrote first draft. YB and QS developed the climate model and induced the assimilation scheme into the short-term climate prediction system. XY downloaded the observation dataset, and updated the prediction experiment. All authors contributed to polishing the manuscript.

FUNDING

This research was jointly supported by the National Natural Science Foundation of China (Grant No. 42075039, 42022042, and 41821004), the China-Korea Cooperation Project on Northwestern Pacific Climate Change and its Prediction, and the CAS Interdisciplinary Innovation Team (JCTD-2020-12).

ACKNOWLEDGMENTS

The numerical experiments in this study were carried out at the National Supercomputer Center in Tianjin (NSCC-TJ) and the Beijing Super Cloud Computing Center (BSCC).

REFERENCES

Banzon, V., Smith, T. M., Steele, M., Huang, B., and Zhang, H.-M. (2020). Improved Estimation of Proxy Sea Surface Temperature in the Arctic. *J. Atmos. Ocean. Technol.* 37 (2), 341–349. doi:10.1175/JTECH-D-19-0177.1

Bao, Y., Song, Z., and Qiao, F. (2020). FIO-ESM Version 2.0: Model Description and Evaluation. *J. Geophys. Res. Oceans* 125. doi:10.1029/2019JC016036

Barnston, A. G., Tippett, M. K., L'Heureux, M. L., Li, S., and DeWitt, D. G. (2012). Skill of Real-Time Seasonal ENSO Model Predictions during 2002-11: Is Our Capability Increasing. *Bull. Amer. Meteorol. Soc.* 93 (5), 631–651. doi:10.1175/bams-d-11-00111.1

Barnston, A. G., Tippett, M. K., Ranganathan, M., and L'Heureux, M. L. (2019). Deterministic Skill of ENSO Predictions from the North American Multimodel Ensemble. *Clim. Dyn.* 53 (21), 7215–7234. doi:10.1007/s00382-017-3603-3

Behringer, D. W., Ji, M., and Leetmaa, A. (1998). An Improved Coupled Model for ENSO Prediction and Implications for Ocean Initialization. Part I: The Ocean Data Assimilation System. *Mon. Wea. Rev.* 126 (4), 1013–1021. doi:10.1175/1520-0493(1998)126<1013:aicmfe>2.0.co;2

Cane, M. A., Zebiak, S. E., and Dolan, S. C. (1986). Experimental Forecasts of El Niño. *Nature* 321, 827–832. doi:10.1038/321827a0

Chen, D., Cane, M. A., Kaplan, A., Zebiak, S. E., and Huang, D. (2004). Predictability of El Niño over the Past 148 Years. *Nature* 428, 733–736. doi:10.1038/nature02439

Chen, H., Yin, X., Bao, Y., and Qiao, F. (2015). Ocean Satellite Data Assimilation Experiments in FIO-ESM Using Ensemble Adjustment Kalman Filter. *Sci. China Earth Sci.* 59 (3), 484–494. doi:10.1007/s11430-015-5187-2

Dai, A. G., Wigley, T., Boville, B. A., Kiehl, J. T., and Buja, L. E. (2014). Climates of the Twentieth and Twenty-First Centuries Simulated by the NCAR Climate System Model. *J. Clim.* 14 (4), 485–519. doi:10.1175/1520-0442(2001)0142.0.CO;2

Drosdowsky, W. (2006). Statistical Prediction of ENSO (Nino 3) Using Sub-surface Temperature Data. *Geophys. Res. Lett.* 33 (3), L03710. doi:10.1029/2005GL024866

Ducet, N., Le Traon, P. Y., and Reverdin, G. (2000). Global High-Resolution Mapping of Ocean Circulation from TOPEX/Poseidon and ERS-1 and -2. *J. Geophys. Res.* 105, 19477–19498. doi:10.1029/2000jc900063

Hirahara, S., Ishii, M., and Fukuda, Y. (2014). Centennial-scale Sea Surface Temperature Analysis and its Uncertainty. *J. Clim.* 27 (1), 57–75. doi:10.1175/JCLI-D-12-00837.1

Hu, Z.-Z., Kumar, A., Huang, B., Zhu, J., and Guan, Y. (2014). Prediction Skill of north Pacific Variability in NCEP Climate Forecast System Version 2: Impact of ENSO and beyond. *J. Clim.* 27 (11), 4263–4272. doi:10.1175/JCLI-D-13-00633.1

Jin, E. K., Kinter, J. L., Wang, B., Park, C.-K., Kang, I.-S., Kirtman, B. P., et al. (2008). Current Status of ENSO Prediction Skill in Coupled Ocean-Atmosphere Models. *Clim. Dyn.* 31 (6), 647–664. doi:10.1007/s00382-008-0397-3

Kim, S. T., Jeong, H.-I., and Jin, F.-F. (2017). Mean Bias in Seasonal Forecast Model and ENSO Prediction Error. *Sci. Rep.* 7, 6029. doi:10.1038/s41598-017-05221-3

Liao, H., Wang, C., and Song, Z. (2021). ENSO Phase-Locking Biases from the CMIP5 to CMIP6 Models and a Possible Explanation. *Deep Sea Res. Part Topical Stud. Oceanography* 189-190, 104943. doi:10.1016/j.dsr2.2021.104943

Luo, J.-J., Yuan, C., Sasaki, W., Behera, S. K., Masumoto, Y., Yamagata, T., et al. (2016). "Current Status of Intraseasonal-Seasonal-To-Interannual Prediction of the Indo-pacific Climate," in *Indo-Pacific Climate Variability and Predictability*. Editors S. Behera and T. Yamagata (Singapore: The World Scientific Publisher), 63–107. doi:10.1142/9789814696623_0003

Qiao, F., Song, Z., Bao, Y., Song, Y., Shu, Q., Huang, C., et al. (2013). Development and Evaluation of an Earth System Model with Surface Gravity Waves. *J. Geophys. Res. Oceans* 118, 4514–4524. doi:10.1002/jgrc.20327.2013

Qiao, F., Yuan, Y., Ezer, T., Xia, C., Yang, Y., Lü, X., et al. (2010). A Three-Dimensional Surface Wave-Ocean Circulation Coupled Model and its Initial Testing. *Ocean Dyn.* 60 (5), 1339–1355. doi:10.1007/s10236-010-0326-y

Qiao, F., Yuan, Y., Yang, Y., Zheng, Q., Xia, C., and Ma, J. (2004). Wave-induced Mixing in the Upper Ocean: Distribution and Application to a Global Ocean Circulation Model. *Geophys. Res. Lett.* 31, a–n. doi:10.1029/2004GL019824

Ren, H.-L., Wu, Y., Bao, Q., Ma, J., Liu, C., Wan, J., et al. (2019). The China Multi-Model Ensemble Prediction System and its Application to Flood-Season Prediction in 2018. *J. Meteorol. Res.* 33 (3), 540–552. doi:10.1007/s13351-019-8154-6

Reynolds, R. W., Smith, T. M., Liu, C., Chelton, D. B., Casey, K. S., and Schlax, M. G. (2007). Daily High-Resolution-Blended Analyses for Sea Surface Temperature. *J. Clim.* 20 (22), 5473–5496. doi:10.1175/2007JCLI1824.1

Song, Y., Zhao, Y., Yin, X., Bao, Y., and Qiao, F. (2020). Evaluation of FIO-ESM v1.0 Seasonal Prediction Skills over the north Pacific. *Front. Mar. Sci.* 7. doi:10.3389/fmars.2020.00504

Song, Z., Shu, Q., Bao, Y., Yin, X., and Qiao, F. (2015). The Prediction on the 2015/16 El Niño Event from the Perspective of FIO-ESM. *Acta Oceanol. Sin.* 34 (12), 67–71. doi:10.1007/s13131-015-0787-4

Wyrtki, K. (1975). El Niño–The Dynamic Response of the Equatorial Pacific Ocean to Atmospheric Forcing. *J. Phys. Oceanogr* 5, 572–584. doi:10.1175/1520-0485(1975)005<0572:ENTDRO>2.0.CO;2

Zhang, S., Liu, Z., Zhang, X., Wu, X., Han, G., Zhao, Y., et al. (2020). Coupled Data Assimilation and Parameter Estimation in Coupled Ocean-Atmosphere Models: a Review. *Clim. Dyn.* 54 (9), 5127–5144. doi:10.1007/s00382-020-05275-6

Zhao, Y., Yin, X., Song, Y., and Qiao, F. (2019). Seasonal Prediction Skills of FIO-ESM for north pacific Sea Surface Temperature and Precipitation. *Acta Oceanol. Sin.* 38, 5–12. doi:10.1007/s13131-019-1366-x

Zheng, F., and Yu, J.-Y. (2017). Contrasting the Skills and Biases of Deterministic Predictions for the Two Types of El Niño. *Adv. Atmos. Sci.* 34 (12), 1395–1403. doi:10.1007/s00376-017-6324-y

Zheng, F., and Zhu, J. (2010). Coupled Assimilation for an Intermediated Coupled Enso Prediction Model. *Ocean Dyn.* 60 (5), 1061–1073. doi:10.1007/s10236-010-0307-1

Zheng, F., and Zhu, J. (2016). Improved Ensemble-Mean Forecasting of ENSO Events by a Zero-Mean Stochastic Error Model of an Intermediate Coupled Model. *Clim. Dyn.* 47 (12), 3901–3915. doi:10.1007/s00382-016-3048-0

Zheng, F., Zhu, J., and Zhang, R.-H. (2007). Impact of Altimetry Data on ENSO Ensemble Initializations and Predictions. *Geophys. Res. Lett.* 34, a–n. doi:10.1029/2007GL030451

Zheng, F., Zhu, J., Zhang, R.-H., and Zhou, G.-Q. (2006). Ensemble Hindcasts of SST Anomalies in the Tropical pacific Using an Intermediate Coupled Model. *Geophys. Res. Lett.* 33, L19604. doi:10.1029/2006GL026994

Zhou, T., Chen, Z., Zou, L., Chen, X., Yu, Y., Wang, B., et al. (2020). Development of Climate and Earth System Models in china: Past Achievements and New Cmip6 Results. *J. Meteorol. Res.* 34 (1), 1–19. doi:10.1007/s13351-020-9164-0

Zhu, J., Kumar, A., Wang, W., Hu, Z. Z., Huang, B., and Balmaseda, M. A. (2017). Importance of Convective Parameterization in ENSO Predictions. *Geophys. Res. Lett.* 44, 6334–6342. doi:10.1002/2017GL073669

Conflict of Interest: The authors declare that the research was conducted in the absence of any commercial or financial relationships that could be construed as a potential conflict of interest.

The reviewer (LM) declared a past co-authorship with the authors (YB, ZS) to the handling Editor.

Publisher's Note: All claims expressed in this article are solely those of the authors and do not necessarily represent those of their affiliated organizations, or those of the publisher, the editors and the reviewers. Any product that may be evaluated in this article, or claim that may be made by its manufacturer, is not guaranteed or endorsed by the publisher.

frontiers in Earth Science

CORRECTION
published: 11 March 2022
doi: 10.3389/feart.2022.876874

Corrigendum: The Short-Term Climate Prediction System FIO-CPS v2.0 and Its Prediction Skill in ENSO

Yajuan Song[1,2,3], *Qi Shu*[1,2,3], *Ying Bao*[1,2,3], *Xiaodan Yang*[1,2,3] *and Zhenya Song*[1,2,3]*

[1]Key Laboratory of Marine Science and Numerical Modeling, First Institute of Oceanography, Ministry of Natural Resources, Qingdao, China, [2]Laboratory for Regional Oceanography and Numerical Modeling, Pilot National Laboratory for Marine Science and Technology, Qingdao, China, [3]Shandong Key Laboratory of Marine Science and Numerical Modeling, Qingdao, China

Keywords: short-term climate prediction system, seasonal prediction, ENSO, climate model, sea surface temperature, FIO-CPS

OPEN ACCESS

Edited and reviewed by:
Ruihuang Xie,
Ocean University of China, China

***Correspondence:**
Zhenya Song
songroy@fio.org.cn

Specialty section:
This article was submitted to Atmospheric Science, a section of the journal Frontiers in Earth Science

Received: *16 February 2022*
Accepted: *18 February 2022*
Published: *11 March 2022*

Citation:
Song Y, Shu Q, Bao Y, Yang X and Song Z (2022) Corrigendum: The Short-Term Climate Prediction System FIO-CPS v2.0 and Its Prediction Skill in ENSO. Front. Earth Sci. 10:876874. doi: 10.3389/feart.2022.876874

A Corrigendum on

The Short-Term Climate Prediction System FIO-CPS v2.0 and Its Prediction Skill in ENSO
by Song, Y., Shu, Q., Bao, Y., Yang, X., and Song, Z. (2021). Front. Earth Sci. 9:759339. doi:10.3389/feart.2021.759339

In the original article, there was a mistake in **Figure 5** as published. The color bar for **Figure 5A** is inconsistent with the other figures, so the values in **Figure 5A** cannot represent the real prediction skills of FIO-CPS v1.0. The corrected **Figure 5** appears below.

The authors apologize for this error and state that this does not change the scientific conclusions of the article in any way. The original article has been updated.

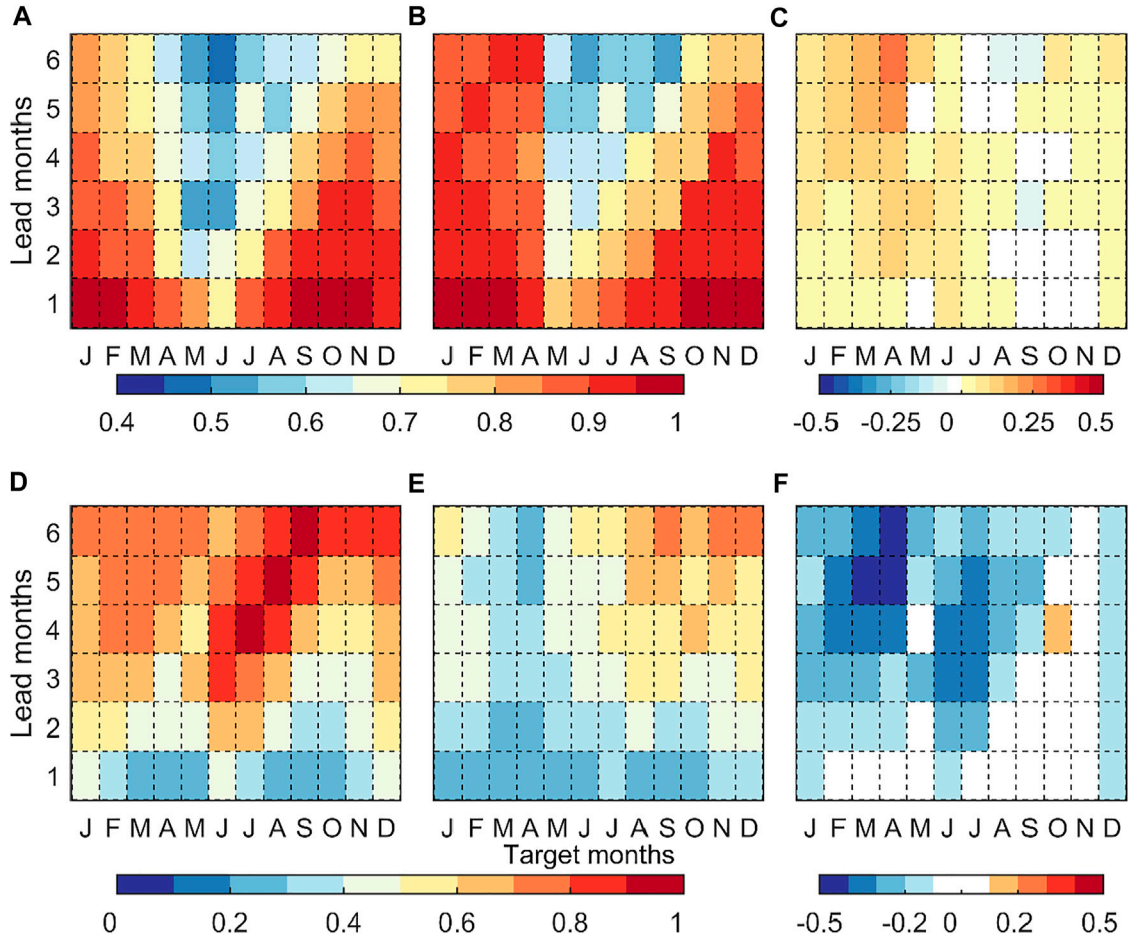

FIGURE 5 | ACC and RMSE of the Niño 3.4 SSTA as a function of the target month and lead month obtained using the **(A,D)** FIO-CPS v1.0; **(B,E)** FIO-CPS v2.0; **(C,F)** the differences between FIO-CPS v2.0 and FIO-CPS v1.0.

frontiers in Earth Science

ORIGINAL RESEARCH
published: 25 March 2022
doi: 10.3389/feart.2022.873040

Impacts of Central Tropical Pacific SST on the Reversal of December and January Surface Air Temperature Anomalies Over Central Asia

Haishan Li[1,2], *Ke Fan*[3]*, *Hua Li*[4] *and Zhiqing Xu*[1]

[1]Institute of Atmospheric Physics, Chinese Academy of Sciences, Beijing, China, [2]University of the Chinese Academy of Sciences, Beijing, China, [3]School of Atmospheric Science, Sun Yat-sen University, and Southern Marine Science and Engineering Guangdong Laboratory (Zhuhai), Zhuhai, China, [4]Collaborative Innovation Center on Forecast and Evaluation of Meteorological Disasters, Nanjing University of Information Science and Technology, Nanjing, China

The reversal of winter surface air temperature anomalies (SATAs) over Central Asia (CA) between December and January is investigated in this study and found to be closely related to the sea surface temperature anomalies (SSTAs) over the central tropical Pacific (CTP). The cold CTP SSTAs can lead to positive (negative) SATAs over CA in December (January). The different responses of SATAs over CA to the SSTAs are attributed to different Rossby wave propagations. In December, a wave train from the North Pacific directly reaches CA, while in January it mainly propagates in the meridional direction and cannot reach CA. The January SATAs of CA are influenced by a wave train from the North Atlantic, which is induced by CTP SSTAs indirectly. The wave trains from the North Pacific are mainly driven by the Gill-type response to the cold CTP SSTA in both December and January. In January, since the climatological subtropical jet stream over the North Pacific is stronger and situated more towards the equator, a stronger Gill-type response is excited and causes the meridional propagation of the Rossby waves. Then, this stronger Gill-type response can cause strong zonal wind anomalies over the East Pacific. Local anomalies of the synoptic-scale transient eddy can be further caused by the zonal wind anomalies and travel eastward to the North Atlantic. The eddy-induced geopotential anomalies over the North Atlantic can further trigger Rossby waves and cause the negative SATAs over CA. Numerical simulations reproduce these mechanisms.

Keywords: central Asia, surface air temperature anomaly, sea surface temperature anomaly, central tropical Pacific, Rossby wave

OPEN ACCESS

Edited by:
Wenjun Zhang,
Nanjing University of Information Science and Technology, China

Reviewed by:
Han-Ching Chen,
University of Hawaii at Manoa, United States
Shangfeng Chen,
Institute of Atmospheric Physics (CAS), China

***Correspondence:**
Ke Fan
fank8@mail.sysu.edu.cn

Specialty section:
This article was submitted to Atmospheric Science, a section of the journal Frontiers in Earth Science

Received: *10 February 2022*
Accepted: *09 March 2022*
Published: *25 March 2022*

Citation:
Li H, Fan K, Li H and Xu Z (2022) Impacts of Central Tropical Pacific SST on the Reversal of December and January Surface Air Temperature Anomalies Over Central Asia. Front. Earth Sci. 10:873040. doi: 10.3389/feart.2022.873040

1 INTRODUCTION

Central Asia (35°–65°N, 50°–100°E, CA), lying in the hinterland of the Eurasian continent and far from the ocean, is characterized by a typical continental climate (Lioubimtseva and Henebry 2009; Mirzabaev 2013; Li et al., 2015). During the winter season (November–February), the surface air temperature (SAT) over CA not only reaches its minimum but also shows its largest variability in the annual cycle (**Figure 1A**). Variation of winter SAT over CA can cause severe damage in terms of population health (Grjibovski et al., 2013; Zafren 2013; Nyssanbayeva et al., 2019), livestock (Kerven et al., 2004) and environment (Darynova et al., 2018). Thus, further

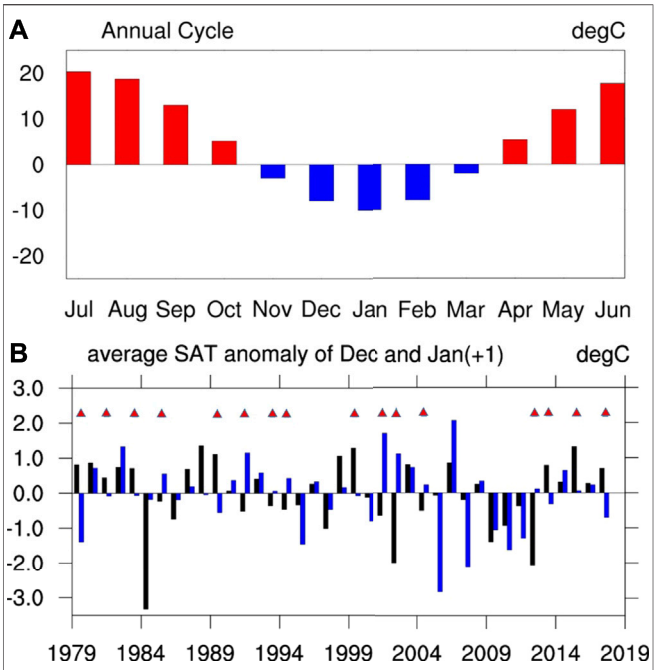

FIGURE 1 | (A) Annual cycle of monthly mean SAT of CA (35°–65°N, 50°–100°E) (bars; °C) and its standard deviation (black line; °C) during the period 1979–2018 **(B)** Anomalies of monthly mean SAT of CA (°C) in December (black bars) and the following January (blue bars) during the period 1979–2018. The red triangles represent the year in which the December and following-January SATA are of opposite sign.

studies on the winter SAT over CA and its variability are necessary for the socioeconomic development of this region.

Previous studies have revealed that the leading mode of SAT anomalies (SATAs) over CA, as a part of the Eurasian continent, is characterized by a same-sign pattern in winter (Miyazaki and Yasunari 2008; Wu and Chen 2020). The variation of winter Eurasian SATAs is largely controlled by the large-scale atmospheric circulation and teleconnections over this region. As a critical semi-permanent winter system over the Eurasian continent, the Siberian high plays an important role (Cohen et al., 2001; Gong and Ho 2002; Kim et al., 2005; Wu et al., 2011). A strengthened Siberian high is associated with cooling over most of the Eurasian continent, which may be due to the associated change in the radiation condition and heat budget over this region (Cohen et al., 2001; Gong and Ho 2002). Previous studies have also found that the positive (negative) phase of the Arctic Oscillation (AO)/North Atlantic Oscillation (NAO) is associated with positive (negative) winter Eurasian SATAs (Hurrell and Van Loon 1997; Thompson and Wallace 2000; Cattiaux et al., 2010). In addition, Liu et al. (2014) pointed out that the three types of Eurasian (EU) patterns (i.e., the traditional EU pattern, Scandinavian pattern, and East Atlantic/West Russia pattern) can exert different influences on the Eurasian SATAs in winter.

Besides the atmospheric circulation and teleconnections, the Eurasian SATAs can also be affected by remote forcing, such as the El Niño–Southern Oscillation (ENSO) (Graf and Zanchettin 2012; Zhang et al., 2015; Feng et al., 2017; García-Serrano et al., 2017), sea surface temperature (SST) anomalies (SSTAs) over the North Atlantic (Liu et al., 2014; Wang et al., 2019; Chen et al., 2020), sea ice (Mori et al., 2014; Chen H. W. et al., 2016; Chen et al., 2019; Cohen et al., 2019), and snow cover (Cohen et al., 2001; Saito et al., 2001; Chen S. et al., 2016).

Zhang et al. (2015) and Feng et al. (2017) found that the central Pacific (CP) El Niño (La Niña) can lead to negative (positive) AO/NAO-like atmospheric responses with negative (positive) geopotential height anomalies over the subtropical Atlantic and Eurasia as well as a cooler (warmer) winter, and part of the mechanism can be explained by the tropospheric bridge according to Graf and Zanchettin (2012).

The role of North Atlantic SSTAs has been studied, revealing that through a sea-air interaction, the North Atlantic SSTAs can cause anomalous atmospheric circulation and Rossby wave trains and impact the Eurasian SATAs. For example, wave trains can be emanated by the North Atlantic SSTAs and directly influence the Eurasian SATAs (Liu et al., 2014; Chen et al., 2020); the North Atlantic SSTAs in preceding summer and autumn can impact the winter NAO pattern and subsequently influence the Eurasian SATAs indirectly (Czaja and Frankignoul 1999; Czaja and Frankignoul 2002; Tian and Fan 2015). The North Atlantic SSTAs can also modulate the influence of ENSO on Eurasian SATAs (Chen and Wu 2017; Chen et al., 2018). Arctic sea ice also plays an important role in the variation of Eurasian SATAs (Mori et al., 2014; Vihma 2014). The decline in Arctic sea ice in preceding summer/autumn may modulate the winter Eurasian SATAs via the increasing heat flux from ocean to atmosphere, which may cause a negative phase of the AO/NAO (Vihma 2014) or lead to more frequent Eurasian blocking situations (Mori et al., 2014). Similar relationship was also found between the autumn Arctic sea ice and spring AO (Chen et al., 2019). The association between snow cover and the variation of Eurasian SATAs has also been researched. Saito et al. (2001) suggested that the autumn Eurasian snow cover anomalies may influence the winter Eurasian SATAs not only by acting as a lower boundary forcing to the tropospheric circulation but also by changing the upward propagating Rossby waves that can influence the AO. Chen H. W. et al. (2016) found that in spring, the snow cover anomalies can contribute partly to Eurasian SATAs by modulating surface net shortwave radiation.

Most of the studies mentioned above focused on the variation of the seasonal average SATAs over Eurasia; however, the sub-seasonal variation of the SATAs in this region has largely been ignored, especially the sub-seasonal out-of-phase variation, which may cause huge socioeconomic impacts. For example, Begzsuren et al. (2004) pointed out that severe winter weather such as sudden cooling and snowfall may be one of the main reasons behind pastoral livestock mortality in cold and dry regions; and Casson et al. (2019) highlighted that a warm period followed by a cold period may cause damage to vegetation, as the warm weather can break the dormancy of vegetation and the subsequent cold weather can result in significant damage. In CA, a reversal of the SATAs between winter months occurs frequently. In **Figure 1B**, we can see that 16 of the total 39 winters, which amounts to 40%, show opposite signs of SATAs between December and January during the period 1979–2018. Such a monthly reversal of SATAs

could be hidden by taking a simple seasonal average, and is therefore worthy of further investigation.

The monthly reversal of the winter SATAs in East Asia has attracted considerable attention among scientists in recent years (Geng et al., 2017; Xu et al., 2018; Dai et al., 2019; Lü et al., 2019). For example, Geng et al. (2017) pointed out that the rapid reversal of East Asia from a warm spell to a cold surge can be attributed to the super El Niño during the boreal winter of 2015/16, which caused a northward shift of the subtropical jet and led to the reversal of the NAO phase. Dai et al. (2019) suggested that the reversal of the winter SATAs over Northeast China between December and January–February can be attributed to the variations of sea ice in different Arctic regions. Li et al. (2021) found that the CP ENSO-related cooling SSTAs may be responsible for the reversal of SATAs over China in December and January since 1997. They found that, compared with the period before 1997, a westward-extended Walker circulation can be caused by the CP ENSO-related cooling SSTAs the over the South China Sea and Kuroshio Extension. The westward-extended Walker circulation, coupled with the different climatological circulation between December and January, can lead to different meridional circulations over China and its SATAs in the months. Although previous studies have focused on this topic, there is still no research concerning the December–January reversal of the SATAs over CA.

As one of the most important predictors for global climate variations, tropical Pacific SSTAs can impact the atmospheric circulation (Zhang et al., 2015; Feng et al., 2017; García-Serrano et al., 2017). It would therefore be interesting to discuss whether the tropical Pacific SSTAs can influence the monthly reversal of the winter SATAs of CA. Accordingly, we seek to answer the following questions in this paper:

(1) What are the main features of the December–January reversal of the SATAs over CA and how can we describe these features?
(2) What's the relationship between the monthly reversal of SATAs and the variation of the SSTAs over the tropical Pacific?
(3) How the monthly reversal of SATAs is influenced by the tropical Pacific SSTAs?

The rest of the paper is organized as follows: **Section 2** describes the data and methods employed in the study. **Section 3** details the out-of-phase mode of the December–January SATAs over CA, its connection to the central tropical Pacific SSTAs (CTP SSTAs), and an analysis of the possible mechanisms behind the connection. **Section 4** provides a summary and some further discussion.

2 DATA AND METHODS

2.1 Datasets

Four datasets were employed in this study, each spanning a period of 40°years from 1979 to 2018, as follows:

(1) The atmospheric reanalysis data used in this study are from the National Centers for Environmental Prediction/National Center for Atmospheric Research (NCEP/NCAR), with a 2.5 horizonal resolution from 1,000 to 10 hPa comprising 17 pressure levels (Kalnay et al., 1996), including the monthly mean SAT, geopotential height, and zonal and meridional winds.
(2) The monthly mean SAT from Global Historical Climatology Network (GHCN) weather stations is also employed to further examine the change in SAT over CA (Peterson and Vose 1997). Moreover, the missing values in these records in each year are excluded and the processed SAT records then interpolated to the 2.5 × 2.5 grid for further verification.
(3) The monthly mean SST data are derived from the Japan Meteorological Agency Centennial Observation-Based Estimates of SST dataset, version 2, with a 1.0° horizonal resolution (Hirahara et al., 2014).
(4) The monthly mean interpolated outgoing longwave radiation (OLR) with a 2.5° horizonal resolution provided by the National Oceanic and Atmospheric Administration (Liebmann and Smith 1996) are employed as the proxy of the intensity of convective heating.

2.2 Statistical and Analysis Method

The multivariate empirical orthogonal function (MV-EOF) analysis method (Wang 1992) is adopted here to distinguish the leading variability modes that combine the variations of the December and following-January SATAs of CA during 1979–2018. In this study, an area-weighted correlation coefficient matrix is constructed for the combined SATA (weighted by the square root of the cosine of latitude) over CA in December and the following January during 1979–2018 to carry out the MV-EOF. The method has been widely applied in climate research. For example, Li et al. (2021) pointed out that the MV-EOF method can distinguish the mode of the reversal of December and January SATAs over China.

The wave activity flux (Takaya and Nakamura 2001) is employed to describe the stationary Rossby wave propagation. This wave flux is parallel to the local group velocity of a stationary Rossby wave train in the Wentzel–Karmers–Brillouin approximation. The horizontal flux is calculated as follows:

$$W = \frac{P}{2\left|\vec{U}\right|}\begin{Bmatrix} U\left(v'^2 - \psi' v_x'\right) + V\left(v'u' - \psi' u_x'\right) \\ U\left(-u'v' - \psi' u_x'\right) + V\left(u'^2 - \psi' u_y'\right) \end{Bmatrix} \quad (1)$$

where P is the pressure scaled by 1,000 hPa, (U, V) denotes the horizontal mean winds, ψ' is the perturbation geostrophic streamfunction, and (u', v') denotes the perturbed winds. The climatological mean values are calculated during the period 1979–2018.

The strength of the synoptic-scale transient eddy activity (STEA) is measured by $\overline{v'^2}$ at 300 hPa, where v' denotes the synoptic-scale daily meridional winds subject to a 2.5–6-day band-pass filter, and the overbar represents averaging over a month (Ren et al., 2010). The eddy-induced geopotential height tendency defined in Lau and Nath (2014) is calculated as follows:

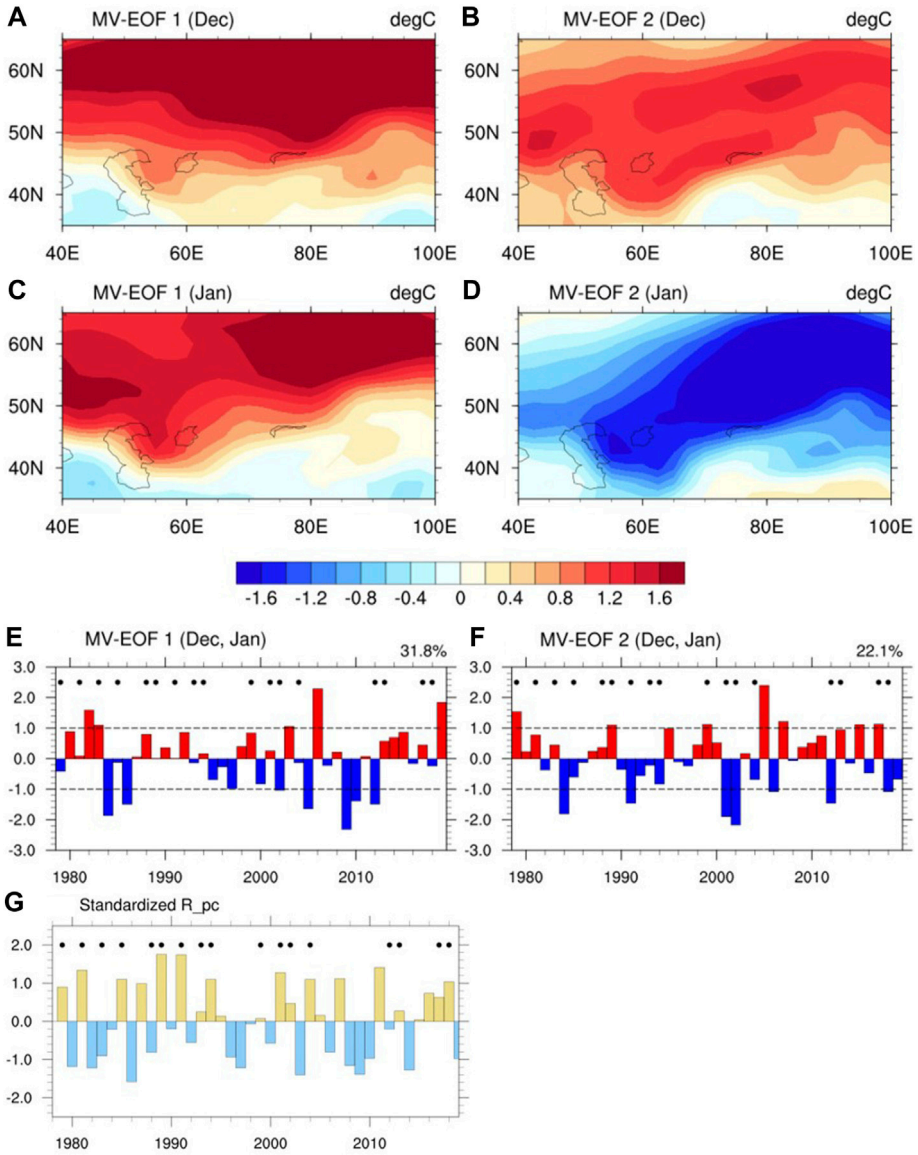

FIGURE 2 | Spatial distributions of the first MV-EOF mode of **(A)** December and **(C)** January SATAs during 1979–2017 **(E)** Normalized time series of the standardized first principal component (PC1), with the proportion of the explained covariance of the first mode given in the top-right corner **(B,D,F)** As in **(A,C,E)** but for the second MV-EOF mode and PC2 **(G)** Time series of the standardized R_{pc2} during 1979–2017. The black dots represent the year in which the December and following-January SATA are of opposite sign.

$$\left(\frac{\partial Z}{\partial t}\right)_{eddy} = \frac{f}{g}\nabla^{-2}\left[-\nabla\left(\overrightarrow{v}'\zeta'\right)\right] \tag{2}$$

where Z is the monthly mean geopotential height; g is the gravitational acceleration; $\overrightarrow{v}' = (u', v')$ and ζ' are the synoptic-scale daily winds and relative vorticity at 300 hPa, respectively, subject to 2.5–6-day bandpass filtering.

The Student's t-test was used to estimate levels of statistical significance, and the linear trends of all data used for regression and correlation were removed. The number of equivalent degrees of freedom for regression was calculated following Zwiers and von Storch (1995).

2.3 Numerical Model

An atmospheric general circulation model, ECHAM5 (Roeckner et al., 2003), is employed to validate the mechanisms given in this study. The ECHAM5 simulations were performed with the spectral T63 horizontal resolution and 19 vertical levels (T63L19). The detailed experimental design is given in **section 3d**.

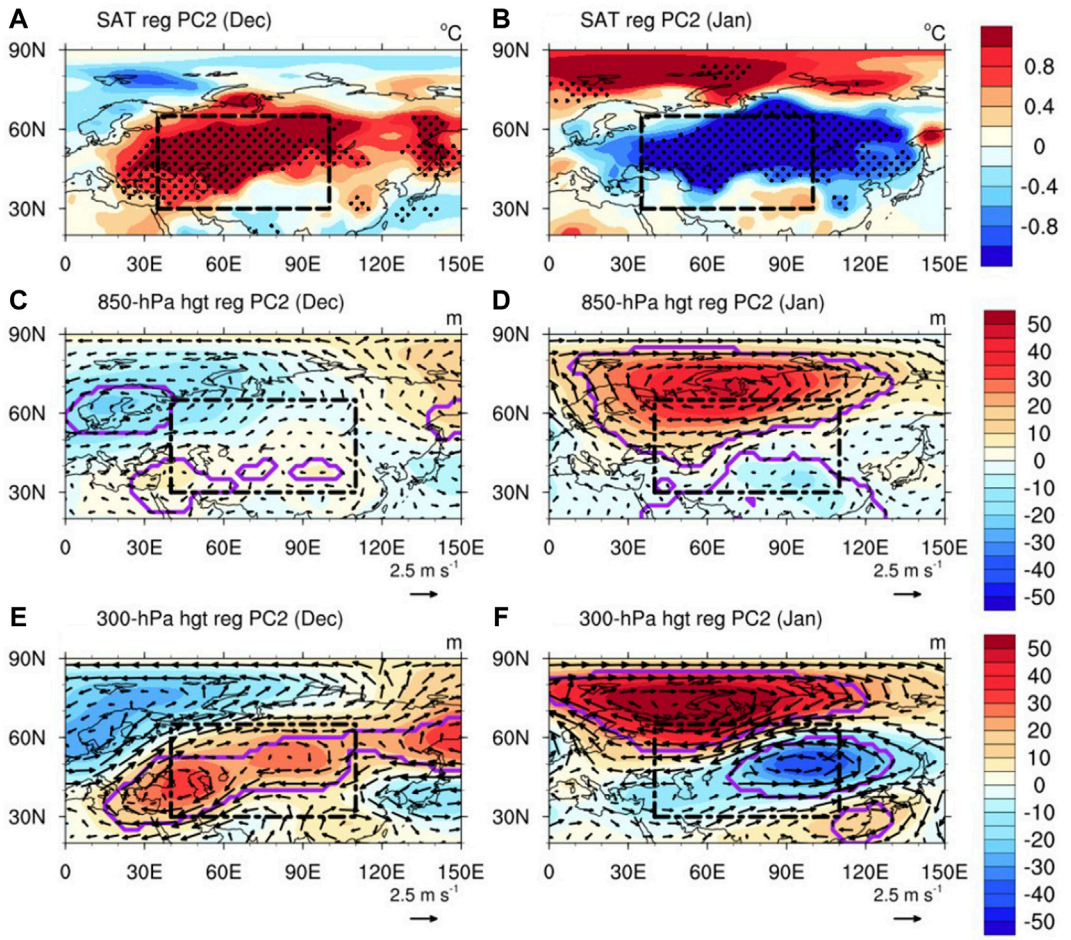

FIGURE 3 | Regressions of December **(A)** SAT (shading; °C) and (C) 850 hPa and (E) 300 hPa geopotential height (shading; m) and winds (vectors; m s^{-1}) onto the PC2 for the period 1979–2017 **(B,D,F)** As in **(A,C,E)** but for January during 1980–2018. The black dashed boxes show the region of CA; anomalies significant at the 95% confidence level are denoted by dots and purple contour lines, as estimated by the Student's *t*-test.

3 RESULTS

3.1 Reversal of the SATAs Over CA Between December and January

Figure 2 shows the spatial patterns of the first two leading modes (MV-EOF1 and MV-EOF2) and corresponding time series (PC1 and PC2). The first and the second leading modes explain 30.7 and 22.3% of the total covariance, respectively, and are both well separated in accordance with the method given by North et al. (1982). MV-EOF1 is an in-phase variation mode, which has similar spatial patterns in December and January, with strong amplitudes situated over the middle and northern part of CA (**Figure 2A,B**). MV-EOF2, meanwhile, shows maximum amplitudes distributed along the northeast–southwest of CA in December and exhibits nearly opposite anomalies in the same region in January (**Figure 2C,D**), which presents the out-of-phase nature of the SATAs between December and January. Similar in-phase and out-of-phase modes can be separated using the GHCN dataset, which have nearly the same spatial distributions as MV-EOF1 and MV-EOF2 (not shown), and the corresponding time series are also highly correlated with PC1 and PC2 (higher than 0.97). Thus, the reversal of the SATAs between December and January over CA can be represented by MV-EOF2.

To examine the atmospheric circulation anomalies associated with MV-EOF2, the PC2-related SATAs and the 850 and 300 hPa geopotential height and wind anomalies in December and January are analyzed (**Figure 3**). The positive PC2 corresponds to the remarkable December warming and January cooling (**Figures 3A,B**). In December, anomalous southeasterlies can be seen over CA at 850-hPa, with a southwest–northeast distribution pattern (**Figure 3C**). The distribution pattern of the anomalous southeasterlies corresponds well with that of the SATAs (**Figure 3A,C**), which indicates that the anomalous warm advection brought by the southeasterlies may contribute to the SATAs in December. Besides, significant southwest–northeast positive height anomalies appear at 300 hPa (**Figure 3E**), which can induce a decline in cloud cover. Thus, enhanced downward shortwave radiation may also contribute to the warm SATAs over CA in December. In January, significant positive geopotential height anomalies appear over the

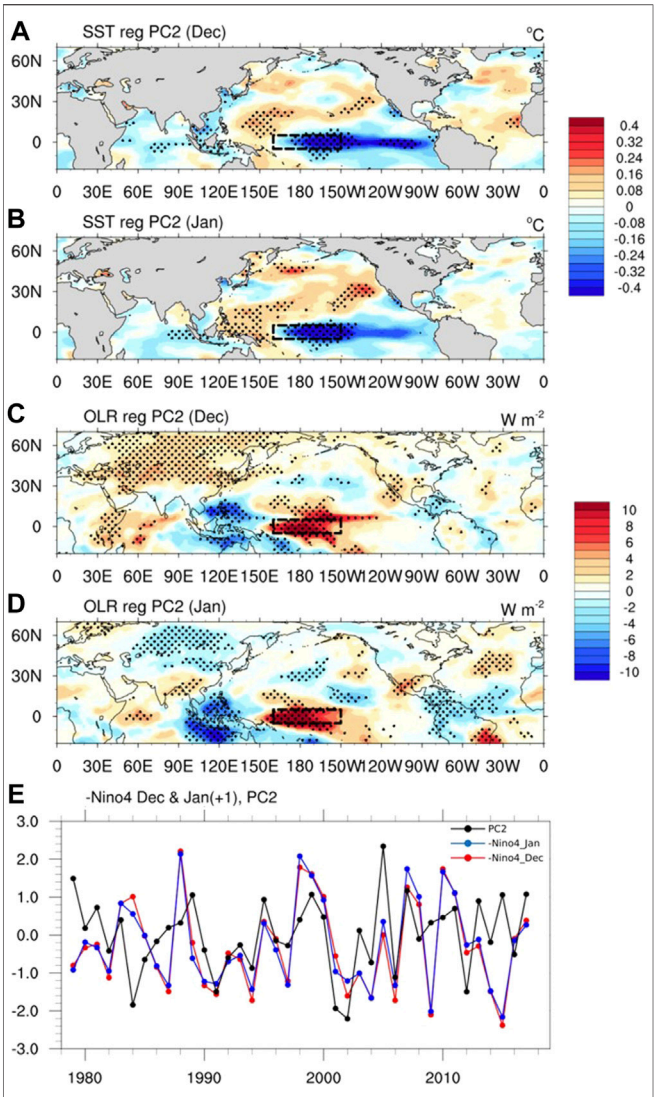

FIGURE 4 | Regressions of **(A)** SST (shading; °C) and (C) OLR (shading; W m^{-2}) onto the PC2 for the period 1979–2017 **(B,D)** As in **(A,C)** but for January during 1980–2018 **(E)** Time series of the standardized –Niño4 index in December (red line), January (blue line) and PC2 (black line) during 1979–2018. Anomalies significant at the 95% confidence level are denoted by dots, as estimated by the Student's *t*-test. The black dashed boxes in (A, B, C, D) show the Niño4 region (5°S–5°N, 160°–150°W).

north side of CA at both 850 hPa and 300 hPa (**Figure 3E**), accompanied by anomalous northeasterlies over CA. The cold advection brought by these anomalous northeasterlies may cause the cold anomalies over northern CA. The contrasting atmospheric circulation anomalies between December and January play an essential role in the reversal of the SATAs over CA.

Because MV-EOF2 represents an out-of-phase relationship between the December and January SATAs, the signs of the mean SATAs of the 2 months are more likely to be opposite when the amplitude of MV-EOF2 is "relatively stronger" than that of MV-EOF1. Years with opposite signs are marked in **Figure 2E,F**. A higher PC2 is likely to appear in these years. To verify this, the index $R_{pc2} = |PC2|/(|PC1| + |PC2|)$ is defined to represent the "relative strength" of MV-EOF2, and the standardized time series of R_{pc2} is given in **Figure 2G**. The years in which the December and January average SATAs are of opposite sign are marked in **Figure 2G**. It can be seen that most of these years show positive standardized values. The average value for the years with opposites signs (16 years) is 0.67, while for the years with same signs (24 years) is −0.46, the difference between the two values is statistically significant at the 95% level according to the Student's *t*-test.

3.2 Relationship Between the Cold CTP SSTAs and the Reversal of the SATAs Over CA

To reveal the remarkable remote SST forcing that modulates the reversal of the SATAs between December and January over CA, the PC2-related SSTAs and outgoing longwave radiation (OLR) in December and January are analyzed (**Figure 4**). Significant negative SSTAs appear over CTP within the Niño4 region (5°S–5°N, 160°–150°W) in both December and January (**Figure 4A,B**), and the pattern of the SSTAs resembles that of CP La Niña (Yuan and Yan, 2013, see their **Figure 2B**). Furthermore, positive OLR anomalies appear in the Niño4 region in both December and January, and these positive OLR anomalies correspond well to the SSTAs (**Figure 4C,D**). This indicates that the PC2-related diabatic heating is directly associated with the SSTAs in the 2 months. As the Niño4 index is defined as the area-averaged SSTA over the Niño4 region (Kug et al., 2009), the –Niño4 index is adopted to represent the variation of the CTP SSTAs. The correlation coefficients between the –Niño4 index in December and January and PC2 are 0.37 and 0.38 (both statistically significant at the 99% level), respectively. Thought the correlation coefficients are not too high, the result still suggests that a significant correlation exist between the between the cold CTP SSTAs and the MV-EOF2.

Moreover, the –Niño4-related SATAs and circulation anomalies over CA are analyzed (**Figure 5**). In December, weak positive SATAs are located over northern and western CA, corresponding to the anomalous southerlies and southwesterlies over western and northern CA at both 850 and 300 hPa (Figures C and E). The warm advection by the anomalous winds may induce the weak positive SATAs in December. In January, negative SATAs appear over CA, corresponding to the significant negative geopotential height anomalies at 300 hPa and anomalous northeasterlies at both 850 and 300 hPa (**Figures 5B,F**), which indicates the cold advection by the anomalous winds may cause the cold anomalies over CA. Besides, the decline of the downward shortwave radiation caused by the negative geopotential height anomalies at 300 hPa may also contribute to the cold anomalies. Though differences exist between the PC2 and –Niño4-related warm SATAs over CA in December (**Figures 3A**, **5A**), similarity at some level still exists between the PC2 and –Niño4-related anomalous geopotential height and winds. Furthermore, the abrupt change in the influence of the cold CTP SSTAs on the SATAs in December and January may contribute to the reversal of the SATAs over CA. The results also imply that the cold CTP

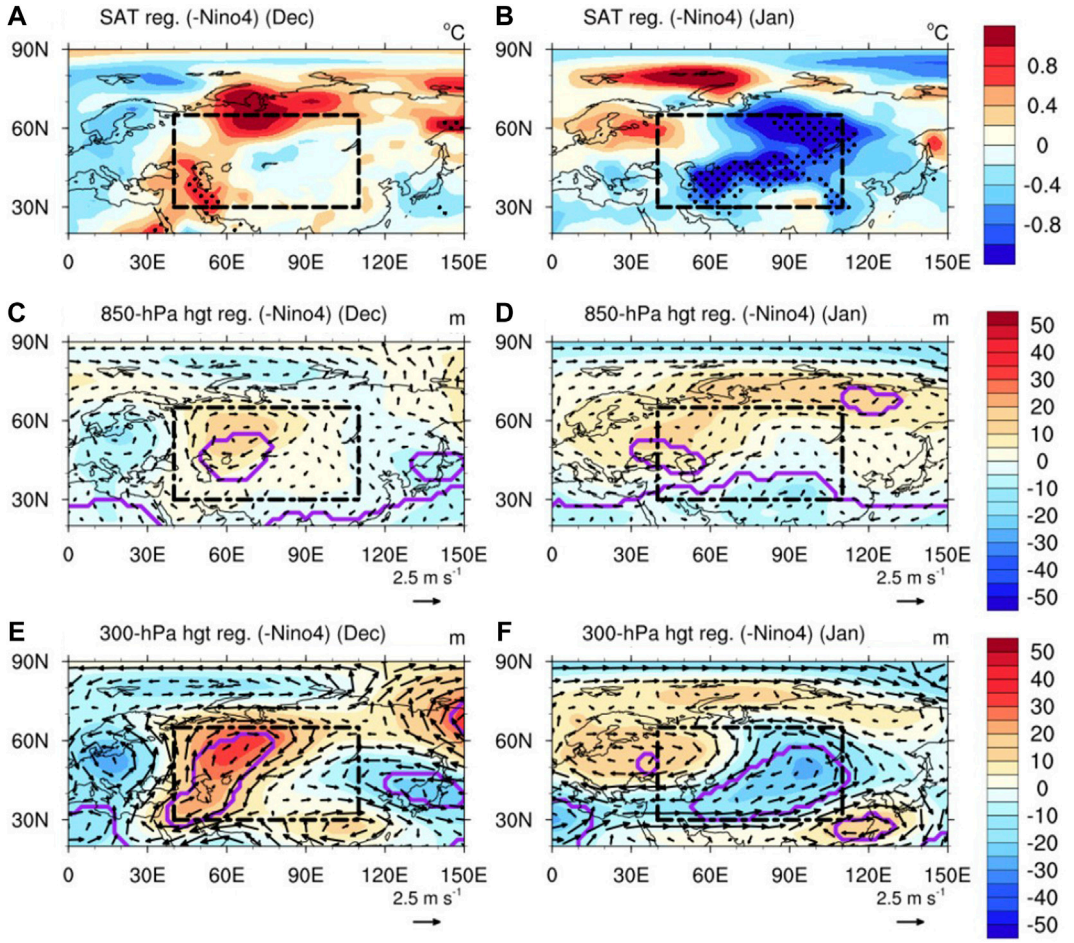

FIGURE 5 | Regressions of December **(A)** SAT (shading; °C) and **(C)** 850 hPa and **(E)** 300 hPa geopotential height (shading; m) and winds (vectors; m s^{-1}) onto the −Niño4 for the period 1979–2017 **(B,D,F)** As in **(A,C,E)** but for January during 1980–2018. The black dashed boxes show the region of CA; anomalies significant at the 95% confidence level are denoted by dots and purple contour lines, as estimated by the Student's *t*-test.

SSTAs may not be the single factor for the reversal of SATAs over CA, however, it is out of the scope of this study but deserves further investigations in the future.

3.3 Possible Mechanisms of the Impacts of Cold CTP SSTAs on the Reversal of SATAs Over CA

To explore the possible physical mechanisms behind the impact of remote SST forcing on the reversal of SATAs between December and January over CA, the −Niño4-related 300 hPa geopotential height anomalies and the wave activity fluxes in December and January are analyzed (**Figure 6**). In December, a wave train extends from the North Pacific to CA, crossing North America and the North Atlantic. This wave train consequently results in the positive geopotential height anomalies over CA (**Figure 6A**). In contrast, in January, the wave train originates from the mid-latitude North Pacific and mainly propagates in the meridional direction (**Figure 6B**). This wave train cannot reach CA to influence the local SATAs. Interestingly, a wave train starting from the North Atlantic could reach CA and result in the local negative geopotential anomalies and SATAs. Therefore, two questions are raised regarding the possible mechanisms underlying the different roles of the wave trains associated with the −Niño4 between December and January: 1) why does the propagation of the wave train from the North Pacific differ between December and January; and 2) how do the cold CTP SSTAs in January cause the negative SATAs over CA in January?

For the first question, the different Gill-type responses to the cold CTP SSTA between December and January may play a key role. The Gill-type response is the stationary Rossby wave response to the tropical SST anomalies (Gill, 1980). The Gill-type response corresponding to the cooling SST anomalies of La Niña winters can be characterized by a pair of low-level anticyclonic anomalies residing at the northern and southern sides of the equator, along with low-level easterly wind anomalies and cyclonic anomalies symmetrical about the equator at the upper level of the troposphere (Yuan and Yan, 2013; Zhang et al., 2015). In **Figure 7**, the Gill-type response to the CTP SSTAs is remarkable: on the one hand, anomalous easterlies and

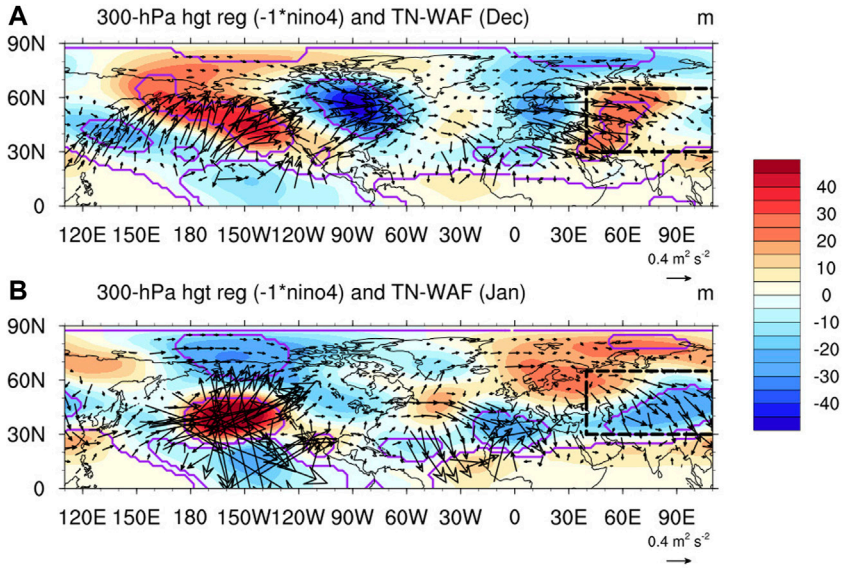

FIGURE 6 | (A) Regression of December 300 hPa geopotential height (shading; m) onto the –Niño4 for the period 1979–2017; and the associated horizonal components of the wave activity flux (vectors; $m^2\ s^{-2}$) **(B)** As in (a) but for January during 1980–2018. Anomalies significant at the 95% confidence level are denoted by purple contour lines, as estimated by the Student's *t*-test.

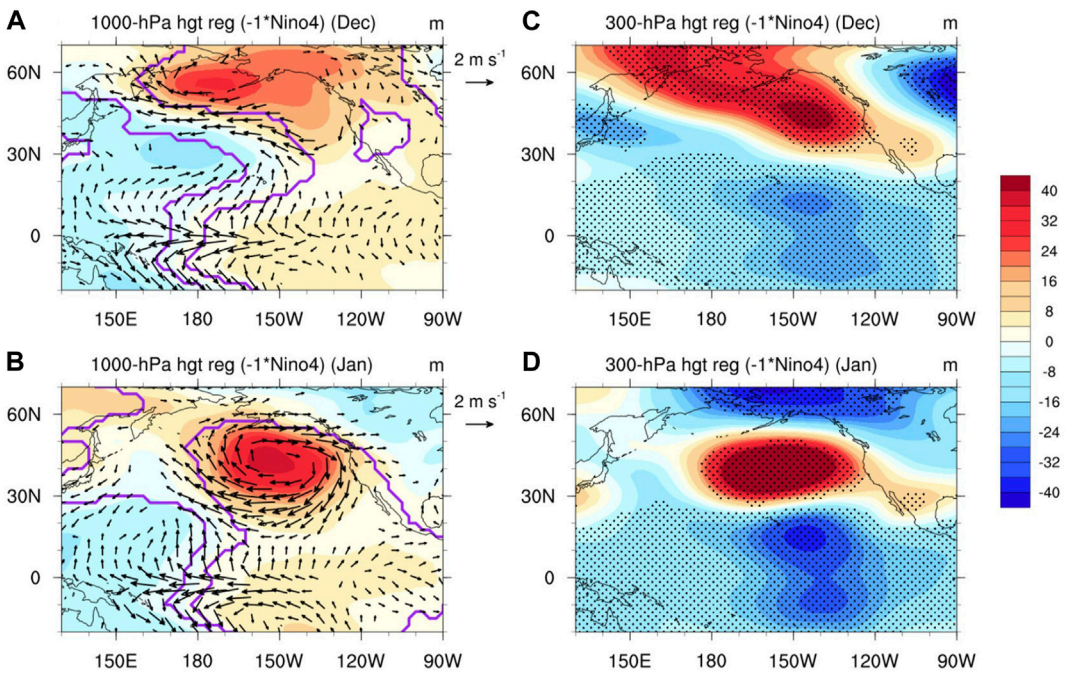

FIGURE 7 | Regressions of the December **(A)** 1,000 hPa geopotential height (shading; m) and winds (vectors; m s^{-1}), and **(C)** 300 hPa geopotential height (shading; m) onto the –Niño4 for the period 1979–2017 over the Pacific **(B,D)** As in (A, C) but for January during 1980–2018. Anomalies significant at the 95% confidence level are denoted by dots and purple contour lines, and vectors represent the anomalous winds significant at the 95% confidence level, as estimated by the Student's *t*-test.

symmetric anticyclones at 1,000 hPa appear around the region (20°S–20°N, 170°E–120°W) in both December and January (**Figures 7A,B**), and the easterly anomalies are relatively stronger in January than in December; whilst on the other hand, in both December and January, a pair of cyclonic anomalies appears over the CTP at 300 hPa, and these

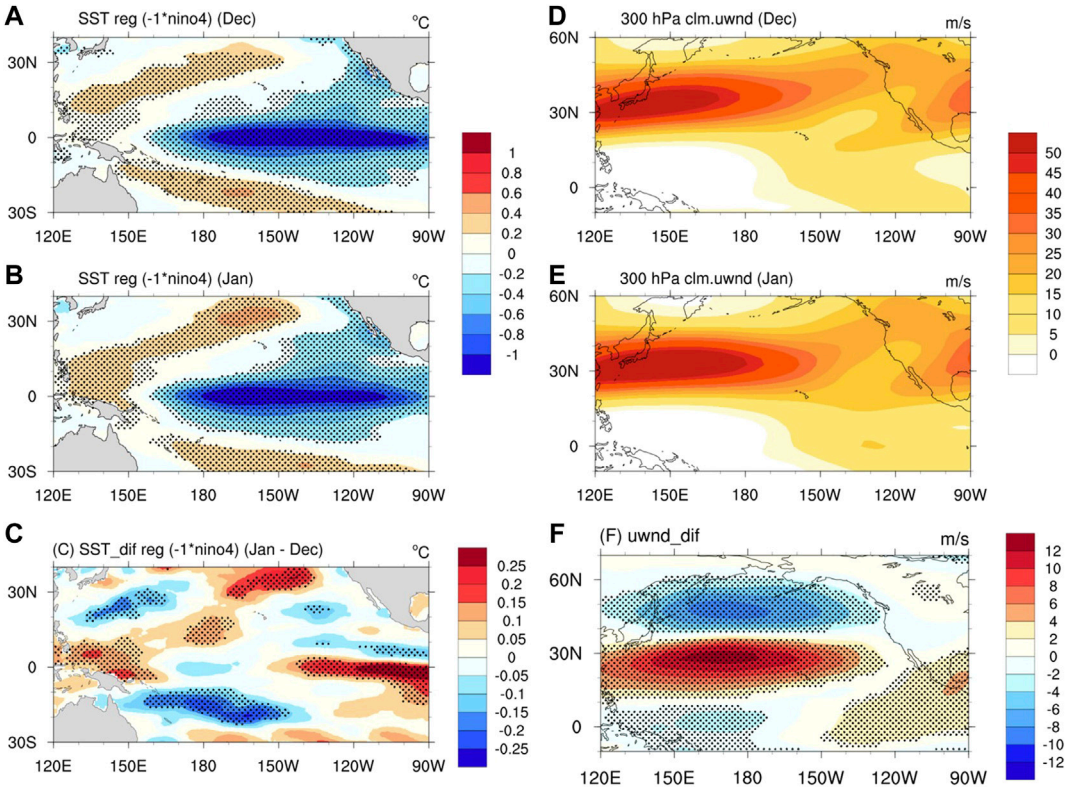

FIGURE 8 | (A) Regressions of December SST over the Pacific onto the –Niño4 (shading; °C) for the period 1979–2017 **(B)** As in (A) but for January during 1980–2018 **(C)**. Regression of the SST difference between January and December over the Pacific onto the –Niño4 (shading; °C) for the period 1979–2017 **(D)** Climatological December 300 hPa zonal wind (shading; m s^{-1}) for the period 1979–2017 **(E)** As in (D) but for January **(F)** Difference in the climatological 300 hPa zonal wind between January and December (shading; m s^{-1}) for the period 1979–2017. Anomalies significant at the 95% confidence level are denoted by dots, as estimated by the Student's *t*-test.

anomalous cyclones in January are much stronger than they are in December (**Figure 7C,D**). The result implies that the Gill-type response to the cold CTP SSTAs in January is stronger than in December.

With the enhanced Gill-type response in January, the influence of cold CTP SSTAs on the extratropical atmosphere over the North Pacific are strengthened. In January, corresponding to the enhanced 300 hPa cyclonic anomalies in the region (0°–20°N, 160°–130°W), stronger positive geopotential height anomalies appear in the region (30°–60°N, 180°–150°W) (**Figure 7C,D**). Consequently, intensified wave activity fluxes are driven by the positive geopotential height anomalies, as seen in **Figure 6**. Also, the more remarkable meridional dipole structure of the geopotential height anomalies over the North Pacific might cause the meridional propagation of the Rossby waves.

Additionally, the reason why the Gill-type response to the cold CTP SSTAs in January is stronger than that in December is explored. Previous studies have revealed that a strengthening of the tropical heating could lead to a stronger Gill-type response (Xing et al., 2014). Besides, Lee et al. (2009) suggested that a stronger and more equatorward jet stream could result in a stronger Gill-type response in the tropical atmosphere, along with stronger responses in the extratropical atmosphere. **Figure 8** shows the CTP SSTI-related SSTAs and the climatological 300 hPa zonal winds in December and January. The cold SSTAs in the CTP region in January are slightly stronger than these in December, but their difference is not statistically significant (**Figure 8A–C**). Additionally, the subtropical jet stream over the North Pacific in January is stronger and situated more towards the equator (**Figure 8D–F**), which may lead to the strengthened Gill-type response in the tropics, as indicated by Lee et al. (2009). Thus, the CTP SSTAs in December and January may excite different Gill-type responses in the tropical atmosphere due to the difference in the climatological jet stream. Subsequently, the different Gill-type and extratropical atmospheric responses finally lead to a different propagation of Rossby waves between December and January.

In terms of the second question, the strong 300 hPa zonal wind anomalies associated with the CTP SSTAs may play a crucial role. In January, significant positive and negative 300 hPa zonal wind anomalies appear in the regions (40°–60°N, 180°–120°W) and (20°–40°N, 180°–120°W), respectively (**Figure 9A**). The meridional structure of the anomalous zonal wind can be linked to the dipole structure of the geopotential height anomalies in the January (**Figure 7D**). Corresponding to the wind anomalies, significant positive and negative STEA

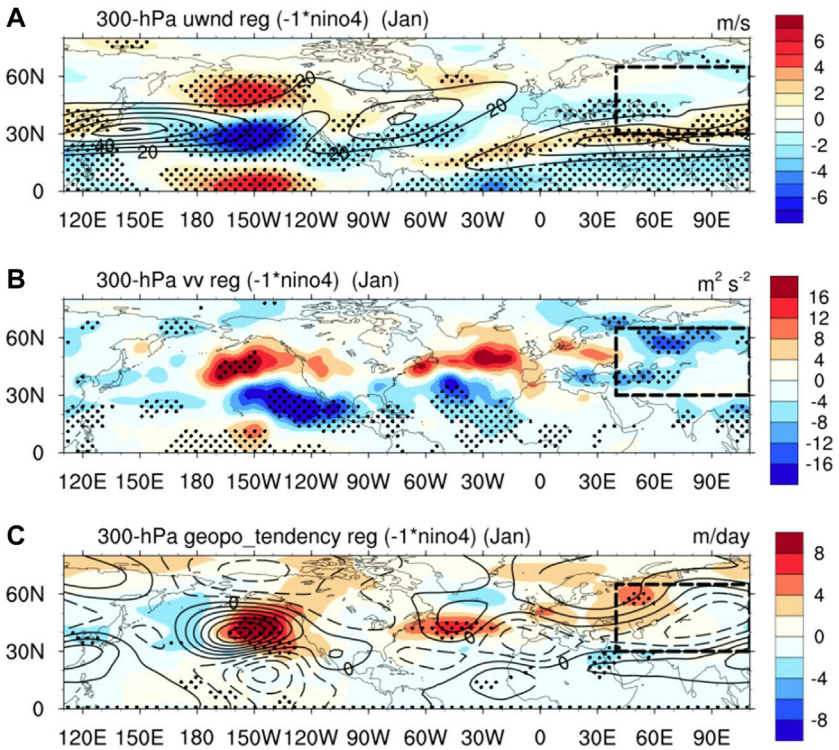

FIGURE 9 | (A) Regression of January 300 hPa zonal wind onto the –Niño4 (shading; m s^{-1}) and the climatological January 300 hPa zonal wind (contours; m s^{-1}) for the period 1980–2018 **(B)** Regression of January 300 hPa STEA onto the –Niño4 (shading; m^2 s^{-2}) for the period 1980–2018 **(C)** Regression of the January 300 hPa eddy-induced geopotential height tendency (shading; m day^{-1}) and geopotential height (contours; m) onto the –Niño4 for the period 1980–2018. In (C), zero contours are omitted and negative values are dashed. The black dashed boxes show the region of CA; anomalies significant at the 95% confidence level are denoted by dots, as estimated by the Student's *t*-test.

anomalies appear over the eastern North Pacific (**Figure 9A,B**). These STEA anomalies can travel eastwards to the North Atlantic via the downstream development of wave packets (Rivière and Orlanski, 2007; Li and Lau 2012a, Li and Lau 2012b). Accordingly, the strength of STEA over the North Atlantic shows non-significant positive anomalies over (40°–60°N, 60°–30°W) and significant negative anomalies over (20°–40°N, 60°–30°W) (**Figure 9B**). Such a dipole structure of STEA anomalies facilitates a positive geopotential height tendency over the region (40°–50°N, 60°–30°W) (Lau and Holopainen 1984), which may lead to the positive geopotential height anomalies associated with the –Niño4 index (**Figure 9C**). Hence, the CTP SSTAs may influence the STEA over the North Atlantic, by which the positive geopotential height over the North Atlantic can be forced, and then the Rossby waves excited by the positive geopotential height can propagate to CA to cause the local cold SATAs in January. Moreover, the positive geopotential height over northwestern CA forced by the anomalous STEA may also contribute to the driving of the Rossby waves and the cold SATAs.

3.4 Validation by Model Experiments

In this section, three experiments were designed to validate the mechanisms given above. The first one forces the model with the climatological seasonal cycle of global SST and sea ice (referred to as Ctrl). Ctrl was integrated for 50°years, and the first 20°years were used for model spin-up and the remaining years were used for analysis. In the second experiment (referred to as Run1), the boundary forcing was changed to the climatological seasonal cycle of global SST with additional SSTAs over the tropical Pacific region (10°S–10°N, 150°E–90°W) from December to the following January. The SSTAs used here were the regressions of the December (January) SST onto the simultaneous –Niño4 index during 1979–2017 (1980–2018), and keeping the same value in December (January). Run1 included 30 members. Each member was integrated from 30 November to 31 January of the following year with the initial conditions taken from Ctrl. The third experiment (referred to as Run2) was similar to Run1, except that the SSTAs added to the climatological seasonal cycle of the global SST in December and January were both from the regression of the December SST onto the –Niño4 index during 1979–2017.

The composite differences in the SAT and 300 hPa geopotential height between Run1 and the control run are given in **Figure 10**. In December, although the SATAs over CA in Run1 are weak and non-significant (**Figure 10A**), the geopotential height in December is similar to the –Niño4 index-related geopotential height anomalies (**Figure 10C**). The Gill-type geopotential height anomalies appear over the tropical Pacific and match with the obvious result. Furthermore, the positive anomalies over the Bering Strait, the negative

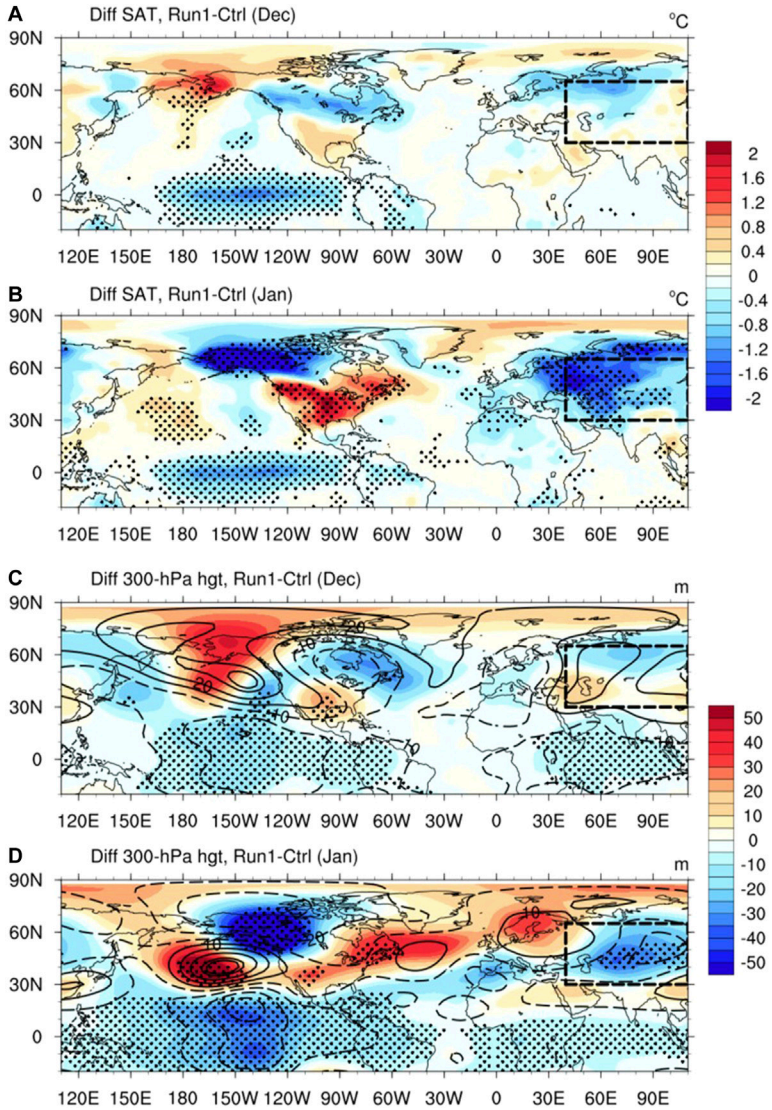

FIGURE 10 | Composite difference in the **(A)** December SAT (shading; °C) and **(C)** geopotential height (shading; m) between Run1 and Ctrl **(B,D)** As in (A, C) but for January. The contours in (C, D) show the regression of the 300 hPa geopotential height onto the −Niño4 index for December during 1979–2017 and January during 1980–2018, respectively, in which zero contours are omitted and negative values are dashed. The black dashed boxes show the region of CA; anomalies significant at the 95% confidence level are denoted by dots, as estimated by the Student's *t*-test.

anomalies over North America, and the weak negative anomalies over western Europe in Run1 correspond to the −Niño4 index-related geopotential height anomalies. Thus, the numerical experiments roughly reproduce the mechanism of the −Niño4 index's impacts on CA in December. In January, strong and significant negative SATAs appear over CA (**Figure 10B**), and the geopotential height anomalies are similar to the observational anomalies (**Figure 10D**). Interestingly, the Gill-type geopotential height anomalies over the tropical Pacific are stronger than in December, as expected. The results from Run1 in December and January support the proposed mechanism. On the one hand, in December, there is a similarity between the geopotential height anomalies and the −Niño4-related geopotential height anomalies, which validates the suggestion that an eastward-propagating Rossby wave train may be excited by the anomalous cold CTP SSTA in December. On the other hand, in January, a stronger Gill-type response in the tropical Pacific is excited by −Niño4-related SSTAs, and may cause significant negative SATAs over CA.

Since the SST forcings used in Run1 in December and January were different, as shown in **Figure 8C**, it is possible that the different responses in Run1 are caused by the difference in the SST forcings. Thus, in Run2, the same SST forcing [the −Niño4-related SSTAs over the region (10°S–10°N, 150°E–90°W) in December] was added in December and January. The composite differences in the SAT and 300 hPa geopotential height between Run2 and Ctrl are given in **Figure 11**. The results closely resemble those of Run1. The similarity between Run1 and Run2 provides further support to the notion that

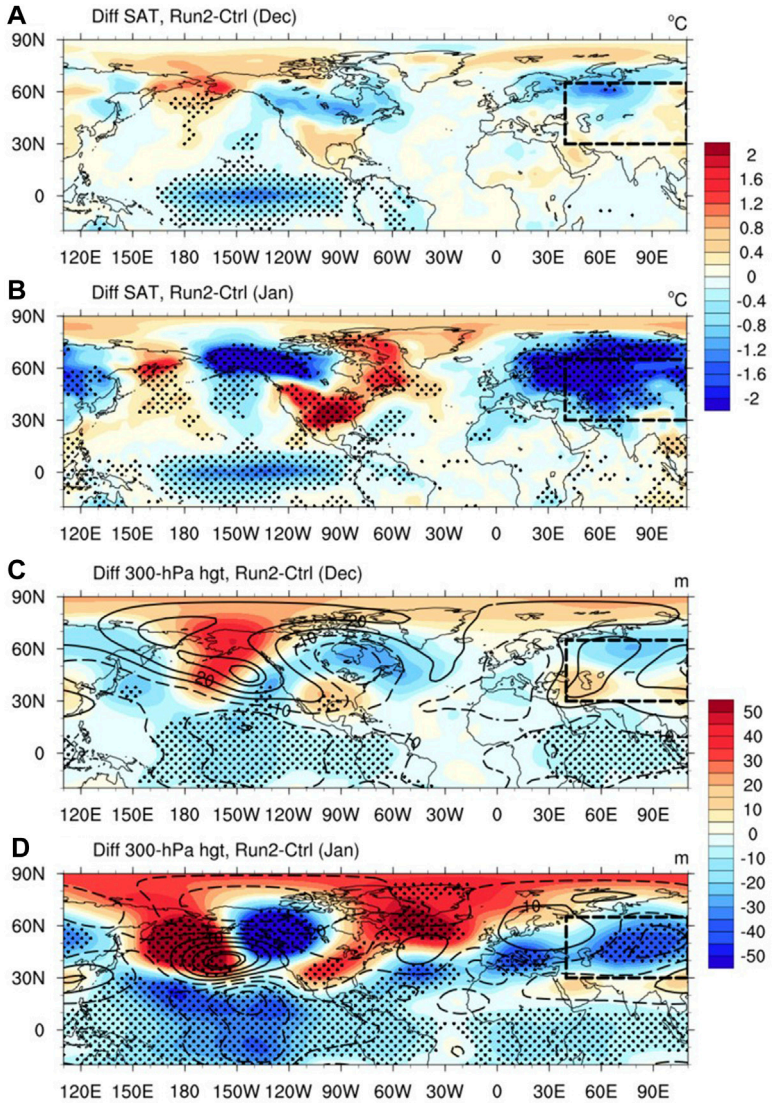

FIGURE 11 | As in **Figure 10** but for Run2.

changing climatological background winds might play an important role in the reversal of the SATAs over CA.

4 CONCLUSION AND DISCUSSION

Subseasonal changes in winter SATAs over CA can cause severe damage in terms of socioeconomic development in this region. In this study, the monthly reversal of the December and January SATAs over CA was investigated.

The MV-EOF analysis method was employed to identify the leading modes of the monthly variation of the SATAs. The second leading mode of MV-EOF represents the monthly reversal of the SATAs, which corresponds to contrasting geopotential height anomalies between December and January (**Figure 3C–F**). The relationship between the MV-EOF2 and remote forcing of the cold CTP SSTAs was studied. Significant negative SSTAs appear over the CTP within the Niño4 region in both December and January, and the −Niño4 index was adopted to represent the variation of the CTP SSTAs (**Figure 4**). The −Niño4-related SATAs and geopotential potential height anomalies were checked. In December, the CTP SSTAs can lead to positive but weak SATAs over western and northern CA, while in January, the CTP SSTAs may lead to strong cold SATAs over CA (**Figure 5**). The abrupt change in the influence of the cold CTP SSTAs on the SATAs in the 2 months can contribute to the reversal of the SATAs over CA.

The mechanisms behind the different impacts of remote SST forcing in December and January were studied, and two interesting phenomena were noticed (**Figure 6**). First, in December, the wave train from the North Pacific can reach CA, while in January the wave train form the North Pacific mainly propagates in the meridional direction and cannot reach CA. Second, the January SATAs of CA are

influenced by the wave train from the North Atlantic. The following research of this study revolved around these two phenomena.

Firstly, the difference between the wave train propagation in December and January was researched. It was found that the negative CTP SSTAs in December and January can excite a Gill-type response in the tropical atmosphere of the Pacific. In December, the Gill-type response can excite eastward-propagating Rossby waves over the North Pacific, which can then directly cause the positive geopotential height anomalies and positive SATAs over CA. In January, as the climatological subtropical jet stream over the North Pacific is stronger and situated more towards the equator, the Gill-type response over the North Pacific is stronger than that in December. The Rossby wave train over the North Pacific propagates mainly in the meridional direction and is unable to reach CA.

Secondly, the process was studied by which the cold CTP SSTAs can cause the cold SATAs over CA in January. The intensified positive and negative wind anomalies in January over the North Pacific can cause stronger STEA, which can extend to the North Atlantic and influence the local STEA. Accordingly, the eddy-induced positive geopotential height anomalies will excite Rossby waves and cause the negative geopotential height anomalies and negative SATAs in January. To validate the mechanism, especially the roles of the SSTAs and changing climatological background winds, two sensitivity experiments were designed. The results roughly reproduced the influence of the cold CTP SSTAs on CA, and therefore lend support to the proposed mechanism.

In this work, the impact of the CTP SSTAs on the reversal of SATAs over CA in December and January was treated as the major remote forcing to be investigated. However, it is also true that the correlation coefficient between the −Niño4 index and PC2 is not large, and the PC2-related SATAs over CA in December are different from the −Niño4-related SATAs and the model results over CA. The differences between the PC2 and −Niño4-related SATAs in December imply that other climatic factors may also roles in the reversal of SATAs over CA. The atmospheric circulation over northern Eurasia could be very important in driving the response of the SATAs over CA. For example, the positive phase of Scandinavian Pattern is associated with cooling over central Russia and western Europe (Bueh and Nakamura, 2007; Liu et al., 2014). Besides, boundary forcings, such as North Atlantic SST, Arctic sea ice and snow cover may also have an influence (Mori et al., 2014; Chen et al., 2019; Chen et al., 2020). For example, Mori et al. (2014) pointed out that the SATAs over Eurasia could be influenced by the Warm Arctic–Cold Continental pattern, which is modulated by the Arctic sea-ice variability. As to the model results, two possible reasons may be responsible the differences between the model results and the PC2-related SATAs in December. First, the performance of the AGCM may be limited for the variability of atmospheric circulation at monthly scale. Second, as discussed above, other possible climatic factors may play a role in the reversal of SATAs over CA, such as the North Atlantic SSTAs. However, the cold CTP SSTAs is the only boundary forcing that are added in our experiment, which may lead to a deviation from the observational results. Though the performance of the AGCM in December is different from our expectation, the sudden cooling in the January is well simulated by the AGCM. The significantly different influence on the SATAs over CA shown in the experiments indicates that the cold CTP SSTAs plays an important role in the reversal of the SATAs over CA. In short, consideration of other factors and careful experimental design are needed to provide a full understanding of the reversal of the SATAs over CA in December and January.

DATA AVAILABILITY STATEMENT

The original contributions presented in the study are included in the article/Supplementary Material, further inquiries can be directed to the corresponding author.

AUTHOR CONTRIBUTIONS

HL: Conceptualization, Methodology, Software, Investigation, Formal Analysis, Writing—Original Draft; KF: Conceptualization, Methodology, Supervision, Validation, Project Administration, Funding Acquisition, Review and Editing HL: Conceptualization, Methodology, Software, Review and Editing ZX: Methodology, Software, Review and Editing.

FUNDING

This research was supported by the National Natural Science Foundation of China (grant number 41730964 and 42088101), the National Key R&D Program of China (grant number 2017YFA0603802), the Innovation Group Project of Southern Marine Science and Engineering Guangdong Laboratory (Zhuhai) (No 311021001).

REFERENCES

Begzsuren, S., Ellis, J. E., Ojima, D. S., Coughenour, M. B., and Chuluun, T. (2004). Livestock Responses to Droughts and Severe winter Weather in the Gobi Three Beauty National Park, Mongolia. *J. Arid Environments* 59 (4), 785–796. doi:10.1016/j.jaridenv.2004.02.001

Bueh, C., and Nakamura, H. (2007). Scandinavian Pattern and its Climatic Impact. *Q.J.R. Meteorol. Soc.* 133 (629), 2117–2131. doi:10.1002/qj.173

Casson, N. J., Contosta, A. R., Burakowski, E. A., Campbell, J. L., Crandall, M. S., Creed, I. F., et al. (2019). Winter Weather Whiplash: Impacts of Meteorological Events Misaligned with Natural and Human Systems in Seasonally Snow-Covered Regions. *Earth's Future* 7 (12), 1434–1450. doi:10.1029/2019EF001224

Cattiaux, J., Vautard, R., Cassou, C., Yiou, P., Masson-Delmotte, V., and Codron, F. (2010). Winter 2010 in Europe: A Cold Extreme in a Warming Climate. *Geophys. Res. Lett.* 37 (20), L20704. doi:10.1029/2010GL044613

Chen, H. W., Alley, R. B., and Zhang, F. (2016). Interannual Arctic Sea Ice Variability and Associated winter Weather Patterns: A Regional Perspective for 1979-2014. *J. Geophys. Res. Atmos.* 121 (24), 14433–14455. doi:10.1002/2016JD024769

Chen, S., Wu, R., and Chen, W. (2019). Enhanced Impact of Arctic Sea Ice Change during Boreal Autumn on the Following spring Arctic Oscillation since the Mid-1990s. *Clim. Dyn.* 53 (9), 5607–5621. doi:10.1007/s00382-019-04886-y

Chen, S., and Wu, R. (2017). Interdecadal Changes in the Relationship Between Interannual Variations of Spring North Atlantic SST and Eurasian Surface Air Temperature. *J. Clim.* 30 (10), 3771–3787. doi:10.1175/jcli-d-16-0477.1

Chen, S., Wu, R., and Chen, W. (2018). Modulation of Spring Northern Tropical Atlantic Sea Surface Temperature on the El Niño-Southern Oscillation-East Asian Summer Monsoon Connection. *Int. J. Climatol.* 38 (13), 5020–5029. doi:10.1002/joc.5710

Chen, S., Wu, R., Chen, W., Hu, K., and Yu, B. (2020). Structure and Dynamics of a Springtime Atmospheric Wave Train over the North Atlantic and Eurasia. *Clim. Dyn.* 54 (11), 5111–5126. doi:10.1007/s00382-020-05274-7

Chen, S., Wu, R., and Liu, Y. (2016). Dominant Modes of Interannual Variability in Eurasian Surface Air Temperature during Boreal Spring. *J. Clim.* 29 (3), 1109–1125. doi:10.1175/jcli-d-15-0524.1

Cohen, J., Saito, K., and Entekhabi, D. (2001). The Role of the Siberian High in Northern Hemisphere Climate Variability. *Geophys. Res. Lett.* 28 (2), 299–302. doi:10.1029/2000gl011927

Cohen, J., Zhang, X., Francis, J., Jung, T., and Yoon, J. (2019). Divergent Consensuses on Arctic Amplification Influence on Midlatitude Severe winter Weather. *Nat. Clim. Change* 10 (6), 1–10. doi:10.1038/s41558-019-0662-y

Czaja, A., and Frankignoul, C. (1999). Influence of the North Atlantic SST on the Atmospheric Circulation. *Geophys. Res. Lett.* 26 (19), 2969–2972. doi:10.1029/1999GL900613

Czaja, A., and Frankignoul, C. (2002). Observed Impact of Atlantic SST Anomalies on the North Atlantic Oscillation. *J. Clim.* 15 (6), 606–623. doi:10.1175/1520-0442(2002)015<0606:oioasa>2.0.co;2

Dai, H., Fan, K., and Liu, J. (2019). Month-to-Month Variability of Winter Temperature over Northeast China Linked to Sea Ice over the Davis Strait-Baffin Bay and the Barents-Kara Sea. *J. Clim.* 32 (19), 6365–6384. doi:10.1175/jcli-d-18-0804.1

Darynova, Z., Maksot, A., Kulmukanova, L., Malekipirbazari, M., Sharifi, H., Torkmahalleh, M. A., et al. (2018). Evaluation of NO2 Column Variations over the Atmosphere of Kazakhstan Using Satellite Data. *J. Appl. Rem. Sens.* 12 (4), 042610. doi:10.1117/1.JRS.12.042610

Feng, J., Chen, W., and Li, Y. (2017). Asymmetry of the Winter Extra-Tropical Teleconnections in the Northern Hemisphere Associated With Two Types of ENSO. *Clim. Dyn.* 48 (7), 2135–2151. doi:10.1007/s00382-016-3196-2

García-Serrano, J., Cassou, C., Douville, H., Giannini, A., and Doblas-Reyes, F. J. (2017). Revisiting the ENSO Teleconnection to the Tropical North Atlantic. *J. Clim.* 30 (17), 6945–6957. doi:10.1175/jcli-d-16-0641.1

Geng, X., Zhang, W., Stuecker, M. F., and Jin, F.-F. (2017). Strong Sub-seasonal Wintertime Cooling over East Asia and Northern Europe Associated with Super El Niño Events. *Sci. Rep.* 7 (1), 3770. doi:10.1038/s41598-017-03977-2

Gill, A. E. (1980). Some Simple Solutions for Heat-Induced Tropical Circulation. *Q. J. R. Meteorol. Soc.* 106 (449), 447–462. doi:10.1002/qj.49710644905

Gong, D.-Y., and Ho, C.-H. (2002). The Siberian High and Climate Change over Middle to High Latitude Asia. *Theor. Appl. Climatology* 72 (1), 1–9. doi:10.1007/s007040200008

Graf, H.-F., and Zanchettin, D. (2012). Central Pacific El Niño, the "subtropical Bridge," and Eurasian Climate. *J. Geophys. Res.* 117 (D1), D01102. doi:10.1029/2011JD016493

Grjibovski, A., Kozhakhmetova, G., Kosbayeva, A., and Menne, B. (2013). Associations between Air Temperature and Daily Suicide Counts in Astana, Kazakhstan. *Medicina* 49 (8), 59. doi:10.3390/medicina49080059

Hirahara, S., Ishii, M., and Fukuda, Y. (2014). Centennial-Scale Sea Surface Temperature Analysis and its Uncertainty. *J. Clim.* 27 (1), 57–75. doi:10.1175/jcli-d-12-00837.1

Hurrell, J. W., and Van Loon, H. (1997). Decadal Variations in Climate Associated with the North Atlantic Oscillation. *Clim. Change* 36 (3), 301–326. doi:10.1023/A:1005314315270

Kalnay, E., Kanamitsu, M., Kistler, R., Collins, W., Deaven, D., Gandin, L., et al. (1996). The NCEP/NCAR 40-Year Reanalysis Project. *Bull. Amer. Meteorol. Soc.* 77 (3), 437–471. doi:10.1175/1520-0477(1996)077<0437:tnyrp>2.0.co;2

Kerven, C., Alimaev, I. I., Behnke, R., Davidson, G., Franchois, L., Malmakov, N., et al. (2004). Retraction and Expansion of Flock Mobility in Central Asia: Costs and Consequences. *Afr. J. Range Forage Sci.* 21 (3), 159–169. doi:10.2989/10220110409485848

Kim, D.-W., Byun, H.-R., and Lee, Y.-I. (2005). The Long-Term Changes of Siberian High and winter Climate over the Northern Hemisphere. *Asia-Pacific J. Atmos. Sci.* 41 (2-1), 275–283.

Kug, J.-S., Jin, F.-F., and An, S.-I. (2009). Two Types of El Niño Events: Cold Tongue El Niño and Warm Pool El Niño. *J. Clim.* 22 (6), 1499–1515. doi:10.1175/2008jcli2624.1

Lau, N.-C., and Holopainen, E. O. (1984). Transient Eddy Forcing of the Time-Mean Flow as Identified by Geopotential Tendencies. *J. Atmos. Sci.* 41 (3), 313–328. doi:10.1175/1520-0469(1984)041<0313:tefott>2.0.co;2

Lau, N.-C., and Nath, M. J. (2014). Model Simulation and Projection of European Heat Waves in Present-Day and Future Climates. *J. Clim.* 27 (10), 3713–3730. doi:10.1175/jcli-d-13-00284.1

Lee, S.-K., Wang, C., and Mapes, B. E. (2009). A Simple Atmospheric Model of the Local and Teleconnection Responses to Tropical Heating Anomalies. *J. Clim.* 22 (2), 272–284. doi:10.1175/2008jcli2303.1

Li, C., Zhang, C., Luo, G., Chen, X., Maisupova, B., Madaminov, A. A., et al. (2015). Carbon Stock and its Responses to Climate Change in C Entral A Sia. *Glob. Change Biol.* 21 (5), 1951–1967. doi:10.1111/gcb.12846

Li, H., Fan, K., He, S., Liu, Y., Yuan, X., and Wang, H. (2021). Intensified Impacts of Central Pacific ENSO on the Reversal of December and January Surface Air Temperature Anomaly over China since 1997. *J. Clim.* 34 (5), 1601–1618. doi:10.1175/jcli-d-20-0048.1

Li, Y., and Lau, N.-C. (2012a). Contributions of Downstream Eddy Development to the Teleconnection between ENSO and the Atmospheric Circulation over the North Atlantic. *J. Clim.* 25 (14), 4993–5010. doi:10.1175/jcli-d-11-00377.1

Li, Y., and Lau, N.-C. (2012b). Impact of ENSO on the Atmospheric Variability over the North Atlantic in Late Winter-Role of Transient Eddies. *J. Clim.* 25 (1), 320–342. doi:10.1175/jcli-d-11-00037.1

Liebmann, B., and Smith, C. A. (1996). Description of a Complete (Interpolated) Outgoing Longwave Radiation Dataset. *Bull. Am. Meteorol. Soc.* 77 (6), 1275–1277.

Lioubimtseva, E., and Henebry, G. M. (2009). Climate and Environmental Change in Arid Central Asia: Impacts, Vulnerability, and Adaptations. *J. Arid Environments* 73 (11), 963–977. doi:10.1016/j.jaridenv.2009.04.022

Liu, Y., Wang, L., Zhou, W., and Chen, W. (2014). Three Eurasian Teleconnection Patterns: Spatial Structures, Temporal Variability, and Associated winter Climate Anomalies. *Clim. Dyn.* 42 (11), 2817–2839. doi:10.1007/s00382-014-2163-z

Lü, Z., He, S., Li, F., and Wang, H. (2019). Impacts of the Autumn Arctic Sea Ice on the Intraseasonal Reversal of the Winter Siberian High. *Adv. Atmos. Sci.* 36 (2), 173–188. doi:10.1007/s00376-017-8089-8

Mirzabaev, A. (2013). Impacts of Weather Variability and Climate Change on Agricultural Revenues in Central Asia. *Q. J. Int. Agric.* 52 (3), 1–16. doi:10.22004/ag.econ.173648

Miyazaki, C., and Yasunari, T. (2008). Dominant Interannual and Decadal Variability of Winter Surface Air Temperature over Asia and the Surrounding Oceans. *J. Clim.* 21 (6), 1371–1386. doi:10.1175/2007jcli1845.1

Mori, M., Watanabe, M., Shiogama, H., Inoue, J., and Kimoto, M. (2014). Robust Arctic Sea-Ice Influence on the Frequent Eurasian Cold winters in Past Decades. *Nat. Geosci* 7 (12), 869–873. doi:10.1038/ngeo2277

North, G. R., Bell, T. L., Cahalan, R. F., and Moeng, F. J. (1982). Sampling Errors in the Estimation of Empirical Orthogonal Functions. *Mon. Wea. Rev.* 110 (7), 699–706. doi:10.1175/1520-0493(1982)110<0699:seiteo>2.0.co;2

Nyssanbayeva, A. S., Cherednichenko, A. V., Cherednichenko, V. S., Abayev, N. N., and Madibekov, A. S. (2019). Bioclimatic Conditions of the winter Months in Western Kazakhstan and Their Dynamics in Relation to Climate Change. *Int. J. Biometeorol.* 63 (5), 659–669. doi:10.1007/s00484-018-1513-7

Peterson, T. C., and Vose, R. S. (1997). An Overview of the Global Historical Climatology Network Temperature Database. *Bull. Amer. Meteorol. Soc.* 78 (12), 2837–2849. doi:10.1175/1520-0477(1997)078<2837:aootgh>2.0.co;2

Ren, X., Yang, X., and Chu, C. (2010). Seasonal Variations of the Synoptic-Scale Transient Eddy Activity and Polar Front Jet over East Asia. *Front. Jet Over East. Asia* 23 (12), 3222–3233. doi:10.1175/2009jcli3225.1

Rivière, G., and Orlanski, I. (2007). Characteristics of the Atlantic Storm-Track Eddy Activity and its Relation with the North Atlantic Oscillation. *J. Atmos. Sci.* 64 (2), 241–266. doi:10.1175/jas3850.1

Roeckner, E., Bäuml, G., Bonaventura, L., Brokopf, R., Esch, M., Giorgetta, M. S., et al. (2003). The Atmospheric General Circulation Model ECHAM 5. PART I: Model Description. Max Planck Institute for Meteorology. MPI-Report No. 349.

Saito, K., Cohen, J., and Entekhabi, D. (2001). Evolution of Atmospheric Response to Early-Season Eurasian Snow Cover Anomalies. *Mon. Wea. Rev.* 129 (11), 2746–2760. doi:10.1175/1520-0493(2001)129<2746:eoarte>2.0.co;2

Takaya, K., and Nakamura, H. (2001). A Formulation of a Phase-independent Wave-Activity Flux for Stationary and Migratory Quasigeostrophic Eddies on a Zonally Varying Basic Flow. *J. Atmos. Sci.* 58 (6), 608–627. doi:10.1175/1520-0469(2001)058<0608:afoapi>2.0.co;2

Thompson, D. W. J., and Wallace, J. M. (2000). Annular Modes in the Extratropical Circulation. Part I: Month-To-Month Variability*. *J. Clim.* 13 (5), 1000–1016. doi:10.1175/1520-0442(2000)013<1000:amitec>2.0.co;2

Tian, B., and Fan, K. (2015). A Skillful Prediction Model for Winter NAO Based on Atlantic Sea Surface Temperature and Eurasian Snow Cover. *Weather Forecast.* 30 (1), 197–205. doi:10.1175/waf-d-14-00100.1

Vihma, T. (2014). Effects of Arctic Sea Ice Decline on Weather and Climate: A Review. *Surv. Geophys.* 35 (5), 1175–1214. doi:10.1007/s10712-014-9284-0

Wang, B. (1992). The Vertical Structure and Development of the ENSO Anomaly Mode during 1979-1989. *J. Atmos. Sci.* 49 (8), 698–712. doi:10.1175/1520-0469(1992)049<0698:tvsado>2.0.co;2

Wang, L., Liu, Y., Zhang, Y., Chen, W., and Chen, S. (2019). Time-varying Structure of the Wintertime Eurasian Pattern: Role of the North Atlantic Sea Surface Temperature and Atmospheric Mean Flow. *Clim. Dyn.* 52 (3), 2467–2479. doi:10.1007/s00382-018-4261-9

Wu, B., Su, J., and Zhang, R. (2011). Effects of Autumn-Winter Arctic Sea Ice on Winter Siberian High. *Chi. Sci. Bull.* 56 (30), 3220. doi:10.1007/s11434-011-4696-4

Wu, R., and Chen, S. (2020). What Leads to Persisting Surface Air Temperature Anomalies from Winter to Following Spring over Mid- to High-Latitude Eurasia? *J. Clim.* 33 (14), 5861–5883. doi:10.1175/jcli-d-19-0819.1

Xing, N., Li, J., and Li, Y. (2014). Response of the Tropical Atmosphere to Isolated Equatorially Asymmetric Heating. *Chin. J. Atmos. Sci.* 38 (6), 1147–1158. doi:10.3878/j.issn.1006-9895.1401.13275

Xu, X., Li, F., He, S., and Wang, H. (2018). Subseasonal Reversal of East Asian Surface Temperature Variability in Winter 2014/15. *Adv. Atmos. Sci.* 35 (6), 737–752. doi:10.1007/s00376-017-7059-5

Yuan, Y., and Yan, H. (2013). Different Types of La Niña Events and Different Responses of the Tropical Atmosphere. *Chin. Sci. Bull.* 58 (3), 406–415. doi:10.1007/s11434-012-5423-5

Zafren, K. (2013). Frostbite: Prevention and Initial Management. *High Alt. Med. Biol.* 14 (1), 9–12. doi:10.1089/ham.2012.1114

Zhang, W., Wang, L., Xiang, B., Qi, L., and He, J. (2015). Impacts of Two Types of La Niña on the NAO during Boreal winter. *Clim. Dyn.* 44 (5), 1351–1366. doi:10.1007/s00382-014-2155-z

Zwiers, F. W., and von Storch, H. (1995). Taking Serial Correlation into Account in Tests of the Mean. *J. Clim.* 8 (2), 336–351. doi:10.1175/1520-0442(1995)008<0336:tsciai>2.0.co;2

Conflict of Interest: The authors declare that the research was conducted in the absence of any commercial or financial relationships that could be construed as a potential conflict of interest.

frontiers in Earth Science

ORIGINAL RESEARCH
published: 31 March 2022
doi: 10.3389/feart.2022.866241

Atlantic Multidecadal Oscillation Modulates the Relation of ENSO With the Precipitation in the Central-Western Indian Ocean

Chiyu Zhao[1,2,3], *Xin Geng*[1,2]* *and Li Qi*[1,2]

[1]CIC-FEMD/ILCEC, Key Laboratory of Meteorological Disaster of Ministry of Education (KLME), Nanjing University of Information Science and Technology, Nanjing, China, [2]School of Atmospheric Sciences, Nanjing University of Information Science and Technology, Nanjing, China, [3]Shaoxing Meteorological Burea, Shaoxing, China

It is well known that the El Niño-Southern Oscillation (ENSO) could affect the precipitation anomalies in the central-western Indian Ocean (CWIP) through modifying the Walker circulation, with an El Niño generally accompanied by an enhanced CWIP. In this study, we find that this positive association is modulated by the Atlantic Multidecadal Oscillation (AMO). When ENSO and AMO are out-of-phase combinations (i.e., AMO-/El Niño and AMO+/La Niña), the CWIP is significantly stronger than that when they are in-phase cooperated. It is suggested that the AMO's modulating effect mainly comprises two pathways that influence ENSO's linkage with the CWIP. On one hand, AMO could modulate the SST variability in the central-eastern tropical Pacific with a stronger ENSO SST amplitude during its negative phase, thus influencing the ENSO-CWIP relationship. On the other hand, AMO is associated with a multidecadal atmospheric variation in the Walker circulation. The weakened circulation during the negative AMO phase favors an anomalous ascending flow over the central-western Indian Ocean, thereby favoring an enhanced CWIP there. Therefore, El Niño is accompanied by a more pronounced CWIP during the negative AMO phase compared to that during a positive AMO phase. For La Niña episodes, however, these two pathways have opposite modulation effects. Although AMO+/La Niña is weaker than AMO-/La Niña, the accompanied CWIP is relatively stronger as an multidecadal dry background induced by the Atlantic warming reinforces the negative CWIP anomaly generated by La Niña. We here highlight that the AMO decadal forcing needs to be considered when investigating the Indian Ocean atmospheric variabilities during ENSO events.

Keywords: enso, Indian ocean precipitation, walker circulation, atlantic multidecadal oscillation, teleconnection

OPEN ACCESS

Edited by:
Hong-Li Ren,
Chinese Academy of Meteorological Sciences, China

Reviewed by:
Youichi Kamae,
University of Tsukuba, Japan
Sen Zhao,
University of Hawaii at Manoa, United States

***Correspondence:**
Xin Geng
gengxin@nuist.edu.cn

Specialty section:
This article was submitted to Atmospheric Science, a section of the journal Frontiers in Earth Science

Received: *31 January 2022*
Accepted: *28 February 2022*
Published: *31 March 2022*

Citation:
Zhao C, Geng X and Qi L (2022) Atlantic Multidecadal Oscillation Modulates the Relation of ENSO With the Precipitation in the Central-Western Indian Ocean. Front. Earth Sci. 10:866241. doi: 10.3389/feart.2022.866241

INTRODUCTION

As the predominant year-to-year climate variability on the planet, El Niño-Southern Oscillation (ENSO) arises through the coupled air-sea interactions in the tropical Pacific. Although rooted in the tropical Pacific, ENSO can lead to global atmospheric circulation and patterns of climate variability worldwide (e.g., van Loon and Madden, 1981; Ropelewski and Halpert, 1987; Trenberth et al., 1998; Trenberth and Caron, 2000; McPhaden et al., 2006). When El Niño events occur, the atmospheric anomalies are first felt in the tropical Pacific. The warm sea surface temperature (SST) anomalies

cause the edge of the Pacific warm pool extending eastward, leading to a reorganization of tropical atmospheric convection with the heating source moving farther east of its normal position. Thus, anomalous ascending motions and wet conditions occur in the central-eastern Pacific, while subsidence and precipitation deficits emerge in the west, weakening the Walker circulation (Ropelewski and Halpert, 1987). These reorganizations of the Walker circulation and atmospheric convection are further responsible for generating remote atmospheric or SST teleconnections (e.g., Klein et al., 1999; Lau and Nath, 2003). For example, the eastward shift of the Walker cell during El Niño events induces anomalous subsidence over the central-western Indian Ocean (Trenberth et al., 1998; Xie et al., 2016; Wang, 2019), reducing precipitation and cloudiness there with anticyclonic anomalies, which contribute to increasing SST with a warm Indian Ocean basin mode (IOBM) pattern through both enhanced downward solar and reduced latent upward heat fluxes (Klein et al., 1999; Lau and Nath, 2003; Tokinaga and Tanimoto, 2004).

However, observations have shown that ENSO teleconnections exhibit considerable multi-scale spatio-temporal variabilities (e.g., Wang et al., 2000; Mariotti et al., 2002; Chen et al., 2014; Geng et al., 2017; 2020). For instance, the anomalous western North Pacific (WNP) anticyclone, which bridges ENSO and the East Asian monsoon, is detected to have been weakened since the mid-1990s (Chen et al., 2014; Geng et al., 2020). The decadal variations in ENSO teleconnections are demonstrated to be closely associated with the change of ENSO properties modulated by interdecadal natural variabilities (e.g., Lu and Dong, 2008; Zhang et al., 2014; Geng et al., 2020). It is argued that the Pacific Decadal Oscillation (PDO) could play some role in modulating ENSO decadal behaviors (Fedorov and Philander, 2000, 2001; Verdon and Franks, 2006; Kravtsov, 2012; Chung and Li, 2013) and thus modifying ENSO teleconnections (Feng et al., 2014; Watanabe and Yamazaki, 2014; Liu et al., 2021). However, these viewpoints are challenged by the argument that the Pacific multidecadal mean state changes could result from averaging over the skewed ENSO system (Schopf and Burgman, 2006) and thus a substantial fraction of the PDO signal may be caused by ENSO (Alexander et al., 2002; Newman et al., 2003; Wang et al., 2012; Di Lorenzo et al., 2015).

As the basin-wide SST mode in the North Atlantic region with a period of 60–80 years, the Atlantic Multidecadal Oscillation (AMO) has also been widely proposed as an important forcing modulating ENSO's decadal variabilities (Dong et al., 2006; Dong and Sutton, 2007; Kang et al., 2014; Yu et al., 2015; Levine et al., 2017; Wang et al., 2017; Cai et al., 2019; Wang, 2019). A multidecadal Atlantic warming is associated with strengthened Walker circulation and trade winds in the western and central tropical Pacific. This background change is conducive to a deepened thermocline and weakened vertical stratification in the equatorial Pacific, which weakens the coupled instability via which ENSO events grow (Zebiak and Cane, 1987; Jin et al., 2006), thus reducing the ENSO SST amplitude (Dong et al., 2006; Dong and Sutton, 2007; Timmermann et al., 2007; Li et al., 2016; Levine et al., 2017; Gong et al., 2020). In addition, there may also exists a physical linkage between the North Atlantic warming and the zonal structure change of El Niño SST anomalies (Yu et al., 2015). Correspondingly, ENSO teleconnections are also found to be modulated by the AMO through modifying the amplitude or zonal structure of ENSO SST anomalies (e.g., Lu and Dong., 2008; Chen et al., 2014; Geng et al., 2017, 2020).

Although previous studies have demonstrated that ENSO could affect the central-western Indian Ocean precipitation (CWIP), but the nonstationary features of this teleconnection have not been sufficiently elucidated. In particular, previous studies have revealed that ENSO amplitude and spatial pattern is modulated by the AMO forcing on decadal time scales (e.g., Dong et al., 2006; Kang et al., 2014; Gong et al., 2020), it is interesting to explore whether the relation of ENSO with the CWIP is modulated by the AMO. Because of a larger amplitude of ENSO SST anomaly in the negative AMO phase, the CWIP anomaly during ENSO mature winters is expected to be stronger than those in the positive phase. However, in this paper, we find that the intensity of CWIP anomaly during ENSO winters is not necessarily consistent with the decadal amplitude changes in the ENSO SST anomaly. This mismatch between ENSO SST and CWIP anomaly can be largely attributed to AMO's another modulating pathway through generating a multidecadal atmospheric variation in the Walker circulation. In the remainder of this paper, *Data and Methodology* describes the utilized datasets, methodologies, and model simulations. In *The Relation of ENSO With the CWIP Modulated by AMO*, we explore the modulation effect of the relation between ENSO and CWIP by the AMO. Next, based on observations and a suit of idealized pacemaker experiments from a coupled general circulation model (CGCM), the possible mechanisms that can explain this AMO modulation effect are presented in *Possible Mechanisms*. *Conclusion and Discussion* presents the main conclusion discussions.

DATA AND METHODOLOGY

Datasets

We primarily utilize monthly datasets (1948–2019) in this work. Global SST is derived from the National Oceanic and Atmospheric Administration (NOAA) Extended Reconstructed SST analysis, version 3 (ERSST, Smith et al., 2008). Atmospheric circulations are analyzed based on the National Centers for the Environmental Prediction/National Center for the Atmospheric Research (NCEP/NCAR) reanalysis data (Kalnay et al., 1996). The precipitation anomalies are examined using the NOAA's precipitation reconstruction dataset (PREC) (Chen et al., 2002). To further test our results, we also utilize the atmospheric circulations from the NOAA-CIRES-DOE 20th Century Reanalysis version 3 (20CRv3) (Slivinski et al., 2019) and the precipitation provided by the Climate Prediction Center (CPC) Merged Analysis of Precipitation (CMAP) (Xie et al., 1997). The horizontal spatial resolutions are $2 \times 2^{\circ}$ for the SST dataset and $2.5 \times 2.5^{\circ}$ for the atmospheric circulation and precipitation datasets, respectively.

TABLE 1 | El Niño and La Niña events for the 1948–2018 period.

El Niño events	La Niña events
1951, 1953, 1957, 1958, 1963, 1965, 1968, 1969, 1972, 1976, 1977, 1982, 1986, 1987, 1991, 1994, 1997, 2002, 2004, 2006, 2009, 2015, 2018	1949, 1950, 1954, 1955, 1964, 1967, 1970, 1971, 1973, 1974, 1975, 1984, 1988, 1995, 1998, 1999, 2000, 2005, 2007, 2008, 2010, 2011, 2012, 2013, 2016, 2017

Methodologies

Several climatic indices are used to facilitate our analysis. We define an AMO index as the area-averaged SST anomalies within the domain of 0°–60°N and 0°–80°W (Trenberth and Shea, 2006). A 10-year low-pass fast Fourier transform (FFT) filter is utilized to extract its inherent decadal variability (conclusion does not change when other filters, such as 9- and 11-year low-pass filters, is used). Based on the time evolution of the AMO index, we select the 1948–1967 and 1998–2018 periods as positive AMO phases and the 1968–1997 period as a negative AMO phase according to the filtered AMO index. The Niño-3.4 index, which is calculated as the area-averaged SST anomalies in the Niño-3.4 region (5°S–5°N, 120°–170°W), is adopted to describe ENSO intensity. Following conventions, ENSO events are defined by a threshold of ±0.5 standard deviation of the Niño-3.4 index during the boreal winter season (December-February: DJF). With this method, we can identify 23 El Niño and 26 La Niña events (**Table 1**). Note that all the datasets are analyzed for the boreal winter season (December-February: DJF) and the winter of 1948 represents December 1948-February 1949. All the above indices are normalized before our investigations. The linear trends have been removed from all anomalies to avoid possible interferences associated with the long-term trend. Statistical significance tests are all performed based on the two-tailed Student's *t* test. It should be mentioned that the filtered decadal data are highly autocorrelated and thus the effective number of degrees of freedom, N^{eff}, is adjusted and calculated as:

$$\frac{1}{N^{eff}} \approx \frac{1}{N} + \frac{2}{N}\sum_{j=1}^{N}\frac{N-j}{N}\rho_{xx}(j)\rho_{yy}(j)$$

where N is the sample size and $\rho_{xx}(j)$ and $\rho_{yy}(j)$ are the autocorrelations of two sampled time series at time lag-j (Pyper and Peterman, 1998).

Model Simulations

Due to the relatively short observational period, we further verify our hypotheses by employing the idealized Atlantic Multidecadal Variability (AMV, referred to as the Atlantic Multidecadal Oscillation or AMO in this paper) pacemaker simulations with the Earth System coupled climate model EC-Earth3 (EC-Earth3; Döscher et al., 2021), which were performed as part of the Decadal Climate Prediction Project (DCPP). Following the DCPP-C protocol (Boer et al., 2016), two sets of ensemble simulations have been performed, in which time-invariant SST anomalies corresponding to the warm (AMO+) and cold (AMO-) phases of the observed AMO were imposed upon the 12-months model climatology over the North Atlantic (from 10° to 65°N) using SST nudging. The model is allowed to evolve freely outside this target region. An 8°-wide buffer zone is applied at the edge of the nudging area to minimize shocks and to suppress instabilities due to artificial SST gradients. All the external forcings are set to their preindustrial values. An ensemble of 32 members is conducted for each AMO phase and each realization is integrated over a 10-year period. The first 11 months of integration are considered as a spin-up period and are discarded for the current analysis. We can thus obtain 9 winters in each ensemble of the simulations. More extensive description of the experimental protocol is provided in the technical note for AMV DCPP-C simulations: https://www.wcrpclimate.org/wgsip/documents/Tech-Note-1.pdf. We note that, when calculating anomalies in this suit of model simulations, the average of AMO+ and AMO- experiments for each realization is considered as the corresponding reference state. If the DJF SST departure from the reference state is greater than 0.5°C or less than −0.5°C, we define it as an ENSO winter.

THE RELATION OF ENSO WITH THE CWIP MODULATED BY AMO

We first display the regressed precipitation and atmospheric anomalies onto the DJF Niño-3.4 index from 1948 to 2018 in **Figure 1**. It can be seen that an El Niño winter is accompanied by anomalous ascending flows in the central-eastern tropical Pacific and in the western tropical Indian Ocean. And the western tropical Pacific is controlled by an evident descending flow (**Figure 1B**). This Walker circulation reorganization leads to low-level easterly wind anomalies over the tropical Indian Ocean, causing enhanced precipitation in the central-western part of the Ocean (**Figure 1A**). To show the temporal variability, we define a CWIP index as the area-average precipitation anomalies in the region of 30°S-6°N, 50°E-90°E and then display its time evolution with the Niño-3.4 index in **Figure 2**. It is clear that the CWIP index exhibits conspicuous interannual variability, which is significantly correlated the Niño-3.4 index. Their temporal correlation coefficient reaches up to 0.50 (exceeding the 99% confidence level), suggesting that the CWIP intensity is positively proportional to the ENSO SST amplitude. These results are in well agreements with many previous studies (e.g., Xie et al., 2002; Kao and Yu, 2009; Liu and Alexander, 2007).

Previous studies have suggested that ENSO SST amplitude shows considerable decadal variations and is significantly modulated by the AMO. ENSO events during the negative AMO phase are generally stronger than those during the positive phase (e.g., Dong et al., 2006; Kang et al., 2014; Gong et al., 2020). Thus, it is compelling to expect that the CWIP anomaly in ENSO winters is stronger during the AMO negative

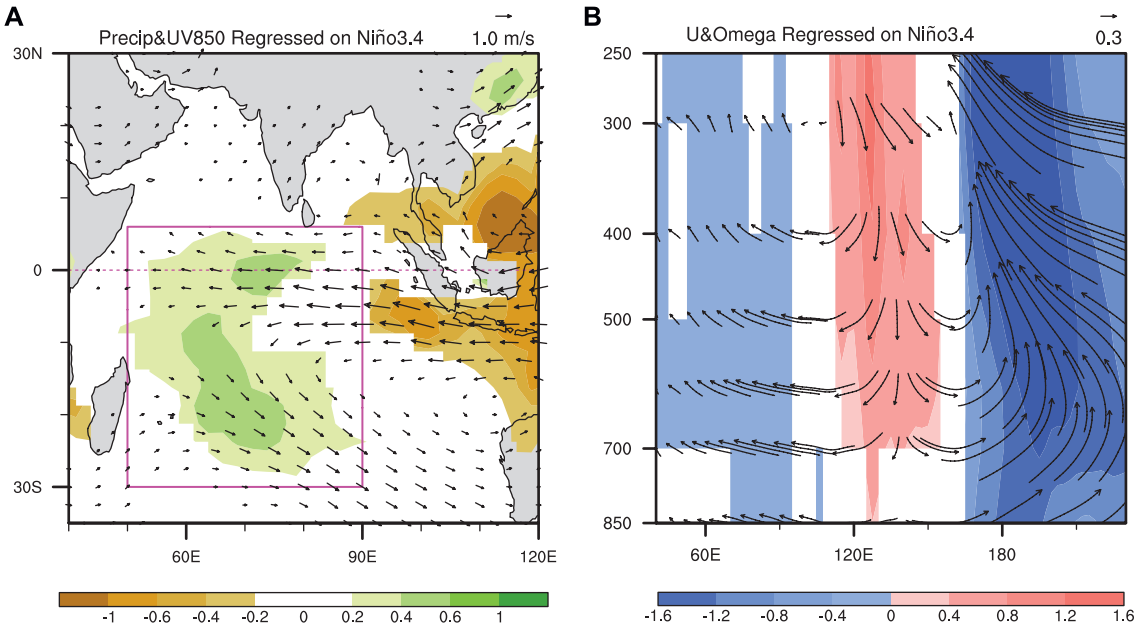

FIGURE 1 | Regressed DJF anomalous **(A)** 850-hPa wind (vectors in m s^{-1}), precipitation (shading in mm day^{-1}), **(B)** Walker circulation and vertical velocity (shading in Pa s^{-1}) onto the Niño-3.4 index for the 1948–2018 period. Note that the vertical velocity anomalies are multiplied by a factor of -100 for better visualization. The magenta box outlines the domain used as the definition of the CWIP index. The precipitation, 850-hPa wind and vertical velocity anomalies are only displayed when they are significant at the 90% confidence level.

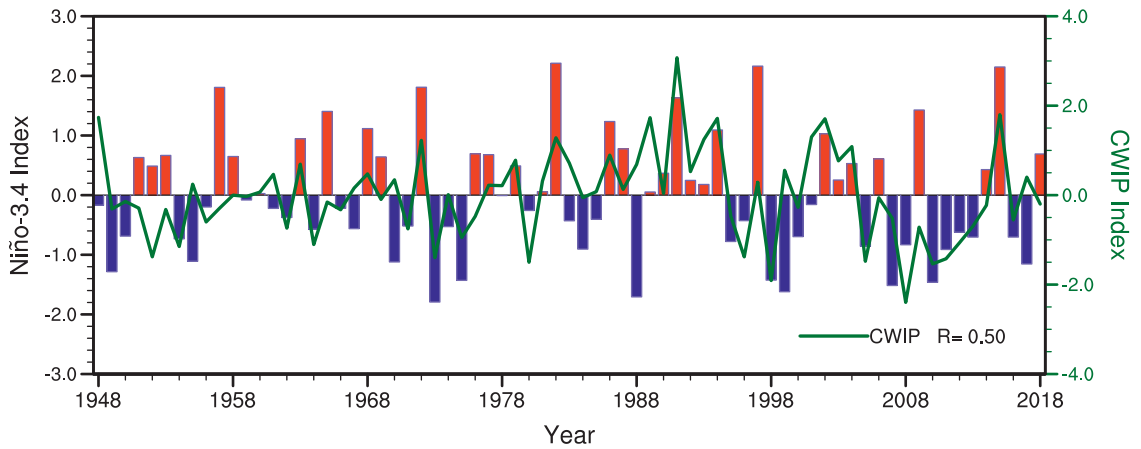

FIGURE 2 | Time evolution of the DJF Niño-3.4 (bar) and CWIP (green curve) indices for the 1948–2018 period. The correlation coefficient (R) is also displayed and is significant at the 99% confidence level.

phase. To verify this hypothesis, we first categorize the ENSO events into four types according to the AMO phase, that is, El Niño events with a positive AMO phase (AMO+/El Niño), El Niño events with a negative AMO phase (AMO-/El Niño), La Niña events with a positive AMO phase (AMO+/La Niña), and La Niña events with a negative AMO phase (AMO-/La Niña) (**Table 2**). And then display the composite SST (**Figure 3**) and precipitation (**Figure 5**) anomalies for these four cases. It can be seen that, compared with those during the positive AMO phase, both El Niño and La Niña events during the negative AMO phase mature with weaker SST anomalies in the central-eastern tropical Pacific. The composite Niño-3.4 indices in AMO+/El Niño, AMO-/El Niño, AMO+/La Niña and AMO-/La Niña winters are 1.05, 1.28, −0.95 and −1.11, respectively (**Figure 4**), consistent well with previous studies (Dong et al., 2006; Kang et al., 2014; Gong et al., 2020). In accordance with this decadal amplitude change in ENSO SST anomaly due to AMO modulation, we speculate that the accompanied CWIP anomaly during ENSO

TABLE 2 | Category of ENSO events for the 1948–2018 period according to the AMO phase.

AMO+/El Niño	AMO-/El Niño	AMO+/La Niña	AMO-/La Niña
1951, 1953, 1957, 1958, 1963, 1965, 2002, 2004, 2006, 2009, 2015, 2018	1968, 1969, 1972, 1976, 1977, 1982, 1986, 1987, 1991, 1994, 1997	1949, 1950, 1954, 1955, 1964, 1967, 1998, 1999, 2000, 2005, 2007, 2008, 2010, 2011, 2012, 2013, 2016, 2017	1970, 1971, 1973, 1974, 1975, 1984, 1988, 1995

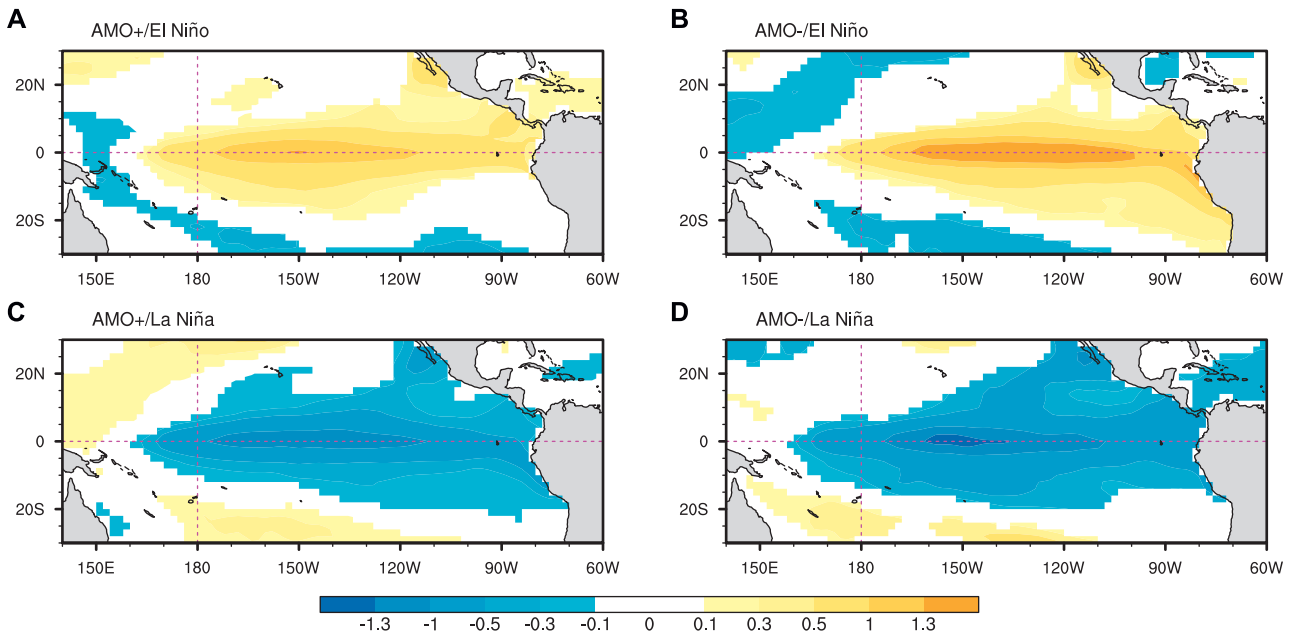

FIGURE 3 | Composite SST anomalies (shading in°C) during the **(A)** AMO+/El Niño, **(B)** AMO-/El Niño, **(C)** AMO+/La Niña, and **(D)** AMO-/La Niña boreal winters. The SST anomalies are only displayed when they are significant at the 90% confidence level.

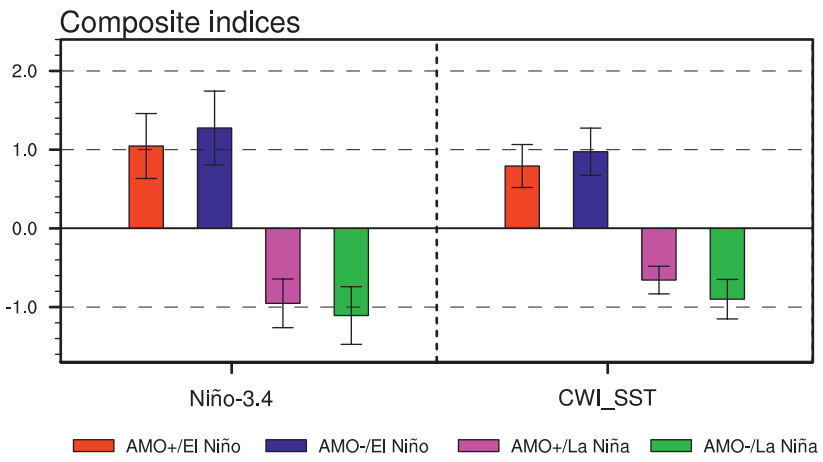

FIGURE 4 | Composite Niño-3.4 and central-western Indian Ocean SST (30°S-6°N, 50°E-90°E) indices during the AMO+/El Niño (red bar), AMO-/El Niño (blue bar), AMO+/La Niña (magenta bar), and AMO-/La Niña (green bar) boreal winters. The solid bars indicate the composites exceeding the 90% confidence level. The error bars represent one standard deviation for the indices during four ENSO cases.

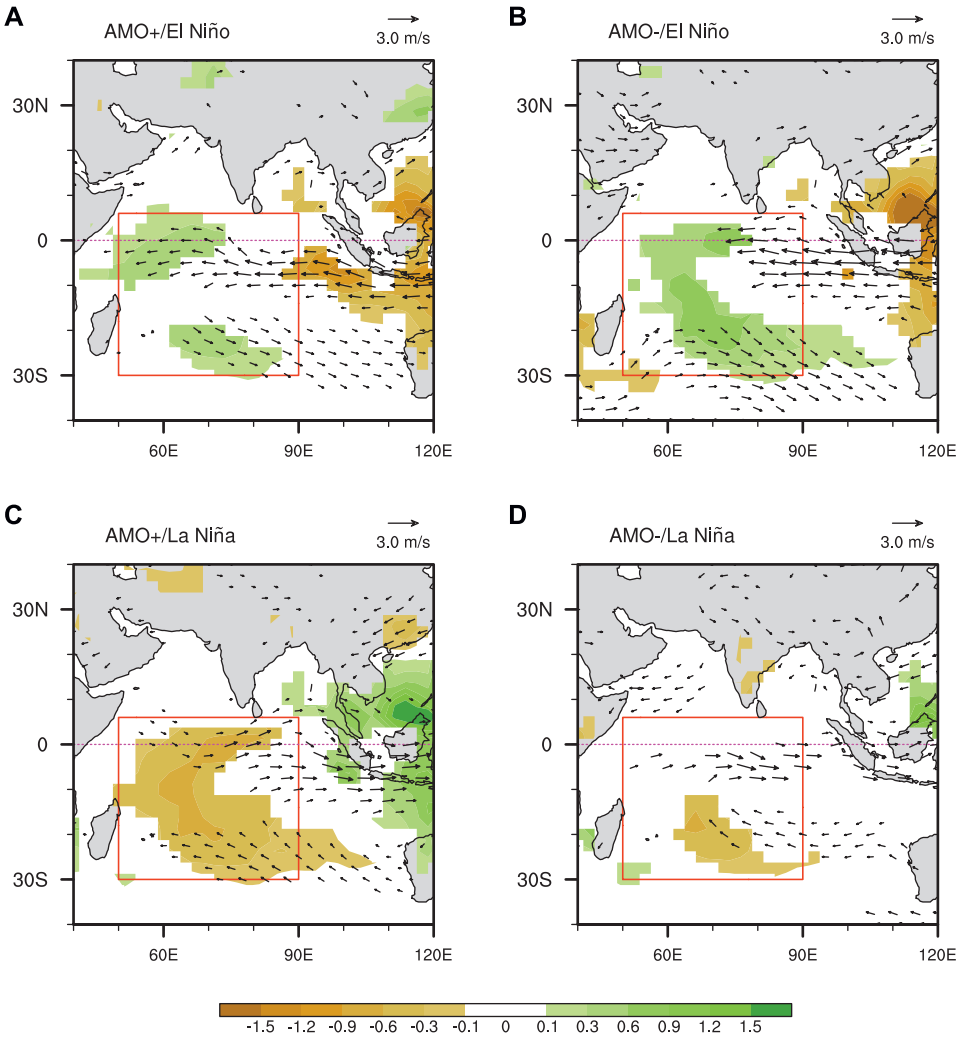

FIGURE 5 | Composite 850-hPa wind (vectors in m s^{-1}) and precipitation (shading in mm day^{-1}) anomalies during the **(A)** AMO+/El Niño, **(B)** AMO-/El Niño, **(C)** AMO+/La Niña, and **(D)** AMO-/La Niña boreal winters. The red box outlines the domain used as the definition of the CWIP index. The wind and precipitation anomalies are only displayed when they are significant at the 90% confidence level.

winters exhibit similar intensity difference. However, an unexpected result is obtained when checking the composite precipitation anomalies (**Figure 5**). For El Niño episodes, the DJF CWIP anomalies are more pronounced during the negative AMO phase compared to those during the positive phase. The composite CWIP indices for the AMO+/El Niño and AMO-/El Niño cases are 0.27 and 0.79 respectively (**Figure 9**), corresponding well to ENSO SST amplitude difference for these two cases. In contrast, La Niña winters during the negative AMO phase are accompanied by a weaker CWIP (**Figures 5C,D**), although their Niño-3.4 SST anomalies are stronger than those during the positive phase (**Figure 4**). In other words, the intensity difference of the CWIP anomalies does not match the amplitude difference of La Niña tropical Pacific SST anomalies associated with the AMO modulation.

Then, to examine the possible roles of local air-sea interaction, the Indian Ocean local SST indices (30°S-6°N, 50°E-90°E) during the four cases are also displayed in **Figure 4**. They show similar features as the Niño-3.4 indices. The SST anomaly in the tropical Indian Ocean is stronger for AMO-/La Niña winters, inconsistent with the weaker CWIP anomaly, either. It seems that, apart from via modifying ENSO-related SST amplitudes, AMO may also modulate the relation of ENSO with the CWIP in a different pathway.

POSSIBLE MECHANISMS

Previous studies have shown that the AMO are closely connected with the climate variabilities in Indian Ocean region (e.g., Sun et al., 2019; Xie et al., 2021). A positive AMO could generate an anomalous descending flow in the central Indian Ocean via Atlantic-Indian Ocean multidecadal atmospheric teleconnections (Xie et al., 2021). Therefore, we speculate that

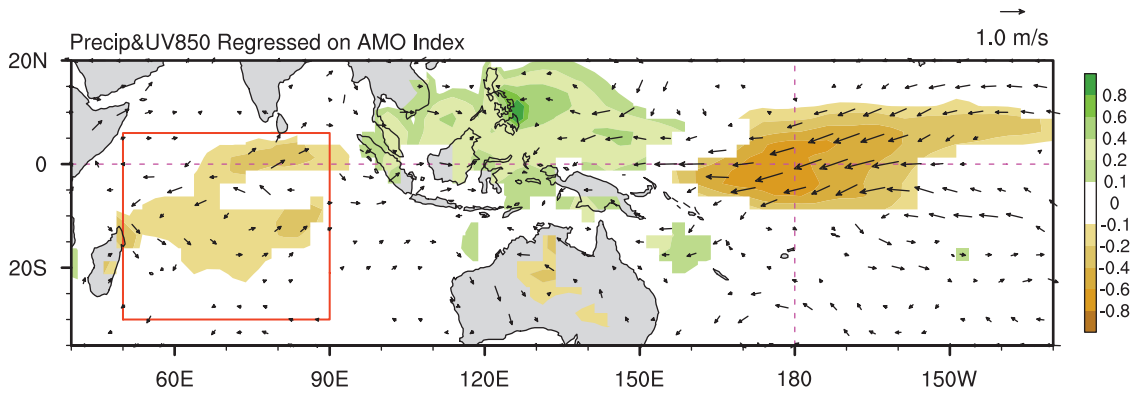

FIGURE 6 | Regressed DJF 850-hPa wind (vectors in m s^{-1}) and precipitation (shading in mm day^{-1}) anomalies onto the AMO index for the 1948–2018 period. The red box outlines the domain used as the definition of the CWIP index. The precipitation and 850-hPa wind anomalies are only displayed when they are significant at the 90% confidence level.

there may also exist an atmospheric pathway through which AMO modifies the relation of ENSO with the CWIP. **Figure 6** shows the regression patterns of DJF precipitation anomalies onto the AMO index. We can see that the precipitation anomalies in tropical Pacific and central-western Indian Ocean are both significantly associated with AMO. A positive AMO favors weakened precipitation anomalies in the central tropical Pacific and in the central-western Indian Ocean, but leads to strengthened precipitation anomalies in the western tropical Pacific. The anomalies are generally reversed during a negative AMO phase.

To understand how the AMO physically affects the CWIP multidecadal variability, we display the regression profiles of DJF Walker circulation onto the AMO index in **Figure 7**. An Atlantic SST warming is accompanied by anomalous ascending flows in the western equatorial Atlantic and western equatorial Pacific regions. Meanwhile, descending flows can be observed over the central-eastern equatorial Pacific and central-western Indian Ocean. As a result of the local descending flows over the central-western Indian Ocean, the CWIP is reduced. These results are well consistent with previous studies (McGregor et al., 2014; Xie et al., 2021). Previous studies have demonstrated that the AMO is also positively correlated with the SST anomalies in the WNP region through extratropical inter-basin atmospheric teleconnections (Sun et al., 2017; 2021). During the positive AMO phase, the induced WNP warming may establish positive feedback with the anomalous Walker circulation, which could also play a role in AMO's influence on the CWIP. This can also explain why we observe a relatively stronger WNP SST anomaly in the AMO-/El Niño and AMO+/La Niña winters in **Figure 3**. Nevertheless, by comparing **Figure 1** with **Figures 6**, **7**, we can find that the tropical Walker circulation and CWIP anomalies are significantly associated with both ENSO and AMO. But the impacts seem to be opposite in phase. An El Niño and a negative AMO favor ascending flows and enhanced precipitation anomalies in the central-western Indian Ocean, while La Niña events and positive AMO phases are conducive to atmospheric sinking motions and reduced precipitation

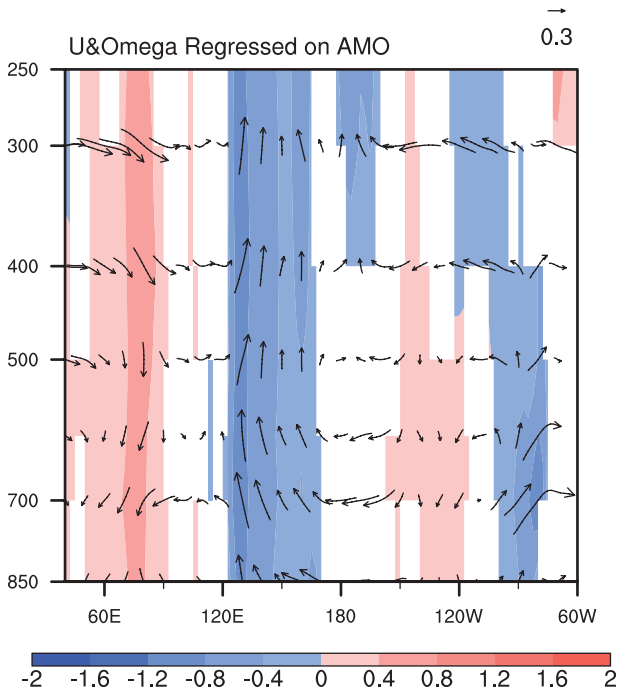

FIGURE 7 | Regressed DJF Walker circulation and vertical velocity (shading in Pa s^{-1}) anomalies onto the AMO index for the 1948–2018 period. Note that the vertical velocity anomalies are multiplied by a factor of −100 for better visualization and are displayed only when they are significant at the 90% confidence level.

anomalies there. As a result, compared with those during the positive AMO phase, El Niño winters during the negative AMO phase are accompanied by more robust ascending motions the precipitation anomalies due to their in-phase impacts (**Figures 8A,B**). This amplitude difference of the atmospheric anomalies between AMO+/El Niño and AMO-/El Niño winters are further reinforced because stronger El Niño events in the negative AMO phase (**Figures 3A,B**) also leads to more robust ascending

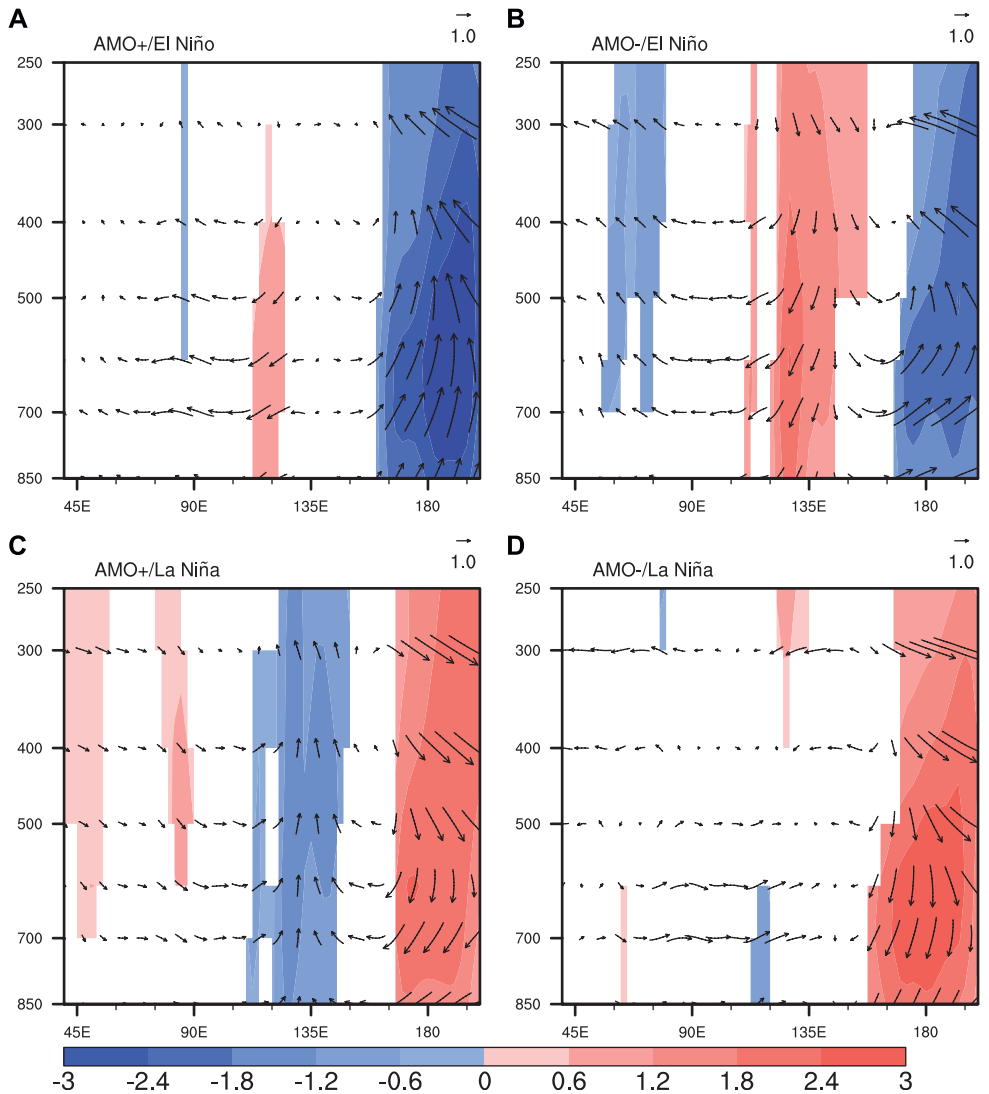

FIGURE 8 | Composite Walker circulation and vertical velocity (shading in Pa s^{-1}) anomalies during the **(A)** AMO+/El Niño, **(B)** AMO-/El Niño, **(C)** AMO+/La Niña, and **(D)** AMO-/La Niña boreal winters. Note that the anomalous vertical velocity anomalies are multiplied by a factor of −100 for better visualization and are displayed only when they are significant at the 90% confidence level.

motions and stronger CWIP. On the other hand, although La Niña events in the negative AMO phase are stronger than those in the positive phase (**Figures 3C,D**), the atmospheric perturbations induced by La Niña anomalous SST are partly counteracted by the opposite impacts by the remote Atlantic multidecadal forcing, thereby resulting in weaker anomaly amplitudes (**Figure 8D**). In comparison, AMO+/La Niña winters are accompanied by stronger descending flows and precipitation anomalies in the central-western Indian Ocean due to the in-phase influences from ENSO and AMO SST forcings (**Figure 8C**). These results suggest that the AMO may exert two different pathways modifying the ENSO-CWIP relationship. While AMO's indirect modulation effect on the relation of ENSO with the CWIP is through modifying the ENSO SST anomaly amplitude, AMO's direct influence is via generating a multidecadal atmospheric variation in the Walker circulation, which leads to the mismatch between intensities of La Niña anomalous SST and the accompanied CWIP anomaly.

We next compare the composite DJF CWIP indices for the four cases based on the original (i.e., observational), single-factor (Niño-3.4 index) and two-factor (Niño-3.4 and AMO indices) reconstructed anomalies in **Figure 9**. When only the Niño-3.4 index is considered, the reconstructed DJF CWIP anomalies during ENSO events are stronger in the AMO negative phase because of a stronger ENSO SST anomaly amplitude, which is consistent with our observed composite results for El Niño winters, suggesting a role of AMO's indirect modulation effect via modifying the ENSO SST anomaly amplitude. This effect can be quantificationally expressed by the difference between the AMO+/El Niño and AMO-/El Niño (or the AMO+/La Niña and

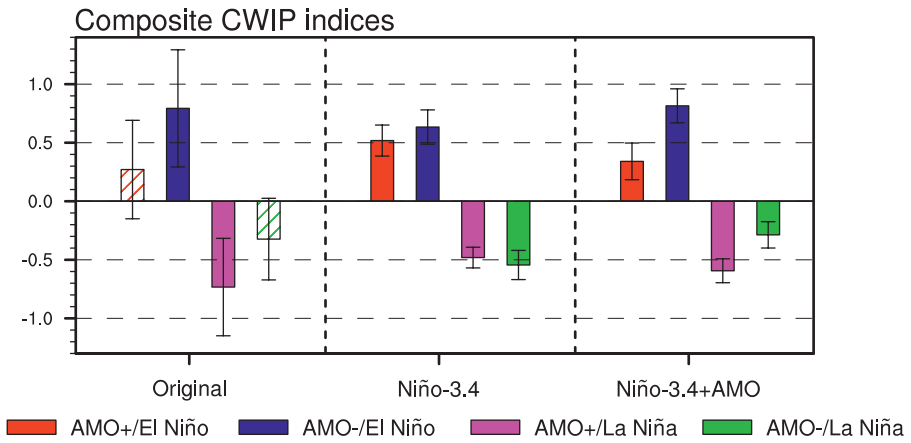

FIGURE 9 | Composite CWIP indices based on the original, single-factor (i.e., Niño-3.4 index) and two-factor (i.e., Niño-3.4 and AMO indices) reconstructed anomalies for the AMO+/El Niño (red bar), AMO-/El Niño (blue curve), AMO+/La Niña (magenta bar), and AMO-/La Niña (green bar) boreal winters. The solid bars indicate the composites significant at the 90% confidence level. The error bars represent one standard deviation for the indices during four ENSO cases.

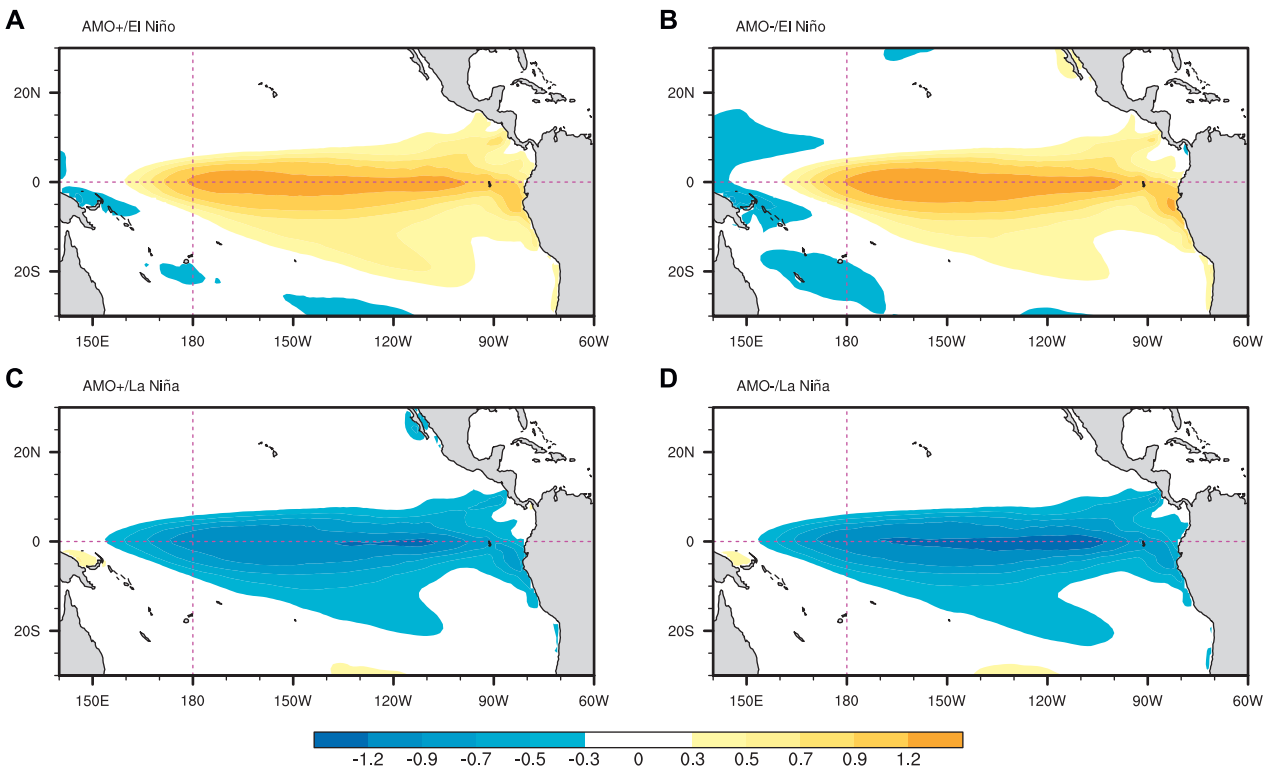

FIGURE 10 | The same as **Figure 3** but for the composite SST anomalies based on the EC-Earth3 DCPP-C simulations.

AMO-/La Niña) composites based on this single-factor (Niño-3.4) reconstructed CWIP index, which are −0.11 and −0.06 for El Niño and La Niña winters, respectively. However, for La Niña episodes, the single-factor reconstructed composite CWIP indices are inconsistent with the observational results, which indicates that pure ENSO SST impacts cannot explain why the CWIP anomaly in AMO+/La Niña winters is stronger than that in AMO-/La Niña winters. Only when the AMO decadal influence is considered together can the composite CWIP anomalies for the four ENSO cases show better agreements with the observational

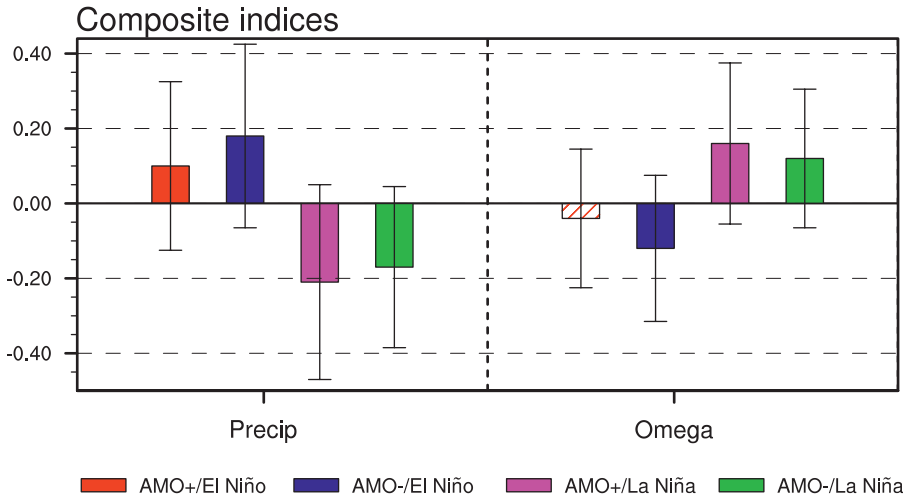

FIGURE 11 | Composite anomalous precipitation and vertical velocity indices in central-western Indian Ocean (30°S-6°N, 50°E-90°E) for the AMO+/El Niño (red bar), AMO-/El Niño (blue curve), AMO+/La Niña (magenta bar), and AMO-/La Niña (green bar) boreal winters in the EC-Earth3 DCPP-C simulations. The solid bars indicate that the composite significant at the 90% confidence level. The error bars represent one standard deviation for the indices during four ENSO cases.

results. To quantitatively express this AMO direct decadal modulation, we first subtract the single-factor reconstructed composite CWIP indices from the two-factor reconstructed composite CWIP indices for these four ENSO cases (i.e., −0.18, 0.18, −0.11, and 0.27 respectively for AMO+/El Niño, AMO-/El Niño, AMO+/La Niña, and AMO-/La Niña winters). Then, we calculate the differences between the AMO+/El Niño and AMO-/El Niño values (or the AMO+/La Niña and AMO-/La Niña values), which are −0.36 and −0.38 for El Niño and La Niña, respectively. By comparing the direct and indirect AMO effects on the CWIP anomaly during ENSO winters, we further suggest that the AMO's direct decadal modulation pathway through modifying the Walker circulation plays a key role in causing the observed relation of ENSO with the CWIP.

To further consolidate our conclusion, we conduct a parallel analysis based on the atmospheric circulations derived from the NOAA-CIRES-DOE 20CRv3 dataset (**Supplementary Figures S1–S5**). It should be noted that the obtained Walker circulation anomalies induced by ENSO and AMO in the Indian Ocean (**Supplementary Figures S1B, S4**) are slightly weaker than the results based on the NCEP/NCAR dataset (**Figures 1B**, **7**), which may be related to the different schemes of data assimilation or model performance of these two reanalysis datasets (Yang et al., 2022). Despite some discrepancy, the features of precipitation and atmospheric circulation anomalies based on this NOAA-CIRES-DOE 20CRv3 dataset remain qualitatively unchanged compared to the NCEP/NCAR results. We also use the precipitation dataset from the CPC CMAP to test our hypotheses. Although the time period is relatively short (i.e., 1979–2018), similar AMO's modulation effect can also be qualitatively reproduced (**Supplementary Figures S6–S9**). Next, we use a suit of idealized AMO pacemaker simulations with the coupled model EC-Earth3 that comply with the Model Intercomparison phase six (CMIP6)/DCPP-C protocol (Boer et al., 2016, see *Data and Methodology* for details). The ENSO events in each AMO + or AMO- realization is first identified, and then the spatial distributions of composite SST anomaly for the four ENSO cases in all AMO + or AMO- realizations are displayed in **Figure 10**. We can see that in the AMO- simulations, both El Niño and La Niña events are stronger than those in the AMO- experiments, which is consistent with the observational results. The simulated DJF atmospheric anomalies in the central-western Indian Ocean for the four cased are then displayed in **Figure 11**. Despite a relatively large spreads in the EC-Earth3 DCPP-C model simulations, both the vertical velocity and the precipitation anomalies in the central-western Indian Ocean are also relatively stronger in AMO-/El Niño and AMO+/La Niña winters, qualitatively consistent with the observational results. This consistency between the observations and model experiments further increases our confidence for the aforementioned hypothesis about the AMO modulation effects on DJF ENSO-CWIP relationship.

CONCLUSION AND DISCUSSION

It has been well known that ENSO can exert significant impacts on the CWIP via modifying the Walker circulation. Based on both observations and a suit of coupled model idealized pacemaker simulations, the present study demonstrates that this positive ENSO-CWIP association is modulated of by the AMO. We suggest that AMO's modulation effects include two pathways. On the one hand, AMO could affect ENSO SST variability through "atmospheric bridge-thermocline feedback" (e.g., Dong et al., 2006; Dong and Lu, 2013; Gong et al., 2020). During a negative AMO phase, ENSO events mature with stronger SST anomalies in the central-eastern tropical Pacific.

Therefore, the relation of ENSO with the CWIP should be enhanced during the negative AMO phase, with stronger CWIP anomalies in the AMO-/El Niño and AMO-/La Niña winters. However, we find that the CWIP anomalies of ENSO winters during different AMO phases are not necessarily consistent with the ENSO SST amplitude changes. While El Niño in the negative AMO phase corresponds to stronger CWIP anomalies due to its stronger central-eastern tropical Pacific SST anomaly than that in the positive AMO phase, a different picture is observed for La Niña. Compared with those in the positive AMO phase, La Niña events in the negative AMO phase are accompanied by a weaker CWIP, although their SST anomalies in the central-eastern tropical Pacific are stronger. There exists a mismatch between the intensities of La Niña tropical SST and central-western Indian Ocean atmospheric anomalies. Strong La Niña SST anomaly during the negative AMO phase does not necessarily concur with strong CWIP anomalies.

We suggest that this mismatch for La Niña events are largely attributed to AMO's another direct decadal modulation pathway through the atmospheric teleconnection in Walker circulation. Besides the significant relationship with ENSO on the interannual time scale, The DJF CWIP anomaly is also significantly associated with the AMO SST forcing on decadal time scales. But the influences from AMO and ENSO are opposite in phase. An AMO warming could generate an anomalous descending flow in the central-western Indian Ocean through changing the Walker circulation, thus reducing the CWIP anomalies there. Therefore, when La Niña coincides with a positive AMO, the anomalous descending flows in central-western Indian Ocean is superimposed, which gives rise to a stronger negative CWIP anomaly. In contrast, during AMO-/La Niña winters, the atmospheric descending anomalies in central-western Indian Ocean induced by La Niña anomalous SST are partly counteracted by the multidecadal anomalous ascending flow associated with the AMO, thus resulting in weaker CWIP anomaly. For El Niño episodes, the enhanced precipitation is strengthened and weakened during the negative and positive AMO phases, respectively, which further reinforces the amplitude difference of the CWIP anomaly caused by El Niño SST anomaly in the central-eastern tropical Pacific. The idealized AMO pacemaker experiments based on the coupled model EC-Earth3 can well capture these observational results, further consolidating the two pathways through which AMO modulates the relation of ENSO with the CWIP.

In the present study, we emphasize the Atlantic multidecadal (i.e., AMO) SST modulation effects on the relation of ENSO with the CWIP during the boreal winter. The conclusions carry important implications for our climate research community. To accurately simulate the atmospheric anomalies in the Indian Ocean during ENSO events, especially during La Niña events, the remote AMO decadal modulation needs to be considered besides the contribution from ENSO interannual SST variability itself. It should be noted that, we basically regard the atmospheric anomalies in the central-western Indian Ocean as passive responses to the anomalous ENSO-related SST during the mature winter in this study. It would be interesting to investigate whether these atmospheric anomalies can feedback on the subsequent SST evolution characteristics in the tropical oceans. In addition, as an important source of atmospheric perturbations, different atmospheric anomalies in the Indian Ocean will certainly produce different ENSO extra-tropical teleconnections and climate impacts, which are also important targets for further investigations.

DATA AVAILABILITY STATEMENT

The original contributions presented in the study are included in the article/**Supplementary Material**, further inquiries can be directed to the corresponding author.

AUTHOR CONTRIBUTIONS

XG conceived the idea. CZ and XG conducted the data analysis and prepared the tables and figures. All authors discussed the results. CZ wrote the original draft and XG reviewed and edited this paper.

FUNDING

This work is supported by the National Natural Science Foundation of China (42088101, 41905073).

ACKNOWLEDGMENTS

The authors would like to thank the editor and two reviewers for their constructive suggestions and comments that significantly improved this paper.

SUPPLEMENTARY MATERIAL

The Supplementary Material for this article can be found online at: https://www.frontiersin.org/articles/10.3389/feart.2022.866241/full#supplementary-material

REFERENCES

Alexander, M. A., Bladé, I., Newman, M., Lanzante, J. R., Lau, N.-C., and Scott, J. D. (2002). The Atmospheric Bridge: The Influence of ENSO Teleconnections on Air-Sea Interaction over the Global Oceans. *J. Clim.* 15 (16), 2205–2231. doi:10.1175/1520-0442(2002)015<2205:TABTIO>2.0.CO

Boer, G. J., Smith, D. M., Cassou, C., Doblas-Reyes, F., Danabasoglu, G., Kirtman, B., et al. (2016). The Decadal Climate Prediction Project (DCPP) Contribution to CMIP6. *Geosci. Model. Dev.* 9 (10), 3751–3777. doi:10.5194/gmd-9-3751-2016

Cai, W., Wu, L., Lengaigne, M., Li, T., McGregor, S., Kug, J.-S., et al. (2019). Pantropical Climate Interactions. *Science* 363 (6430). doi:10.1126/science.aav4236

Chen, M., Xie, P., Janowiak, J. E., and Arkin, P. A. (2002). Global Land Precipitation: A 50-yr Monthly Analysis Based on Gauge Observations. *J. Hydrometeor* 3 (3), 249–266. doi:10.1175/1525-7541(2002)003%3c0249:GLPAYM%3e2.0

Chen, W., Lu, R., and Dong, B. (2014). Intensified Anticyclonic Anomaly over the Western North Pacific during El Niño Decaying Summer under a Weakened Atlantic Thermohaline Circulation. *J. Geophys. Res. Atmos.* 119 (24), 13637–13650. doi:10.1002/2014JD022199

Chung, P.-H., and Li, T. (2013). Interdecadal Relationship between the Mean State and El Niño Types*. *J. Clim.* 26 (2), 361–379. doi:10.1175/JCLI-D-12-00106.1

Di Lorenzo, E., Liguori, G., Schneider, N., Furtado, J. C., Anderson, B. T., and Alexander, M. A. (2015). ENSO and Meridional Modes: A Null Hypothesis for Pacific Climate Variability. *Geophys. Res. Lett.* 42 (21), 9440–9448. doi:10.1002/2015GL066281

Dong, B., and Lu, R. (2013). Interdecadal Enhancement of the Walker Circulation over the Tropical Pacific in the Late 1990s. *Adv. Atmos. Sci.* 30 (2), 247–262. doi:10.1007/s00376-012-2069-9

Dong, B., and Sutton, R. T. (2007). Enhancement of ENSO Variability by a Weakened Atlantic Thermohaline Circulation in a Coupled GCM. *J. Clim.* 20 (19), 4920–4939. doi:10.1175/JCLI4284.1

Dong, B., Sutton, R. T., and Scaife, A. A. (2006). Multidecadal Modulation of El Niño-Southern Oscillation (ENSO) Variance by Atlantic Ocean Sea Surface Temperatures. *Geophys. Res. Lett.* 33 (8). doi:10.1029/2006GL025766

Döscher, R., Acosta, M., Alessandri, A., Anthoni, P., Arneth, A., Arsouze, T., et al. (2021). The EC-Earth3 Earth System Model for the Climate Model Intercomparison Project 6. *Geoscientific Model. Develop. Discuss.*, 1–90.

Fedorov, A. V., and Philander, S. G. (2001). A Stability Analysis of Tropical Ocean-Atmosphere Interactions: Bridging Measurements and Theory for El Niño. *J. Clim.* 14 (14), 3086–3101. doi:10.1175/1520-0442(2001)014%3c3086:ASAOTO%3e2.0

Fedorov, A. V., and Philander, S. G. (2000). Is El Nino Changing? *Science* 288 (5473), 1997–2002. doi:10.1126/science.288.5473.1997

Feng, J., Wang, L., and Chen, W. (2014). How Does the East Asian Summer Monsoon Behave in the Decaying Phase of El Niño during Different PDO Phases? *J. Clim.* 27 (7), 2682–2698. doi:10.1175/jcli-d-13-00015.1

Geng, X., Zhang, W., Jin, F.-F., Stuecker, M. F., and Levine, A. F. Z. (2020). Modulation of the Relationship between ENSO and its Combination Mode by the Atlantic Multidecadal Oscillation. *J. Clim.* 33 (11), 4679–4695. doi:10.1175/JCLI-D-19-0740.1

Geng, X., Zhang, W., Stuecker, M. F., Liu, P., Jin, F.-F., and Tan, G. (2017). Decadal Modulation of the ENSO-East Asian winter Monsoon Relationship by the Atlantic Multidecadal Oscillation. *Clim. Dyn.* 49 (7), 2531–2544. doi:10.1007/s00382-016-3465-0

Gong, Y., Li, T., and Chen, L. (2020). Interdecadal Modulation of ENSO Amplitude by the Atlantic Multi-Decadal Oscillation (AMO). *Clim. Dyn.* 55 (9), 2689–2702. doi:10.1007/s00382-020-05408-x

Jin, F.-F., Kim, S. T., and Bejarano, L. (2006). A Coupled-Stability index for ENSO. *Geophys. Res. Lett.* 33 (23). doi:10.1029/2006GL027221

Kalnay, E., Kanamitsu, M., Kistler, R., Collins, W., Deaven, D., Gandin, L., et al. (1996). The NCEP/NCAR 40-year Reanalysis Project. *Bull. Amer. Meteorol. Soc.* 77 (3), 437–471. doi:10.1029/2006GL02722110.1175/1520-0477(1996)077<0437:tnyrp>2.0.co;2

Kang, I.-S., No, H.-h., and Kucharski, F. (2014). ENSO Amplitude Modulation Associated with the Mean SST Changes in the Tropical central Pacific Induced by Atlantic Multidecadal Oscillation. *J. Clim.* 27 (20), 7911–7920. doi:10.1175/JCLI-D-14-00018.1

Kao, H.-Y., and Yu, J.-Y. (2009). Contrasting Eastern-Pacific and central-Pacific Types of ENSO. *J. Clim.* 22 (3), 615–632. doi:10.1175/2008JCLI2309.1

Klein, S. A., Soden, B. J., and Lau, N.-C. (1999). Remote Sea Surface Temperature Variations during ENSO: Evidence for a Tropical Atmospheric Bridge. *J. Clim.* 12 (4), 917–932. doi:10.1175/1520-0442(1999)012<0917:RSSTVD>2.0.CO

Kravtsov, S. (2012). An Empirical Model of Decadal ENSO Variability. *Clim. Dyn.* 39 (9), 2377–2391. doi:10.1007/s00382-012-1424-y

Lau, N.-C., and Nath, M. J. (2003). Atmosphere-Ocean Variations in the Indo-Pacific Sector during ENSO Episodes. *J. Clim.* 16 (1), 3–20. doi:10.1175/1520-0442(2003)016<0003:AOVITI>2.0.CO

Levine, A. F. Z., McPhaden, M. J., and Frierson, D. M. W. (2017). The Impact of the AMO on Multidecadal ENSO Variability. *Geophys. Res. Lett.* 44 (8), 3877–3886. doi:10.1002/2017GL072524

Li, X., Xie, S.-P., Gille, S. T., and Yoo, C. (2016). Atlantic-induced Pan-Tropical Climate Change over the Past Three Decades. *Nat. Clim Change* 6 (3), 275–279. doi:10.1038/nclimate2840

Liu, F., Zhang, W., Jin, F.-F., and Hu, S. (2021). Decadal Modulation of the ENSO-Indian Ocean Basin Warming Relationship during the Decaying Summer by the Interdecadal Pacific Oscillation. *J. Clim.* 34 (7), 2685–2699. doi:10.1175/jcli-d-20-0457.1

Liu, Z., and Alexander, M. (2007). Atmospheric Bridge, Oceanic Tunnel, and Global Climatic Teleconnections. *Rev. Geophys.* 45 (2). doi:10.1029/2005RG000172

Lu, R., and Dong, B. (2008). Response of the Asian Summer Monsoon to Weakening of Atlantic Thermohaline Circulation. *Adv. Atmos. Sci.* 25 (5), 723–736. doi:10.1007/s00376-008-0723-z

Mariotti, A., Zeng, N., and Lau, K. M. (2002). Euro-Mediterranean Rainfall and ENSO-A Seasonally Varying Relationship. *Geophys. Res. Lett.* 29 (12), 59–515954. doi:10.1029/2001GL014248

McGregor, S., Timmermann, A., Stuecker, M. F., England, M. H., Merrifield, M., Jin, F.-F., et al. (2014). Recent Walker Circulation Strengthening and Pacific Cooling Amplified by Atlantic Warming. *Nat. Clim Change* 4 (10), 888–892. doi:10.1038/nclimate2330

McPhaden, M. J., Zebiak, S. E., and Glantz, M. H. (2006). ENSO as an Integrating Concept in Earth Science. *science* 314 (5806), 1740–1745. doi:10.1126/science.1132588

Newman, M., Compo, G. P., and Alexander, M. A. (2003). ENSO-forced Variability of the Pacific Decadal Oscillation. *J. Clim.* 16 (23), 3853–3857. doi:10.1175/1520-0442(2003)016<3853:EVOTPD>2.0.CO

Pyper, B. J., and Peterman, R. M. (1998). Comparison of Methods to Account for Autocorrelation in Correlation Analyses of Fish Data. *Can. J. Fish. Aquat. Sci.* 55 (9), 2127–2140. doi:10.1139/f98-104

Ropelewski, C. F., and Halpert, M. S. (1987). Global and Regional Scale Precipitation Patterns Associated with the El Niño/Southern Oscillation. *Mon. Wea. Rev.* 115 (8), 1606–1626. doi:10.1175/1520-0493(1987)115%3c1606

Schopf, P. S., and Burgman, R. J. (2006). A Simple Mechanism for ENSO Residuals and Asymmetry. *J. Clim.* 19 (13), 3167–3179. doi:10.1175/JCLI3765.1

Slivinski, L. C., Compo, G. P., Whitaker, J. S., Sardeshmukh, P. D., Giese, B. S., McColl, C., et al. (2019). Towards a More Reliable Historical Reanalysis: Improvements for Version 3 of the Twentieth century Reanalysis System. *Q. J. R. Meteorol. Soc.* 145 (724), 2876–2908. doi:10.1002/qj.3598

Smith, T. M., Reynolds, R. W., Peterson, T. C., and Lawrimore, J. (2008). Improvements to NOAA's Historical Merged Land-Ocean Surface Temperature Analysis (1880-2006). *J. Clim.* 21 (10), 2283–2296. doi:10.1175/2007JCLI2100.1

Sun, C., Kucharski, F., Li, J., Jin, F. F., Kang, I. S., and Ding, R. (2017). Western Tropical Pacific Multidecadal Variability Forced by the Atlantic Multidecadal Oscillation. *Nat. Commun.* 8 (1), 15998. doi:10.1038/ncomms15998

Sun, C., Li, J., Kucharski, F., Kang, I. S., Jin, F. F., Wang, K., et al. (2019). Recent Acceleration of Arabian Sea Warming Induced by the Atlantic-Western Pacific Trans-basin Multidecadal Variability. *Geophys. Res. Lett.* 46 (3), 1662–1671. doi:10.1029/2018GL081175

Sun, C., Liu, Y., Xue, J., Kucharski, F., Li, J., and Li, X. (2021). The Importance of Inter-basin Atmospheric Teleconnection in the SST Footprint of Atlantic Multidecadal Oscillation over Western Pacific. *Clim. Dyn.* 57 (1), 239–252. doi:10.1007/s00382-021-05705-z

Timmermann, A., Okumura, Y., An, S.-I., Clement, A., Dong, B., Guilyardi, E., et al. (2007). The Influence of a Weakening of the Atlantic Meridional Overturning Circulation on ENSO. *J. Clim.* 20 (19), 4899–4919. doi:10.1175/JCLI4283.1

Tokinaga, H., and Tanimoto, Y. (2004). Seasonal Transition of SST Anomalies in the Tropical Indian Ocean during El Nino and Indian Ocean Dipole Years. *J. Meteorol. Soc. Jpn.* 82 (4), 1007–1018. doi:10.2151/jmsj.2004.1007

Trenberth, K. E., Branstator, G. W., Karoly, D., Kumar, A., Lau, N.-C., and Ropelewski, C. (1998). Progress during TOGA in Understanding and

Modeling Global Teleconnections Associated with Tropical Sea Surface Temperatures. *J. Geophys. Res.* 103 (C7), 14291–14324. doi:10.1029/97JC01444

Trenberth, K. E., and Caron, J. M. (2000). The Southern Oscillation Revisited: Sea Level Pressures, Surface Temperatures, and Precipitation. *J. Clim.* 13 (24), 4358–4365. doi:10.1175/1520-0442(2000)013%3c4358:TSORSL%3e2.0

Trenberth, K. E., and Shea, D. J. (2006). Atlantic Hurricanes and Natural Variability in 2005. *Geophys. Res. Lett.* 33 (12). doi:10.1029/2006GL026894

van Loon, H., and Madden, R. A. (1981). The Southern Oscillation. Part I: Global Associations with Pressure and Temperature in Northern winter. *Mon. Wea. Rev.* 109 (6), 1150–1162. doi:10.1175/1520-0493(1981)109%3c1150

Verdon, D. C., and Franks, S. W. (2006). Long-term Behaviour of ENSO: Interactions with the PDO over the Past 400 Years Inferred from Paleoclimate Records. *Geophys. Res. Lett.* 33 (6). doi:10.1029/2005GL025052

Wang, B., Wu, R., and Fu, X. (2000). Pacific-east Asian Teleconnection: How Does ENSO Affect East Asian Climate? *J. Clim.* 13 (9), 1517–1536. doi:10.1175/1520-0442(2000)013<1517:PEATHD>2.0.CO

Wang, C. (2019). Three-ocean Interactions and Climate Variability: A Review and Perspective. *Clim. Dyn.* 53 (7), 5119–5136. doi:10.1007/s00382-019-04930-x

Wang, H., Kumar, A., Wang, W., and Xue, Y. (2012). Seasonality of the Pacific Decadal Oscillation. *J. Clim.* 25 (1), 25–38. doi:10.1175/2011JCLI4092.1

Wang, L., Yu, J. Y., and Paek, H. (2017). Enhanced Biennial Variability in the Pacific Due to Atlantic Capacitor Effect. *Nat. Commun.* 8 (1), 14887–7. doi:10.1038/ncomms14887

Watanabe, T., and Yamazaki, K. (2014). Decadal-Scale Variation of South Asian Summer Monsoon Onset and its Relationship with the Pacific Decadal Oscillation. *J. Clim.* 27 (13), 5163–5173. doi:10.1175/jcli-d-13-00541.1

Xie, P., and Arkin, P. A. (1997). Global Precipitation: A 17-year Monthly Analysis Based on Gauge Observations, Satellite Estimates, and Numerical Model Outputs. *Bull. Amer. Meteorol. Soc.* 78 (11), 2539–2558. doi:10.1175/1520-0477(1997)078<2539:GPAYMA>2

Xie, S.-P., Annamalai, H., Schott, F. A., and McCreary, J. P. (2002). Structure and Mechanisms of South Indian Ocean Climate Variability. *J. Clim.* 15 (8), 864–878. doi:10.1175/1520-0442(2002)015<0864:SAMOSI>2.0

Xie, S.-P., Kosaka, Y., Du, Y., Hu, K., Chowdary, J. S., and Huang, G. (2016). Indo-western Pacific Ocean Capacitor and Coherent Climate Anomalies in post-ENSO Summer: A Review. *Adv. Atmos. Sci.* 33 (4), 411–432. doi:10.1007/s00376-015-5192-6

Xie, T., Li, J., Chen, K., Zhang, Y., and Sun, C. (2021). Origin of Indian Ocean Multidecadal Climate Variability: Role of the North Atlantic Oscillation. *Clim. Dyn.* 56 (9), 3277–3294. doi:10.1007/s00382-021-05643-w

Yang, Y., Li, Q., Song, Z., Sun, W., and Dong, W. (2022). A Comparison of Global Surface Temperature Variability, Extremes and Warming Trend Using Reanalysis Datasets and CMST-Interim. *Intl J. Climatology*. doi:10.1002/joc.7551

Yu, J.-Y., Kao, P.-k., Paek, H., Hsu, H.-H., Hung, C.-w., Lu, M.-M., et al. (2015). Linking Emergence of the Central Pacific El Niño to the Atlantic Multidecadal Oscillation. *J. Clim.* 28 (2), 651–662. doi:10.1175/JCLI-D-14-00347.1

Zebiak, S. E., and Cane, M. A. (1987). A Model El Niñ-Southern Oscillation. *Mon. Wea. Rev.* 115 (10), 2262–2278. doi:10.1175/1520-0493(1987)115<2262:ameno>2.0.co;2

Zhang, W., Jin, F.-F., and Turner, A. (2014). Increasing Autumn Drought over Southern China Associated with ENSO Regime Shift. *Geophys. Res. Lett.* 41 (11), 4020–4026. doi:10.1002/2014GL060130

Conflict of Interest: The authors declare that the research was conducted in the absence of any commercial or financial relationships that could be construed as a potential conflict of interest.

Publisher's Note: All claims expressed in this article are solely those of the authors and do not necessarily represent those of their affiliated organizations, or those of the publisher, the editors and the reviewers. Any product that may be evaluated in this article, or claim that may be made by its manufacturer, is not guaranteed or endorsed by the publisher.

frontiers | Frontiers in Earth Science

ORIGINAL RESEARCH
published: 06 April 2022
doi: 10.3389/feart.2022.884604

Seasonally Evolving Impacts of Multiyear La Niña on Precipitation in Southern China

Guansheng Huang[1], *Run Wang*[2]*, *Jingpeng Liu*[3], *Li Gao*[4], *Minghong Liu*[2] *and Quanliang Chen*[1]

[1]Plateau Atmosphere and Environment Key Laboratory of Sichuan Province, School of Atmospheric Sciences, Chengdu University of Information Technology, Chengdu, China, [2]State Key Laboratory of Severe Weather, Chinese Academy of Meteorological Sciences, Beijing, China, [3]Key Laboratory for Climate Studies, National Climate Center, China Meteorological Administration, Beijing, China, [4]CMA Earth System Modeling and Prediction Centre (CEMC), Beijing, China

The multiyear La Niña (MYLN) is characterized by longer duration, bimodal feature, more continuous circulation anomaly, and different climate impacts compared to the canonical single-peak La Niña. In this study, we focus on the evolving impacts of the MYLN on precipitation in southern China, which mainly occur in boreal winter and summer and correspond to significantly less precipitation and frequency of extreme rainfall. Results show that such impacts have remarkable differences between the first and second half of the MYLN lifecycle. In the first boreal winter when the MYLN reaches its first peak, the precipitation in southern China decreases significantly, while it tends to be insignificantly anomalous in the next winter. In the summer after its first peak, the MYLN has no apparent impact on precipitation in southern China, but when it basically disappears in the next summer, precipitation decreases significantly in southern China. Such seasonally evolving features in the impacts of the MYLN on precipitation in southern China can be mainly interpreted by the patterns of the anomalous cyclonic circulation in northwestern subtropical Pacific during the first peak winter and the decaying summer of the MYLN, which favors an anomalous reduction of moisture supply over southern China.

Keywords: multiyear La Niña, double-peak, precipitation, southern China, cyclonic circulation

OPEN ACCESS

Edited by:
Tao Lian,
Ministry of Natural Resources, China

Reviewed by:
Lin Chen,
Nanjing University of Information Science and Technology, China
Xianghui Fang,
Fudan University, China

***Correspondence:**
Run Wang
wangrun@cma.gov.cn

Specialty section:
This article was submitted to Atmospheric Science, a section of the journal Frontiers in Earth Science

Received: *26 February 2022*
Accepted: *21 March 2022*
Published: *06 April 2022*

Citation:
Huang G, Wang R, Liu J, Gao L, Liu M and Chen Q (2022) Seasonally Evolving Impacts of Multiyear La Niña on Precipitation in Southern China. Front. Earth Sci. 10:884604. doi: 10.3389/feart.2022.884604

1 INTRODUCTION

The El Niño-Southern Oscillation (ENSO) is the strongest interannual variability in the tropical ocean-atmosphere coupled system. El Niño and La Niña are the warm and cold phases of ENSO which usually last for 1–2 years and have a period of about 2–7 years. ENSO is characterized by strong phase-locking with developing in boreal spring and summer and peaking in winter (Jin, 1996; Neelin et al., 2000; Fang and Zheng, 2021). ENSO is one of the most important precursors that can influence the climate in East Asia, especially the precipitation in China (e.g., Zhang et al., 1996; Wang et al., 2000; Chen, 2002; Zhang et al., 2011). For example, during the developing year of El Niño, the summer and winter precipitation in southern China tends to increase (Zhang et al., 1996; Lim and Kim, 2007; Feng et al., 2010; Feng et al., 2011; Feng and Li, 2011; Zhang et al., 2011; Yuan and Yang, 2012; Li et al., 2016; Xu et al., 2016).

The anomalous Northwest Pacific anticyclone (NWPAC) plays a key role in connecting ENSO with the precipitation in eastern China (Zhang et al., 1996). The southeasterly wind anomalies associated with the NWPAC transport warm and humid air from the South China Sea to eastern

China, favoring the positive precipitation anomalies in eastern China. Several theories have been proposed to explain how ENSO excites and maintains an anomalous NWPAC, such as the warm pool atmosphere-ocean interaction mechanism (Zhang et al., 1996; Wang et al., 2000), the Indian Ocean capacitor mechanism (Xie et al., 2009, 2016), the moist enthalpy advection/Rossby wave modulation theory (Wu et al., 2017), and the ENSO-annual cycle combination mode (Stuecker et al., 2013; Stuecker et al., 2015; Zhang et al., 2016). Compared with El Niño, during the mature stage of La Niña, there is an anomalous low-level cyclone in the northwestern subtropical Pacific, which reinforce the East Asian winter monsoon and leads to anomalously dry conditions in East Asia (Huang et al., 2012; Li and Ma, 2012; Zhang R. et al., 2014; Xu et al., 2018). However, some studies have also found that the climate impacts of La Niña over southern China are much weaker than those of El Niño in recent decades, which show clearly asymmetric climate impacts between the two ENSO phases (Zhou et al., 2007).

In recent years, more attention has been paid to the asymmetry between El Niño and La Niña (Ohba and Ueda, 2009; Karori et al., 2013; Zhang R. et al., 2014; Zhang et al., 2015; Guo et al., 2017; Timmermann et al., 2018; Geng et al., 2019; Chen et al., 2022; Song et al., 2022). The El Niño has more super strong events and decays much faster than the La Niña (Song et al., 2022), while the La Niña tends to sustain longer and is more likely to re-intensify after the first peak, i.e., develop to the multiyear La Niña (denoted as MYLN) (Zheng et al., 2015; Okumura et al., 2017). For example, in the most recent 3 years, 2020–2022, there were the 2020/2021 and the following 2021/2022 La Niña events, though the latter is still evolving by now.

As a common type of La Niña, the MYLN is getting more and more attention in recent years and progress has been made on understanding its complex process and dynamic mechanism (Okumura and Deser, 2010; Zheng et al., 2015; Yu and Fang, 2018; Iwakiri and Watanabe, 2021; Kim and An, 2021; Kim and Yu, 2021; Park et al., 2021). Okumura and Deser (2010) suggested that the nonlinear response of atmospheric deep convection to SSTs in the western tropical Pacific, which leads to a westward shift of anomalous precipitation, enhances the duration of local zonal wind anomalies during La Niña and leads to the prolongation of La Niña. Kim and An (2021) attributed the double-peak feature to a strong seasonal modulation of the ENSO growth rate, which results in a seasonal gap of ENSO phase locking and a bifurcation of the peak time of ENSO. Moreover, the preceding strong El Niño, the incursion of off-equatorial subsurface cold water, and the subtropical air-sea coupled forcing are also suggested to be important for increasing the complexity of ENSO evolution and tend to produce MYLN events (Zheng et al., 2015; Yu and Fang, 2018; Iwakiri and Watanabe, 2021; Kim and Yu, 2021; Park et al., 2021).

Though the dynamics of MYLN remains controversial, several studies have focused on the lingering climate impacts of MYLN due to its bimodal feature, long duration, and continuous circulation anomaly, which are different from the single-peak type (Okumura et al., 2017; Prasanna et al., 2019; Raj Deepak et al., 2019; Tokinaga et al., 2019; Iwakiri and Watanabe, 2021). For example: a MYLN event can trigger an Atlantic Niño by enhancing the Walker circulation, but a single-year event cannot establish such a teleconnection (Tokinaga et al., 2019). Compared to the first winter during an MYLN event, the second winter has a strengthened and zonally elongated atmospheric circulation anomalies in the North Pacific and a northeastward shift of United States drought region (Okumura et al., 2017). The East Asian monsoon region is also suggested to have contrary anomalous rainfall patterns in the first and second summers of MYLN events (Raj Deepak et al., 2019), which is a sign indicating that impacts between the first and second years of the MYLN events may be different in southern China where rainfall is highly affected by ENSO (Feng et al., 2010; Feng et al., 2011; Feng and Li, 2011).

In this study, we intend to investigate the seasonally evolving impacts of the MYLN on precipitation in southern China and find out the key factors causing such impacts. The remainder of this paper is organized as follows. The data and methods are introduced in *Data and Methods*. Characteristics of MYLN and its impacts on precipitation in southern China are investigated in *Characteristics of MYLN and Its Impacts on Precipitation in Southern China*. Mechanisms of the MYLN impacting precipitation in southern China are analyzed in *Mechanisms of the MYLN Impacting Precipitation in Southern China*. A summary and a discussion are provided in *Summary and Discussion*.

2 DATA AND METHODS

In this study, the monthly SST dataset is derived from the Hadley Centre Sea Ice and Sea Surface Temperature dataset (HadISST) spanning from 1980 to 2021 with a horizontal resolution of 1° latitude × 1° longitude (Rayner et al., 2003). The daily precipitation data at 699 Chinese meteorological stations for the period 1980–2020 is from the daily precipitation dataset of the Chinese surface climate data (V3.0) provided by the National Meteorological Information Center of the China Meteorological Administration (CMA). The atmosphere reanalysis data is from the fifth generation of the European Centre for Medium-Range Weather Forecasts (ECMWF) atmospheric reanalysis (ERA5, Hersbach et al., 2020) with a horizontal resolution of 0.25° × 0.25°. The climatology is taken as the period 1980–2020. Anomalies are defined as the departure from the climatological calendar mean and linear trends are removed.

MYLN events are selected according to the criterion in Okumura et al. (2017): when the Niño-3.4 index (5°S–5°N, 170–120°W) falls below −0.75 standard deviations in any month during October (0) to February (1) and remains below −0.5 standard deviations in any month during October (1) to February (2). Here, the Niño-3.4 index has been smoothed with a 3-months running mean and removed the long-term linear trend, the standard deviation is calculated separately for each month, and the year in which La Niña first begins to develop is defined as Year (0). Based on this criterion, four MYLN events after 1980 (1983–1985, 1998–2000, 2007–2009, and 2010–2012) were identified (**Figure 1A**). For simplicity, we divide the lifecycle

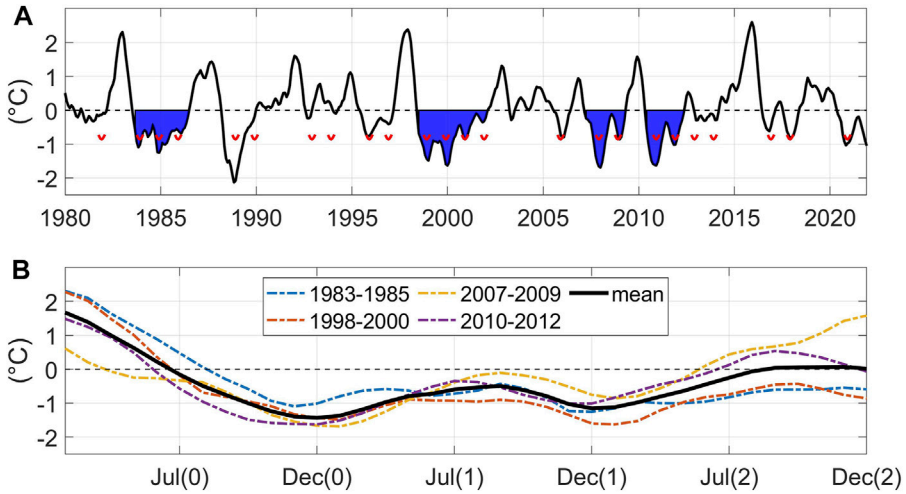

FIGURE 1 | (A) Time series of Niño-3.4 index (black line). Red lines are −0.75 standard deviations of Niño-3.4 index for each calendar month from October to February. The blue shadings denote the MYLN events. **(B)** Evolutions of MYLN events from year (0) to year (2) and their composite.

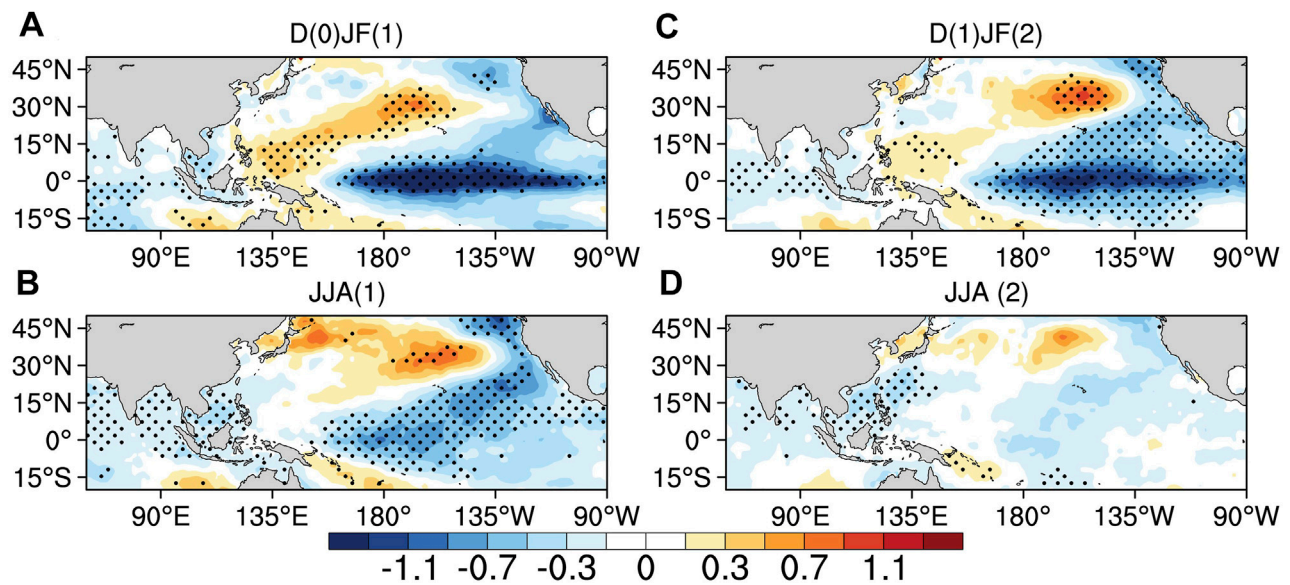

FIGURE 2 | Composites of SST anomalies (units: °C) for MYLN in **(A)** D (0) JF (1), **(B)** JJA (1), **(C)** D (1) JF (2), and **(D)** JJA (2). Dotted areas indicate values exceeding the 90% confidence level determined using a two-tailed Student's *t* test.

of MYLN in half according to the beginning time of the re-developing stage after the first La Niña peak.

3 CHARACTERISTICS OF MYLN AND ITS IMPACTS ON PRECIPITATION IN SOUTHERN CHINA

Composite evolution of the Niño-3.4 index for the four MYLN events (1983–1985, 1998–2000, 2007–2009, and 2010–2012) are shown in **Figure 1B** (black line). It is obvious that the first peak (−1.43°C) is stronger than the second peak (−1.15°C), which is consistent with previous studies (Okumura and Deser, 2010; Okumura et al., 2017; Tokinaga et al., 2019). The MYLN slowly decays after the first peak in D (0) JF (1) and begins to re-intensify in JJA (1) and develops into the second relatively weak peak in D (1) JF (2). During the time between the first and second peaks, the Niño-3.4 index remains negative, reflecting the long duration of the La Niña state in the equatorial Pacific, which is remarkably different from the conventional ENSO cycle.

Figure 2 shows composites of D (0) JF (1), JJA (1), D (1) JF (2), and JJA (2) SST anomalies of the MYLN. In D (0) JF (1), the

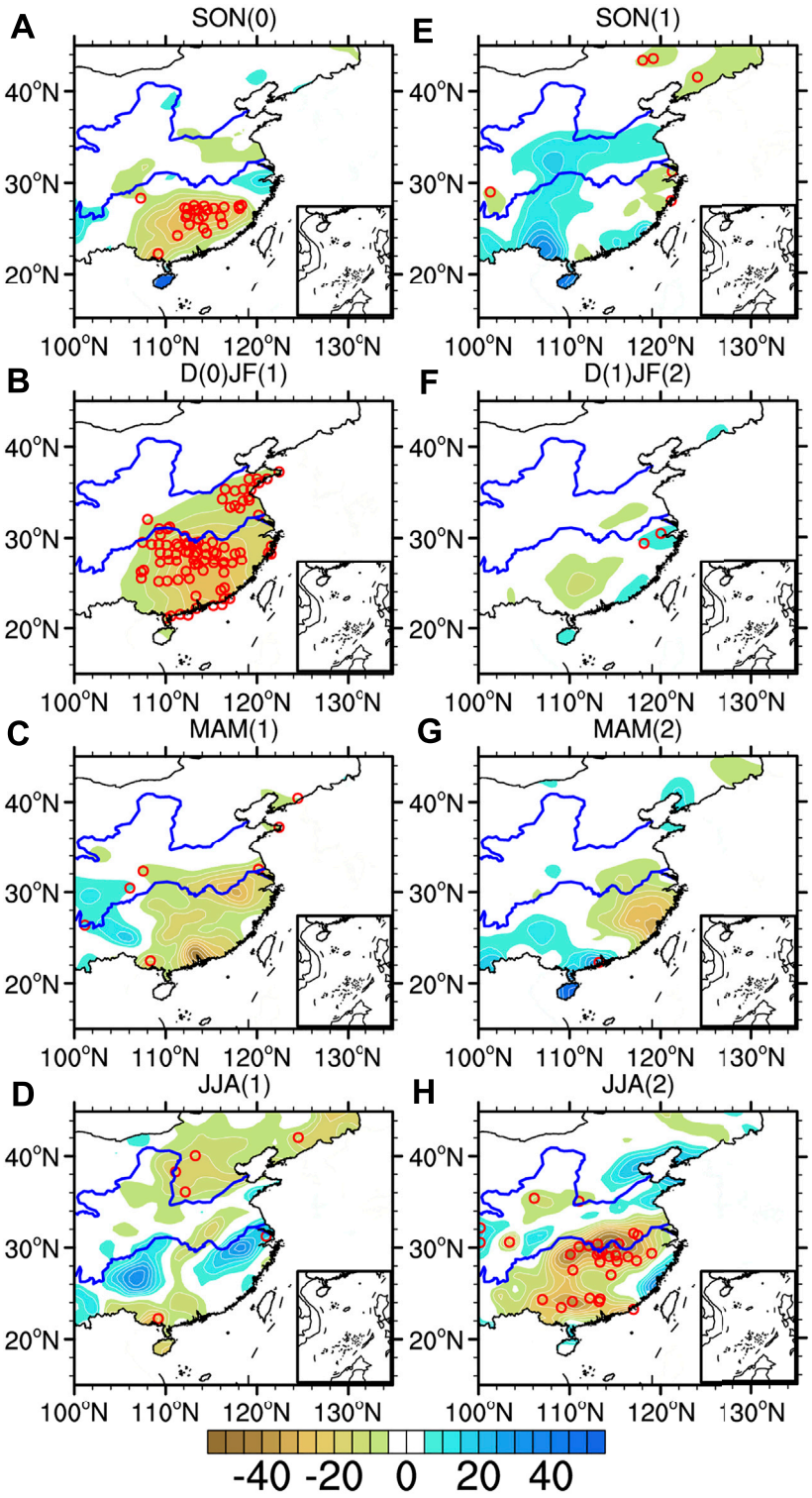

FIGURE 3 | Composites of precipitation anomalies (units: mm) in southern China during **(A)** SON (0), **(B)** D (0) JF (1), **(C)** MAM (1), **(D)** JJA (1), **(E)** SON (1), **(F)** D (1) JF (2), **(G)** MAM (2), and **(H)** JJA (2). Red circles indicate values at 699 meteorological stations exceeding the 90% confidence level determined using a two-tailed Student's *t* test.

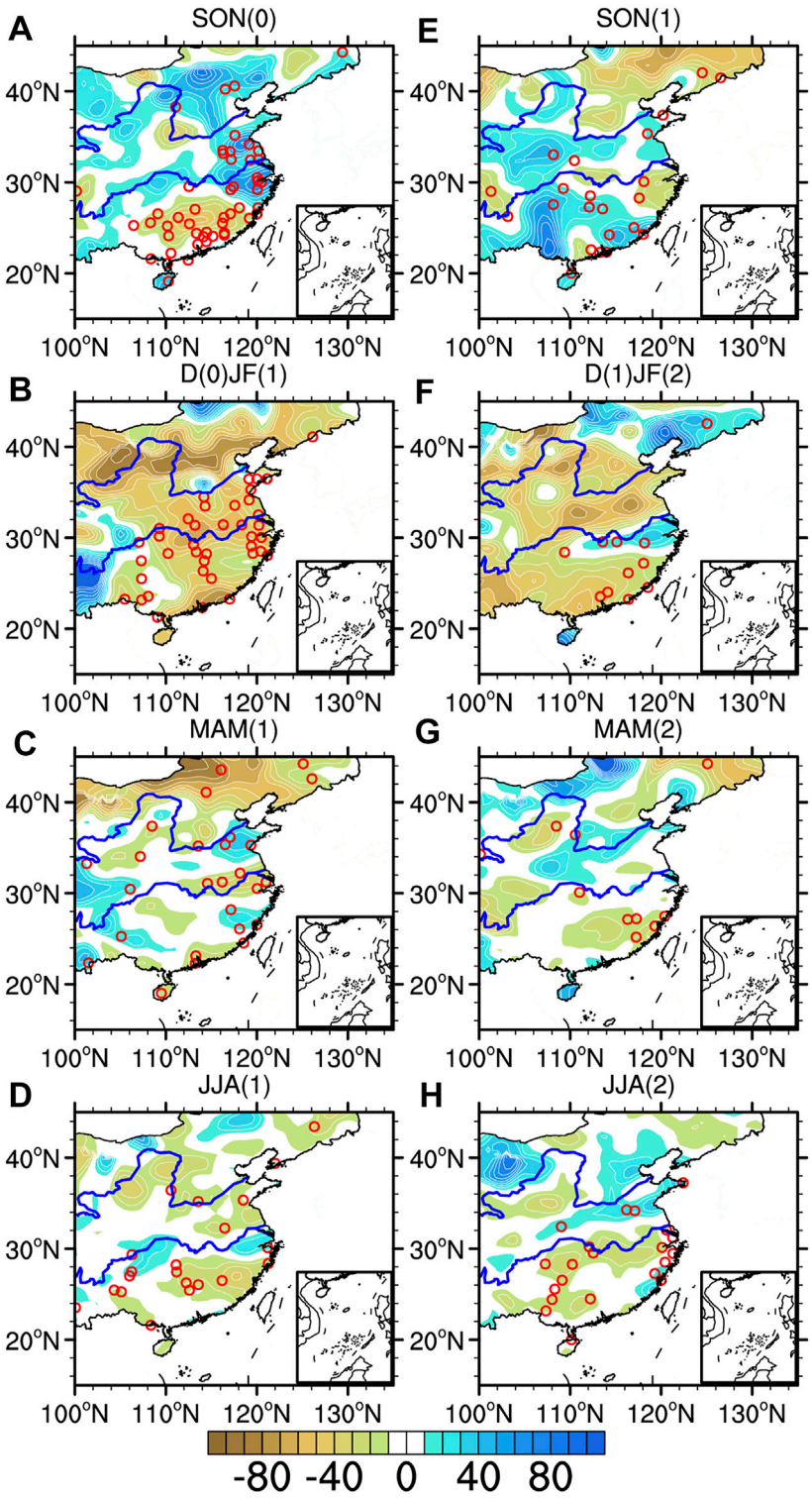

FIGURE 4 | Composites of probability changes (units: %) in southern China during **(A)** SON (0), **(B)** D (0) JF (1), **(C)** MAM (1), **(D)** JJA (1), **(E)** SON (1), **(F)** D (1) JF (2), **(G)** MAM (2), and **(H)** JJA (2). Red circles indicate values at 699 meteorological stations exceeding the 90% confidence level determined using a two-tailed Student's *t* test.

MYLN reaches its first peak, the negative SST anomalous center is located at around 165°W in the central equatorial Pacific. A significant positive SST anomalies region extends from the western equatorial Pacific to the north subtropical Pacific continuously. In D (1) JF (2), the MYLN reaches its second peak, the spatial pattern of SST anomalies in the tropical Indian Ocean and Pacific is similar to that at its first peak, but the strength weakens obviously. However, the meridional width of the significant region in the central and eastern equatorial Pacific is much larger than that at the first peak. Besides, there are significant signals in the Indian Ocean and Warm Pool area during the duration of MYLN. The anomalous circulation system in this area plays an important role in affecting the precipitation in southern China (Zhang et al., 2022). In JJA (2), the MYLN basically decays to neutral, but there are significant negative SST anomalies in the surrounding sea areas of northern Southeast Asia.

After the MYLN events had been identified, we further investigated the seasonally evolving impacts of MYLN on precipitation in southern China (**Figure 3**). Overall, during the duration of MYLN, precipitation in southern China generally decreases, but there are remarkable differences between the first and second half of the MYLN lifecycle. In SON (0), the MYLN is in its developing stage, and precipitation in the area south of the lower reaches of the Yangtze River decreases, which is consistent with the previous study (Zhang W. et al., 2014). While, in SON (1), the re-developing stage of MYLN, the distribution of the precipitation anomalies are insignificant in southern China. In the first boreal winter [D (0) JF (1)], the MYLN reaches its first peak and the precipitation in southern China decreases significantly, while the MYLN seems to be irrelevant to the precipitation in the next winter [D (1) JF (2)]. In the decaying stage after the first peak [MAM (1) and JJA (1)], the precipitation anomalies are insignificant, and so is in MAM (2). In JJA (2), when the MYLN basically disappears, the precipitation in southern China decreases significantly again, which is also the most conspicuous influence among seasons during the second half of the MYLN lifecycle.

In addition, we also investigated whether the MYLN modulates the probability of extreme precipitation days (**Figure 4**). Following the previous studies (Xiao et al., 2017), we define the historical 95th percentile precipitation for each season as the extreme threshold of this season, and any day with precipitation exceeding the corresponding threshold would be recognized as an extreme precipitation day. Further, the frequency change of extreme precipitation in the MYLN (ΔP_{ML}) events relative to the normal years is measured as the following:

$$\Delta \boldsymbol{P}_{\boldsymbol{ML}} = \frac{\boldsymbol{P}_{\boldsymbol{ML}}\ (\boldsymbol{x} \geq \boldsymbol{x}_{\boldsymbol{t}}) - \boldsymbol{P}_{\boldsymbol{cli}}\ (\boldsymbol{x} \geq \boldsymbol{x}_{\boldsymbol{t}})}{\boldsymbol{P}_{\boldsymbol{cli}}\ (\boldsymbol{x} \geq \boldsymbol{x}_{\boldsymbol{t}})} \times \mathbf{100\%} \qquad (1)$$

Where, P_{ML} on the right-hand side is the occurrence probability of extreme precipitation days in the MYLN years, and $P_{cli} = 0.05$ is the occurrence probability of extreme precipitation under the normal status. Here, the so-called probability is just proxied by the frequency calculated with our data samples. x represents the daily precipitation value in the target seasons and x_t is the extreme threshold of the seasonal precipitation. As shown in **Figure 4**, in the first developing stage of MYLN [SON (0)], the occurrence probability of extreme precipitation days has been decreased in areas south of the Yangtze River, and the affected area extends throughout the lower reaches of the Yangtze River in the first mature stage [D (0) JF (1)]. However, after that, the MYLN seems to have very limited significant impacts on the extreme precipitation over southern China.

4 MECHANISMS OF THE MYLN IMPACTING PRECIPITATION IN SOUTHERN CHINA

Since impacts of MYLN on precipitation in southern China mainly occurs in boreal winter and summer, we further analyzed what causes the differences in the responses of precipitation in southern China to the first and second half of MYLN. In the first mature stage of MYLN [D (0) JF (1)], the negative SST anomalous center is located in the central equatorial Pacific, and positive SST anomalies are located in a belt that stretch from the Maritime Continent to the subtropical central North Pacific (**Figure 2A**). The easterly 850 hPa wind anomalies in the western and central equatorial Pacific can strengthen the trade winds and enhance the Walker circulation, the convection is suppressed in the eastern tropical Pacific but enhanced in the Indo-Pacific warm pool, and an anticyclonic circulation is formed in the north of the Maritime Continent (**Figure 5A**). The southwesterly wind anomalies in the northwestern tropical Pacific induced by the equatorial La Niña cold SST anomalies are contrary to the trade winds, which suppress the local evaporation and lead to anomalous SST warming. Eventually, an anomalous lower-tropospheric cyclonic circulation in the northwestern subtropical Pacific is formed at around 30°N, 160°E as a response to the anomalous SST warming (Wang et al., 2000). The northerly wind anomalies on the west side of the anomalous cyclonic circulation are in eastern China, strengthening the East Asian winter monsoon. Therefore, due to the influence of the anomalous cyclonic circulation in the northwestern subtropical Pacific, southern China is drier than usual winter, which has been mentioned in Karori et al. (2013).

Figure 6A is the composite of anomalous vertically integrated moisture fluxes (VIMFs, 1000–300 hPa vertically integrated) and their divergence in D (0) JF (1). The distribution of anomalous VIMFs is similar to that of the 850 hPa wind anomalies (**Figures 5A**, **6A**). In the western and central equatorial Pacific, the easterly wind anomalies transport moisture to the west and north. The anomalous divergence of VIMFs is positive in southern China and negative in South China sea. Meanwhile, under the influence of the anomalous cyclonic circulation in the northwestern subtropical Pacific, moisture is transported from the former to the latter, which means that the precipitation in southern China will become less. **Figure 7A** shows the composite of the zonal circulation over the northern hemispheric Indo-Pacific region (5-20°N) in D (0) JF (1). The ascending motion around 120°E is strong, which reflects the strong large-scale modulation of Walker circulation by matured La Niña. Moreover, the lower-level easterly wind anomalies are in the east of the date line, which suggested that the formation of the anomalous cyclonic circulation in the northwestern subtropical Pacific is closely associated with the off-equatorial Rossby wave response (Wang et al., 2000).

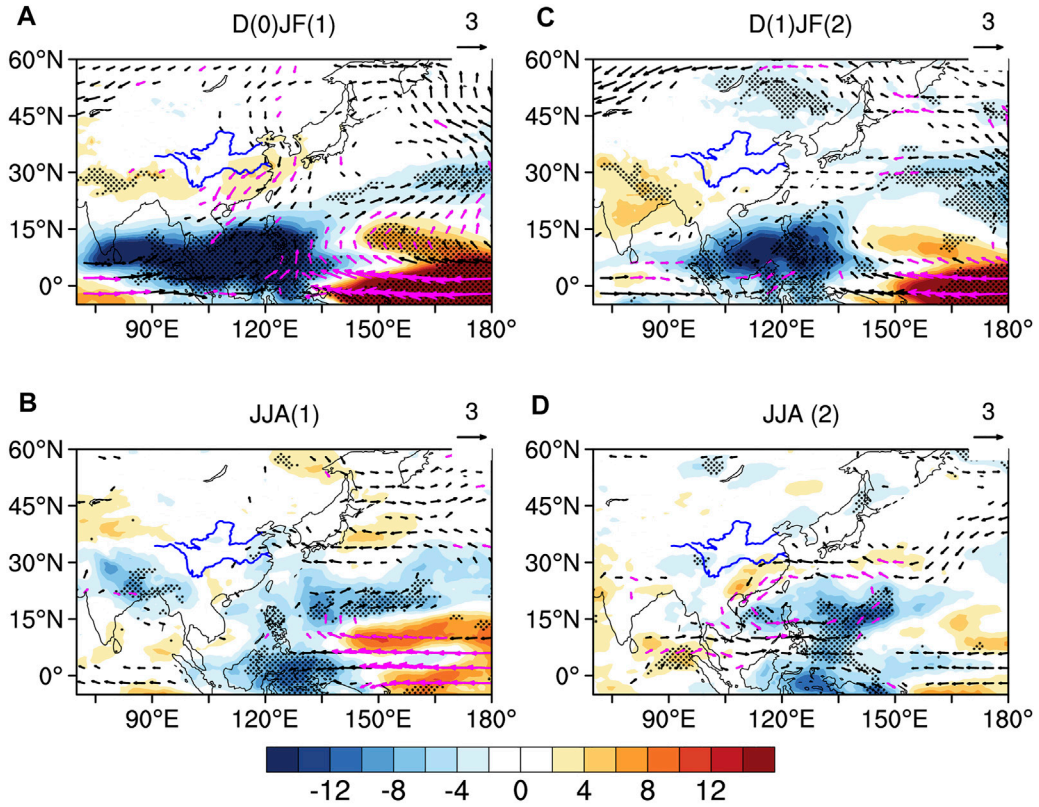

FIGURE 5 | Composites of outgoing longwave radiation (shaded, units: W/m^2) and 850hPa wind anomalies (vector, units: m/s) during **(A)** D (0) JF (1), **(B)** JJA (1), **(C)** D (1) JF (2), and **(D)** JJA (2). Dotted areas and purple vectors indicate values exceeding the 90% confidence level determined using a two-tailed Student's *t* test.

Compared with the first La Niña peak in D (0) JF (1), the second peak in D (1) JF (2) has a similar La Niña SST pattern in the tropical Pacific with weaker amplitude (**Figures 1B**, **2C**), and the anomalous zonal circulation in the north of the equatorial Pacific weakens remarkably in D (1) JF (2) (**Figure 7C**). Furthermore, there are no obvious warming in the northwestern subtropical Pacific, so the local response of the lower-level atmospheric circulation is weak that cannot form a closed anomalous cyclonic circulation (**Figure 5C**). As a result, there are neither significant northerly wind anomalies nor anomalous VIMFs in eastern China (**Figures 5C**, **6C**), which cannot significantly influence the East Asian winter monsoon. Therefore, the second peak of MYLN cannot significantly affect the precipitation in southern China.

In JJA (1), the positive SST anomalies are disappeared in the western equatorial Pacific, but the negative SST anomalies in the central equatorial Pacific persist (**Figure 2B**). Easterly wind anomalies are observed in the east of the Maritime Continent (**Figure 5B**). However, there are almost no significant signals of low-level atmospheric circulation and moisture transport in the off-equatorial northwestern Pacific (**Figures 6B**, **7B**). In addition, the north Indian Ocean is dominated by the easterly wind anomalies and no conspicuous descending motion (**Figures 5B**, **7B**), which has no contributions to the maintenance of the anomalous cyclonic circulation in the northwestern subtropical Pacific.

In JJA (2), the SST anomalies in the equatorial Pacific have almost completely disappeared and the MYLN has decayed to a neutral state (**Figure 2D**). The easterly wind anomalies in the equatorial Pacific that prevailed during the lifecycle of the MYLN have also become weak (**Figure 5D**). However, negative SST anomalies in the northern tropical Indian Ocean are still significant. On their east side, the westerly wind anomalies responded to the negative SST anomalies with strong cyclonic shear, forming an anomalous cyclonic circulation over the Philippine sea, which is consistent with the Indian Ocean capacitor theory proposed by Xie et al. (2009). The northerly wind anomalies in the west of the anomalous cyclonic circulation are opposite to the prevailing southerly winds of East Asian summer monsoon, which weakens the latter. Meanwhile, under the influence of the anomalous cycle, moisture diverges in southern China (**Figure 6D**), resulting in less precipitation in this region. In **Figure 7D**, the northwest tropical Pacific is characterized by anomalous ascending motion, which forms an anomalous zonal atmospheric circulation with the descending motion in the tropical Indian Ocean, also suggesting the maintenance of the anomalous cyclonic circulation in the north of the Philippines in summer may be closely related to the Indian Ocean capacitor effect (Wu et al., 2009; Xie et al., 2009; Li et al., 2017).

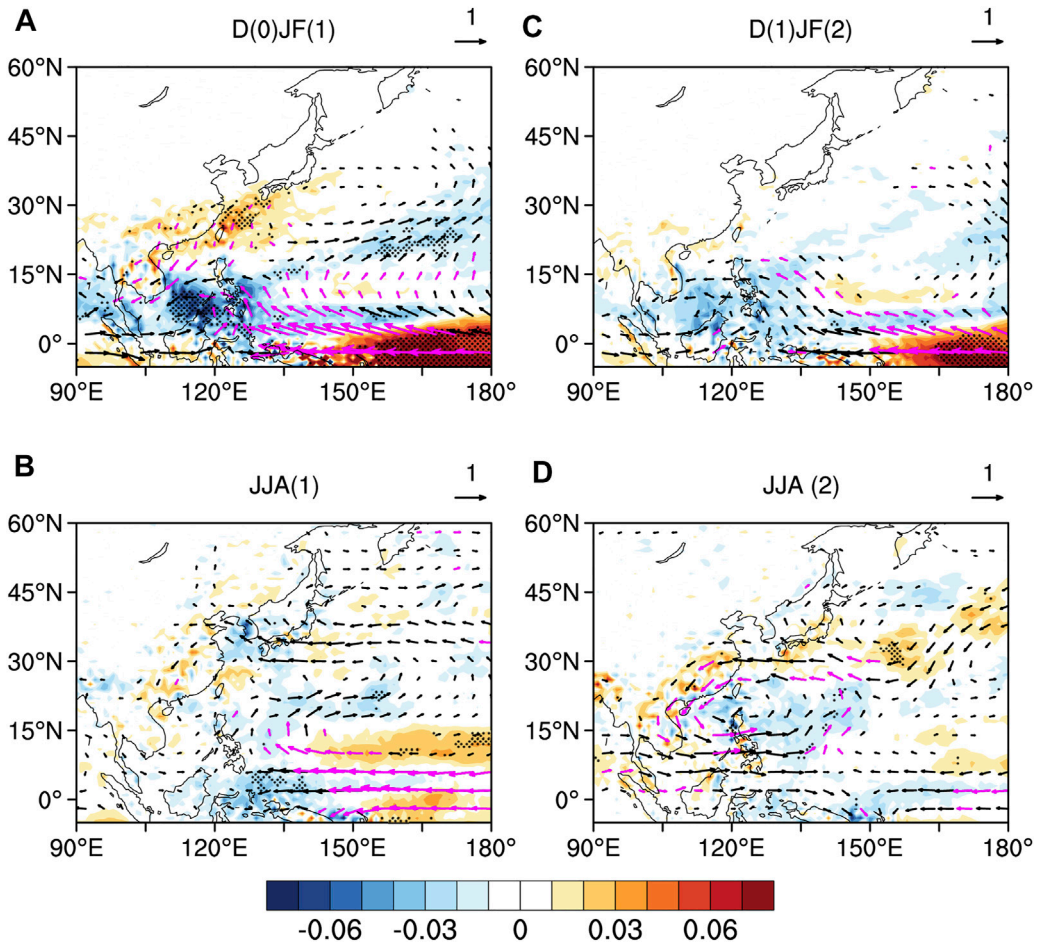

FIGURE 6 | Composites of anomalous VIMFs (vector, units: 10^{-5} g m^{-1} s^{-1}) and their divergence (shaded, units: 10^{-5} g m^{-2} s^{-1}) during **(A)** D (0) JF (1), **(B)** JJA (1), **(C)** D (1) JF (2), and **(D)** JJA (2). Dotted areas and purple vectors indicate values exceeding the 90% confidence level determined using a two-tailed Student's *t* test.

5 SUMMARY AND DISCUSSION

In this study, we focused on the seasonally evolving impacts of the MYLN on precipitation in southern China. After 1980, there are four MYLN events (1983–1985, 1998–2000, 2007–2009, and 2010–2012). We found that impacts of MYLN on precipitation in southern China mainly occur in boreal winter and summer and correspond to significantly less precipitation and frequency of extreme rainfall in southern China. Such impacts have remarkable differences between the first and second half of the MYLN lifecycle.

In the first boreal winter [D (0) JF (1)], the MYLN reaches its first peak and the precipitation in southern China decreases significantly, and the probability of extreme precipitation days is also apparently depressed, while the MYLN tends to be irrelevant to the precipitation in the next winter [D (1) JF (2)]. In the first mature stage of MYLN [D (0) JF (1)], the negative SST anomalous center is located in the central equatorial Pacific, and positive SST anomalies are located in a belt that stretch from the Maritime Continent to the subtropical central North Pacific. An anomalous lower-tropospheric cyclonic circulation in the northwestern subtropical Pacific is formed at around 30°N, 160°E as a response to the anomalous SST warming (Wang et al., 2000). The northerly wind anomalies on the west side of the anomalous cyclonic circulation are in eastern China, strengthening the East Asian winter monsoon. Therefore, due to the influence of the anomalous cyclonic circulation in the northwestern subtropical Pacific, moisture is transported from southern China to South China sea, and southern China is drier than usual winter, which has been mentioned in Karori et al. (2013). Compare with the first La Niña peak in D (0) JF (1), the second peak in D (1) JF (2) cannot form a closed anomalous cyclonic circulation in the northwestern subtropical Pacific. As a result, there are no significant northerly wind anomalies in eastern China, which cannot significantly affect the precipitation in southern China.

In the summer after the first La Niña peak [JJA (1)], the MYLN have no significant contributions to the precipitation in southern China, but when the MYLN basically disappears in the last summer [JJA (2)], the precipitation in southern China decreases significantly, which is also the most conspicuous influence among seasons during the second half of the MYLN

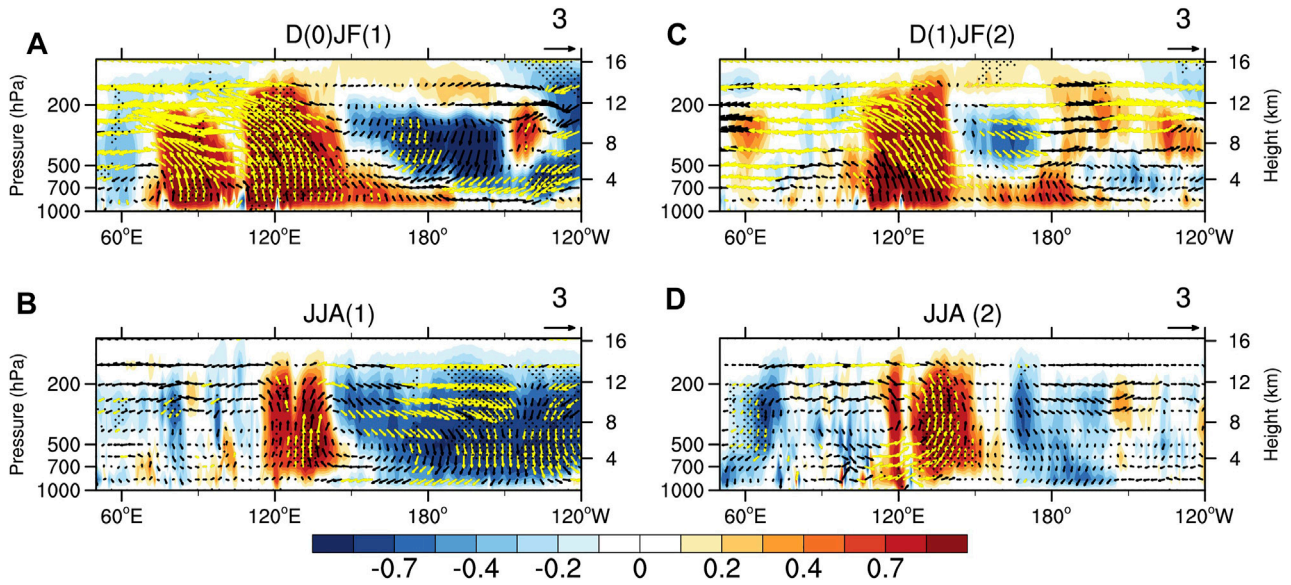

FIGURE 7 | Composites of anomalous zonal circulation over the northern hemispheric tropical region (5–20°N) with speed in the vertical direction (shaded, units: m/s) and zonal vertical velocity (vector, units: m/s) during **(A)** D (0) JF (1), **(B)** JJA (1), **(C)** D (1) JF (2), and **(D)** JJA (2). Dotted areas and yellow vectors indicate values exceeding the 90% confidence level determined using a two-tailed Student's t test.

lifecycle. In JJA (1), the positive SST anomalies disappear in the western equatorial Pacific, but the negative SST anomalies in the central equatorial Pacific persist. However, there are almost no significant signals of low-level atmospheric circulation and moisture transport in the off-equatorial northwestern Pacific. In JJA (2), the SST anomalies in the equatorial Pacific have almost completely disappeared and the MYLN has decayed to a neutral state, while negative SST anomalies in the northern tropical Indian Ocean are still significant. On the east side of the northern tropical Indian Ocean, the westerly wind anomalies responded to the negative SST anomalies, contributing to the deepened convection in the Philippine sea and forming an anomalous cyclonic circulation over the Philippine sea. Meanwhile, the northwest tropical Pacific is characterized by anomalously ascending motion, which forms an anomalous zonal atmospheric circulation with the descending motion in the tropical Indian Ocean, suggesting the maintenance of the anomalous cyclonic circulation in the north of the Philippines in summer may be closely related to the Indian Ocean capacitor effect (Wu et al., 2009; Xie et al., 2009; Li et al., 2017). The northerly wind anomalies in the west of the anomalous cyclonic circulation weaken the prevailing southerly winds of East Asian summer monsoon and correspond to significantly less precipitation in southern China.

The MYLN in its lifecycle mainly depressed the precipitation and frequency of extreme rainfall over southern China, which can be mainly interpreted by the patterns of the anomalous cyclonic circulation in northwestern subtropical Pacific. However, in its first developing stage [SON(0)], the occurrence probability of extreme precipitation days has an increase in the Yangtze-Huaihe Region, but the seasonal mean precipitation in this region has no significant changes, which may be due to the MYLN contributing to the formation of local atmospheric conditions in this region that is conducive to the extreme precipitation. Due to the limited number of MYLN events, the understanding of such type of La Niña in its dynamic processes and evolving impacts is still insufficient, as well as its predictability. Therefore, it is necessary to use coupled ocean-atmosphere models to further analyze mechanisms of the climate impacts of MYLN in future.

DATA AVAILABILITY STATEMENT

Publicly available datasets were analyzed in this study. This data can be found here: ERA5 data is available *via* https://cds.climate.copernicus.eu/cdsapp#!/dataset/reanalysis-era5-pressure-levels-monthly-means?tab=overview. The daily precipitation dataset of the Chinese surface climate data (V3.0) is available *via* http://data.cma.cn/. HadISST data is available *via* https://www.metoffice.gov.uk/hadobs/hadisst/index.html.

AUTHOR CONTRIBUTIONS

All authors listed have made a substantial, direct, and intellectual contribution to the work and approved it for publication.

FUNDING

This work was jointly supported by the National Natural Science Foundation of China (42005041, 42105067, 42175015, and 41975094), and the Basic Research and Operational Special Project of CAMS (2021Z007).

REFERENCES

Chen, N., Fang, X., and Yu, J.-Y. (2022). A Multiscale Model for El Niño Complexity. *Npj. Clim. Atmos. Sci.* 5, 16. doi:10.1038/s41612-022-00241-x

Chen, W. (2002). Impacts of El Niño and La Niña on the Cycle of the East Asian winter and Summer Monsoon. *Chin. J. Atmos. Sci.* 26, 595–610. (in Chinese). doi:10.3878/j.issn.1006-9895.2002.05.02

Fang, X.-H., and Zheng, F. (2021). Effect of the Air-Sea Coupled System Change on the ENSO Evolution from Boreal spring. *Clim. Dyn.* 57, 109–120. doi:10.1007/s00382-021-05697-w

Feng, J., Chen, W., Tam, C.-Y., and Zhou, W. (2011). Different Impacts of El Niño and El Niño Modoki on China Rainfall in the Decaying Phases. *Int. J. Climatol.* 31, 2091–2101. doi:10.1002/joc.2217

Feng, J., and Li, J. (2011). Influence of El Niño Modoki on spring Rainfall over south China. *J. Geophys. Res.* 116, D13102. doi:10.1029/2010jd015160

Feng, J., Wang, L., Chen, W., Fong, S. K., and Leong, K. C. (2010). Different Impacts of Two Types of Pacific Ocean Warming on Southeast Asian Rainfall during Boreal winter. *J. Geophys. Res.* 115, D24122. doi:10.1029/2010jd014761

Geng, T., Cai, W., Wu, L., and Yang, Y. (2019). Atmospheric Convection Dominates Genesis of ENSO Asymmetry. *Geophys. Res. Lett.* 46, 8387–8396. doi:10.1029/2019gl083213

Guo, Z., Zhou, T., and Wu, B. (2017). The Asymmetric Effects of El Niño and La Niña on the East Asian winter Monsoon and Their Simulation by CMIP5 Atmospheric Models. *J. Meteorol. Res.* 31, 82–93. doi:10.1007/s13351-017-6095-5

Hersbach, H., Bell, B., Berrisford, P., Hirahara, S., Horányi, A., Muñoz-Sabater, J., et al. (2020). The ERA5 Global Reanalysis. *Q.J.R. Meteorol. Soc.* 146, 1999–2049. doi:10.1002/qj.3803

Huang, R., Chen, J., Wang, L., and Lin, Z. (2012). Characteristics, Processes, and Causes of the Spatio-Temporal Variabilities of the East Asian Monsoon System. *Adv. Atmos. Sci.* 29, 910–942. doi:10.1007/s00376-012-2015-x

Iwakiri, T., and Watanabe, M. (2021). Mechanisms Linking Multi-Year La Niña with Preceding strong El Niño. *Sci. Rep.* 11, 17465. doi:10.1038/s41598-021-96056-6

Jin, F.-F. (1996). Tropical Ocean-Atmosphere Interaction, the Pacific Cold Tongue, and the El Niño-Southern Oscillation. *Science* 274, 76–78. doi:10.1126/science.274.5284.76

Karori, M. A., Li, J., and Jin, F.-F. (2013). The Asymmetric Influence of the Two Types of El Niño and La Niña on Summer Rainfall over Southeast China. *J. Clim.* 26, 4567–4582. doi:10.1175/jcli-d-12-00324.1

Kim, J. W., and Yu, J. Y. (2021). Evolution of Subtropical Pacific-Onset El Niño: How its Onset Location Controls its Decay Evolution. *Geophys. Res. Lett.* 48, e2020GL091345. doi:10.1029/2020GL091345

Kim, S.-K., and An, S.-I. (2021). Seasonal Gap Theory for ENSO Phase Locking. *J. Clim.* 34, 1–44. doi:10.1175/jcli-d-20-0495.1

Li, C., and Ma, H. (2012). Relationship between ENSO and winter Rainfall over Southeast China and its Decadal Variability. *Adv. Atmos. Sci.* 29, 1129–1141. doi:10.1007/s00376-012-1248-z

Li, T., Wang, B., Wu, B., Zhou, T., Chang, C. P., and Zhang, R. (2017). Theories on Formation of an Anomalous Anticyclone in Western North Pacific During El Niño: A Review.. *J. Meteorol. Res.* 31, 987–1006. doi:10.1007/s13351-017-7147-6

Lim, Y.-K., and Kim, K.-Y. (2007). ENSO Impact on the Space-Time Evolution of the Regional Asian Summer Monsoons. *J. Clim.* 20, 2397–2415. doi:10.1175/jcli4120.1

Neelin, J. D., Jin, F.-F., and Syu, H.-H. (2000). Variations in ENSO Phase Locking. *J. Clim.* 13, 2570–2590. doi:10.1175/1520-0442(2000)013<2570:viepl>2.0.co;2

Ohba, M., and Ueda, H. (2009). Role of Nonlinear Atmospheric Response to SST on the Asymmetric Transition Process of ENSO. *J. Clim.* 22, 177–192. doi:10.1175/2008jcli2334.1

Okumura, Y. M., and Deser, C. (2010). Asymmetry in the Duration of El Niño and La Niña. *J. Clim.* 23, 5826–5843. doi:10.1175/2010JCLI3592.1

Okumura, Y. M., DiNezio, P., and Deser, C. (2017). Evolving Impacts of Multiyear La Niña Events on Atmospheric Circulation and U.S. Drought. *Geophys. Res. Lett.* 44, 11614–11623. doi:10.1002/2017gl075034

Park, J. H., An, S. I., Kug, J. S., Yang, Y. M., Li, T., and Jo, H. S. (2021). Mid-latitude Leading Double-dip La Niña. *Int. J. Climatol.* 41, E1353–E1370. doi:10.1002/joc.6772

Prasanna, K., Singh, P., Chowdary, J. S., Naidu, C. V., Parekh, A., Gnanaseelan, C., et al. (2019). Northeast Monsoon Rainfall Variability over the Southern Peninsular India Associated with Multiyear La Niña Events. *Clim. Dyn.* 53, 6265–6291. doi:10.1007/s00382-019-04927-6

Raj Deepak, S. N., Chowdary, J. S., Dandi, A. R., Srinivas, G., Parekh, A., Gnanaseelan, C., et al. (2019). Impact of Multiyear La Niña Events on the South and East Asian Summer Monsoon Rainfall in Observations and CMIP5 Models. *Clim. Dyn.* 52, 6989–7011. doi:10.1007/s00382-018-4561-0

Rayner, N. A., Parker, D. E., Horton, E., Folland, C. K., Alexander, L. V., Rowell, D., et al. (2003). Global Analyses of Sea Surface Temperature, Sea Ice, and Night marine Air Temperature since the Late Nineteenth century. *J. Geophys. Res.* 108, 4407. doi:10.1029/2002JD002670

Song, X., Zhang, R., and Rong, X. (2022). Dynamic Causes of ENSO Decay and its Asymmetry. *J. Clim.* 35, 445–462. doi:10.1175/jcli-d-21-0138.1

Stuecker, M. F., Jin, F.-F., Timmermann, A., and McGregor, S. (2015). Combination Mode Dynamics of the Anomalous Northwest Pacific Anticyclone. *J. Clim.* 28, 1093–1111. doi:10.1175/JCLI-D-14-00225.1

Stuecker, M. F., Timmermann, A., Jin, F.-F., McGregor, S., and Ren, H.-L. (2013). A Combination Mode of the Annual Cycle and the El Niño/Southern Oscillation. *Nat. Geosci* 6, 540–544. doi:10.1038/ngeo1826

Timmermann, A., An, S.-I., Kug, J.-S., Jin, F.-F., Cai, W., Capotondi, A., et al. (2018). El Niño-Southern Oscillation Complexity. *Nature* 559, 535–545. doi:10.1038/s41586-018-0252-6

Tokinaga, H., Richter, I., and Kosaka, Y. (2019). ENSO Influence on the Atlantic Niño, Revisited: Multi-Year versus Single-Year ENSO Events. *J. Clim.* 32, 4585–4600. doi:10.1175/JCLI-D-18-0683.1

Wang, B., Wu, R., and Fu, X. (2000). Pacific-east Asian Teleconnection: How Does ENSO Affect East Asian Climate? *J. Clim.* 13, 1517–1536. doi:10.1175/1520-0442(2000)013<1517:peathd>2.0.co;2

Wu, B., Zhou, T., and Li, T. (2009). Seasonally Evolving Dominant Interannual Variability Modes of East Asian Climate. *J. Cli.* 22, 2992–3005. doi:10.1175/2008JCLI2710.1

Wu, B., Zhou, T., and Li, T. (2017). Atmospheric Dynamic and Thermodynamic Processes Driving the Western North Pacific Anomalous Anticyclone during El Niño. Part I: Maintenance Mechanisms. *J. Clim.* 30, 9621–9635. doi:10.1175/JCLI-D-16-0489.1

Xiao, M., Zhang, Q., and Singh, V. P. (2017). Spatiotemporal Variations of Extreme Precipitation Regimes during 1961-2010 and Possible Teleconnections with Climate Indices across China. *Int. J. Climatol.* 37, 468–479. doi:10.1002/joc.4719

Xie, S.-P., Hu, K., Hafner, J., Tokinaga, H., Du, Y., Huang, G., et al. (2009). Indian Ocean Capacitor Effect on Indo-Western Pacific Climate during the Summer Following El Niño. *J. Clim.* 22, 730–747. doi:10.1175/2008jcli2544.1

Xie, S.-P., Kosaka, Y., Du, Y., Hu, K., Chowdary, J. S., and Huang, G. (2016). Indo-western Pacific Ocean Capacitor and Coherent Climate Anomalies in post-ENSO Summer: A Review. *Adv. Atmos. Sci.* 33, 411–432. doi:10.1007/s00376-015-5192-6

Xu, K., Huang, Q.-L., Tam, C.-Y., Wang, W., Chen, S., and Zhu, C. (2018). Roles of Tropical SST Patterns during Two Types of ENSO in Modulating Wintertime Rainfall over Southern China. *Clim. Dyn.* 52, 523–538. doi:10.1007/s00382-018-4170-y

Xu, K., Zhu, C., and Wang, W. (2016). The Cooperative Impacts of the El Niño-Southern Oscillation and the Indian Ocean Dipole on the Interannual Variability of Autumn Rainfall in China. *Int. J. Climatol.* 36, 1987–1999. doi:10.1002/joc.4475

Yu, J. Y., and Fang, S. W. (2018). The Distinct Contributions of the Seasonal Footprinting and Charged-Discharged Mechanisms to ENSO Complexity. *Geophys. Res. Lett.* 45, 6611–6618. doi:10.1029/2018gl077664

Yuan, Y., and Yang, S. (2012). Impacts of Different Types of El Niño on the East Asian Climate: Focus on ENSO Cycles. *J. Clim.* 25, 7702–7722. doi:10.1175/jcli-d-11-00576.1

Zhang, L., Shi, R., Fraedrich, K., and Zhu, X. (2022). Enhanced Joint Tffects of ENSO and IOD on Southeast China Winter Precipitation After 1980s. *Clim. Dyn.* 58, 277–292. doi:10.1007/s00382-021-05907-5

Zhang, R., Li, T., Wen, M., and Liu, L. (2014). Role of Intraseasonal Oscillation in Asymmetric Impacts of El Niño and La Niña on the Rainfall over Southern China in Boreal winter. *Clim. Dyn.* 45, 559–567. doi:10.1007/s00382-014-2207-4

Zhang, R., Sumi, A., and Kimoto, M. (1996). Impact of El Niño on the East Asian Monsoon. *J. Meteorol. Soc. Jpn.* 74, 49–62. doi:10.215/jmsj1965.74.1_4910.2151/jmsj1965.74.1_49

Zhang, W., Jin, F.-F., Li, J., and Ren, H.-L. (2011). Contrasting Impacts of Two-type El Nino over the Western North Pacific during Boreal Autumn. *J. Meteorol. Soc. Jpn.* 89, 563–569. doi:10.2151/jmsj.2011-510

Zhang, W., Jin, F.-F., and Turner, A. (2014). Increasing Autumn Drought over Southern China Associated with ENSO Regime Shift. *Geophys. Res. Lett.* 41, 4020–4026. doi:10.1002/2014GL060130

Zhang, W., Li, H., Jin, F.-F., Stuecker, M. F., Turner, A. G., and Klingaman, N. P. (2015). The Annual-Cycle Modulation of Meridional Asymmetry in ENSO's Atmospheric Response and its Dependence on ENSO Zonal Structure. *J. Clim.* 28, 5795–5812. doi:10.1175/jcli-d-14-00724.1

Zhang, W., Li, H., Stuecker, M. F., Jin, F.-F., and Turner, A. G. (2016). A New Understanding of El Niño's Impact over East Asia: Dominance of the ENSO Combination Mode. *J. Clim.* 29, 4347–4359. doi:10.1175/jcli-d-15-0104.1

Zhang, W., Li, H., Stuecker, M. F., Jin, F.-F., and Turner, A. G. (2016). A New Understanding of El Niño's Impact over East Asia: Dominance of the ENSO Combination Mode. *J. Clim.* 29, 4347–4359. doi:10.1175/JCLI-D-15-0104.1

Zheng, F., Feng, L., and Zhu, J. (2015). An Incursion of Off-Equatorial Subsurface Cold Water and its Role in Triggering the "double Dip" La Niña Event of 2011. *Adv. Atmos. Sci.* 32, 731–742. doi:10.1007/s00376-014-4080-9

Zhou, W., Wang, X., Zhou, T. J., Li, C., and Chan, J. C. L. (2007). Interdecadal Variability of the Relationship between the East Asian winter Monsoon and ENSO. *Meteorol. Atmos. Phys.* 98, 283–293. doi:10.1007/s00703-007-0263-6

Conflict of Interest: The authors declare that the research was conducted in the absence of any commercial or financial relationships that could be construed as a potential conflict of interest.

Publisher's Note: All claims expressed in this article are solely those of the authors and do not necessarily represent those of their affiliated organizations, or those of the publisher, the editors and the reviewers. Any product that may be evaluated in this article, or claim that may be made by its manufacturer, is not guaranteed or endorsed by the publisher.

frontiers | Frontiers in Earth Science

ORIGINAL RESEARCH
published: 14 April 2022
doi: 10.3389/feart.2022.885846

Possible Impact of Boreal Winter Siberian High on ENSO Development in the Following Year

Jiayu Fu, Minghong Liu, Run Wang, Yuwen Wang and Shuo Zhao*

State Key Laboratory of Severe Weather, Institute of Tibetan Plateau and Polar Meteorology, Chinese Academy of Meteorological Sciences, Beijing, China

Siberian High (SH) is the dominant pressure system located in the mid-high latitudes of Eurasia during boreal wintertime. This study reveals a triggering impact of SH variation in preceding winter on the following ENSO events, and gives a possible explanation *via* diagnosing the SH-associated air-sea response over the tropical Pacific and North Pacific. When SH is anomalously enhanced (suppressed) during boreal winter, an Aleutian Low enhanced (suppressed) response will occur over the downstream North Pacific. The Aleutian Low response gradually evolves into a meridional dipole structure similar to the negative (positive) phase of the North Pacific Oscillation (NPO) during the following spring and early summer. Correspondingly, the oceanic response in the North Pacific features a pattern similar to the negative (positive) phase of the Victoria mode. These SH-associated air-sea responses over the subtropical North Pacific will be maintained and further delivered into the tropical Pacific through the so-called seasonal footprinting mechanism, which favors the Bjerknes feedback established around boreal summer and finally grows into a La Niña (El Niño).

Keywords: Siberian High, El Niño-Southern Oscillation, North Pacific, seasonal footprinting mechanism, wind-evaporation-SST feedback

OPEN ACCESS

Edited by:
Ruihuang Xie,
Ocean University of China, China

Reviewed by:
Gen Li,
Hohai University, China
Ruiqiang Ding,
Beijing Normal University, China

****Correspondence:***
Minghong Liu
liuminghong18@mails.ucas.ac.cn

Specialty section:
This article was submitted to Atmospheric Science, a section of the journal Frontiers in Earth Science

Received: *28 February 2022*
Accepted: *28 March 2022*
Published: *14 April 2022*

Citation:
Fu J, Liu M, Wang R, Wang Y and Zhao S (2022) Possible Impact of Boreal Winter Siberian High on ENSO Development in the Following Year. Front. Earth Sci. 10:885846. doi: 10.3389/feart.2022.885846

INTRODUCTION

The El Niño-Southern Oscillation (ENSO) is the dominant interannual variability in the tropical Pacific, which can directly impact the weather and climate in the tropical Pacific and adjacent continents, and have remote effects worldwide through some teleconnection processes (Rasmusson and Carpenter, 1982; Philander, 1983; Jin, 1996; Trenberth et al., 1998; Paegle and Mo, 2002). Nowadays, ENSO plays an important role in seasonal and interannual climate predictions in plenty of regions (e.g., Zhang et al., 1996; McPhaden et al., 2006a; Zhang et al., 2015; Infanti and Kirtman, 2016; Luo et al., 2016). Thus, it is of great value for sciences and social benefits to understand the dynamics and climate impacts of ENSO.

In recent decades, substantial attention has been paid to the ENSO diversity and complexity, and one important part is the diversity of ENSO triggers (Timmermann et al., 2018; Ren et al., 2020). Many studies have indicated that the tropical Pacific air-sea interaction plays a fundamental role in the ENSO dynamics (Bjerknes, 1969; Neelin et al., 1998; Wang, 2018; Ren et al., 2020). However, forcings from the extratropical Pacific are also of great importance in modulating the ENSO outbreaks (e.g., Terray, 2011; Wang et al., 2011). For example, North Pacific Oscillation (NPO) can cause a sea surface temperature (SST) "footprint" when its subtropical portion (0°–20°N) forces the overlying atmosphere, resulting in zonal wind stress anomalies that favor the initiation of an ENSO event (Vimont et al., 2001,

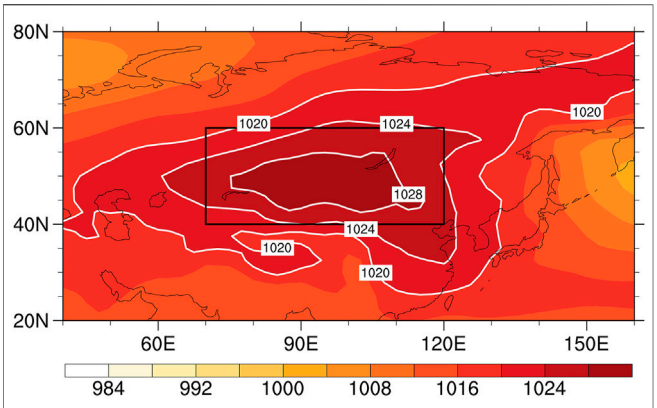

FIGURE 1 | Winter (January-February-March) sea level pressure climatology. Reference period is 1981–2010. Only pressures exceeding 1020hPa are shown as white lines. The values of SLP for the box region are averaged to define the intensity index of the winter Siberian High.

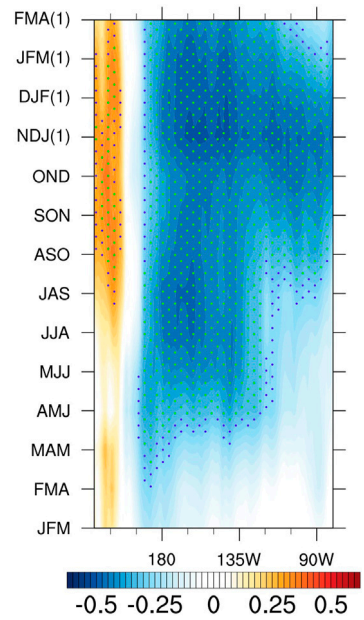

FIGURE 2 | Evolution of equatorial (5°S–5°N-averaged) SST anomalies (Unit: °C) obtained by correlation on the normalized JFM SHI index. Stippled regions in green (purple) indicate anomalies significant at the 90% (95%) confidence level according to the Student's *t* test.

2003; Amaya, 2019). The Victoria Mode (VM), a vital interannual-scale mode of the North Pacific SST anomaly, was also demonstrated to be a potential ENSO precursor (Ding et al., 2015a; 2015b). In addition, the anomalous SST warming in the Indian and Atlantic Oceans could influence the ENSO development *via* interbasin interactions (Li and Mu, 2000; Wang et al., 2017).

Previous studies were more like to seek the possible ENSO triggers in oceans, while there was relatively little attention paid to the impact from atmospheric circulation systems located on the inner continent. The Siberian High (SH) is the most vital high-pressure system in the lower troposphere over Mongolia-Siberia during boreal wintertime, which dominates the low-level atmospheric circulation and the associated anomalous events in almost the whole Asian continent (Ding, 1990; Miyazaki et al., 1999; Gong and Ho, 2002). Moreover, SH can modulate the hemispheric-scale circulation over the downstream Pacific Ocean and more distant regions (Cohen et al., 2001; Wu and Wang, 2002). Given that the tropical air-sea interaction has been found closely tied to variabilities in North Pacific (Bond et al., 2003), it is reasonable to deduce that SH may also have a remote impact on ENSO.

This paper intends to examine the possible impact of the boreal winter SH on the ENSO development in the subsequent year, and explain how the SH-associated impacts maintain and propagate to the tropical Pacific. The remainder of this paper is organized as follows. *Data and Methodology* introduces the data and methods. *Relationship Between the Preceding SH and ENSO in the Following Winter* reveals the linkage between the preceding boreal winter SH and the ENSO in the following winter. The associated physical processes of how SH affects the following ENSO development are described in *Possible Mechanisms Linking the Preceding SH to ENSO*. *Summary and Discussion* gives a summary and brief discussion.

DATA AND METHODOLOGY

The present study employs monthly SST data from the Met Office, Hadley Centre Sea Ice and Sea Surface Temperature dataset (HadISST), with a horizontal resolution of 1° × 1° (Rayner et al., 2003). Atmospheric variables, including monthly sea level pressure (SLP), surface wind stress, pressure-level winds, and surface upward latent heat flux are obtained from the fifth-generation European Center for Medium-Range Weather Forecasts (ECMWF) reanalysis of the global climate (ERA5; Hersbach et al., 2020) at 1° × 1° resolution. All analyses are conducted with a period of 1980–2020. Anomaly is obtained as the departure from the climatological mean of 1981–2010. In order to remove the influence of climate change, the long-term linear trend has been removed.

Following the previous studies (Gong and Ho, 2002), we focus on the variation of SH during late winter (January-February-March, JFM). Siberian High intensity (SHI) index is defined as the mean SLP over a key region (70°–120°E, 40°–60°N), which generally covers the central regions of SH (**Figure 1**). Niño-3.4 index, defined as the averaged SST anomalies over 5°S–5°N and 170°–120°W, is employed to represent the ENSO variability. Regression, correlation, and composite analyses are used to clarify the typical characteristics of the SH-associated air-sea responses, and their statistical significance is determined with the two-tailed Student's *t* test.

RELATIONSHIP BETWEEN THE PRECEDING SH AND ENSO IN THE FOLLOWING WINTER

In this section, we first examined the relationship between the winter SH and tropical Pacific SST anomalies in the following

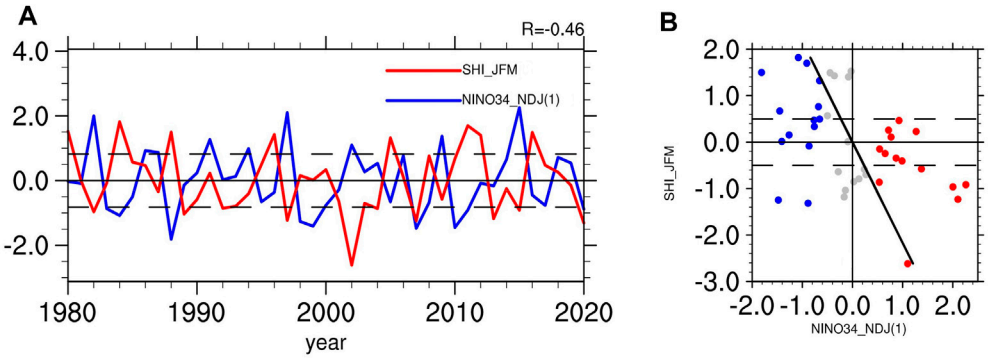

FIGURE 3 | (A) Time series of the JFM SHI index and NDJ (1) Niño-3.4 index during 1980–2020. The correlation coefficient shown in the upper right corner is the correlation with JFM SHI index leading NDJ (1) Niño-3.4 index. **(B)** Scatter plots of the JFM SHI and NDJ (1) Niño-3.4 indices. Both indices are normalized by their standard deviations (STDs), and the red (blue) points are the years with Niño-3.4 indices greater than 0.5 STDs (less than –0.5 STDs), indicating strong El Niño (La Niña) events; grey spots are neutral events. The lines represent the regression fit. Dashed lines indicate that JFM SHI index is equal to 0.5 STDs.

year. **Figure 2** shows the correlation evolution of the JFM SH with the lagged meridional mean (5°S–5°N) of tropical SST anomalies. In total, it highly resembles a typical eastward propagation of ENSO development. A significant negative correlation between the winter SH and following SST anomalies in the equatorial Pacific establishes in the late spring, firstly occurring in the western and central Pacific. This negative correlation will be rapidly enhanced and eastward spread in the following seasons. The strongest correlation between SH and SST anomalies over the Niño-3.4 region occurs at the end of the year (November-December-January (1), NDJ (1), where (1) indicates time comes to the next year). Therefore, the preceding SH variation is likely to be a precursor of an ENSO development in the following year.

Motivated by the high correlation between the winter SH and tropical Pacific SST anomalies in the following winter, we then examine the yearly correspondence of the normalized JFM SHI and NDJ (1) Niño-3.4 indices during the period of 1980–2020, as shown in **Figure 3**. The correlation coefficient of these two indices is −0.46, which is statistically significant at the 99% confidence level. In the previous winter of the three super El Niño events after 1980 (i.e., El Niños in 1982/1983, 1997/1998, and 2015/2016), the SHs were all relatively suppressed. Meanwhile, preceding some typical La Niña events (e.g., La Niñas in 1988/1989, 2010/2011), there were enhanced SHs in winter (**Figure 3A**). In specific, after 12 enhanced SH winters [JFM SHI index >0.5 standard deviations (STDs)], there are 6 years with a La Niña event (NDJ (1) Niño-3.4 index < -0.5 STDs) developed in the subsequent winter. Comparatively, in 9 years out of 15 suppressed winter SH years (JFM SHI index < -0.5 STDs), the Niño-3.4 region becomes anomalous warming in the following, and six of them grow into an El Niño winter (NDJ (1) Niño-3.4 index >0.5 STDs) (**Figure 3B**). The high correspondence of the two indices suggests again that there is a close relationship between the SH variation in the preceding winter and the development of ENSO in the following winter. Moreover, the potential impact of preceding SH on ENSO is generally symmetric between the enhanced and suppressed SH.

To explore the typical characteristics of the potential impacts of the preceding SH, we select the historical years when apparent SH variation leads to the following ENSO events and conduct a composite analysis on the atmospheric and oceanic anomalies during these years. The six La Niña years with enhanced SH (1984, 1988, 2005, 2008, 2010, 2011) are identified as years with the JFM SHI index exceeding 0.5 STDs and NDJ (1) Niño-3.4 index lower than -0.5 STDs. Similarly, six El Niño years with suppressed SH (1982, 1997, 2002, 2004, 2009, 2015) are years with the JFM SHI index lower than -0.5 STDs and NDJ (1) Niño-3.4 index higher than 0.5 STDs. As shown in **Figure 4A**, when the SH is anomalously enhanced during the boreal wintertime, there is no significant synchronized SST response in the tropical Pacific, but some easterly wind anomalies occur over the warm pool. In the North Pacific, there is a significant low-level westerly wind anomaly over around 30°–40°N, with a strong anticyclonic atmospheric circulation at its southern flank. Accordingly, there are weak SST warming responses excited underlying the anomalous winds (**Figure 4A**). Coming to the late spring (April-May-June, AMJ), the subtropical anticyclone and corresponding horseshoe-shaped SST response are further intensified. The negative SST anomalies in the subtropical Pacific are enhanced and southward extend to the tropical central Pacific and eastern Pacific. In addition, the easterly wind anomalies only covering the warm pool in the preceding season also extend to the tropical central-eastern Pacific (**Figure 4B**).

Entering the second half of the year, the meridional horseshoe-shaped pattern of SST response in the North Pacific shows little changes except the westward extending of warming SST to the Asian coasts and warm pool area. In the tropics, the negative SST anomalies are further enhanced, and the center of anomalies gradually extends from the western Pacific to the central-eastern Pacific. Meanwhile, the easterly wind anomalies develop and cover the whole Pacific equatorial band (**Figures 4C,D**). These variations can be attributed to the positive feedback of zonal wind and SST gradient, namely, the so-called Bjerknes feedback (Bjerknes, 1969; Neelin et al., 1998; Wang, 2018; Ren et al., 2020). The above composite analysis implies that the North

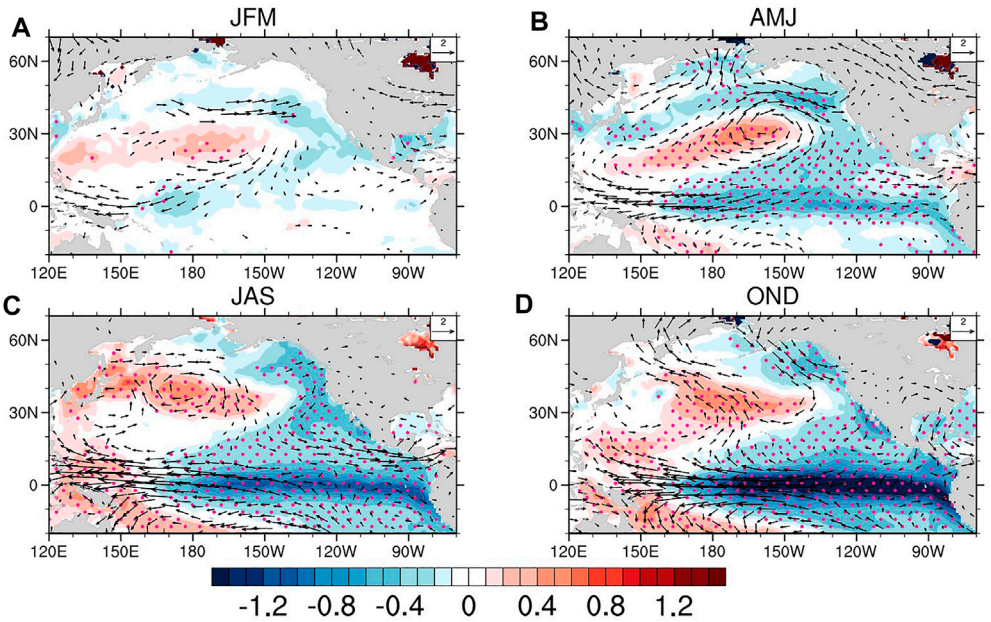

FIGURE 4 | Composite SST (°C) and 850-hPa winds (vectors; m s^{-1}) in the La Niña years with enhanced SH and El Niño years with suppressed SH (multiply by a factor of -1) during **(A)** January-February-March (JFM), **(B)** April-May-June (AMJ), **(C)** July-August-September (JAS) and **(D)** October-November-December (OND). Stippled regions indicate anomalies significant at the 90% confidence level. Only wind anomalies significant at the 90% confidence level are plotted.

Pacific may be a critical passway of the SH impacts, where the anomalous signal maintains and propagates before the Bjerknes feedback established in the second half of the year.

POSSIBLE MECHANISMS LINKING THE PRECEDING SH TO ENSO

The above results have shown that the JFM SH, as a precursor, may influence the occurrence and development of ENSO. There is no doubt that the strong tropical Bjerknes feedback dominates the development of ENSO during the second half of the year. However, how the preceding SH initiates the Bjerknes feedback in the first half of the year remains unclear. Given that North Pacific may be the vital passway, next, we examined the evolutionary features of North Pacific air-sea anomalies associated with the SH during the first half of the year to clarify the possible mechanisms.

Figure 5 illustrates regressions of the North Pacific SLP and 850-hPa wind anomalies in JFM and AMJ upon the JFM SHI index. The JFM SLP anomalies exhibit a negative response over the mid-latitude North Pacific, resembling an enhanced Aleutian Low (AL) anomaly (**Figure 5A**) (Overland et al., 1999). The corresponding variation between the SH and AL reflects the connectivity among atmospheric centers of action. Referring to previous work (Chen et al., 2020), an AL intensity (ALI) index is defined to describe the strength variation of AL (**Table 1**). As shown in **Figure 6**, the AL response over the North Pacific to the JFM SH begins quickly and remains throughout the winter and spring. The negative correlation reaches the highest when AL lags SH about 1 month. Affected by the enhanced AL, significant low-level westerly wind anomalies occur at the southern flank of AL. Besides, there are easterly wind anomalies confined over the warm pool (**Figure 5A**). Moreover, the westerly wind anomalies at the southern flank of AL are opposite to the background winds, which may cause the warm SST anomalies observed in the central subtropical North Pacific (**Figure 7A**) by weakening the local evaporation (**Figure 8A**) (Chen et al., 2020).

The anomalous AL response in the mid-latitude North Pacific diminishes rapidly in spring (**Figure 5B**). The SH-related SLP anomalies change from the anomalous AL pattern to a meridional dipole pattern with centers in the 60°N and 30° N North Pacific, respectively, which is similar to the pattern of NPO (Wallace and Gutzler, 1981). Several studies have suggested that such variation may be attributed to the interaction between the synoptic-scale eddy activity and mean flow and associated vorticity transportation. Westerly wind anomalies at the southern flank of the enhanced AL are accompanied by an increased synoptic-scale eddy activity, which will excite an anomalous anticyclonic circulation in the subtropical North Pacific (Chen et al., 2014; Chen et al., 2020). Connected with atmospheric circulation changes, a remarkable northeast-southwest dipole mode of SST anomalies occurs in the North Pacific in late spring (AMJ), namely, the so-called VM pattern (Bond et al., 2003; Ding et al., 2015b). The positive SST anomalies in the central subtropical North Pacific are enhanced. Moreover, significant negative SST anomalies occur at the northern and southern flanks of the positive anomalies, extending from the coast of North America to the central subtropical North Pacific (**Figure 7B**).

The correlation evolution of indices between the JFM SHI and associated air-sea responses in the North Pacific also reflects the

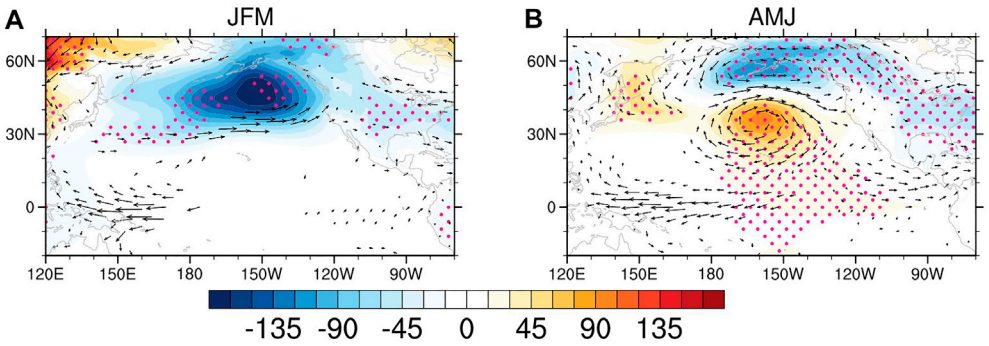

FIGURE 5 | Regression of 850-hPa winds (vectors; m s^{-1}) and SLP (shading; hPa) anomalies in **(A)** JFM, **(B)** AMJ onto the normalized JFM SHI index. Stippled regions indicate SLP anomalies significant at the 90% confidence level. Only wind anomalies significant at the 90% confidence level are plotted.

TABLE 1 | Definitions of the AL, NPO and VM indices.

	Definitions	Sources
AL	area-averaged SLP anomalies over 30°–65°N, 160°E–140°W	Chen et al. (2020)
NPO	PC time series corresponding to EOF2 of SLP anomalies over 120°E–80°W, 20°–60°N	Yu and Kim, (2011)
VM	PC time series corresponding to EOF2 of the North Pacific (124.5°E–100.5°W, 20.5°N–65.5°N) monthly SST anomalies (after removing the monthly mean global average SST anomalies)	Ding et al. (2015b)

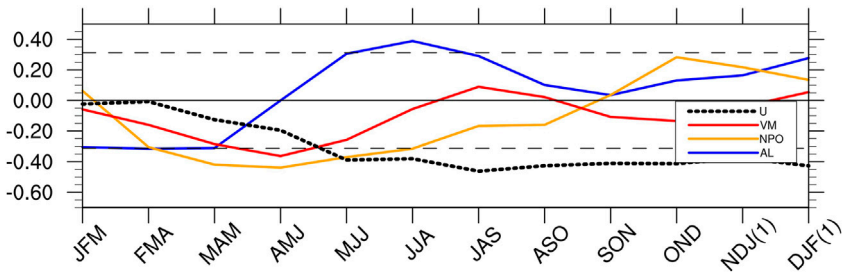

FIGURE 6 | Lag correlation coefficients between the JFM SHI and the AL (blue), NPO (yellow), VM (red), U (black) indices during 1979–2020. The U index is defined as the regional mean 10-m zonal wind anomaly in the equatorial eastern-central Pacific (10°S–10°N, 180° E–120°W). The horizontal axis represents the target month of used AL, NPO, VM, and U indices. The dashed lines indicate the correlation coefficient significant at the 95% confidence level. Time notations indicate the year alongside and (1) indicate time comes to the next year.

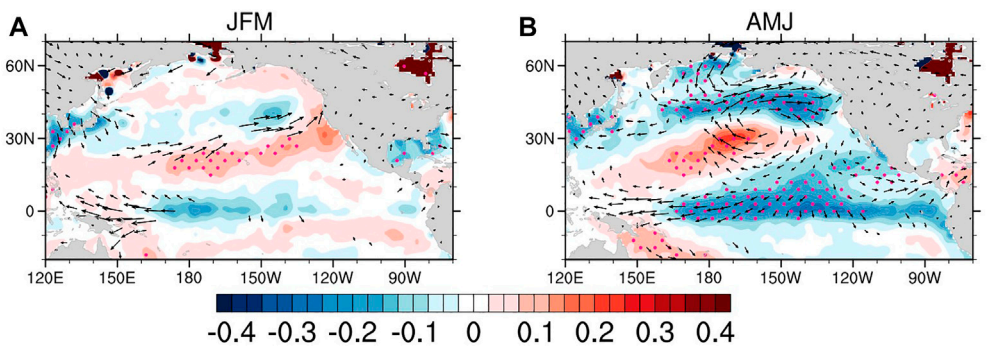

FIGURE 7 | Regression of SST anomalies (°C) and 10-m winds (vectors; m s^{-1}) anomalies in **(A)** JFM and **(B)** AMJ onto the normalized JFM SHI index. Stippled regions indicate anomalies significant at the 90% confidence level. Only wind anomalies significant at the 90% confidence level are plotted.

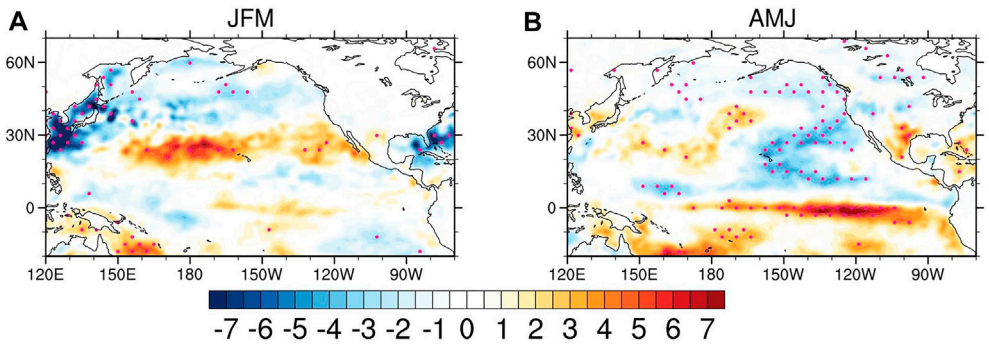

FIGURE 8 | Regression of surface upward latent heat flux (shading; W m^{-2}) anomalies in **(A)** JFM, **(B)** AMJ onto the normalized JFM SHI index. Stippled regions indicate latent heat flux anomalies significant at the 90% confidence level. Downward fluxes are positive, indicating the transfer of energy from the atmosphere to the ocean.

aforementioned processes (**Figure 6**). The SHI index poorly correlates with the NPO and VM indices in late winter. While in spring, when the relationship between SH and AL decays, the correlation between JFM SH and NPO becomes significant and can last throughout the whole summer, indicating that the SH-related atmospheric response gradually changes into an NPO-like pattern. Meanwhile, the negative correlation between the VM and JFM SH also becomes significant in late spring.

Previous studies suggested that the NPO-induced SLP anomalies linking with the North Pacific trade winds can excite surface and subsurface temperature anomalies in the equatorial Pacific, which is beneficial to developing ENSO events (Vimont et al., 2001; Vimont et al., 2003; Anderson et al., 2013). Moreover, the SST anomalies featuring a VM pattern can also transfer the anomaly from extratropical North Pacific to equatorial Pacific and support the occurrence of ENSO events (Ding et al., 2015a; Ding et al., 2015b). When SH is enhanced in the preceding winter, the NPO-like pattern in late spring features an anticyclonic circulation over the subtropical North Pacific. The northeasterly wind anomalies at its southern side strengthen the trade winds (**Figure 5B**), thus sharpening the evaporation over the subtropical northeastern Pacific (**Figure 8B**) and leading to the local cooling anomalies (**Figure 7B**). The cooling anomalies can further strengthen the northeasterly wind anomalies and evaporation through the so-called wind-evaporation-SST feedback, which can sustain and stretch to the central equatorial Pacific during the spring and summer (Xie and Philander, 1994; Chiang and Vimont, 2004). The coupled easterly winds and cooling SST anomalies extending to the equator will enhance the zonal air-sea interaction over the equatorial Pacific. Besides, the associated off-equatorial wind stress curl anomalies may lead to a discharge of the subsurface heat content (Ding et al., 2015b; Amaya, 2019). Both processes contribute to establishing the tropical Bjerknes feedback, favoring the subsequent ENSO development. As shown in **Figure 6**, the negative correlation between zonal wind anomalies in the central-eastern equatorial Pacific and JFM SHI is insignificant until summer. With the development of ENSO, this negative correlation will last in the second half of the year.

SUMMARY AND DISCUSSION

As one of the vital atmospheric circulation systems in the northern hemisphere during boreal wintertime, SH has remote impacts on the hemispheric-scale atmospheric circulation over the downstream regions. Our study found that the SH variation in the previous winter is well correlated with the tropical Pacific SST anomalies in the following year, which can be used as an atmospheric precursor of ENSO. An enhanced SH in the previous winter is likely to trigger a La Niña-related SST anomalous pattern in the central-eastern equatorial Pacific in the following winter. Conversely, a suppressed SH may lead to an El Niño event.

Through diagnosing the air-sea responses over the North Pacific and tropical Pacific, we gave a possible explanation of how the SH impacts maintain, propagate, and eventually trigger an ENSO in the following year. As summarized schematically in **Figure 9**, in response to a strengthened boreal winter SH, an enhanced AL response will occur over the downstream North Pacific. During the late spring (AMJ), this anomalous AL response gradually evolves into an NPO-like SLP structure. Correspondingly, the North Pacific SST anomalies feature a typical VM pattern. In the subtropical North Pacific, the NPO-like atmospheric circulation and VM-associated SST anomalies cause a cooling SST "footprint." This cooling SST and associated northeasterly wind anomalies can be enhanced and delivered to the central Pacific through the seasonal footprinting mechanism. That contributes to the rapid development of the tropical Bjerknes feedback in summer and eventually results in a La Niña event. Similarly, the North Pacific air-sea responses will be in the opposite phase when a suppressed SH occurs, contributing to an El Niño event.

This study links the preceding SH variation and following ENSO development through air-sea interactions over North Pacific. However, it should be noticed that these North Pacific air-sea interactions may be sensitive to the background interdecadal time scales. For example, the Arctic Oscillation showing a substantial interdecadal variability could

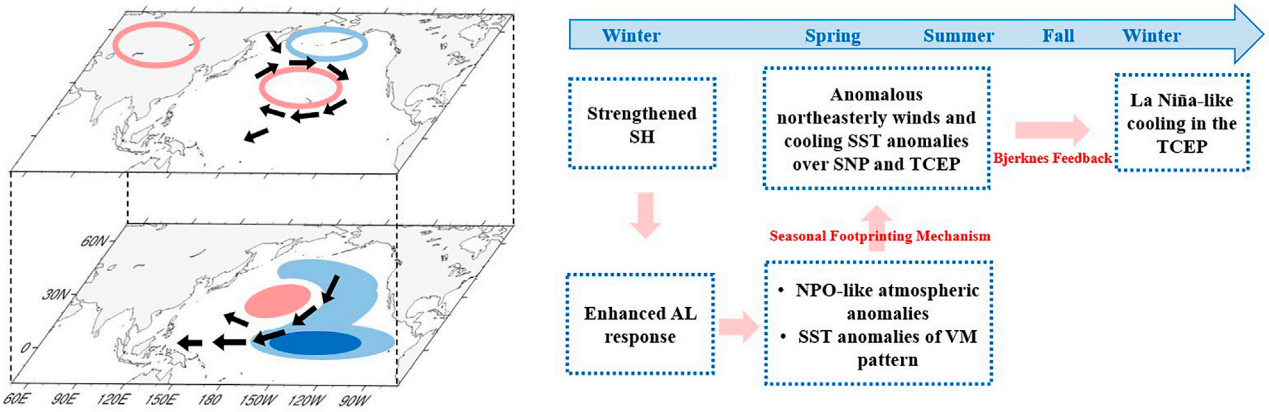

FIGURE 9 | A mechanism diagram showing the processes linking the SH to the subsequent winter ENSO. Red (blue) circles indicate positive (negative) SLP anomalies. Red (blue) shading denotes positive (negative) SST anomalies. Black arrows are surface wind anomalies. SNP and TCEP denote subtropical North Pacific and tropical central-eastern Pacific, respectively.

significantly affect the seasonal footprinting mechanism (Yeo et al., 2012; Chen et al., 2013). Some interdecadal variabilities, such as Pacific Decadal Oscillation, can directly change the linkage between North Pacific and tropical Pacific (Vimont et al., 2003; Krishnamurthy and Krishnamurthy, 2014). How the SH-ENSO relationship will change under different interdecadal modulation, and the detailed mechanisms are worthy of being further investigated. Besides, there may be more possible ways of the SH impact on following ENSO. For example, SH is one of the critical components of the East Asian Winter Monsoon (EAWM) system. Associated with the EAWM variation, there may be anomalous Madden-Julian Oscillation activity and westerly winds over the western equatorial Pacific, thus significantly impacting the following ENSO development (Lengaigne et al., 2004; McPhaden et al., 2006b; Chen et al., 2017). This hypothesis and its detailed mechanism need to be further diagnosed in the future.

The impact of preceding SH on the following ENSO complements the understanding of the complexity and diversity of ENSO developments. It also provides a new explanation for the onset of ENSO events without apparent precursors in the tropical Pacific. However, this understanding is still in infancy, and further numerical validation needs to be carried out in the future. The SH variation is relatively easy to monitor and represent compared to other extratropical ENSO precursors, such as the NAO and VM. Besides, it precedes around 1 year before the following ENSO, which occurs even prior to the spring predictability barrier of ENSO (Webster and Yang, 1992). Thus, the SH variation promises to be an effective long-leading predictor of ENSO, which can help improve the seasonal-interannual ENSO prediction and weaken the predictability barrier if reasonably used.

DATA AVAILABILITY STATEMENT

Publicly available datasets were analyzed in this study. This data can be found here: The Met Office, Hadley Centre Sea Ice and Sea Surface Temperature dataset (HadISST): https://www.metoffice.gov.uk/hadobs/hadisst/, and the ERA-5 dataset of the European Centre for Medium-Range Weather Forecasts: https://cds.climate.copernicus.eu/cdsapp#!/dataset/reanalysis-era5-pressure-levels-monthly-means?tab=overview.

AUTHOR CONTRIBUTIONS

JF, ML, and RW contributed to conception and design of the study. JF organized the database. JF and SZ performed the statistical analysis. JF wrote the first draft of the manuscript. ML, RW, and YW contributed to manuscript revision, read, and approved the submitted version.

FUNDING

This work was jointly supported by the National Natural Science Foundation of China under Grant 42105067, 41975094, and the Basic Research and Operational Special Project of CAMS (2021Z007).

REFERENCES

Amaya, D. J. (2019). The Pacific Meridional Mode and ENSO: a Review. *Curr. Clim. Change Rep.* 5, 296–307. doi:10.1007/s40641-019-00142-x

Anderson, B. T., Perez, R. C., and Karspeck, A. (2013). Triggering of El Niño Onset through Trade Wind-Induced Charging of the Equatorial Pacific.. *Geophys. Res. Lett.* 40, 1212–1216. doi:10.1002/grl.50200

Bjerknes, J. (1969). Atmospheric Teleconnections from the Equatorial Pacific1. *Mon. Wea. Rev.* 97, 163–172. doi:10.1175/1520-0493(1969)097<0163:atftep>2.3.co;2

Bond, N. A., Overland, J. E., Spillane, M., and Stabeno, P. (2003). Recent Shifts in the State of the North Pacific. *Geophys. Res. Lett.* 30, a–n. doi:10.1029/2003GL018597

Chen, S. F., Yu, B., and Chen, W. (2014). An Analysis on the Physical Process of the Influence of AO on ENSO. *Clim. Dyn.* 42, 973–989. doi:10.1007/s00382-012-1654-z

Chen, S., Chen, W., Wu, R., Yu, B., and Graf, H.-F. (2020). Potential Impact of Preceding Aleutian Low Variation on El Niño-Southern Oscillation during the Following Winter. *J. Clim.* 33, 3061–3077. doi:10.1175/JCLI-D-19-0717.1

Chen, S., Chen, W., Yu, B., and Graf, H.-F. (2013). Modulation of the Seasonal Footprinting Mechanism by the Boreal spring Arctic Oscillation. *Geophys. Res. Lett.* 40, 6384–6389. doi:10.1002/2013GL058628

Chen, X., Li, C., Ling, J., and Tan, Y. (2017). Impact of East Asian winter Monsoon on MJO over the Equatorial Western Pacific. *Theor. Appl. Climatol* 127, 551–561. doi:10.1007/s00704-015-1649-x

Chiang, J. C. H., and Vimont, D. J. (2004). Analogous Pacific and Atlantic Meridional Modes of Tropical Atmosphere-Ocean Variability*. *J. Clim.* 17, 4143–4158. doi:10.1175/JCLI4953.1

Cohen, J., Saito, K., and Entekhabi, D. (2001). The Role of the Siberian High in Northern Hemisphere Climate Variability. *Geophys. Res. Lett.* 28, 299–302. doi:10.1029/2000GL011927

Ding, R., Li, J., Tseng, Y.-H., and Ruan, C. (2015a). Influence of the North Pacific Victoria Mode on the Pacific ITCZ Summer Precipitation. *J. Geophys. Res. Atmos.* 120, 964–979. doi:10.1002/2014JD022364

Ding, R., Li, J., Tseng, Y.-H., Sun, C., and Guo, Y. (2015b). The Victoria Mode in the North Pacific Linking Extratropical Sea Level Pressure Variations to ENSO. *J. Geophys. Res. Atmos.* 120, 27–45. doi:10.1002/2014JD022221

Gong, D.-Y., and Ho, C.-H. (2002). The Siberian High and Climate Change over Middle to High Latitude Asia. *Theor. Appl. Climatology* 72, 1–9. doi:10.1007/s007040200008

Hersbach, H., Bell, B., Berrisford, P., Hirahara, S., Horányi, A., Muñoz-Sabater, J., et al. (2020). The ERA5 Global Reanalysis. *Q.J.R. Meteorol. Soc.* 146, 1999–2049. doi:10.1002/qj.3803

Infanti, J. M., and Kirtman, B. P. (2016). North American Rainfall and Temperature Prediction Response to the Diversity of ENSO. *Clim. Dyn.* 46, 3007–3023. doi:10.1007/s00382-015-2749-0

Jin, F.-F. (1996). Atmosphere Interaction, the Pacific Cold Tongue, and the El Niño-Southern Oscillation. *Science* 274, 76–78. doi:10.1126/science.274.5284.76

Krishnamurthy, L., and Krishnamurthy, V. (2014). Influence of PDO on South Asian Summer Monsoon and Monsoon-ENSO Relation. *Clim. Dyn.* 42, 2397–2410. doi:10.1007/s00382-013-1856-z

Lengaigne, M., Boulanger, J.-P., Menkes, C., Delecluse, P., and Slingo, J. (2004). "Westerly Wind Events in the Tropical Pacific and Their Influence on the Coupled Ocean-Atmosphere System: A Review," in *Earth's Climate*. Editors C. Wang, S. Xie, and J. Carton (American Geophysical Union), 147, 49–69. doi:10.1029/147GM03*Geophysical Monograph Series*

Li, C., and Mu, M. (2000). Relationship between East Asian winter Monsoon, Warm Pool Situation and ENSO Cycle. *Chin.Sci.Bull.* 45, 1448–1455. doi:10.1007/BF02898885

Luo, J.-J., Yuan, C., Sasaki, W., Behera, S. K., Masumoto, Y., Yamagata, T., et al. (2016). "Current Status of Intraseasonal-Seasonal-To-Interannual Prediction of the Indo-Pacific Climate," in *Indo-Pacific Climate Variability and Predictability*. Editors T. Yamagata and S. Behera (World Scientific Publisher World Scientific Series on Asia-Pacific Weather and Climate), 7, 63–107. doi:10.1142/9789814696623_0003

McPhaden, M. J., Zebiak, S. E., and Glantz, M. H. (2006a). ENSO as an Integrating Concept in Earth Science. *Science* 314, 1740–1745. doi:10.1126/science.1132588

McPhaden, M. J., Zhang, X., Hendon, H. H., and Wheeler, M. C. (2006b). Large Scale Dynamics and MJO Forcing of ENSO Variability. *Geophys. Res. Lett.* 33, L16702. doi:10.1029/2006GL026786

Miyazaki, S., Yasunari, T., and Adyasuren, T. (1999). Abrupt Seasonal Changes of Surface Climate Observed in Northern Mongolia by an Automatic Weather Station. *J. Meteorol. Soc. Jpn.* 77, 583–593. doi:10.2151/jmsj1965.77.2_583

Neelin, J. D., Battisti, D. S., Hirst, A. C., Jin, F.-F., Wakata, Y., Yamagata, T., et al. (1998). ENSO Theory. *J. Geophys. Res.* 103 (C7), 14261–14290. doi:10.1029/97JC03424

Overland, J. E., Adams, J. M., and Bond, N. A. (1999). Decadal Variability of the Aleutian Low and its Relation to High-Latitude Circulation*. *J. Clim.*, 12. 15422–21548. doi:10.1175/1520–0442(1999)012<1542:DVOTAL>2.010.1175/1520-0442(1999)012<1542:dvotal>2.0.co;2

Paegle, J. N., and Mo, K. C. (2002). Linkages between Summer Rainfall Variability over South America and Sea Surface Temperature Anomalies. *J. Clim.* 15, 1389–1407. doi:10.1175/1520-0442(2002)015<1389:LBSRVO>2.0.CO;2>

Philander, S. G. H. (1983). El Niño Southern Oscillation Phenomena. *Nature* 302, 295–301. doi:10.1038/302295a0

Rasmusson, E. M., and Carpenter, T. H. (1982). Variations in Tropical Sea Surface Temperature and Surface Wind Fields Associated with the Southern Oscillation/El Niño. *Mon. Wea. Rev.* 110, 354–384. doi:10.1175/1520-0493(1982)110<0354:vitsst>2.0.co;2

Rayner, N. A., Parker, D. E., Horton, E., Folland, C. K., Alexander, L. V., Rowell, D., et al. (2003). Global Analyses of Sea Surface Temperature, Sea Ice, and Night marine Air Temperature since the Late Nineteenth century. *J. Geophys. Res.* 108, 4407. doi:10.1029/2002JD002670

Ren, H.-L., Zheng, F., Luo, J.-J., Wang, R., Liu, M., Zhang, W., et al. (2020). A Review of Research on Tropical Air-Sea Interaction, ENSO Dynamics, and ENSO Prediction in China. *J. Meteorol. Res.* 34, 43–62. doi:10.1007/s13351-020-9155-1

Terray, P. (2011). Southern Hemisphere Extra-tropical Forcing: a New Paradigm for El Niño-Southern Oscillation. *Clim. Dyn.* 36, 2171–2199. doi:10.1007/s00382-010-0825-z

Timmermann, A., An, S.-I., Kug, J.-S., Jin, F.-F., Cai, W., Capotondi, A., et al. (2018). El Niño-Southern Oscillation Complexity. *Nature* 559, 535–545. doi:10.1038/s41586-018-0252-6

Trenberth, K. E., Branstator, G. W., Karoly, D., Kumar, A., Lau, N.-C., and Ropelewski, C. (1998). Progress during TOGA in Understanding and Modeling Global Teleconnections Associated with Tropical Sea Surface Temperatures. *J. Geophys. Res.* 103, 14291–14324. doi:10.1029/97JC01444

Vimont, D. J., Battisti, D. S., and Hirst, A. C. (2001). Footprinting: A Seasonal Connection between the Tropics and Mid-latitudes. *Geophys. Res. Lett.* 28, 3923–3926. doi:10.1029/2001GL013435

Vimont, D. J., Wallace, J. M., and Battisti, D. S. (2003). The Seasonal Footprinting Mechanism in the Pacific: Implications for ENSO*. *J. Clim.* 16, 26682–32675. doi:10.1175/1520-0442(2003)016<2668:TSFMIT>2.0.CO10.1175/1520-0442(2003)016<2668:tsfmit>2.0.co;2

Wallace, J. M., and Gutzler, D. S. (1981). Teleconnections in the Geopotential Height Field during the Northern Hemisphere winter. *Mon. Wea. Rev.* 109 (4), 7842–8812. doi:10.1175/1520-0493(1981)109<0784:TITGHF>2.0.CO10.1175/1520-0493(1981)109<0784:titghf>2.0.co;2

Wang, C. (2018). A Review of ENSO Theories. *Natl. Sci. Rev.* 5, 813–825. doi:10.1093/nsr/nwy104

Wang, L., Yu, J.-Y., and Paek, H. (2017). Enhanced Biennial Variability in the Pacific Due to Atlantic Capacitor Effect. *Nat. Commun.* 8, 14887. doi:10.1038/ncommsl488710.1038/ncomms14887

Wang, X., Wang, C., Zhou, W., Wang, D., and Song, J. (2011). Teleconnected Influence of North Atlantic Sea Surface Temperature on the El Niño Onset. *Clim. Dyn.* 37, 663–676. doi:10.1007/s00382-010-0833-z

Webster, P. J., and Yang, S. (1992). Monsoon and ENSO: Selectively Interactive Systems. *Q.J R. Met. Soc.* 118, 877–926. doi:10.1002/qj.49711850705

Wu, B., and Wang, J. (2002). Winter Arctic Oscillation, Siberian High and East Asian winter Monsoon. *Geophys. Res. Lett.* 29, 3–1. doi:10.1029/2002GL015373

Xie, S.-P., and Philander, S. G. H. (1994). A Coupled Ocean-Atmosphere Model of Relevance to the ITCZ in the Eastern Pacific. *Tellus A* 46, 340–350. doi:10.1034/j.1600-0870.1994.t01-1-00001.x

Yeo, S.-R., Kim, K.-Y., Yeh, S.-W., and Kim, W. (2012). Decadal Changes in the Relationship between the Tropical Pacific and the North Pacific. *J. Geophys. Res.* 117, a–n. doi:10.1029/2012JD017775

Yihui, D. (1990). Build-up, Air Mass Transformation and Propagation of Siberian High and its Relations to Cold Surge in East Asia. *Meteorl. Atmos. Phys.* 44, 281–292. doi:10.1007/BF01026822

Yu, J.-Y., and Kim, S. T. (2011). Relationships between Extratropical Sea Level Pressure Variations and the Central Pacific and Eastern Pacific Types of ENSO. *J. Clim.* 24, 708–720. doi:10.1175/2010JCLI3688.1

Zhang, R., Sumi, A., and Kimoto, M. (1996). Impact of El Niño on the East Asian Monsoon. *J. Meteorol. Soc. Jpn.* 74, 49–62. doi:10.215/jmsj1965.74.1_4910. 2151/jmsj1965.74.1_49

Zhang, W., Wang, Y., Jin, F.-F., Stuecker, M. F., and Turner, A. G. (2015). Impact of Different El Niño Types on the El Niño/IOD Relationship. *Geophys. Res. Lett.* 42, 8570–8576. doi:10.1002/2015GL065703

Conflict of Interest: The authors declare that the research was conducted in the absence of any commercial or financial relationships that could be construed as a potential conflict of interest.

frontiers | Frontiers in Earth Science

ORIGINAL RESEARCH
published: 25 April 2022
doi: 10.3389/feart.2022.899323

ENSO Diversity Simulated in a Revised Cane-Zebiak Model

Licheng Geng and Fei-Fei Jin*

Department of Atmospheric Sciences, University of Hawai'i at Mānoa, Honolulu, HI, United States

The El Niño-Southern Oscillation (ENSO) phenomenon features rich sea surface temperature (SST) spatial pattern variations dominated by the Central Pacific (CP) and Eastern Pacific (EP) patterns during its warm phase. Understanding such ENSO pattern diversity has been a subject under extensive research activity. To provide a framework for unveiling the fundamental dynamics of ENSO diversity, an intermediate coupled model based on the Cane-Zebiak-type framework, named RCZ, is established in this study. Compared with the original Cane-Zebiak model, RCZ consists of revised model formulation and well-tuned parameterization schemes. All model components are carefully validated against the observations *via* the standalone mode, in which the observed anomalous SST (wind stress) forcing is prescribed to drive the atmospheric (oceanic) component. The superiority of RCZ's model components over those in the original Cane-Zebiak model is evidenced by their better performance in simulating the observations. Coupled simulation with RCZ satisfactorily reproduces aspects of the observed ENSO characteristics, including the spatial pattern, phase-locking, amplitude asymmetry, and, particularly, ENSO diversity/bi-modality. RCZ serves as a promising tool for studying dynamics of ENSO diversity as it resolves most of the relevant processes proposed in the literature, including atmospheric nonlinear convective heating, oceanic nonlinear dynamical heating, and the ENSO/westerly wind burst interaction.

Keywords: El Niño-Southern Oscillation, ENSO diversity, ENSO bi-modality, Cane-Zebiak model, nonlinear convective heating, subsurface temperature parameterization

OPEN ACCESS

Edited by:
Hong-Li Ren,
Chinese Academy of Meteorological Sciences, China

Reviewed by:
Xin Geng,
Nanjing University of Information Science and Technology, China
Run Wang,
Chinese Academy of Meteorological Sciences, China

****Correspondence:***
Licheng Geng
lgeng@hawaii.edu

Specialty section:
This article was submitted to Atmospheric Science, a section of the journal Frontiers in Earth Science

Received: *18 March 2022*
Accepted: *06 April 2022*
Published: *25 April 2022*

Citation:
Geng L and Jin F-F (2022) ENSO Diversity Simulated in a Revised Cane-Zebiak Model. Front. Earth Sci. 10:899323. doi: 10.3389/feart.2022.899323

1 INTRODUCTION

The El Niño-Southern Oscillation (ENSO), a basin-scale atmosphere-ocean coupled phenomenon, is the dominant interannual climate variability in the tropics. Since the Tropical Ocean-Global Atmosphere (TOGA) decade, extensive observational studies have unveiled the ENSO temporal complexity and inter-event pattern diversity (Timmermann et al., 2018, and references therein). El Niño exhibits rich diversity in the sea surface temperature anomaly (SSTA) pattern at its mature phase and is accordingly categorized into two types/flavors- Eastern Pacific (EP) El Niño and Central Pacific (CP) El Niño (Larkin and Harrison, 2005; Ashok et al., 2007; Kao and Yu, 2009; Kug et al., 2009; Yeh et al., 2009; Ren and Jin, 2011). Corresponding to the contrasting spatial pattern and magnitude of the associated SSTA, the two types of El Niño exhibit substantial differences in their impacts (see review articles by Yang et al., 2018; Taschetto et al., 2020; Cai et al., 2021). In contrast to El Niño, La Niña exhibits less obvious pattern diversity (Kug and Ham, 2011).

The distinct feedback processes associated with the two types of El Niño have been well documented. Growth of SSTA during EP and CP El Niño events is accomplished by different combinations of thermocline feedback and zonal advective feedback, with the latter being more (less)

important for CP (EP) El Niño (Kug et al., 2009; Capotondi, 2013; Ren and Wang, 2020; Wang and Ren, 2020). The discharge/recharge paradigm serves as delayed-negative feedback and thus contributes to the phase transition of EP El Niño. Such a slow oceanic adjustment process, however, is less distinct for CP El Niño (Kug et al., 2010; McPhaden, 2012; Capotondi, 2013; Ren and Jin, 2013).

A large amount of research efforts has been put forth to advance our understanding of the coexistence of the two types of El Niño. The current understanding of ENSO diversity is generally classified into two camps, representing two distinct possible pathways. The first understanding, which is essentially from the linear perspective, underscores the role played by stochastic processes in generating the two types of ENSO through exciting either two coexisting ENSO-like linear modes or distinct optimal growth (Bejarano and Jin, 2008; Newman et al., 2011a; Newman et al., 2011b; Vimont et al., 2014; Vimont et al., 2022; Chen et al., 2015; Hayashi and Watanabe, 2017; Xie and Jin, 2018). The other understanding emphasizes the effect of nonlinear processes and speculates that the two types of ENSO represent the moderate and extreme regimes of the universal ENSO phenomenon (Takahashi et al., 2011; Takahashi and Dewitte, 2016; Okumura, 2019). Due to their limitations, neither of the above two understandings is conclusive; the dynamics of ENSO diversity is still far from being fully understood. A major roadblock is the intertwining of proposed mechanisms in explaining various aspects of ENSO diversity. To unambiguously disentangle its dynamics, one needs to turn to a simple but comprehensive framework that allows a clean separation among the possible mechanisms.

The classic Cane-Zebiak model (CZ model hereafter; Zebiak and Cane, 1987, ZC87 hereafter), along with its simplified variants (e.g., Jin and Neelin, 1993; Jin, 1997), has dramatically advanced ENSO research as it provides a decent framework for studies on ENSO theory, modeling, and prediction. It is also a useful tool for studying ENSO diversity as it allows testing of contribution from various mechanisms by switching on/off relevant processes. Recently, the CZ model has been utilized to investigate 1) the linear ENSO dynamics of relevance to ENSO diversity (Bejarano and Jin, 2008; Xie and Jin, 2018) and 2) the effects of westerly wind bursts and their interaction with ENSO on ENSO diversity (Chen et al., 2015; Hayashi and Watanabe, 2017). It deserves to point out that the CZ model was built more than three decades ago, when there was not enough observational data, especially oceanic data, to test its validity. With the emerging satellite and *in-situ* data not long after the model was established, Perigaud and Dewitte (1996) and Dewitte and Perigaud (1996) were able to identify several deficiencies in the CZ model components. It has been noted in Geng (2021) that characteristics of ENSO diversity exhibit strong sensitivity to the mean state and feedback processes, which effectively determine the ENSO regime. Thus, attempts toward understanding ENSO diversity with the CZ model shall be cautious, especially considering that the mean state and model parameters in such an anomaly model are somewhat arbitrary.

Inspired by the convenience of the Cane-Zebiak-type framework for studying ENSO diversity while acknowledging its deficiencies, we aim to build a revised CZ model in which model formulation and parameterization schemes are improved and carefully validated. The model is referred to as RCZ, with "R" denoting "revised". **Section 2** provides the model description and verification of model components against observations. Characteristics of RCZ-simulated ENSO behavior are summarized in **Section 3**. Summary and some discussions on shortcomings and potential improvements of RCZ are presented in **Section 4**.

2 MODEL DESCRIPTION AND VERIFICATION

2.1 Revisions to the CZ Model

The skeleton of RCZ resembles that of the CZ model, comprising a diagnostic atmospheric model, a prognostic ocean dynamics model, and a prognostic mixed-layer model. All model variables are anomalous fields defined as deviations from the prescribed seasonal-varying mean state. Detailed descriptions of the model equations are provided in the **Supplementary Appendix**. Key differences in model configurations between RCZ and the CZ model are summarized as follows.

2.1.1 Atmospheric Model

In the CZ model, the tropical surface wind stress anomalies are driven by SSTA-related condensation heating and anomalous circulation-determined convective heating, in which the latter is solved iteratively. However, as numerical convergence for iteration is not guaranteed, especially for the linear stability analysis performed with grid point perturbation which has been utilized to study linear ENSO dynamics (Bejarano and Jin, 2008; Xie and Jin, 2018), the iteration method introduces truncation error and artificial randomness. Anomalous diabatic heating in RCZ, therefore, is solely determined by SSTA in the form of

$$\dot{Q}_a = a_Q \exp\left(b_Q \bar{T}\right)\left[b_Q T + \frac{1}{2}\left(b_Q T\right)^2 + \frac{1}{6}\left(b_Q T\right)^3\right] \qquad (1)$$

where $\bar{T}$ and T denote the mean SST and SSTA, respectively. Values of the coefficients a_Q and b_Q are empirically obtained through best-fitting and are provided in the **Supplementary Appendix**. In contrast to the CZ model where the condensation heating is linearly dependent on SSTA, the high-order terms (i.e., the quadratic and cubic terms) on the right-hand-side (RHS) of **Eq. 1** are introduced to describe the nonlinear convective heating which has been suggested to play critical roles in ENSO asymmetry (Kang and Kug, 2002; Ohba and Ueda, 2009; Frauen and Dommenget, 2010; Choi et al., 2013; An and Kim, 2017) and ENSO diversity/bi-modality (Okumura, 2019; Takahashi et al., 2019). The formulation of nonlinearity (i.e., third-order truncation of Taylor expansion for exponential function) is inspired by observing that the local relationship between precipitation and underlying SST generally follows an exponential curve (e.g., Okumura, 2019).

2.1.2 Ocean Dynamics Model

Unlike the CZ model, which adopts the longwave approximation in the ocean dynamics component, RCZ utilizes the full shallow-

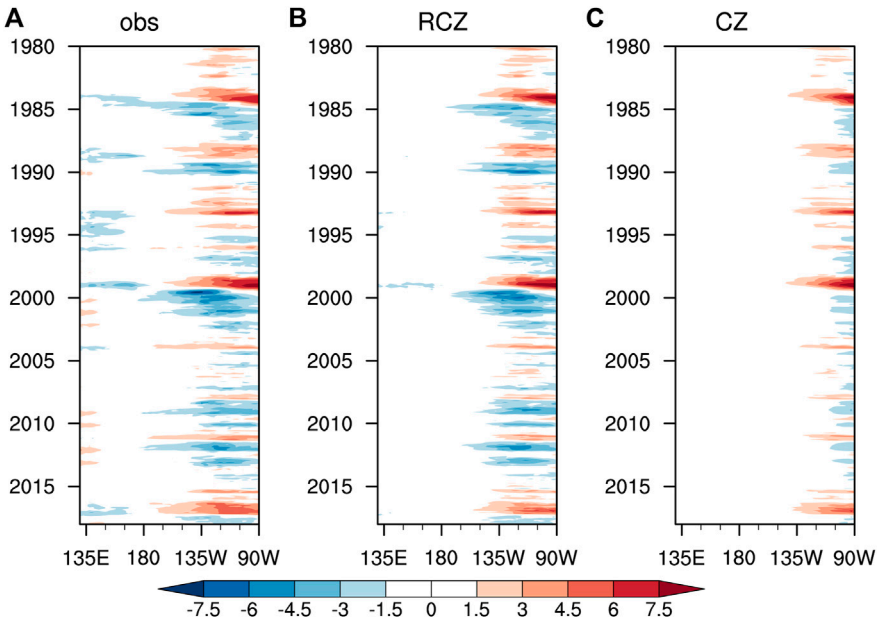

FIGURE 1 | (A) Time evolution of the observed equatorial (5°S–5°N average) subsurface temperature anomalies (unit: °C) over the Pacific during 1980–2018. **(B,C)** Same as **(A)** but for subsurface temperature anomalies parameterized through **Eq. 2** and **Equations A12 and A13** in ZC87, respectively. The subsurface temperature is defined as the temperature at the depth of H_{sub} = 75*m*. Ocean temperature and 20°C-isotherm depth are from the ECMWF ORAS5 dataset.

water model. Instead of separately integrating Kelvin and Rossby wave components as in Cane and Patton (1984) or applying modal decomposition to project oceanic variables onto Hermite polynomials as in Bejarano and Jin (2008), RCZ explicitly resolves the anomalous zonal current, meridional current, and thermocline depth. Furthermore, rather than being assigned a fixed value as in the CZ model, the reduced gravity constant in RCZ is spatial-varying, which effectively relieves the ocean wave over-reflection at the eastern boundary observed in shallow-water model simulations with a fixed reduced gravity constant.

2.1.3 Mixed-Layer Model

The primary difference of the mixed-layer model between RCZ and the CZ model is in the formulation of subsurface temperature parameterization. Yuan et al. (2020) found that the parameterization scheme in the CZ model 1) artificially introduces an over-strong El Niño/La Niña asymmetry and 2) underestimates subsurface temperature anomalies in the central Pacific (also see **Figure 1**). Inspired by ZC87 and Yuan et al. (2020), a subsurface temperature parameterization is proposed as

$$T_{sub} = \gamma A_{sub}\left(\tanh\frac{\bar{h}+h-H_{sub}}{h^{*}} - \tanh\frac{\bar{h}-H_{sub}}{h^{*}}\right) + (1-\gamma)T_{m} \quad (2)$$

where $\bar{h}$ and h denote the mean thermocline depth (i.e., depth of the 20°C-isotherm) and thermocline fluctuation, respectively; and T_m is the mixed layer temperature anomaly (MLTA). The second term on RHS of **Eq. 2** mimics the entrainment process, with $1-\gamma$ measuring the efficiency of entrainment. Definitions and values of other coefficients are provided in the **Supplementary Appendix**. Compared with that proposed in ZC87, this parameterization scheme removes the artificial El Niño/La Niña asymmetry and thus better captures the observed cold equatorial subsurface temperature anomalies during La Niña events (**Figure 1**).

Though the mixed layer depth (MLD) is prescribed and assumed to be fixed in RCZ and the CZ model, it varies spatially and temporally in realistic situations. Variation of mixed layer temperature defined with fixed MLD, which is essentially vertically averaged temperature over the upper-level rather than the real mixed layer, is generally of larger magnitude than that of the corresponding SSTA if the mixed layer is shallower than the prescribed MLD, for instance in the eastern Pacific. Rather than assuming SSTA to be equivalent to MLTA as in the CZ model, RCZ takes into consideration the deficiency of fixed MLD approximation and empirically relates SSTA to MLTA in an empirical way (**Supplementary Appendix Equation A10**). A close relationship between the observed SSTA and that parameterized with MLTA validates our empirical formulation (**Figure 2**).

2.1.4 Stochastic Forcing

The original CZ model introduced in ZC87 is a purely deterministic model in which irregularities emerge primarily through nonlinear processes. In subsequent studies with the CZ model, stochastic processes have been incorporated in the form of white/red noise forcing or episodic westerly wind burst (WWB) occurrences. A parameterization scheme of state-dependent WWBs similar to that in Hayashi and Watanabe

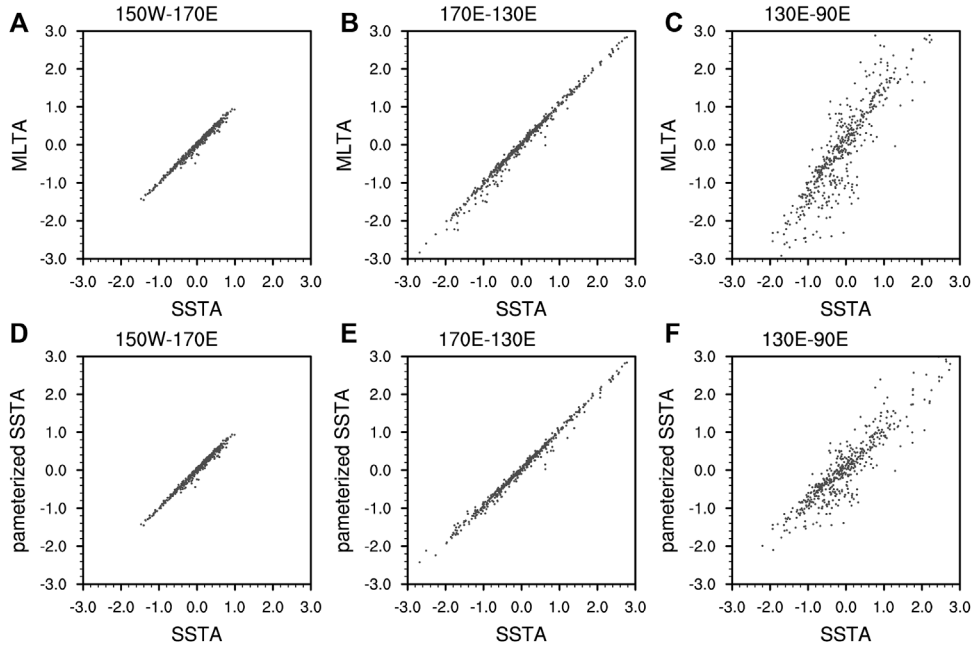

FIGURE 2 | Scatter plot of the observed equatorial (5°S–5°N average) SSTA (unit: °C) vs. MLTA (unit: °C) averaged over **(A)** the western Pacific, **(B)** the central Pacific, and **(C)** the eastern Pacific during 1979–2018. Longitude boundaries of the above three regions are indicated on top of each plot. **(D–F)** Same as **(A–C)** but for the scatter plot of the observed and parameterized equatorial SSTA. The observed SSTA and MLTA are obtained from the ORAS5 dataset; the parameterized SSTA is calculated from the observed MLTA following **Supplementary Appendix Equation A10**. MLTA is defined as the anomalous vertical averaged temperature within the upper 50 m.

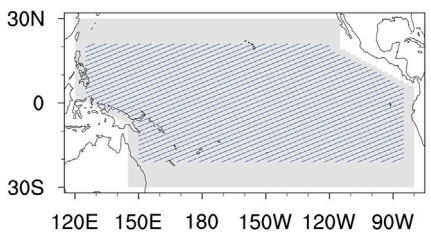

FIGURE 3 | Spatial domain for the ocean dynamics model (gray shading) and mixed layer model (blue hatching) of RCZ.

(2017) is proposed to describe the stochastic forcing. In contrast to some previous studies, both the mechanical and thermal forcing effects from WWBs are included in RCZ.

2.1.5 Numerical Scheme

The model domain for RCZ is within a closed tropical Pacific basin, bounded by a north/south boundary at 30°N/30°S and artificial meridional boundaries mimicking the realistic tilted coastline along the Maritime Continent and North America (**Figure 3**). The model has a resolution of 1° (meridional) × 2.5° (zonal). The ocean dynamics variables are discretized on the staggered Arakawa C-grid. The ocean current is subject to the non-slip and no-normal flow boundary condition. MLTA is subject to the no-flux boundary condition. The advection terms in the mixed layer model are calculated through the upwind finite-difference scheme. The prognostic model components are integrated forward using the semi-implicit Euler method, with a time step of 4 h. All model components are instantaneously coupled at each time step.

2.2 Verification of Model Components

Model components are verified *via* the standalone (i.e., uncoupled) mode. Specifically, observed SSTAs are prescribed to drive the atmospheric model, and observed wind stress anomalies are prescribed to drive the ocean dynamics model and the mixed layer model. Comparison between the observations and the model-simulated responses allows verification of each model component. The above verification procedures are repeated, except that the CZ model is utilized instead, to compare RCZ with the CZ model, The prescribed seasonal-varying mean state is obtained through the ensemble mean of multiple *in-situ* and reanalysis-based datasets listed in **Table 1**. The corresponding observed anomalies, covering 1980–2018, are obtained after removing the long-term climatology and then de-trending.

2.2.1 Atmospheric Model

As meridional wind stress anomalies play a minor role in driving oceanic responses on ENSO timescale, we compare the observed and the model-simulated zonal wind stress anomalies to verify the atmospheric model. Given the observed SSTA, RCZ satisfactorily captures the variation of equatorial zonal wind

TABLE 1 | List of datasets used for model verification.

Fields (variables)	Datasets	Resolution	References
Atmosphere (u_a, v_a)	ERA5	1° × 1°	Hersbach et al. (2020)
	MERRA-2	0.5° × 0.625°	Gelaro et al. (2017)
	NCEP/DOE Reanalysis 2	2.5° × 2.5°	Kanamitsu et al. (2002)
SST	COBE SST	1° × 1°	Hirahara et al. (2014)
	ERSST V5	2° × 2°	Huang et al. (2017)
	HadISST	1° × 1°	Rayner (2003)
	OISST V2	1° × 1°	Reynolds et al. (2002)
Ocean ($u_1, v_1, w, h, T_{sub}, \tau_x, \tau_y$)	GFDL	1° × 1°	Zhang et al. (2007)
	GODAS	0.333° × 1°	Behringer and Xue (2004)
	ECMWF ORAS3	1° × 1°	Balmaseda et al. (2008)
	ECMWF ORAS5	1° × 1°	Zuo et al. (2019)
	SODA3.1.1	0.5° × 0.5°	Carton et al. (2018)

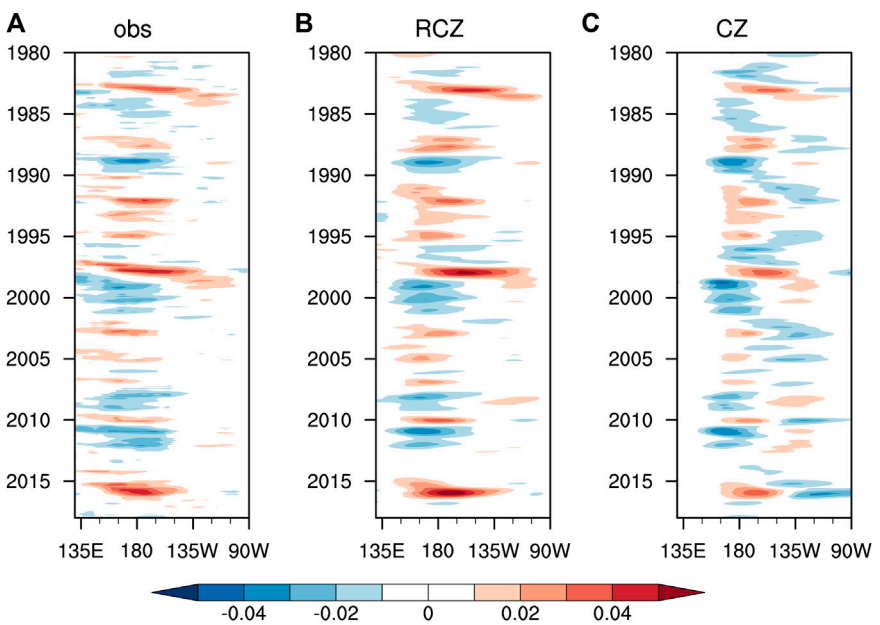

FIGURE 4 | Time evolution of **(A)** the observed, **(B)** the RCZ-simulated, and **(C)** the CZ model-simulated equatorial (5°S–5°N average) zonal wind stress anomalies (unit: N/m^2) during 1980–2018. The model simulations are performed with the atmospheric component only and are driven by the observed SSTA.

stress anomalies (**Figure 4**). The over-strong eastern Pacific wind stress response identified in the CZ model is significantly alleviated in the RCZ simulation. The correlation coefficient between the observed and RCZ-simulated equatorial zonal wind stress anomalies over the western-to-central Pacific, where maximum wind stress anomalies locate, reaches 0.92 (**Figure 5**). In comparison, the CZ model simulation exhibits less correlation with the observation and a larger root mean square error. As indicated by the composite analysis shown in **Figure 6**, the spatial pattern and the magnitude of zonal wind stress anomalies during the mature phase (i.e., November to January) of the two types of El Niño and La Niña are well captured by RCZ. In contrast, the CZ model-simulated equatorial (off-equatorial) zonal wind stress anomalies to the west (east) of SSTA maximum are significantly weaker (stronger) than observed.

The major discrepancy between the observations and the RCZ simulation lies in the meridional structure of wind stress anomalies. During the mature phase of ENSO (i.e., boreal winter), the observed zonal wind stress anomalies center to the south of the equator. The model simulated zonal wind stress anomalies, however, straddle along the equator. Considering that the corresponding SSTA forcing is generally symmetric about the equator, the absence of north-south asymmetry in zonal wind stress anomalies indicates the deficiency of the assumption that SSTA solely determines the atmospheric response. Gong and Li (2021) found that the asymmetric mean state about the equator during boreal winter plays a key role in the southward shift of zonal wind stress anomalies. It is to bear in mind that in the current version of RCZ, an at-rest mean state has been assumed in the atmospheric model. In addition, the moisture processes involved in the

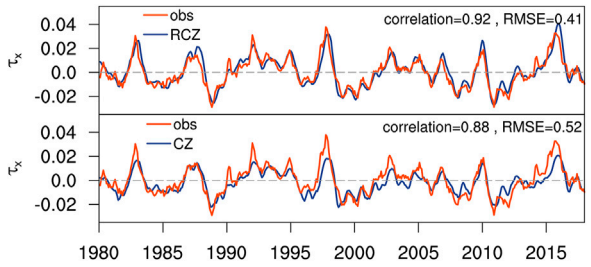

FIGURE 5 | Upper panel: Time series of the observed (red line) and RCZ-simulated (blue line) equatorial (5°S–5°N average) zonal wind stress anomalies averaged between 150°E and 150°W. The correlation between the red line and the blue line, along with the standardized root mean square error of the simulated equatorial zonal wind stress anomalies, is indicated in the upper-right corner. Setting of the model simulation is the same as that in **Figure 4**. The zonal wind stress anomalies have been smoothed through the 3-month running average. Lower panel: Same as the upper panel, except that the blue line denotes the CZ model-simulated equatorial zonal wind stress anomalies.

circulation-convection interaction have not been explicitly incorporated. Thus, the modulation effect of asymmetric mean states shall be taken into consideration in a more realistic atmospheric model with circulation-convection interaction included.

To test the validity of the atmospheric nonlinearity introduced in RCZ, we compare the atmospheric response to prescribed EP and CP El Niño-like SST forcing with varying amplitudes simulated by an AGCM (Community Atmospheric Model, CAM4; Neale et al., 2010) and the atmospheric model of RCZ (not shown). Consistent with the observations, the atmospheric response in CAM4 exhibits relatively strong (weak) nonlinearity to EP (CP) El Niño-like SST forcing. Such atmospheric nonlinearity to prescribed SST forcing is satisfactorily reproduced in RCZ simulation, thus validating the nonlinear formulation of diabatic heating proposed in **Eq. 1**.

2.2.2 Ocean Dynamics Model and Mixed Layer Model

The oceanic component of RCZ, consisting of the ocean dynamics model and the mixed layer model, is verified *via* uncoupled simulation forced with the observed wind stress anomalies. The ocean dynamics responses (i.e., anomalous thermocline depth, surface zonal current, and upwelling) exhibit a strong resemblance to the observations, except that the simulated zonal surface current near the eastern boundaries is slightly weaker than the observations (not shown).

The advantages of RCZ over the CZ model are most evident in the simulation of SSTA. Time evolution of equatorial SSTA indicates that most observed ENSO events are successfully

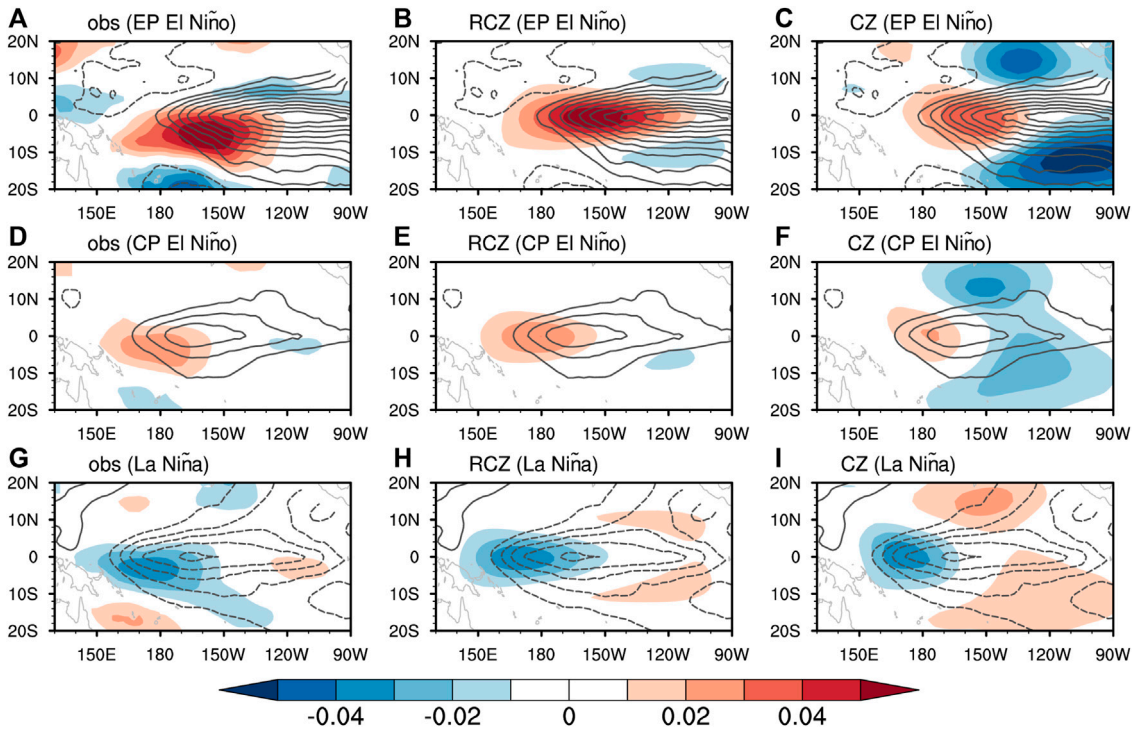

FIGURE 6 | Composited November-December-January (NDJ) average zonal wind stress anomalies (shading; unit: N/m^2) associated with EP El Niño, CP El Niño, and La Niña in **(A,D,G)** the observations, **(B,E,H)** the RCZ atmospheric component simulation, and **(C,F,I)** the CZ model atmospheric component simulation. Contours in each plot denote the corresponding observed SSTA. The contour level is 0.4°C, and dashed contours represent cold SSTA. EP El Niño (1982, 1997)/CP El Niño (1990, 1991, 1994, 2002, 2004, 2009) years are selected as the monthly E-index/C-index (Takahashi et al., 2011) exceeds one standard deviation from October to February. La Niña years (1988, 1998, 1999, 2007, 2010) are similarly selected as Niño 3.4 index is smaller than minus-one standard deviation.

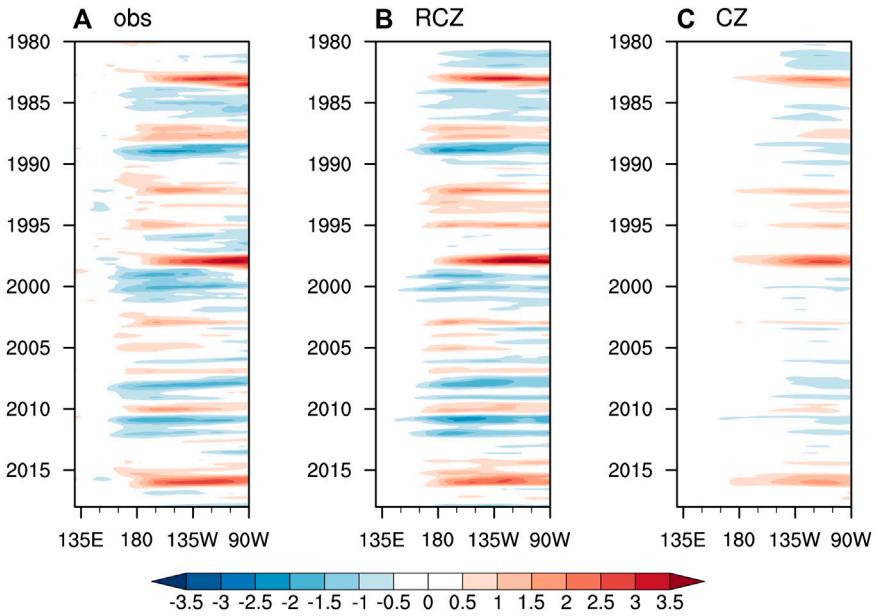

FIGURE 7 | Time evolution of **(A)** the observed, **(B)** the RCZ-simulated, and **(C)** the CZ model-simulated equatorial (5°S–5°N average) SSTA (unit: °C) during 1980–2018. The model simulations are performed with the oceanic component only and are driven by the observed wind stress anomalies.

reproduced in RCZ (**Figures 7A,B**). The correlation coefficients of the eastern Pacific and central Pacific SSTA between the observations and the RCZ simulation reach 0.91 and 0.92, both exceeding the 99.9% confidence level (**Figure 8**). The correlation coefficient/standardized root mean square error for the CZ model simulation is smaller/larger than that for the RCZ simulation. As shown in the composite analysis (**Figure 9**), the observed spatial patterns associated with the two types of El Niño and La Niña are satisfactorily captured in RCZ. The CZ model, however, fails to distinguish CP El Niño from EP El Niño, and it can hardly capture La Niña (**Figures 7C**, **9**). The too-weak CP El Niño and La Niña in the CZ model possibly result from the deficient subsurface temperature parameterization scheme (**Figure 1**). In RCZ, the dynamical damping in the central Pacific is partially offset by the mean advection of subsurface temperature anomalies, thus allowing the emergence of CP El Niño and La Niña. In contrast, such offset is less evident in the CZ model, making the dynamical damping dominate over the mean advection of subsurface temperature anomalies.

Compared with those observed, the EP El Niño SSTA pattern in RCZ extends more westward toward the warm pool. Such excessive warming in the equatorial central-western Pacific is a common bias in climate models and is arguably attributed to the model-simulated stronger-than-observation mean zonal temperature gradient (Chen et al., 2021; Jiang et al., 2021). Interestingly, it is to be noted that the mean zonal temperature gradient in RCZ is prescribed as observed. The reason for the SSTA pattern bias in RCZ is thus worthy of further investigation. In addition, the RCZ-simulated ENSO patterns are of a slightly smaller meridional scale, for which the reason is possibly related to the biased ocean circulation response and needs to be further studied.

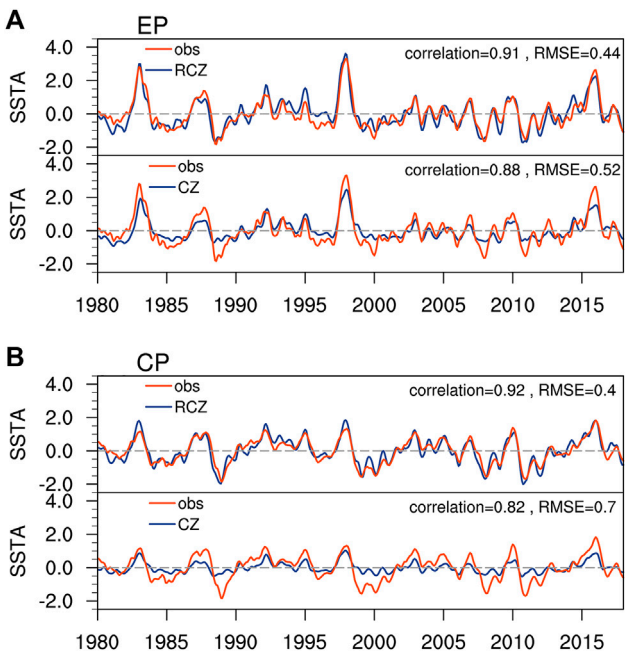

FIGURE 8 | (A) *upper panel*: Time series of the observed (red line) and RCZ-simulated (blue line) equatorial (5°S–5°N average) EP SSTA (i.e., averaged between 140°W and 90°W). The correlation between the red line and the blue line, along with the standardized root mean square error of the simulated EP SSTA, is indicated in the upper-right corner. Settings of the model simulation are the same as that in **Figure 5**. SSTA has been smoothed through the 3-month running average. **(A)** *lower panel*: Same as the upper panel, except that the blue line denotes the CZ model-simulated equatorial EP SSTA. **(B)** Same as **(A)** but for the equatorial CP SSTA (i.e., averaged between 170°E and 140°W).

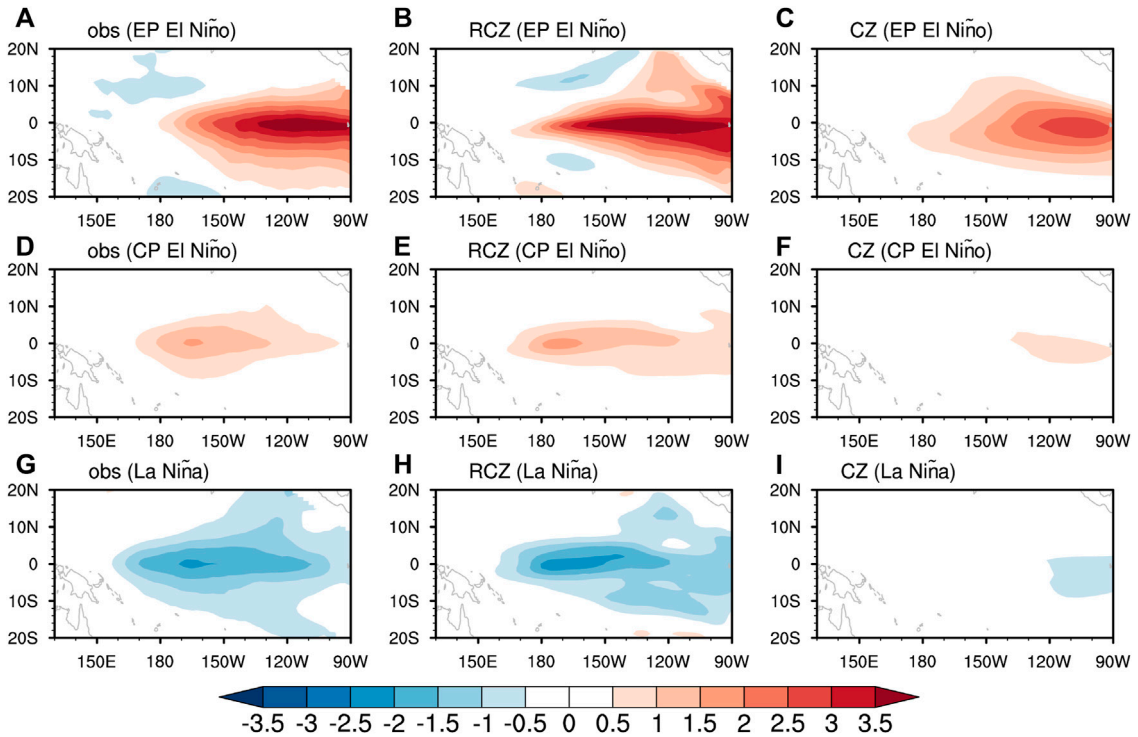

FIGURE 9 | Composited November-December-January (NDJ) average SSTA (shading; unit: °C) associated with EP El Niño, CP El Niño, and La Niña in **(A,D,G)** the observations, **(B,E,H)** the RCZ oceanic component simulation, and **(C,F,I)** the CZ model oceanic component simulation. EP El Niño, CP El Niño, and La Niña years are selected as in **Figure 6**.

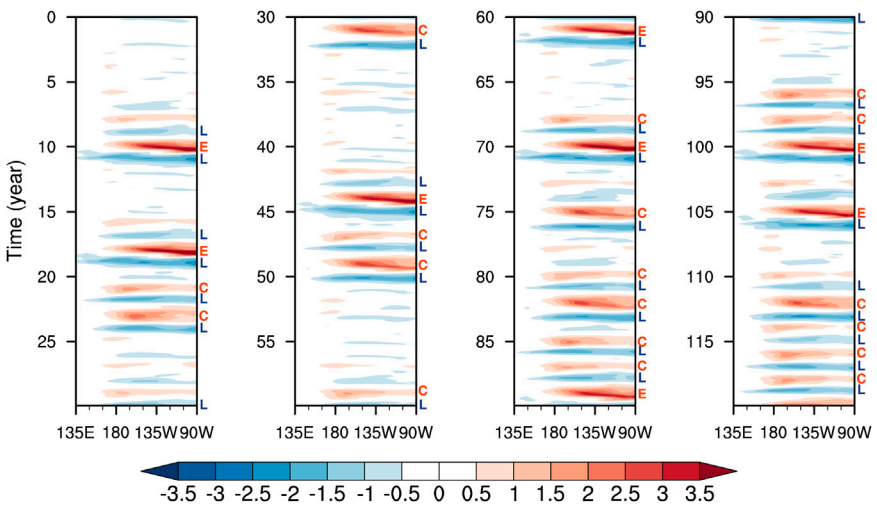

FIGURE 10 | Hovmöller diagram of 120-year RCZ simulated equatorial (5°S–5°N average) SSTA (unit: °C). The 120-year segment of data is from the 5000-year simulation and is separated into four consecutive 30-year segments for display. The type of each ENSO event is indicated on the right-hand-side of the Hovmöller diagram, with red "E" denoting EP El Niño, red "C" denoting CP El Niño, and blue "L" denoting La Niña.

3 ENSO DIVERSITY IN RCZ

3.1 General ENSO Behavior

To evaluate the performance of RCZ in simulating ENSO features, we perform a 5000-year coupled simulation with default model settings. The prescribed seasonal-varying mean state is obtained from the long-term averaged observations. The Hovmöller diagram of a 120-year segment of the RCZ-simulated equatorial SSTA, as shown in **Figure 10**, exhibits intermittency of ENSO activity, with more or less frequent occurrences of ENSO

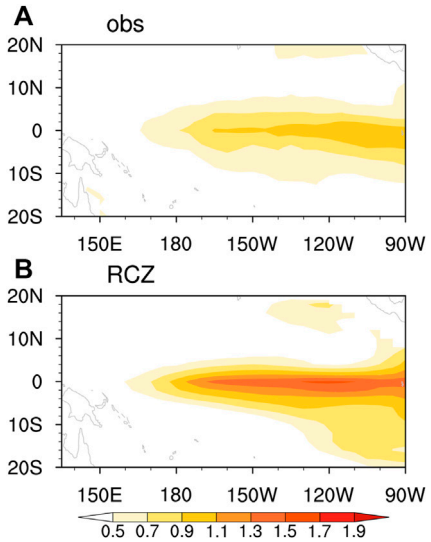

FIGURE 11 | The standard deviation of SSTA (unit: °C) in **(A)** the observations and **(B)** the 5000-year RCZ coupled simulation. The observed standard deviation is calculated with the HadISST dataset covering 1900–2018.

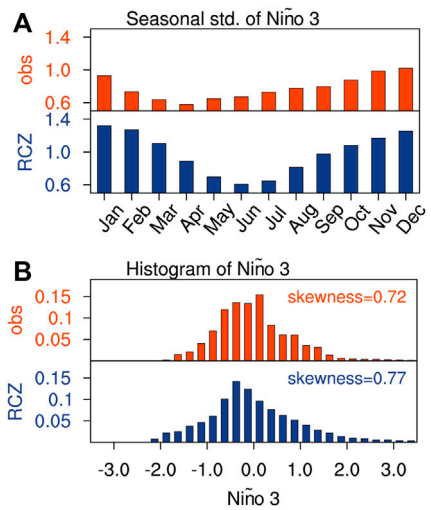

FIGURE 12 | (A) Seasonal standard deviation of Niño 3 index (unit: °C) in the observations (upper panel; red bars) and the RCZ simulation (lower panel; blue bars). **(B)** Histogram of the monthly Niño 3 index (unit: °C) in the observations (upper panel; red bars) and the RCZ simulation (lower panel; blue bars). The bin size is 0.2°C.

events in various epochs/decades. The intensity of the tropical Pacific interannual variability, measured by the standard deviation of SSTA, is shown in **Figure 11**. Consistent with the observations, RCZ-simulated SSTA variability is strongest in the central-eastern Pacific. However, the amplitude of SSTA variability is stronger in RCZ than in the observations. Such inconsistency is partly due to the fact that ENSO simulated in RCZ exhibits less irregularity than in the observations. As shown

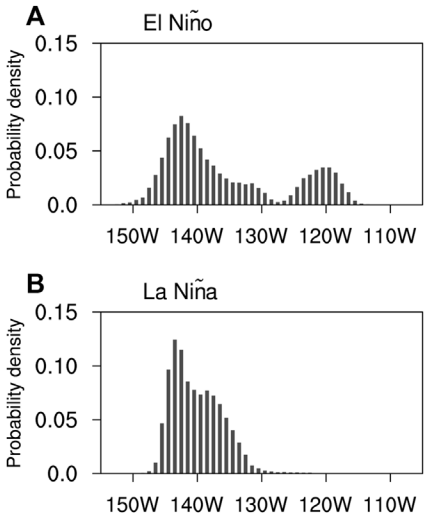

FIGURE 13 | Probability density function (PDF) for the centroid longitude of equatorial SSTA at the peak phase of **(A)** El Niño events and **(B)** La Nina events. The PDF is estimated based on binned histograms from the 5000-year simulation. The width of the bins is one degree in longitude.

in the Hovmöller diagram of equatorial SSTA in **Figure 10**, warm and cold events tend to occur alternatively in active ENSO epochs. In contrast, observed El Niño events, especially for CP El Niño, are more-or-less episodic-like rather than being regularly followed by La Niña events (**Figure 7A**). The underestimated irregularity in RCZ indicates that ENSO behavior in active decades may reside in the self-sustained regime.

The phase-locking behavior of ENSO is examined *via* the seasonal standard deviation of the Niño 3 index (**Figure 12A**). Again, the standard deviation in the RCZ simulation is stronger than in the observations. Consistent with the observations, ENSO events tend to see peak phases in boreal winter, as indicated by the strongest Niño 3 index variability from November to January. The minimum amplitude of Niño 3 index variability in RCZ, however, is slightly shifted by 2-month compared with the observations. The relationship between seasonal ENSO stability and ENSO phase locking has been well noted (e.g., Chen and Jin, 2020). In the current version of RCZ, the stability of the coupled system is solely determined by the seasonal cycle of oceanic variables. By considering the atmospheric control over the ENSO stability associated with the seasonal migration of the Intertropical Convergence Zone (ITCZ) and the South Pacific Convergence Zone (SPCZ), the simulated ENSO phase-locking may be further improved.

The observed El Niño/La Niña asymmetry is also successfully reproduced in RCZ (**Figure 12B**). The monthly Niño 3 index is skewed toward the positive end in the observations and the RCZ simulation, with the skewness [calculated following An and Jin (2004)] being 0.72 and 0.77, respectively.

3.2 Characteristics of ENSO Bi-Modality

ENSO pattern diversity can be clearly identified in the Hovmöller diagram of the RCZ-simulated equatorial SSTA (**Figure 10**).

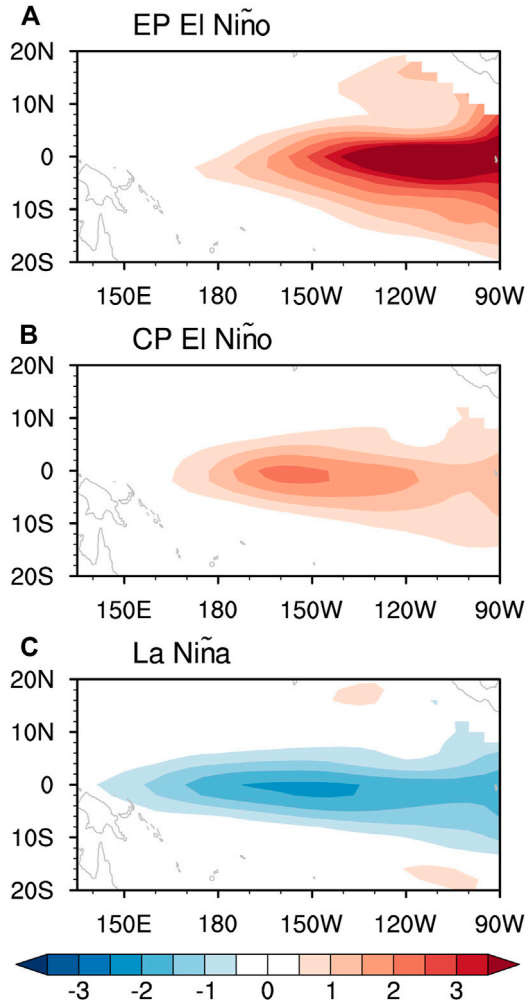

FIGURE 14 | Composites of SSTA pattern at the peak phase of **(A)** EP El Niño, **(B)** CP El Niño, and **(C)** La Niña. See text for criteria of the El Niño/La Niña events.

Warm events are generally categorized into two groups, with maximum SSTA at the peak phase located either over the eastern Pacific or slightly to the east of the dateline. Consistent with previous observational findings (e.g., Kug and Ham, 2011), cold events exhibit less pattern diversity, and the associated SSTA spans broadly over the central-to-eastern Pacific. To better distinguish the different ENSO types, El Niño events are first identified according to the following criteria: equatorial SSTA averaged over the eastern Pacific region (i.e., 140°W–90°W) or the central Pacific region (i.e., 170°E–140°W) exceeds 0.5°C for five consecutive months. La Niña events are similarly identified but with the threshold being −0.5°C. As shown in **Figure 13A**, the probability density function (PDF) for the centroid longitude of equatorial SSTA at the peak phase of El Niño events exhibits double peaks. In contrast, only a single peak exists in the PDF for La Niña's centroid longitude (**Figure 13B**). Here, the centroid longitude of SSTA is defined as $\lambda_c = \int_{\lambda_W}^{\lambda_E} \lambda T d\lambda / \int_{\lambda_W}^{\lambda_E} T d\lambda$, with λ being the longitude and λ_W (λ_E) being the western (eastern) mixed layer model boundary. The PDF for the longitude of SSTA maximum is qualitatively similar to the PDF for SSTA centroid longitude, except for being less smooth because identification of SSTA maximum is subject to some ambiguity, especially in situations where SSTA exhibit multiple local maxima. Next, by observing the two PDF peaks in **Figure 13A**, El Niño events are classified into EP/CP type with SSTA centroid longitude located to the east/west of 127.5°W. In total, 352 EP El Niño events and 999 CP El Niño events are identified in the 5000-year simulation. In the observations, EP El Niño, especially extreme EP El Niño, generally sees fewer occurrences than CP El Niño as well. The direct comparison of the relative frequency associated with the two types of El Nino between the observations and the RCZ simulation, however, is less straightforward. Classification of El Niño events in the observations is subject to the limited sample size and suffers from large uncertainty associated with varying datasets (Dieppois et al., 2021, see their Figure 2A) and metrics for identifying ENSO types (Wiedermann et al., 2016, see their Table 1; Capotondi et al., 2020, see their Table 4.1). As shown in **Figure 14**, composited SSTA patterns associated with the EP El Niño, CP El Niño, and La Niña generally resemble those observed (**Figure 9**), except for a slightly stronger amplitude and eastward-shifted SSTA center during CP El Niño. To test the robustness of the SSTA pattern against the definition of ENSO types, the E-index and C-index introduced in Takahashi et al. (2011) have been utilized to identify EP and CP El Niño. Firstly, we perform an Empirical Orthogonal Function (EOF) analysis of the boreal winter (i.e., November to January) averaged tropical Pacific SSTA. Then the E-index is defined as $E = (PC1 - PC2)/\sqrt{2}$ and the C-index as $C = (PC1 + PC2)/\sqrt{2}$, with PC1 and PC2 denoting the first and second principal component, respectively. The SSTA patterns associated with the E-index and the C-index are shown in **Figures 15A,B**. Consistent with that identified with the observations (Takahashi et al., 2011), the SSTA pattern associated with the E-index and C-index center in the eastern Pacific and central Pacific, respectively. In comparison with that shown in Takahashi et al. (2011), the RCZ-simulated E-pattern is less confined along the South American coast but slightly shifted westward. This may be attributed to the fact that the coastal El Niño events cannot be captured in RCZ due to a lack of local air-sea interaction processes (Garreaud, 2018; Rodríguez-Morata et al., 2019). Next, EP and CP El Niño events are selected if the E-index and C-index exceed one standard deviation, respectively. A total of 379 EP El Niño events and 1125 CP El Niño events are identified. The associated SSTA patterns, as shown in **Figures 15C,D**, closely resemble those obtained according to the SSTA centroid longitude criteria. The similarity of the relative frequency and SSTA pattern of the two types of El Niño between the above two identification criteria indicates that characteristics of ENSO diversity/bi-modality simulated in RCZ are insensitive to the definition of ENSO types.

Besides the centroid longitude of SSTA, the intensity of ENSO events exhibits bi-modality as well. As shown in **Figure 16**, the trajectory of ENSO events generally features two distinct orbits (i.e., one with a larger amplitude and the other one with a smaller amplitude), reminiscent of the strong and moderate ENSO

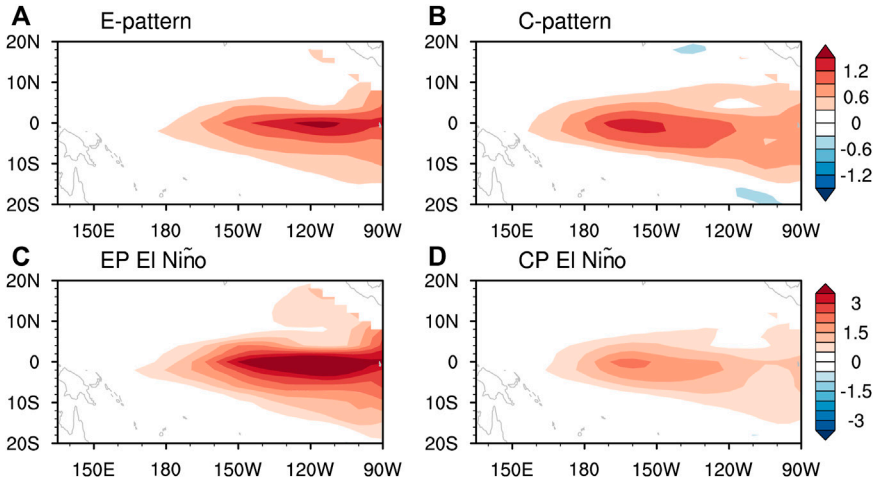

FIGURE 15 | Regressed SSTA pattern against the November-December-January average **(A)** E-index and **(B)** C-index. See text for the definition of the indices. **(C,D)** Composites of SSTA pattern associated with EP El Niño and CP El Niño. The two types of El Niño are identified with the E-index and C-index exceeding their respective one standard deviation.

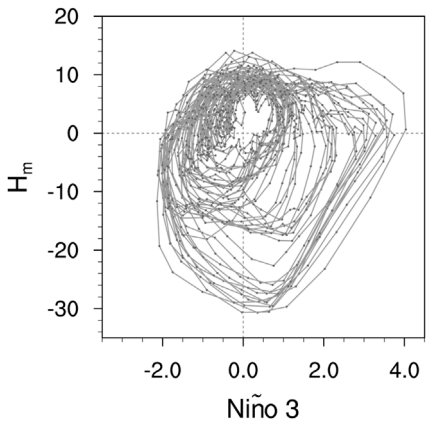

FIGURE 16 | Trajectories of ENSO events in the Niño 3 index (unit: °C; horizontal axis)–zonal mean thermocline fluctuation (unit: m; vertical axis) phase space. A total of ten percent of all the simulated ENSO events are randomly chosen for display.

regimes identified in Takahashi and Dewitte (2016) and Takahashi et al. (2019). The two aspects of ENSO bi-modality shall bear strong correspondence with each other.

4 SUMMARY AND DISCUSSION

By acknowledging its potential practical usage in investigating dynamics of ENSO diversity while observing some shortcomings in its model components, the CZ model has been revised in terms of the model formulation and parameterization schemes while keeping the model skeleton unchanged. The new model, named RCZ, is carefully validated against observations through the standalone mode. When forced with observed SSTA (wind stress anomalies), the simulated atmospheric (oceanic) responses in RCZ resemble those observed to a much more satisfying extent than that in the CZ model. Aspects of the observed ENSO characteristics (i.e., ENSO amplitude, phase-locking, and El Niño/La Niña asymmetry) are reasonably reproduced in the coupled simulation with RCZ. In addition, the observed ENSO bi-modality is well captured in RCZ, where EP and CP El Niño, of which the spatial patterns resemble those observed, are clearly distinguished. A number of studies using various intermediate coupled models, including the CZ model, have arguably simulated ENSO diversity/complexity to a satisfying extent (Chen et al., 2015; Hayashi and Watanabe, 2017; Xie and Jin, 2018; Chen et al., 2022). Though the two types of El Niño identified with RCZ exhibit more realistic characteristics than some of the previous studies, it is not the purpose of this study to argue that RCZ outperforms other intermediate coupled models in simulating the observed ENSO diversity. Instead, this study aims to provide a framework in which all the model components accurately describe the realistic physical processes so as to ensure that ENSO diversity is simulated for the right reason. It is to bear in mind that interpretation of ENSO diversity in a model with biased physics may be misleading.

The major discrepancy between the observed and RCZ-simulated ENSO behavior is its temporal characteristics. In comparison with the observations, RCZ-simulated ENSO events exhibit less irregularity. The underestimated irregularity may be attributed to a lack of tropical basin-interaction (Ham et al., 2013a; Ham et al., 2013b), ENSO's interaction with Pacific Meridional Modes (Yu et al., 2010; Vimont et al., 2014; Vimont et al., 2022), and ENSO-Tropical Instability Wave (TIW) interaction (An, 2008). Furthermore, RCZ fails to capture the observed El Niño/La Niña duration asymmetry and the

contrasting time-evolution of the two types of ENSO (Dommenget et al., 2013). Generally, in the observations, EP El Niño experiences rapid termination and phase transition after the mature phase, whereas the subsequent La Niña persists through the second year or longer (Okumura and Deser, 2010). CP El Niño, on the other hand, is more episodic-like and exhibits less apparent phase reversal. Several nonlinear processes (e.g., ENSO-TIW interaction, nonlinear convective heating response, and nonlinear radiative fluxes) have been suggested to play some role in the ENSO duration asymmetry. Whether incorporating these nonlinear processes in RCZ benefits the simulation of ENSO duration asymmetry deserves to be further explored.

As discussed in **Section 2.2**, the major flaw associated with the atmospheric model of RCZ resides in parameterizing diabatic heating as being solely dependent on SSTA. The important role of circulation-convection interaction in shaping tropical atmospheric response has been widely acknowledged (Webster, 1981; Weare, 1986; Kleeman, 1991; Gong and Li, 2021). Furthermore, Wu et al. (2000) noticed that the atmospheric response is sensitive to the vertical structure of convective heating, further casting doubts on the appropriateness of the Gill model. In the future version of RCZ, we seek to replace the Gill-type atmospheric model with a simplified primitive equation model.

The shallow water approximation, on the other hand, is suggested to be insufficient in capturing equatorial ocean dynamics by noticing the significant contribution to surface zonal current and sea surface height anomalies from multiple baroclinic modes, especially in the vicinity of the dateline (Dewitte et al., 1999; Dewitte, 2000; Zhao et al., 2021). On the other hand, the high-order baroclinic modes contribute to a vertically slanted structure of upper-level ocean temperature anomaly in the central Pacific, thus degrading the assumption that the subsurface temperature anomaly at a fixed depth can be parameterized as being linearly related to the thermocline fluctuation (Zhao et al., 2021). In the future version of RCZ, we aim to implement a simplified linear continuously stratified model with which the integrated effects of high-order baroclinic modes are empirically parameterized.

The well-calibrated and validated RCZ allows a systematic investigation of the linear and nonlinear dynamics of ENSO diversity. Effects of atmospheric convective nonlinearity, stochastic processes, and ENSO's interaction with various tropical climate variability will be further studied in a forthcoming paper.

DATA AVAILABILITY STATEMENT

Publicly available datasets were analyzed in this study. This data can be found here: https://psl.noaa.gov/data/gridded/; http://apdrc.soest.hawaii.edu/data/data.php.

AUTHOR CONTRIBUTIONS

LG designed the model, performed the research, and wrote the manuscript. F-FJ contributed to discussion and revision of the manuscript.

FUNDING

This study is supported by the United States National Science Foundation (AGS-1813611) and the United States Department of Energy (DESC0005110).

SUPPLEMENTARY MATERIAL

The Supplementary Material for this article can be found online at: https://www.frontiersin.org/articles/10.3389/feart.2022.899323/full#supplementary-material

REFERENCES

An, S.-I. (2008). Interannual Variations of the Tropical Ocean Instability Wave and ENSO. *J. Clim.* 21, 3680–3686. doi:10.1175/2008jcli1701.1

An, S.-I., and Jin, F.-F. (2004). Nonlinearity and Asymmetry of ENSO*. *J. Clim.* 17, 2399–2412. doi:10.1175/1520-0442(2004)017<2399:naaoe>2.0.co;2

An, S.-I., and Kim, J.-W. (2017). Role of Nonlinear Ocean Dynamic Response to Wind on the Asymmetrical Transition of El Niño and La Niña. *Geophys. Res. Lett.* 44, 393–400. doi:10.1002/2016GL071971

Ashok, K., Behera, S. K., Rao, S. A., Weng, H., and Yamagata, T. (2007). El Niño Modoki and its Possible Teleconnection. *J. Geophys. Res.* 112. doi:10.1029/2006jc003798

Balmaseda, M. A., Vidard, A., and Anderson, D. L. T. (2008). The ECMWF Ocean Analysis System: ORA-S3. *Monthly Weather Rev.* 136, 3018–3034. doi:10.1175/2008MWR2433.1

Behringer, D., and Xue, Y. (2004). "January. Evaluation of the Global Ocean Data Assimilation System at NCEP: The Pacific Ocean," in *Proc. Eighth Symp. On Integrated Observing and Assimilation Systems for Atmosphere, Oceans, and Land Surface*. Seattle, WA: Amer. Meteor. Soc., 2.3.

Bejarano, L., and Jin, F.-F. (2008). Coexistence of Equatorial Coupled Modes of ENSO*. *J. Clim.* 21, 3051–3067. doi:10.1175/2007JCLI1679.1

Cai, W., Santoso, A., Collins, M., Dewitte, B., Karamperidou, C., Kug, J.-S., et al. (2021). Changing El Niño-Southern Oscillation in a Warming Climate. *Nat. Rev. Earth Environ.* 2, 628–644. doi:10.1038/s43017-021-00199-z

Cane, M. A., and Patton, R. J. (1984). A Numerical Model for Low-Frequency Equatorial Dynamics. *J. Phys. Oceanogr.* 14, 1853–1863. doi:10.1175/1520-0485(1984)014<1853:anmflf>2.0.co;2

Capotondi, A. (2013). ENSO Diversity in the NCAR CCSM4 Climate Model. *J. Geophys. Res. Oceans* 118, 4755–4770. doi:10.1002/jgrc.20335

Capotondi, A., Wittenberg, A. T., Kug, J.-S., Takahashi, K., and McPhaden, M. J. (2020). *ENSO Diversity, in El Niño Southern Oscillation in a Changing Climate*. Editors M. J. McPhaden, A. Santoso, and W. Cai, Geophysical Monograph Series, AGU, 65–86. doi:10.1002/9781119548164

Carton, J. A., Chepurin, G. A., and Chen, L. (2018). SODA3: A New Ocean Climate Reanalysis. *J. Clim.* 31, 6967–6983. doi:10.1175/JCLI-D-18-0149.1

Chen, D., Lian, T., Fu, C., Cane, M. A., Tang, Y., Murtugudde, R., et al. (2015). Strong Influence of westerly Wind Bursts on El Niño Diversity. *Nat. Geosci* 8, 339–345. doi:10.1038/ngeo2399

Chen, H.-C., and Jin, F.-F. (2020). Fundamental Behavior of ENSO Phase Locking. *J. Clim.* 33, 1953–1968. doi:10.1175/JCLI-D-19-0264.1

Chen, H.-C., Jin, F.-F., Zhao, S., Wittenberg, A. T., and Xie, S. (2021). ENSO Dynamics in the E3SM-1-0, CESM2, and GFDL-CM4 Climate Models. *J. Clim.* 34, 1–59. doi:10.1175/JCLI-D-21-0355.1

Chen, N., Fang, X., and Yu, J.-Y. (2022). A Multiscale Model for El Niño Complexity. *Npj Clim. Atmos. Sci.* 5, 1–13. doi:10.1038/s41612-022-00241-x

Choi, K.-Y., Vecchi, G. A., and Wittenberg, A. T. (2013). ENSO Transition, Duration, and Amplitude Asymmetries: Role of the Nonlinear Wind Stress Coupling in a Conceptual Model. *J. Clim.* 26, 9462–9476. doi:10.1175/JCLI-D-13-00045.1

Dewitte, B., and Perigaud, C. (1996). El Niño-La Niña Events Simulated with Cane and Zebiak's Model and Observed with Satellite or *In Situ* Data. Part II: Model Forced with Observations. *J. Clim.* 9, 1188–1207. doi:10.1175/1520-0442(1996)009<1188:enlnes>2.0.co;2

Dewitte, B., Reverdin, G., and Maes, C. (1999). Vertical Structure of an OGCM Simulation of the Equatorial Pacific Ocean in 1985-94. *J. Phys. Oceanogr.* 29, 1542–1570. doi:10.1175/1520-0485(1999)029<1542:vsoaos>2.0.co;2

Dewitte, B. (2000). Sensitivity of an Intermediate Ocean-Atmosphere Coupled Model of the Tropical Pacific to its Oceanic Vertical Structure. *J. Clim.* 13, 2363–2388. doi:10.1175/1520-0442(2000)013<2363:soaioa>2.0.co;2

Dieppois, B., Capotondi, A., Pohl, B., Chun, K. P., Monerie, P.-A., and Eden, J. (2021). ENSO Diversity Shows Robust Decadal Variations that Must Be Captured for Accurate Future Projections. *Commun. Earth Environ.* 2, 1–13. doi:10.1038/s43247-021-00285-6

Dommenget, D., Bayr, T., and Frauen, C. (2013). Analysis of the Non-linearity in the Pattern and Time Evolution of El Niño Southern Oscillation. *Clim. Dyn.* 40, 2825–2847. doi:10.1007/s00382-012-1475-0

Frauen, C., and Dommenget, D. (2010). El Niño and La Niña Amplitude Asymmetry Caused by Atmospheric Feedbacks. *Geophys. Res. Lett.* 37, a–n. doi:10.1029/2010GL044444

Garreaud, R. D. (2018). A Plausible Atmospheric Trigger for the 2017 Coastal El Niño. *Int. J. Climatol* 38, e1296–e1302. e1302. doi:10.1002/joc.5426

Gelaro, R., McCarty, W., Suárez, M. J., Todling, R., Molod, A., Takacs, L., et al. (2017). The Modern-Era Retrospective Analysis for Research and Applications, Version 2 (MERRA-2). *J. Clim.* 30, 5419–5454. doi:10.1175/JCLI-D-16-0758.1

Geng, L. (2021). *Dynamics of El Niño-Southern Oscillation Diversity in an Intermediate Coupled Model (Ph.D. Dissertation)*. Honolulu: University of Hawai'i at Manoa.

Gong, Y., and Li, T. (2021). Mechanism for Southward Shift of Zonal Wind Anomalies during the Mature Phase of ENSO. *J. Clim.* 1, 1–45. doi:10.1175/jcli-d-21-0078.1

Ham, Y.-G., Kug, J.-S., Park, J.-Y., and Jin, F.-F. (2013b). Sea Surface Temperature in the north Tropical Atlantic as a Trigger for El Niño/Southern Oscillation Events. *Nat. Geosci* 6, 112–116. doi:10.1038/ngeo1686

Ham, Y.-G., Kug, J.-S., and Park, J.-Y. (2013a). Two Distinct Roles of Atlantic SSTs in ENSO Variability: North Tropical Atlantic SST and Atlantic Niño. *Geophys. Res. Lett.* 40, 4012–4017. doi:10.1002/grl.50729

Hayashi, M., and Watanabe, M. (2017). ENSO Complexity Induced by State Dependence of westerly Wind Events. *J. Clim.* 30, 3401–3420. doi:10.1175/JCLI-D-16-0406.1

Hersbach, H., Bell, B., Berrisford, P., Hirahara, S., Horányi, A., Muñoz-Sabater, J., et al. (2020). The ERA5 Global Reanalysis. *Q.J.R. Meteorol. Soc.* 146, 1999–2049. doi:10.1002/qj.3803

Hirahara, S., Ishii, M., and Fukuda, Y. (2014). Centennial-Scale Sea Surface Temperature Analysis and its Uncertainty. *J. Clim.* 27, 57–75. doi:10.1175/JCLI-D-12-00837.1

Huang, B., Thorne, P. W., Banzon, V. F., Boyer, T., Chepurin, G., Lawrimore, J. H., et al. (2017). Extended Reconstructed Sea Surface Temperature, Version 5 (ERSSTv5): Upgrades, Validations, and Intercomparisons. *J. Clim.* 30, 8179–8205. doi:10.1175/JCLI-D-16-0836.1

Jiang, W., Huang, P., Huang, G., and Ying, J. (2021). Origins of the Excessive Westward Extension of ENSO SST Simulated in CMIP5 and CMIP6 Models. *J. Clim.* 34, 2839–2851. doi:10.1175/JCLI-D-20-0551.1

Jin, F.-F. (1997). An Equatorial Ocean Recharge Paradigm for ENSO. Part II: A Stripped-Down Coupled Model. *J. Atmos. Sci.* 54, 830–847. doi:10.1175/1520-0469(1997)054<0830:aeorpf>2.0.co;2

Jin, F.-F., and Neelin, J. D. (1993). Modes of Interannual Tropical Ocean-Atmosphere Interaction-A Unified View. Part I: Numerical Results. *J. Atmos. Sci.* 50, 3477–3503. doi:10.1175/1520-0469(1993)050<3477:moitoi>2.0.co;2

Kanamitsu, M., Ebisuzaki, W., Woollen, J., Yang, S.-K., Hnilo, J. J., Fiorino, M., et al. (2002). NCEP-DOE AMIP-II Reanalysis (R-2). *Bull. Am. Meteorol. Soc.* 83, 1631–1643. doi:10.1175/BAMS-83-11-1631

Kang, I.-S., and Kug, J.-S. (2002). El Niño and La Niña Sea Surface Temperature Anomalies: Asymmetry Characteristics Associated with Their Wind Stress Anomalies. *J. Geophys. Res.* 107, ACL 1-1–ACL 1-10. doi:10.1029/2001JD000393

Kao, H.-Y., and Yu, J.-Y. (2009). Contrasting Eastern-Pacific and central-Pacific Types of ENSO. *J. Clim.* 22, 615–632. doi:10.1175/2008JCLI2309.1

Kleeman, R. (1991). A Simple Model of the Atmospheric Response to ENSO Sea Surface Temperature Anomalies. *J. Atmos. Sci.* 48, 3–19. doi:10.1175/1520-0469(1991)048<0003:asmota>2.0.co;2

Kug, J.-S., Choi, J., An, S.-I., Jin, F.-F., and Wittenberg, A. T. (2010). Warm Pool and Cold Tongue El Niño Events as Simulated by the GFDL 2.1 Coupled GCM. *J. Clim.* 23, 1226–1239. doi:10.1175/2009JCLI3293.1

Kug, J.-S., and Ham, Y.-G. (2011). Are There Two Types of La Nina? *Geophys. Res. Lett.* 38, a–n. doi:10.1029/2011GL048237

Kug, J.-S., Jin, F.-F., and An, S.-I. (2009). Two Types of El Niño Events: Cold Tongue El Niño and Warm Pool El Niño. *J. Clim.* 22, 1499–1515. doi:10.1175/2008JCLI2624.1

Larkin, N. K., and Harrison, D. E. (2005). Global Seasonal Temperature and Precipitation Anomalies during El Niño Autumn and winter. *Geophys. Res. Lett.* 32. doi:10.1029/2005GL022860

McPhaden, M. J. (2012). A 21st century Shift in the Relationship between ENSO SST and Warm Water Volume Anomalies. *Geophys. Res. Lett.* 39, a–n. doi:10.1029/2012GL051826

Neale, R. B., Richter, J. H., Conley, A. J., Park, S., Lauritzen, P. H., Gettelman, A., et al. (2010). Description of the NCAR Community Atmosphere Model (CAM 5.0). *NCAR TechNote NCAR/TN-486+ STR*, 212.

Newman, M., Alexander, M. A., and Scott, J. D. (2011a). An Empirical Model of Tropical Ocean Dynamics. *Clim. Dyn.* 37, 1823–1841. doi:10.1007/s00382-011-1034-0

Newman, M., Shin, S.-I., and Alexander, M. A. (2011b). Natural Variation in ENSO Flavors. *Geophys. Res. Lett.* 38, a–n. doi:10.1029/2011GL047658

Ohba, M., and Ueda, H. (2009). Role of Nonlinear Atmospheric Response to SST on the Asymmetric Transition Process of ENSO. *J. Clim.* 22, 177–192. doi:10.1175/2008JCLI2334.1

Okumura, Y. M., and Deser, C. (2010). Asymmetry in the Duration of El Niño and La Niña. *J. Clim.* 23, 5826–5843. doi:10.1175/2010JCLI3592.1

Okumura, Y. M. (2019). ENSO Diversity from an Atmospheric Perspective. *Curr. Clim. Change Rep.* 5, 245–257. doi:10.1007/s40641-019-00138-7

Perigaud, C., and Dewitte, B. (1996). El Niño-La Niña Events Simulated with Cane and Zebiak's Model and Observed with Satellite or *In Situ* Data. Part I: Model Data Comparison. *J. Clim.* 9, 66–84. doi:10.1175/1520-0442(1996)009<0066:ennesw>2.0.co;2

Rayner, N. A. (2003). Global Analyses of Sea Surface Temperature, Sea Ice, and Night marine Air Temperature since the Late Nineteenth century. *J. Geophys. Res.* 108, 4407. doi:10.1029/2002JD002670

Reynolds, R. W., Rayner, N. A., Smith, T. M., Stokes, D. C., and Wang, W. (2002). An Improved *In Situ* and Satellite SST Analysis for Climate. *J. Clim.* 15, 1609–1625. doi:10.1175/1520-0442(2002)015<1609:AIISAS>2.0.CO;2

Ren, H.-L., and Jin, F.-F. (2011). Niño Indices for Two Types of ENSO. *Geophys. Res. Lett.* 38. doi:10.1029/2010gl046031

Ren, H.-L., and Jin, F.-F. (2013). Recharge Oscillator Mechanisms in Two Types of ENSO. *J. Clim.* 26, 6506–6523. doi:10.1175/jcli-d-12-00601.1

Ren, H.-L., and Wang, R. (2020). Distinct Growth Rates of the Two ENSO Types. *Geophys. Res. Lett.* 47, e2020GL088179. doi:10.1029/2020gl088179

Rodríguez-Morata, C., Díaz, H. F., Ballesteros-Canovas, J. A., Rohrer, M., and Stoffel, M. (2019). The Anomalous 2017 Coastal El Niño Event in Peru. *Clim. Dyn.* 52, 5605–5622. doi:10.1007/s00382-018-4466-y

Takahashi, K., and Dewitte, B. (2016). Strong and Moderate Nonlinear El Niño Regimes. *Clim. Dyn.* 46, 1627–1645. doi:10.1007/s00382-015-2665-3

Takahashi, K., Karamperidou, C., and Dewitte, B. (2019). A Theoretical Model of strong and Moderate El Niño Regimes. *Clim. Dyn.* 52, 7477–7493. doi:10.1007/s00382-018-4100-z

Takahashi, K., Montecinos, A., Goubanova, K., and Dewitte, B. (2011). ENSO Regimes: Reinterpreting the Canonical and Modoki El Niño. *Geophys. Res. Lett.* 38, a–n. doi:10.1029/2011GL047364

Taschetto, A. S., Ummenhofer, C. C., Stuecker, M. F., Dommenget, D., Ashok, K., Rodrigues, R. R., et al. (2020). "ENSO Atmospheric Teleconnections," in *El Niño Southern Oscillation in a Changing Climate*. Editors M. J. McPhaden, A. Santoso, and W. Cai, Geophysical Monograph Series, AGU, 309–335. doi:10.1002/9781119548164.ch14

Timmermann, A., An, S.-I., Kug, J.-S., Jin, F.-F., Cai, W., Capotondi, A., et al. (2018). El Niño-Southern Oscillation Complexity. *Nature* 559, 535–545. doi:10.1038/s41586-018-0252-6

Vimont, D. J., Alexander, M. A., and Newman, M. (2014). Optimal Growth of central and East Pacific ENSO Events. *Geophys. Res. Lett.* 41, 4027–4034. doi:10.1002/2014GL059997

Vimont, D. J., Newman, M., Battisti, D. S., and Shin, S.-I. (2022). The Role of Seasonality and the ENSO Mode in Central and East Pacific ENSO Growth and Evolution. *J. Clim.* 1, 1–46. doi:10.1175/JCLI-D-21-0599.1

Wang, R., and Ren, H.-L. (2020). Understanding Key Roles of Two ENSO Modes in Spatiotemporal Diversity of ENSO. *J. Clim.* 33, 6453–6469. doi:10.1175/jcli-d-19-0770.1

Weare, B. C. (1986). A Simple Model of the Tropical Atmosphere with Circulation Dependent Heating and Specific Humidity. *J. Atmos. Sci.* 43, 2001–2016. doi:10.1175/1520-0469(1986)043<2001:asmott>2.0.co;2

Webster, P. J. (1981). Mechanisms Determining the Atmospheric Response to Sea Surface Temperature Anomalies. *J. Atmos. Sci.* 38, 554–571. doi:10.1175/1520-0469(1981)038<0554:mdtart>2.0.co;2

Wiedermann, M., Radebach, A., Donges, J. F., Kurths, J., and Donner, R. V. (2016). A Climate Network-Based index to Discriminate Different Types of El Niño and La Niña. *Geophys. Res. Lett.* 43, 7176–7185. doi:10.1002/2016gl069119

Wu, Z., Sarachik, E. S., and Battisti, D. S. (2000). Vertical Structure of Convective Heating and the Three-Dimensional Structure of the Forced Circulation on an Equatorial Beta Plane*. *J. Atmos. Sci.* 57, 2169–2187. doi:10.1175/1520-0469(2000)057<2169:vsocha>2.0.co;2

Xie, R., and Jin, F.-F. (2018). Two Leading ENSO Modes and El Niño Types in the Zebiak-Cane Model. *J. Clim.* 31, 1943–1962. doi:10.1175/JCLI-D-17-0469.1

Yang, S., Li, Z., Yu, J.-Y., Hu, X., Dong, W., and He, S. (2018). El Niño-Southern Oscillation and its Impact in the Changing Climate. *Natl. Sci. Rev.* 5, 840–857. doi:10.1093/nsr/nwy046

Yeh, S.-W., Kug, J.-S., Dewitte, B., Kwon, M.-H., Kirtman, B. P., and Jin, F.-F. (2009). El Niño in a Changing Climate. *Nature* 461, 511–514. doi:10.1038/nature08316

Yu, J.-Y., Kao, H.-Y., and Lee, T. (2010). Subtropics-related Interannual Sea Surface Temperature Variability in the central Equatorial Pacific. *J. Clim.* 23, 2869–2884. doi:10.1175/2010jcli3171.1

Yuan, X., Jin, F. F., and Zhang, W. (2020). A Concise and Effective Expression Relating Subsurface Temperature to the Thermocline in the Equatorial Pacific. *Geophys. Res. Lett.* 47, e2020GL087848. doi:10.1029/2020GL087848

Zebiak, S. E., and Cane, M. A. (1987). A Model El Ni&ntilde-Southern Oscillation. *Mon. Wea. Rev.* 115, 2262–2278. doi:10.1175/1520-0493(1987)115<2262:ameno>2.0.co;2

Zhang, S., Harrison, M. J., Rosati, A., and Wittenberg, A. (2007). System Design and Evaluation of Coupled Ensemble Data Assimilation for Global Oceanic Climate Studies. *Monthly Weather Rev.* 135, 3541–3564. doi:10.1175/MWR3466.1

Zhao, S., Jin, F. F., Long, X., and Cane, M. A. (2021). On the Breakdown of ENSO's Relationship with Thermocline Depth in the Central-Equatorial Pacific. *Geophys. Res. Lett.* 48, e2020GL092335. doi:10.1029/2020GL092335

Zuo, H., Balmaseda, M. A., Tietsche, S., Mogensen, K., and Mayer, M., (2019). The ECMWF Operational Ensemble Reanalysis-Analysis System for Ocean and Sea-Ice: a Description of the System and Assessment. *Ocean Sci.*, 15, 779–808. doi:10.5194/os-15-779-2019

Conflict of Interest: The authors declare that the research was conducted in the absence of any commercial or financial relationships that could be construed as a potential conflict of interest.

Publisher's Note: All claims expressed in this article are solely those of the authors and do not necessarily represent those of their affiliated organizations, or those of the publisher, the editors and the reviewers. Any product that may be evaluated in this article, or claim that may be made by its manufacturer, is not guaranteed or endorsed by the publisher.

frontiers | Frontiers in Earth Science

PERSPECTIVE
published: 25 May 2022
doi: 10.3389/feart.2022.899139

Toward Understanding El Niño Southern-Oscillation's Spatiotemporal Pattern Diversity

Fei-Fei Jin *

Department of Atmospheric Sciences, School of Ocean and Earth Science and Technology, University of Hawai'i at Mānoa, Honolulu, HI, United States

The El Niño Southern Oscillation (ENSO) phenomenon, manifested by the great swings of large-scale sea surface temperature (SST) anomalies over the equatorial central to eastern Pacific oceans, is a major source of interannual global shifts in climate patterns and weather activities. ENSO's SST anomalies exhibit remarkable spatiotemporal pattern diversity (STPD), with their spatial pattern diversity dominated by Central Pacific (CP) and Eastern Pacific (EP) El Niño events and their temporal diversity marked by different timescales and intermittency in these types of events. By affecting various Earth system components, ENSO and its STPD yield significant environmental, ecological, economic, and societal impacts over the globe. The basic dynamics of ENSO as a canonical oscillator generated by coupled ocean–atmosphere interactions in the tropical Pacific have been largely understood. A minimal simple conceptual model such as the recharge oscillator paradigm provides means for quantifying the linear and nonlinear seasonally modulated growth rate and frequency together with ENSO's state-dependent noise forcing for understanding ENSO's amplitude and periodicity, boreal winter-time phase locking, and warm/cold phase asymmetry. However, the dynamical mechanisms explaining the key features of ENSO STPD associated with CP and EP events remain to be better understood. This article provides a summary of the recent active research on the dynamics of ENSO STPD together with discussions on challenges and outlooks for theoretical, diagnostic, and numerical modeling approaches to advance our understanding and modeling of ENSO, its STPD, and their broad impacts.

Keywords: El Niño Southern Oscillation phenomenon, spatiotemporal pattern diversity, phase locking, ENSO asymmetry, recharge oscillator paradigm

OPEN ACCESS

Edited by:
Hong-Li Ren,
Chinese Academy of Meteorological Sciences, China

Reviewed by:
Antonietta Capotondi,
University of Colorado Boulder, United States
Youmin Tang,
University of Northern British Columbia Canada, Canada

***Correspondence:**
Fei-Fei Jin
jff@hawaii.edu

Specialty section:
This article was submitted to Atmospheric Science, a section of the journal Frontiers in Earth Science

Received: *18 March 2022*
Accepted: *19 April 2022*
Published: *25 May 2022*

Citation:
Jin F-F (2022) Toward Understanding El Niño Southern-Oscillation's Spatiotemporal Pattern Diversity. Front. Earth Sci. 10:899139. doi: 10.3389/feart.2022.899139

INTRODUCTION OF ENSO STPD

ENSO is the most prominent phenomenon of year-to-year fluctuations in the global climate system. It interacts strongly with the rest of the weather–climate continuum involving timescales ranging from synoptic through multidecadal to centennial, affecting not only the global climate system but also marine and terrestrial ecosystems, fisheries, human health, and other societal and economic aspects of the Earth system (cf. McPhaden et al., 2006; Cashin et al., 2017; Timmermann et al., 2018; Boucharel et al., 2021). The primary dynamical mechanisms for ENSO's basic features as a canonical oscillator have been extensively investigated in terms of a leading coupled ocean–atmosphere model of the tropical Pacific essentially described by the simple conceptual delayed oscillator/recharge oscillator paradigm (Cane and Zebiak, 1985; Suarez and Schopf, 1988; Battisti and Hirst, 1989;

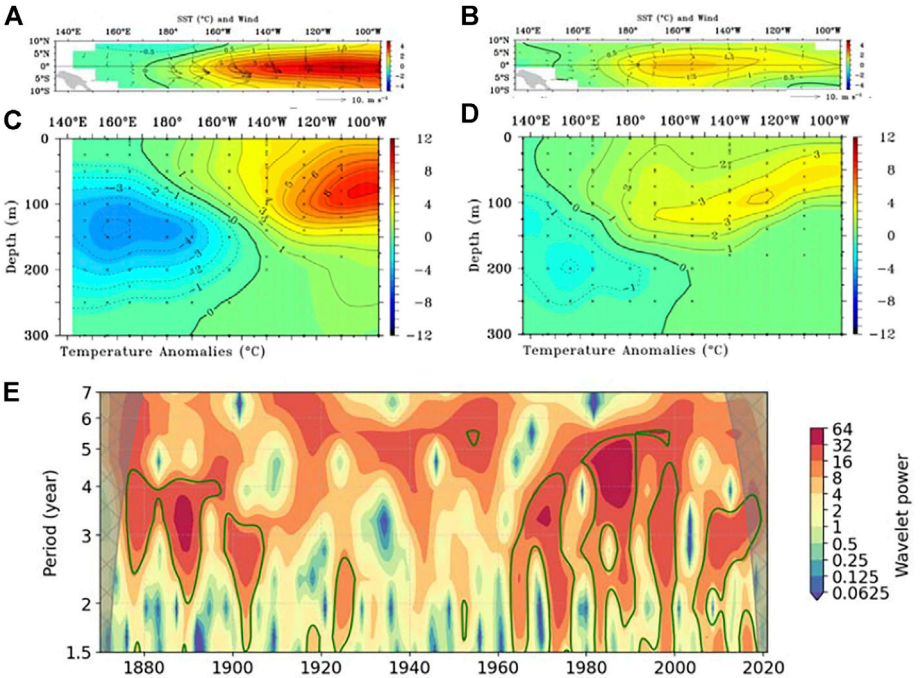

FIGURE 1 | November–December–January mean SST anomalies **(A,B)** and subsurface temperature anomalies at the equator (2°S-2°N) **(C,D)** during the 1997/98 EP **(A,C)** and 2009/10 CP **(B,D)** El Niño events from NOAA/PMEL (https://www.pmel.noaa.gov/tao/drupal/disdel/). **(E)** Wavelet power spectrum of the normalized time series of Niño-3.4 SST anomalies from HadISST (Rayner et al., 2003). The green contour encloses regions of greater than 95% confidence level tested against red noise. Cross-hatched regions on either end indicate the "cone of influence" where edge effects become important.

Philander, 1990; Jin and Neelin, 1993; Neelin and Jin, 1993; Jin, 1997a, 1997b; Neelin et al., 1998; Wang and Picaut, 2004; Jin et al., 2020). Different ENSO-like behaviors observed in nature and simulated in various coupled models were viewed qualitatively as the result of the sensitive dependence of the leading coupled linear mode to variations in the climate background state (Jin and Neelin, 1993; An and Jin, 2000; Fedorov and Philander, 2000, 2001).

In the past 2 decades, new layers of complexity of the ENSO phenomenon were identified with important implications for ENSO's impacts and predictability (Timmermann et al., 2018). It has been widely recognized that the observed ENSO pattern diversity and temporal complexity tend to manifest roughly in two dominant ENSO types known as central Pacific (CP) and eastern Pacific (EP) El Niño events (Larkin and Harrison, 2005a, 2005b; Ashok et al., 2007; Weng et al., 2007; Kug et al., 2009; Kao and Yu, 2009), as exemplified by two typical EP and CP El Niño events shown in **Figures 1A, B**. Associated with the sea surface temperature (SST) anomaly patterns, there is a westward shift of the slanted boundary marking the transition region between positive and negative equatorial ocean subsurface temperature anomalies (**Figures 1C, D**), suggesting that different upper thermocline thermal stratification responses may contribute to different dynamical feedback strengths during CP and EP El Niño events (Zhao et al., 2021a). The pacing or periodicity is different as well, with CP events tending to occur every ~2–3 years (during the epoch of the 2000s, for example), whereas EP events tend to exhibit slower pacing with occurrences every ~4–5 years, as shown in **Figure 1E**. Moreover, there is a modulated intermittency with active/less-active epochs with relatively more/fewer CP over EP events. A detailed and informative overview of the key characteristics of ENSO STPD can be found in the work of Capotondi et al. (2020).

The observed key features of diversity in patterns and temporal evolution of ENSO, referred to ENSO STPD hereafter, are still inadequately captured by state-of-the-art climate models, despite the increasing successes achieved in simulating the ENSO phenomenon due to better process representations and increased in model resolutions (Planton et al., 2021). This is in part due to the fundamentally sensitive nonlinear dynamics of ENSO STPD and the fact that ENSO STPD involves multiscale interactions between ENSO and other major modes of variability, including the Madden Julian Oscillation (MJO) and Westerly Wind Bursts (WWBs), Tropical Instability Waves (TIWs), Pacific Meridional Modes (PMMs), the Interdecadal Pacific Oscillation (IPO) and/or Pacific Decadal Oscillation (PDO), and modes in other tropical ocean basins (see reviews by Timmermann et al., 2018; Wang, 2018; Yang et al., 2018; Cai et al., 2019). As a result, various biases in the climate mean state, seasonal cycle, the composition of key coupled feedback processes of ENSO, and ENSO's interactions with other modes of variability can all play important roles in hindering the state-of-the-art climate model's capabilities of simulating ENSO and its STPD, which shall affect the performances of these models in projecting changes of ENSO and their associated global impacts under global warming. Thus,

advancing our understanding of ENSO STPD and its broad impacts on various aspects of the Earth system has been the subject of active multi-disciplinary research.

KEY SOURCES FOR ENSO STPD

A great amount of work has been directed to understanding the implications of this ENSO STPD in all aspects of ENSO's impacts. At the same time, a surge of research activities aimed at understanding the dynamics of ENSO STPD has led to some significant progress. Much of it has been recently reviewed by several authors, including Capotondi et al. (2015, 2020), Timmermann et al. (2018), and Taschetto et al. (2020). A few hypotheses have been put forth as potential mechanisms for observed ENSO STPD. First, based on linear eigen-analyses of modified versions of the Cane-Zebiak (CZ) model and subsequent nonlinear simulations of CP and EP pattern diversity performed by Bejarano and Jin (2008) and Xie and Jin (2018), the coexistence of CP and EP ENSO-like linear eigenmodes under a given climate basic state and parameter setting were proposed as a promising linear pathway for understanding the observed ENSO STPD (Timmermann et al., 2018). Second, ENSO's interactions with other modes of variability, either in the Pacific Ocean sector or other tropical basins, have been suggested to play some viable roles in generating ENSO STPD (Chiang and Vimont, 2004; Yu et al., 2010; Yu and Kim, 2011; Ham et al., 2013; Lian et al., 2014; Vimont et al., 2014; Zhang et al., 2014; Chen et al., 2015; Fedorov et al., 2015; Jadhav et al., 2015; Hu and Fedorov, 2018). However, the underlying fundamental deterministic dynamics that allow various other modes of variability to be effective in either exciting and/or interacting with ENSO and thereby generating ENSO STPD remains to be addressed. Third, the two types of El Niño were noted to develop under two different combinations of the thermocline feedback and zonal advective feedback, with EP El Niño having relatively stronger thermocline feedback and CP El Niño a relatively stronger zonal advective feedback (Kug et al., 2009; Capotondi et al., 2015, 2020). This notion adds a partial understanding of ENSO STPD but again does not address the key controlling dynamical mechanism that sustains these contrasting ENSO behaviors. Fourth, key nonlinearities residing in 1) the threshold dependence of convective heating on SST (Choi et al., 2013; Takahashi et al., 2019) and 2) the nonlinear zonal advection of SST (Capotondi, 2013; Chen and Majda, 2017) have been suggested important for ENSO nonlinear growth, although how the different nonlinearities effectively alter the linear dynamical processes to generate ENSO STPD remains to be better understood.

A POTENTIAL UNIFYING PARADIGM FOR ENSO STPD

Recently, important progress was made in a newly completed Ph.D. thesis study (Geng, 2021). By uncovering an error in the method of solving the eigen solutions by Bejarano and Jin (2008) and Xie and Jin (2018), this new study dismissed the linear pathway for ENSO STPD proposed by Xie and Jin (2018) and also advocated by Timmermann et al. (2018). This is not only because the proposed linear pathway therein was based on spurious coexistence of unstable linear CP and EP modes but also due to the fact that ENSO STPD simulated by these earlier versions of the CZ-type model and a recently revised CZ model (RCZ hereafter; Geng and Jin, 2022) are all due to a general *nonlinearity/noise-induced regime transitions* (*NIRT*) *mechanism*. To be more specific, when conditions are right, a solo leading linear ENSO mode in the CZ-type model can undergo strong nonlinear modifications owing to advective and/or convective nonlinearities. As a result, it is the nonlinear pathway via the NIRT mechanism that is responsible for the simulated ENSO STPD in the CZ-type model with transitions of EP- and CP-like El Niño events taking place deterministically or stochastically. For this NIRT mechanism to take effect, however, it requires the leading linear ENSO mode to satisfy two stingy constraints: 1) its linear growth rate to be near criticality or supercritical so that nonlinearity becomes effective and 2) its interannual frequency and SST pattern both being highly sensitive to modest changes in the basic state and parameters. Under these strongly double constraints, the leading ENSO mode can lead to irregular transitions between CP and EP El Niño events via deterministic chaos and/or stochastic excitations.

With the RCZ model that underwent careful validations using observational data, Geng (2021) showed that ENSO STPD can be captured only within a narrow range near the best-estimated parameter setting and observed basic state conditions owing to the strongly double constraints. The RCZ model simulated ENSO exhibits basic features reasonably reminiscent of what is observed: intermittency of CP and EP El Niño events with a strong bimodality in the probability density distribution for the SST centroid longitude and some modest decadal to multidecadal modulations of the mean state. In the case without noise forcing and with no annual cycle in the basic state, the leading CP-like ENSO mode will give rise to self-sustained ENSO oscillation whose amplitude increases with stronger supercriticality following the normal manner of Hopf-bifurcation as delineated in the weakly nonlinear regime as in appendix of Jin (1997a). However, under weak to moderate supercritical conditions slightly away from the very limited weakly nonlinear regime, this simple ENSO oscillator itself becomes unstable owing to the sensitive interaction between the ENSO oscillator and the mean state, which generates a regime for ENSO STPD featuring deterministic chaos with CP and EP ENSO regime transitions and quasiperiodic orbits with CP and EP events alternations. When the observed annual cycle in the basic state is included, the parameter range for ENSO STPD is significantly expanded as the route to chaos via the so-called overlap subharmonic resonance (Chang et al., 1994; Jin et al., 1994; Tziperman et al., 1994) becomes effectively activated due to the nonlinear interaction between ENSO and the annual cycle. With stochastic forcing, the ENSO STPD regime broadens further, especially towards the subcritical regime where the leading mode is not self-sustained. It is worthy to emphasize

that ENSO chaos generated by ENSO-annual cycle interaction noted by Jin et al. (1994) only features weak temporal irregularity in simulated ENSO behaviors without exhibiting CP and EP pattern diversity. Similarly, in the slightly stronger subcritical regime where the ENSO linear mode is more damped or in the regimes where the leading mode is insensitive to nonlinear modifications, noise forcing can generate temporal irregularity but does not lead to significant CP and EP diversity. In other words, ENSO STPD can be generated via nonlinear deterministic and stochastic dynamics-induced CP and EP ENSO transitions, but only when the aforementioned doubly constrained conditions are satisfied. This general mechanism can be considered as a potential unifying paradigm because it incorporates the keynoted sources for ENSO STPD, including 1) deterministic nonlinear dynamics, 2) stochastic forcing (which can be largely related to various excitations from other modes of variability), and 3) CP and EP's different mechanisms in terms of relative strengths of the zonal advective feedback and thermocline feedback processes. The doubly constrained conditions for ENSO STPD portrayed by this paradigm make ENSO STPD fundamentally sensitive to modest biases or changes in the climate mean state, seasonal cycle, the composition of feedback processes, and ENSO's interaction with other modes of variability. This sensitivity poses a great challenge for simulating ENSO STPD and projecting ENSO's changes through comprehensive climate models. Further active research of the dynamics of STPD may lead to a better understanding of the observed and climate model simulated ENSO and its STPD and associated broad impacts.

CHALLENGES AND OUTLOOKS

The advance in our understanding of ENSO in the past 4 decades was achieved in multiple areas, including observations, theory and dynamics, modeling and prediction, past and future changes, and impacts, which all have been comprehensively reviewed in a recent AGU monograph by McPhaden et al. (2020). Hierarchical modeling approaches, comprising conceptual models, intermediate complexity models, and comprehensive climate models, have been instrumental in these remarkable advancements. In fact, ENSO's basic features (for example, its amplitude, growth, frequency, noise forcing, and asymmetry) and how they may be affected by a model's compositions of coupled processes, mean state, and annual cycle, have been meaningfully assessed and analyzed in many recent studies with this approach (c.f, Jin et al., 2020; Yu et al., 2016; Chen and Jin, 2020, 2021; Vijayeta and Dommenget, 2018; Zhao et al., 2021b; Levine and Jin, 2010; Levine et al., 2016; Levine and Jin, 2017; Levine et al., 2017; Wengel et al., 2018). For example, using a data-fitted recharge oscillator model, Wengel et al. (2018) demonstrated that the ENSO amplitude simulated by state-of-the-art climate models depends on ENSO's growth rate and its noise excitation. This ENSO growth rate metric can be proven to be nearly the same as the total linear and nonlinear combined growth rate using a Bjerknes Instability index (a measure of the linear ENSO growth rate resulting from the net effect of positive and negative feedbacks) formulation (Jin et al., 2020). Thus, one may gain further insights into ENSO amplitude in terms of linear and nonlinear growth rate and stochastic forcing (Jin et al., 2020). Chen and Jin (2021) demonstrated that the biases of seasonal modulations of the ENSO growth rate are responsible for pronounced biases of ENSO phase locking in climate models. The broad inter-model spread of simulated ENSO phase locking was shown to be understood by the conceptual RO model. Even for models with relatively "good" ENSO simulation capabilities, such as the E3SM-1-0, CESM2, and GFDL-CM4 models, Chen et al. (2021) noted pronounced common biases in the zonal advective feedback in the central to western Pacific and associated ENSO SST pattern biases near the warm pool edge. These common biases may hinder models' ability to simulate EP and CP diversity, which is strongly sensitive to the relative strengths of the zonal advective and thermocline feedbacks according to the NIRT mechanism.

The previous success of the hierarchical modeling approaches and the latest advancements in ENSO theory for understanding ENSO and its STPD pointed to promising ways to address and resolve several main challenging issues concerning ENSO STPD and its implications. For example, can we achieve a conceptual understanding of ENSO STPD through a systematic investigation of various contributing sources in a similar way to the simple recharge oscillator paradigm for our understanding of the basic dynamics of ENSO? Can we achieve a better understanding of the roles of model biases in the climate mean state and its seasonal cycle and in the composition of its main feedback processes in model simulated ENSO STPD and thus identify practical pathways for improving climate models' capability in simulating ENSO and its STPD? Can we achieve a better understanding of ENSO STPD's predictability for ENSO regime behavior as noted by Timmermann and Jin (2005)? Can we achieve a better understanding of the projections of ENSO changes relative to the current observed ENSO STPD regime, which can be fundamentally sensitive to climate change? Can we achieve a better understanding of ENSO STPD's direct and indirect impacts from other modes of variability influenced by ENSO on various aspects of the Earth system?

To further discuss the outlooks to address these questions, a synthesized framework focusing on ENSO STPD is illustrated in **Figure 2**, which is extended from the frameworks schematically depicted in Timmermann et al. (2018) and Wittenberg (2018). This framework highlights three foci in addition to the basic coupled dynamics understood in existing conceptual models and ICMs for ENSO. First, it highlights the newly uncovered NIRT mechanism that is essential for ENSO STPD. Second, it highlights two key physical processes, the convective-radiative feedback in atmospheric moist dynamics (Adames and Kim, 2016) and wind-driven thermal stratification adjustment in the central equatorial Pacific (Zhao et al., 2021a), both of which may have strong effects on the composition of ENSO feedbacks in both nature and comprehensive climate models. Third, it highlights ENSO's interactions with various other modes of variability and the roles of deterministic nonlinearities and stochastic forcing, which all have been suggested to be of importance for ENSO STPD. I will briefly discuss a few areas for potential significant advances with this guiding framework.

On low-order conceptual models for ENSO STPD: Simple conceptual models such as the recharge oscillator model have

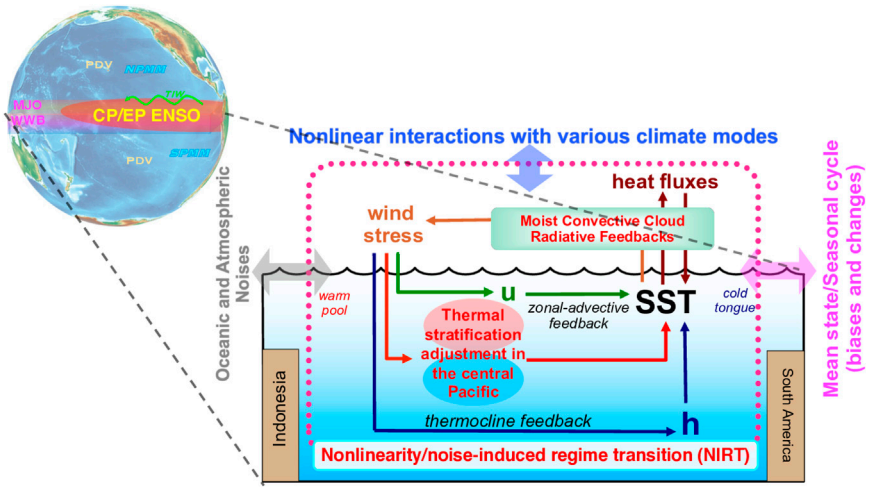

FIGURE 2 | Schematic diagram (modified based on Whittenberg 2018) of major modes of variability in the Pacific and key ENSO atmospheric and oceanic processes.

played an important role in understanding ENSO's basic dynamics and features. To address the need of developing new conceptual models that can serve as useful tools for understanding key features of ENSO STPD, a working group under the CLIVAR Pacific Panel was established in 2020 under the leadership of Dr. Jerome Vialard to review the progress and to discuss prospects for developing such a kind of models. Two SST variables for central and eastern Pacific SST anomalies, T_C and T_E, respectively, are the minimal degrees of freedom that must be considered for capturing the essence of CP and EP pattern diversity. The quasi-steady atmospheric response in terms of wind stress and heat fluxes can be expressed as linear or nonlinear functions of these SST anomalies by making reasonable approximations. These were adopted in attempts to develop simple conceptual models for ENSO diversity (Fang and Mu, 2018). However, an essential issue remaining to be resolved in constructing a low-order conceptual model for capturing ENSO STPD is to derive a minimum low-order component to describe oceanic memories associated with the thermocline and zonal current responses to ENSO's winds. In the recharge oscillator model, this oceanic memory resides in a slow recharge mode which was reduced to 1-degree of freedom in terms of warm pool heat content or zonal mean heat content (Jin, 1997a, 2001). To better capture the rich temporal complexity of ENSO, it may be necessary to include the gravest ocean basin mode noted by Cane and Moore (1981), which is important for better capturing central Pacific zonal currents associated with ENSO as was first noted by Picaut et al. (1997). Moreover, both the slow recharge mode and the fast gravest ocean basin mode can be destabilized into an ENSO-like mode by increasing dynamical coupling, as demonstrated by Cane et al. (1990), Jin (1997b), and more recently by Geng (2021). In fact, it was noted that when the leading ENSO mode has mixed features of the recharge oscillator mode and the wave oscillator mode, it becomes highly sensitive to the composition of the zonal advective feedback and thermocline feedback. It is this sensitivity that allows the nonlinear processes to act very effectively in altering the leading ENSO mode and thereby generate CP and EP ENSO nonlinear intermittent transitions via the so-called NIRT mechanism. It requires at least 3-degrees of freedom for a low-order ocean dynamics model to capture both the slow ocean heat content recharge/discharge mode and the gravest ocean basin mode. Thus, a conceptual model for ENSO STPD may need five or more degrees of freedom. Moreover, proper considerations of nonlinear processes in such a low-order model become much more important. As the developments of low-order ENSO models for its STPD have attracted more attention, some prototypes are emerging and will become useful additions to the hierarchy of modeling tools for assessing and understanding ENSO STPD.

On Intermediate Coupled Models (ICM) for ENSO STPD: CZ-type models have served as the core framework for the advances of ENSO theory during the past 4 decades. Our recent study uncovered the NIRT mechanism for ENSO STPD and again used a CZ-type model. Nevertheless, some essential processes, such as 1) convective cloud radiative feedback associated with moisture dynamics and 2) a key oceanic process involving wind-driven upper thermocline ocean stratification adjustment of the equatorial ocean is highlighted in **Figure 2**, are currently omitted in CZ-type models. The convective cloud radiative feedback associated with moisture dynamics of ENSO affects both the dynamic air-sea coupling through ENSO's wind-SST relationship and the thermodynamic feedback through surface heat flux sensitivity as noted in our study using new versions of a moist linear baroclinic model (mLBM) for the atmosphere (Hayashi and Jin, 2022; Chen et al., 2022, personal communication). These key feedbacks are controlled by the dynamic air-sea coupling parameter and SST thermal damping parameter, both of which can be assessed using climate model outputs and reanalysis data. However, unlike in a CZ-type model, they cannot be arbitrarily changed in climate

models. Thus, using the mLBM as an alternative to the Gill-type atmospheric component to form new versions of ICM models will be useful to examine the role of the convective cloud radiative feedback associated with moisture dynamics in ENSO and its STPD. Similarly, the ocean component of the CZ-type model may be replaced by a linear continuously stratified (LCS) tropical Pacific Ocean model (McCreary, 1981; McPhaden, 1981; Keenlyside and Kleeman, 2002) to capture wind-driven equatorial upper thermocline thermal stratification adjustment, which contributes to ENSO's zonal advective feedback and thermocline feedback differently between EP and CP ENSO events and thus may affect ENSO and its STPD (Zhao et al., 2021a). Clearly, this kind of extension of the CZ-type model will be helpful for better advancing processes-level understanding of the dynamics of ENSO and its STPD.

On the role of ENSO-Annual Cycle Interactions in ENSO STPD: Although ENSO chaos through nonlinear subharmonic overlap resonance as found by Jin et al. (1994), Tziperman et al. (1994), and Chang et al. (1994) was noted as an important deterministic source of ENSO irregularity, it has not gained much further attention because ENSO as part of the climate-weather continuum has been suggested to be more of a noise-driven irregular oscillator. However, some new evidence indicates that the annual cycle can effectively expand the extent of the ENSO STPD regime in the RCZ model (Geng 2021) because the NIRT mechanism provides a natural nonlinearity-induced ENSO frequency sensitivity which allows the nonlinear subharmonic overlap resonance route to chaos to become effective, not only creating temporal irregularity but also spatial pattern diversity of ENSO. Moreover, ENSO-annual cycle interaction with the NIRT mechanism at work may effectively create a frequency cascade toward ENSO decadal timescale variability through readily exciting nonlinear transitions of frequency-locked CP and EP ENSO cycles. For example, if there were pronounced frequency-locked 3-years and 4-year periodic orbit transitions, one would expect a potential 12-years spectral peak. This kind of ENSO frequency cascade can generate low-frequency variability and provides a potentially important driver for both ENSO modulation and Pacific decadal variability. This role of ENSO-annual cycle interactions in ENSO STPD may have implications for paleo and future changes of both ENSO and the tropical climate mean state.

On ENSO's nonlinear interactions with other modes for ENSO STPD: There is a large body of studies suggesting that ENSO may be excited or affected by various other modes of variability both within and outside the tropical Pacific while ENSO, as one of the strongest climatic modes, can affect those modes as well. Depending on the natures of these modes, ENSO's interaction with them may not only affect ENSO's basic features but also serve as sources for ENSO's "noise" forcing and modulations, which all may play important roles in ENSO STPD. For example, one of the most prominent features that are closely associated with ENSO is the enhanced/reduced TIW activity during La Niño/El Niño events. An and Jin (2004) demonstrated that nonlinear ENSO-TIW interaction can affect ENSO asymmetry. Boucharel and Jin (2020) and Xue et al. (2020) built a conceptual model to demonstrate that this nonlinear interaction is highly seasonally modulated. This asymmetric nonlinear interaction may have strong implications for ENSO's rectification on the basic state, which in turn can affect the NIRT pathway to ENSO STPD. Moreover, the strong seasonality in this interaction can serve as another source of seasonal modulation that may affect the extent of the ENSO STPD regime. The work of Boucharel and Jin (2020) and Xue et al. (2020) has paved the way for developing nonlinear and seasonally modulated parameterizations for TIW-induced nonlinear feedback on ENSO, which can be useful for assessing TIW's feedback on ENSO simulated in climate models and can be incorporated into the CZ-type model or other ICMs for studying the impacts of ENSO-TIW interaction on ENSO and its STPD.

There is a large body of studies investigating the roles of the MJO and WWBs in exciting ENSO's complex behaviors and even altering ENSO's growth rate and frequency and predictability using conceptual models, CZ-type models, and coupled climate models. However, simple conceptual and CZ-type ICMs mostly describe MJO/WWB activity and its modulation by ENSO in ad hoc manners, often in terms of state-dependent noise. Developments of conceptual models and ICMs for understanding the dynamics of ENSO's modulation on MJO/WWB will be essential for better understanding ENSO's interaction with MJO/WWB activity, especially for its roles in ENSO STPD.

Several studies suggested that Pacific Meridional Modes (PMMs) may play a potentially important role in ENSO STPD through stochastically exciting ENSO cycles and providing distinct optimal precursors for the two types of ENSO (Amaya, 2019, and references therein; Vimont et al., 2014, 2022; Capotondi and Ricchiardulli, 2021). However, the notion that ENSO serves as a strong driver of PMM makes the PMM's contribution to ENSO and its STPD an open question needing further exploration (Stuecker, 2018). ICMs explicitly resolving the relevant physical processes, particularly the wind-evaporation and cloud-radiation to SST feedbacks that are missing out in most ICMs, may be helpful to advance our understanding of how these PMMs may interact with ENSO to affect the extent of ENSO STPD regimes. Moreover, the wind stress curl in subtropical regions may excite slow ocean adjustment and potentially yield decadal coupled modes once this slow process is connected to coupled dynamics in the equatorial Pacific (Wang et al., 2003a; 2003b). Thus, according to the NIRT mechanism, the presence of PMMs and their associated wind-driven slow ocean adjustment may enhance ENSO's internal low-frequency modulation as the result of nonlinear interaction between ENSO and the mean state. This ENSO low-frequency variability associated with ENSO STPD and its potential enhancement through ENSO-PMM interaction may serve as important sources for the so-called Pacific Decadal Oscillation (PDO) and Interdecadal Pacific Oscillation (IPO). Moreover, ENSO STPD may affect and also be affected by ENSO's interactions with the modes of variability outside the Pacific. Further investigation of inter-basin interactions among ENSO and the modes of variability in other ocean basins shall also shed light on ENSO STPD.

The advances in understanding the dynamics of ENSO STPD will also lead to better assessment and understanding of ENSO

STPD simulated in state-of-the-art climate models, which are mostly still falling short in realistically simulating ENSO STPD. Such models' deficiency is likely attributed to the high sensitivity of ENSO STPD to even modest biases in climate models in terms of simulated climate mean state, its seasonal cycle, and the composition of key feedback processes of ENSO. Nevertheless, better assessing and understanding how these biases or potential reductions of them may affect the capabilities of climate models to more realistically capture ENSO and its STPD may lead to potential pathways for model improvements. Moreover, ENSO STPD, together with ENSO's nonlinearly and seasonally modulated interactions with other modes of variability, make ENSO's influences on various aspects of the Earth system much more complex. That is, ENSO can have not only direct impacts but also indirect impacts through its influences on the other modes of variability in both nonlinear and nonstationary manners. Better assessing, understanding, simulating ENSO and its STPD may provide better understanding and predictive skills for ENSO and its impacts even on the regional but highly destructive and thus hazardous phenomena as demonstrated, for example, in recent research on ENSO's impact on worldwide coastal ocean wave activity and coastal shorelines (Boucharel et al., 2021; Almar et al., 2022, personal communication).

DATA AVAILABILITY STATEMENT

Publicly available datasets were analyzed in this study. These data can be found at: https://www.metoffice.gov.uk/hadobs/hadisst/.

AUTHOR CONTRIBUTIONS

F-FJ designed the study and wrote the manuscript.

FUNDING

The work was supported by the U.S. National Science Foundation (AGS-1813611) and the U.S. Department of Energy (DESC0005110).

ACKNOWLEDGMENTS

The author is grateful to Dr. Sen Zhao who produced the two figures and also to Drs. Licheng Geng, Sen Zhao, Malte Stuecker, and Andrew Wittenberg for valuable comments and edits.

REFERENCES

Adames, Á. F., and Kim, D. (2016). The MJO as a Dispersive, Convectively Coupled Moisture Wave: Theory and Observations. *J. Atmos. Sci.* 73, 913–941. doi:10.1175/JAS-D-15-0170.1

Almar, R., Graffin, M., Boucharel, J., Abessolo, G. O., Thoumyre, G., Papa, F., et al. (2022). *El Niño Controls the Evolution of Shorelines Worldwide*. Preprint Research Square. doi:10.21203/rs.3.rs-1283693/v1

Amaya, D. J. (2019). The Pacific Meridional Mode and ENSO: a Review. *Curr. Clim. Change Rep.* 5, 296–307. doi:10.1007/s40641-019-00142-x

An, S.-I., and Jin, F.-F. (2000). An Eigen Analysis of the Interdecadal Changes in the Structure and Frequency of ENSO Mode. *Geophys. Res. Lett.* 27, 2573–2576. doi:10.1029/1999gl011090

An, S.-I., and Jin, F.-F. (2004). Nonlinearity and Asymmetry of ENSO*. *J. Clim.* 17, 2399–2412. doi:10.1175/1520-0442(2004)017<2399:naaoe>2.0.co;2

Ashok, K., Behera, S. K., Rao, S. A., Weng, H., and Yamagata, T. (2007). El Niño Modoki and its Possible Teleconnection. *J. Geophys. Res.* 112. doi:10.1029/2006jc003798

Battisti, D. S., and Hirst, A. C. (1989). Interannual Variability in a Tropical Atmosphere-Ocean Model: Influence of the Basic State, Ocean Geometry and Nonlinearity. *J. Atmos. Sci.* 46, 1687–1712. doi:10.1175/1520-0469(1989)046<1687:iviata>2.0.co;2

Bejarano, L., and Jin, F.-F. (2008). Coexistence of Equatorial Coupled Modes of ENSO*. *J. Clim.* 21, 3051–3067. doi:10.1175/2007JCLI1679.1

Boucharel, J., Almar, R., Kestenare, E., and Jin, F.-F. (2021). On the Influence of ENSO Complexity on Pan-Pacific Coastal Wave Extremes. *Proc. Natl. Acad. Sci. U.S.A.* 118, 9118. doi:10.1073/pnas.2115599118

Boucharel, J., and Jin, F.-F. (2020). A Simple Theory for the Modulation of Tropical Instability Waves by ENSO and the Annual Cycle. *Tellus A Dyn. Meteorology Oceanogr.* 72, 1–14. doi:10.1080/16000870.2019.1700087

Brunner, A. D. (2000). El Nino and World Primary Commodity Prices: Warm Water or Hot Air? *IMF Work. Pap.* doi:10.5089/9781451874440.001.A001

Cai, W., Wu, L., Lengaigne, M., Li, T., McGregor, S., Kug, J.-S., et al. (2019). Pantropical Climate Interactions. *Science* 363, eaav4236. doi:10.1126/science.aav4236

Cane, M. A., and Moore, D. W. (1981). A Note on Low-Frequency Equatorial Basin Modes. *J. Phys. Oceanogr.* 11, 1578–1584. doi:10.1175/1520-0485(1981)011<1578:anolfe>2.0.co

Cane, M. A., Münnich, M., and Zebiak, S. F. (1990). A Study of Self-Excited Oscillations of the Tropical Ocean-Atmosphere System. Part I: Linear Analysis. *J. Atmos. Sci.* 47, 1562–1577. doi:10.1175/1520-0469(1990)047<1562:asoseo>2.0.co;2

Cane, M. A., and Zebiak, S. E. (1985). A Theory for El Niño and the Southern Oscillation. *Science* 228, 1085–1087. doi:10.1126/science.228.4703.1085

Capotondi, A. (2013). ENSO Diversity in the NCAR CCSM4 Climate Model. *J. Geophys. Res. Oceans* 118, 4755–4770. doi:10.1002/jgrc.20335

Capotondi, A., and Ricciardulli, L. (2021). The Influence of Pacific Winds on ENSO Diversity. *Sci. Rep.* 11, 18672. doi:10.1038/s41598-021-97963-4

Capotondi, A., Wittenberg, A. T., Kug, J. S., Takahashi, K., and McPhaden, M. J. (2020). "ENSO Diversity," in *El Niño Southern Oscillation in a Changing Climate* (American Geophysical Union (AGU)), 65–86. doi:10.1002/9781119548164.ch4

Capotondi, A., Wittenberg, A. T., Newman, M., Di Lorenzo, E., Yu, J.-Y., Braconnot, P., et al. (2015). Understanding ENSO Diversity. *Bull. Amer. Meteor. Soc.* 96, 921–938. doi:10.1175/BAMS-D-13-00117.1

Cashin, P., Mohaddes, K., and Raissi, M. (2017). Fair Weather or Foul? the Macroeconomic Effects of El Niño. *J. Int. Econ.* 106, 37–54. doi:10.1016/j.jinteco.2017.01.010

Chang, P., Wang, B., Li, T., and Ji, L. (1994). Interactions between the Seasonal Cycle and the Southern Oscillation - Frequency Entrainment and Chaos in a Coupled Ocean-Atmosphere Model. *Geophys. Res. Lett.* 21, 2817–2820. doi:10.1029/94GL02759

Chen, D., Lian, T., Fu, C., Cane, M. A., Tang, Y., Murtugudde, R., et al. (2015). Strong Influence of Westerly Wind Bursts on El Niño Diversity. *Nat. Geosci.* 8, 339–345. doi:10.1038/ngeo2399

Chen, H.-C., and Jin, F.-F. (2020). Fundamental Behavior of ENSO Phase Locking. *J. Clim.* 33, 1953–1968. doi:10.1175/JCLI-D-19-0264.1

Chen, H.-C., and Jin, F.-F. (2021). Simulations of ENSO Phase-Locking in CMIP5 and CMIP6. *J. Clim.* 34, 1–42. doi:10.1175/JCLI-D-20-0874.1

Chen, H.-C., Jin, F.-F., Zhao, S., Wittenberg, A. T., and Xie, S. (2021). ENSO Dynamics in the E3SM-1-0, CESM2, and GFDL-CM4 Climate Models. *J. Clim.* 34, 1–59. doi:10.1175/JCLI-D-21-0355.1

Chen, N., and Majda, A. J. (2017). Simple Stochastic Dynamical Models Capturing the Statistical Diversity of El Niño Southern Oscillation. *Proc. Natl. Acad. Sci. U.S.A.* 114, 1468–1473. doi:10.1073/pnas.1620766114

Chiang, J. C. H., and Vimont, D. J. (2004). Analogous Pacific and Atlantic Meridional Modes of Tropical Atmosphere-Ocean Variability*. *J. Clim.* 17, 4143–4158. doi:10.1175/JCLI4953.1

Choi, J., and An, S.-I. (2013). Quantifying the Residual Effects of ENSO on Low-Frequency Variability in the Tropical Pacific. *Int. J. Climatol.* 33, 1047–1052. doi:10.1002/joc.3470

Choi, K.-Y., Vecchi, G. A., and Wittenberg, A. T. (2013). ENSO Transition, Duration, and Amplitude Asymmetries: Role of the Nonlinear Wind Stress Coupling in a Conceptual Model. *J. Clim.* 26, 9462–9476. doi:10.1175/jcli-d-13-00045.1

Fang, X.-H., and Mu, M. (2018). A Three-Region Conceptual Model for Central Pacific El Niño Including Zonal Advective Feedback. *J. Clim.* 31, 4965–4979. doi:10.1175/JCLI-D-17-0633.1

Fedorov, A. V., Hu, S., Lengaigne, M., and Guilyardi, E. (2015). The Impact of Westerly Wind Bursts and Ocean Initial State on the Development, and Diversity of El Niño Events. *Clim. Dyn.* 44, 1381–1401. doi:10.1007/s00382-014-2126-4

Fedorov, A. V., and Philander, S. G. (2001). A Stability Analysis of Tropical Ocean-Atmosphere Interactions: Bridging Measurements and Theory for El Niño. *J. Clim.* 14, 3086–3101. doi:10.1175/1520-0442(2001)014<3086:asaoto>2.0.co;2

Fedorov, A. V., and Philander, S. G. (20002002). Is El Niño Changing? *Science* 288, 1997–2002. doi:10.1126/science.288.5473.1997

Geng, L. (2021). *Dynamics of El Niño-Southern Oscillation Diversity in an Intermediate Coupled Model (Ph.D. Dissertation)*. Honolulu: University of Hawai'i at Manoa.

Geng, L., and Jin, F.-F. (2022). ENSO Diversity Simulated in a Revised Cane-Zebiak Model. *Front. Earth Sci.* 10, 899323. doi:10.3389/feart.2022.899323

Ham, Y.-G., Kug, J.-S., Park, J.-Y., and Jin, F.-F. (2013). Sea Surface Temperature in the North Tropical Atlantic as a Trigger for El Niño/Southern Oscillation Events. *Nat. Geosci.* 6, 112–116. doi:10.1038/NGEO1686

Hu, S., and Fedorov, A. V. (2018). Cross-equatorial Winds Control El Niño Diversity and Change. *Nat. Clim. Change* 8, 798–802. doi:10.1038/s41558-018-0248-0

Jadhav, J., Panickal, S., Marathe, S., and Ashok, K. (2015). On the Possible Cause of Distinct El Niño Types in the Recent Decades. *Sci. Rep.* 5, 17009. doi:10.1038/srep17009

Jin, F.-F. (1997a). An Equatorial Ocean Recharge Paradigm for ENSO. Part I: Conceptual Model. *J. Atmos. Sci.* 54, 811–829. doi:10.1175/1520-0469(1997)054<0811:aeorpf>2.0.co;2

Jin, F.-F. (1997b). An Equatorial Ocean Recharge Paradigm for ENSO. Part II: a Stripped-Down Coupled Model. *J. Atmos. Sci.* 54, 8302–8847. doi:10.1175/1520-0469(1997)054<0830:aeorpf>2.0.co

Jin, F.-F. (2001). Low-Frequency Modes of Tropical Ocean Dynamics*. *J. Clim.* 14, 3874–3881. doi:10.1175/1520-0442(2001)014<3874:lfmoto>2.0.co;2

Jin, F.-F., Neelin, J. D., and Ghil, M. (1994). El Niño on the Devil's Staircase: Annual Subharmonic Steps to Chaos. *Science* 264, 70–72. doi:10.1126/science.264.5155.70

Jin, F.-F., and Neelin, J. D. (1993). Modes of Interannual Tropical Ocean-Atmosphere Interaction-A Unified View. Part I: Numerical Results. *J. Atmos. Sci.* 50, 3477–3503. doi:10.1175/1520-0469(1993)050<3477:MOITOI>2.0.CO10.1175/1520-0469(1993)050<3477:moitoi>2.0.co;2

Jin, F. F., Chen, H. C., Zhao, S., Hayashi, M., Karamperidou, C., Stuecker, M. F., et al. (2020). "Simple ENSO Models," in *El Niño Southern Oscillation in a Changing Climate*. Editors M. J. McPhaden, A. Santoso, and W. Cai (Hoboken, NJ: American Geophysical Union Geophysical Monograph Series) 253, 119–151. doi:10.1002/9781119548164

Kao, H.-Y., and Yu, J.-Y. (2009). Contrasting Eastern-Pacific and Central-Pacific Types of ENSO. *J. Clim.* 22, 615–632. doi:10.1175/2008jcli2309.1

Keenlyside, N., and Kleeman, R. (2002). Annual Cycle of Equatorial Zonal Currents in the Pacific. *J. Geophys. Res.* 107, 8–18. doi:10.1029/2000JC000711

Kug, J.-S., Jin, F.-F., and An, S.-I. (2009). Two Types of El Niño Events: Cold Tongue El Niño and Warm Pool El Niño. *J. Clim.* 22, 1499–1515. doi:10.1175/2008JCLI2624.1

Larkin, N. K., and Harrison, D. E. (2005a). Global Seasonal Temperature and Precipitation Anomalies during El Niño Autumn and Winter. *Geophys. Res. Lett.* 32, 2860. doi:10.1029/2005GL022860

Larkin, N. K., and Harrison, D. E. (2005b). On the Definition of El Niño and Associated Seasonal Average U.S. Weather Anomalies. *Geophys. Res. Lett.* 32, 2738. doi:10.1029/2005GL022738

Levine, A. F. Z., and Jin, F.-F. (2010). Noise-Induced Instability in the ENSO Recharge Oscillator. *J. Atmos. Sci.* 67, 529–542. doi:10.1175/2009JAS3213.1

Levine, A. F. Z., and Jin, F. F. (2017). A Simple Approach to Quantifying the Noise-ENSO Interaction. Part I: Deducing the State-Dependency of the Windstress Forcing Using Monthly Mean Data. *Clim. Dyn.* 48, 1–18. doi:10.1007/s00382-015-2748-1

Levine, A. F. Z., Jin, F. F., and Stuecker, M. F. (2017). A Simple Approach to Quantifying the Noise-ENSO Interaction. Part II: The Role of Coupling between the Warm Pool and Equatorial Zonal Wind Anomalies. *Clim. Dyn.* 48, 19–37. doi:10.1007/s00382-016-3268-3

Levine, A., Jin, F. F., and McPhaden, M. J. (2016). Extreme Noise-Extreme El Niño: How State-dependent Noise Forcing Creates El Niño-La Niña Asymmetry. *J. Clim.* 29, 5483–5499. doi:10.1175/JCLI-D-16-0091.1

Lian, T., Chen, D., Tang, Y., and Wu, Q. (2014). Effects of Westerly Wind Bursts on El Niño: A New Perspective. *Geophys. Res. Lett.* 41, 3522–3527. doi:10.1002/2014GL059989

McCreary, J. P. (1981). A Linear Stratified Ocean Model of the Equatorial Undercurrent. *Phil. Trans. R. Soc. Lond. A* 298, 603–635. doi:10.1098/rsta.1981.0002

McPhaden, M. J. (1981). Continuously Stratified Models of the Steady-State Equatorial Ocean. *J. Phys. Oceanogr.* 11, 337–354. doi:10.1175/1520-0485(1981)011<0337:csmots>2.0.co;2

McPhaden, M. J., Santoso, A., and Cai, W. (2020). *El Niño Southern Oscillation in a Changing Climate*. John Wiley & Sons.

McPhaden, M. J., Zebiak, S. E., and Glantz, M. H. (2006). ENSO as an Integrating Concept in Earth Science. *Science* 314, 1740–1745. doi:10.1126/science.1132588

Neelin, J. D., Battisti, D. S., Hirst, A. C., Jin, F.-F., Wakata, Y., Yamagata, T., et al. (1998). ENSO Theory. *J. Geophys. Res.* 103, 14261–14290. doi:10.1029/97JC03424

Neelin, J. D., and Jin, F.-F. (1993). Modes of Interannual Tropical Ocean-Atmosphere Interaction-A Unified View. Part II: Analytical Results in the Weak-Coupling Limit. *J. Atmos. Sci.* 50, 3504–3522. doi:10.1175/1520-0469(1993)050<3504:moitoi>2.0.co;2

Philander, S. G. (1990). *El Niño, La Niña, and the Southern Oscillation*. Academic Press.

Picaut, J., Masia, F., and du Penhoat, Y. (1997). An Advective-Reflective Conceptual Model for the Oscillatory Nature of the ENSO. *Science* 277, 663–666. doi:10.1126/science.277.5326.663

Planton, Y. Y., Guilyardi, E., Wittenberg, A. T., Lee, J., Gleckler, P. J., Bayr, T., et al. (2021). Evaluating Climate Models with the CLIVAR 2020 ENSO Metrics Package. *Bull. Am. Meteorological Soc.* 102, E193–E217. doi:10.1175/BAMS-D-19-0337.1

Rayner, N. A., Parker, D. E., Horton, E. B., Folland, C. K., Alexander, L. V., Rowell, D. P., et al. (2003). Global Analyses of Sea Surface Temperature, Sea Ice, and Night Marine Air Temperature since the Late Nineteenth Century. *J. Geophys. Res.* 108. doi:10.1029/2002JD002670

Stuecker, M. F. (2018). Revisiting the Pacific Meridional Mode. *Sci. Rep.* 8, 3216. doi:10.1038/s41598-018-21537-0

Suarez, M. J., and Schopf, P. S. (1988). A Delayed Action Oscillator for ENSO. *J. Atmos. Sci.* 45, 32832–33287. doi:10.1175/1520-0469(1988)045<3283:adaofe>2.0.co

Takahashi, K., Karamperidou, C., and Dewitte, B. (2019). A Theoretical Model of Strong and Moderate El Niño Regimes. *Clim. Dyn.* 52, 7477–7493. doi:10.1007/s00382-018-4100-z

Taschetto, A. S., Ummenhofer, C. C., Stuecker, M. F., Dommenget, D., Ashok, K., Rodrigues, R. R., et al. (2020). "ENSO Atmospheric Teleconnections," in *El Niño Southern Oscillation in a Changing Climate* (American Geophysical Union (AGU)), 309–335. doi:10.1002/9781119548164.ch14

Timmermann, A., An, S.-I., Kug, J.-S., Jin, F.-F., Cai, W., Capotondi, A., et al. (2018). El Niño-Southern Oscillation Complexity. *Nature* 559, 535–545. doi:10.1038/s41586-018-0252-6

Timmermann, A., and Jin, F.-F. (2005). in *Predictability of Coupled Processes" in Predictability of Weather and Climate*. Editors T. Palmer and R. Hagedorn (Cambridge University Press), 251–274.

Tziperman, E., Stone, L., Cane, M. A., and Jarosh, H. (1994). El Niño Chaos: Overlapping of Resonances between the Seasonal Cycle and the Pacific Ocean-Atmosphere Oscillator. *Science* 264, 72–74. doi:10.1126/science.264.5155.72

Vijayeta, A., and Dommenget, D. (2018). An Evaluation of ENSO Dynamics in CMIP Simulations in the Framework of the Recharge Oscillator Model. *Clim. Dyn.* 51, 1753–1771. doi:10.1007/s00382-017-3981-6

Vimont, D. J., Alexander, M. A., and Newman, M. (2014). Optimal Growth of Central and East Pacific ENSO Events. *Geophys. Res. Lett.* 41, 4027–4034. doi:10.1002/2014gl059997

Vimont, D. J., Newman, M., Battisti, D. S., and Shin, S.-I. (2022). The Role of Seasonality and the ENSO Mode in Central and East Pacific ENSO Growth and Evolution. *J. Clim.* 1, 1–46. doi:10.1175/jcli-d-21-0599.1

Wang, C. (2018). A Review of ENSO Theories. *Natl. Sci. Rev.* 5, 813–825. doi:10.1093/nsr/nwy104

Wang, C., and Picaut, J. (2004). "Understanding ENSO Physics - A Review," in *Earth's Climate: The Ocean-Atmosphere Interaction, Geophysical Monograph Series*. Editors C. Wang, S. -P. Xie, and J. A. Carton (Washington, D. C.: AGU), 21–48.

Wang, X., Jin, F.-F., and Wang, Y. (2003a). A Tropical Ocean Recharge Mechanism for Climate Variability. Part I: Equatorial Heat Content Changes Induced by the Off-Equatorial Wind. *J. Clim.* 16, 3585–3598. doi:10.1175/1520-0442(2003)016<3585:atormf>2.0.co;2

Wang, X., Jin, F.-F., and Wang, Y. (2003b). A Tropical Ocean Recharge Mechanism for Climate Variability. Part II: A Unified Theory for Decadal and ENSO Modes. *J. Clim.* 16, 3599–3616. doi:10.1175/1520-0442(2003)016<3599:atormf>2.0.co;2

Weng, H., Ashok, K., Behera, S. K., Rao, S. A., and Yamagata, T. (2007). Impacts of Recent El Niño Modoki on Dry/wet Conditions in the Pacific Rim during Boreal Summer. *Clim. Dyn.* 29, 113–129. doi:10.1007/s00382-007-0234-0

Wengel, C., Dommenget, D., Latif, M., Bayr, T., and Vijayeta, A. (2018). What Controls ENSO-Amplitude Diversity in Climate Models? *Geophys. Res. Lett.* 45, 1989–1996. doi:10.1002/2017gl076849

Wittenberg, A. T. (2018). ENSO in Climate Models: Progress and Opportunities. IV International Conference On El Niño Southern Oscillation: ENSO in a Warmer Climate, CLIVAR Workshop, FIEC, ESPOL, Guayaquil, Ecuador. Available at: https://extranet.gfdl.noaa.gov/~atw/yr/2018/wittenberg_20181017.ppt (Assessed February 2, 2022).

Xie, R., and Jin, F.-F. (2018). Two Leading ENSO Modes and El Niño Types in the Zebiak-Cane Model. *J. Clim.* 31, 1943–1962. doi:10.1175/JCLI-D-17-0469.1

Xue, A., Jin, F. F., Zhang, W., Boucharel, J., Zhao, S., and Yuan, X. (2020). Delineating the Seasonally Modulated Nonlinear Feedback onto ENSO from Tropical Instability Waves. *Geophys. Res. Lett.* 47, e2019GL085863. doi:10.1029/2019GL085863

Yang, S., Li, Z., Yu, J.-Y., Hu, X., Dong, W., and He, S. (2018). El Niño-Southern Oscillation and its Impact in the Changing Climate. *Natl. Sci. Rev.* 5, 840–857. doi:10.1093/nsr/nwy046

Yu, J.-Y., Kao, H.-Y., and Lee, T. (2010). Subtropics-Related Interannual Sea Surface Temperature Variability in the Central Equatorial Pacific. *J. Clim.* 23, 2869–2884. doi:10.1175/2010JCLI3171.1

Yu, J.-Y., and Kim, S. T. (2011). Relationships between Extratropical Sea Level Pressure Variations and the Central Pacific and Eastern Pacific Types of ENSO. *J. Clim.* 24, 708–720. doi:10.1175/2010JCLI3688.1

Yu, Y., Dommenget, D., Frauen, C., Wang, G., and Wales, S. (2016). ENSO Dynamics and Diversity Resulting from the Recharge Oscillator Interacting with the Slab Ocean. *Clim. Dyn.* 46, 1665–1682. doi:10.1007/s00382-015-2667-1

Zhang, H., Clement, A., and Di Nezio, P. (2014). The South Pacific Meridional Mode: A Mechanism for ENSO-like Variability. *J. Clim.* 27, 769–783. doi:10.1175/JCLI-D-13-00082.1

Zhao, S., Jin, F. F., Long, X., and Cane, M. A. (2021a). On the Breakdown of ENSO's Relationship with Thermocline Depth in the Central-Equatorial Pacific. *Geophys Res. Lett.* 48, e2020GL092335. doi:10.1029/2020GL092335

Zhao, S., Jin, F. F., and Stuecker, M. F. (2021b). Understanding Lead Times of Warm Water Volumes to ENSO Sea Surface Temperature Anomalies. *Geophys Res. Lett.* 48, e2021GL094366. doi:10.1029/2021GL094366

Conflict of Interest: The author declares that the research was conducted in the absence of any commercial or financial relationships that could be construed as a potential conflict of interest.

Publisher's Note: All claims expressed in this article are solely those of the authors and do not necessarily represent those of their affiliated organizations, or those of the publisher, the editors and the reviewers. Any product that may be evaluated in this article, or claim that may be made by its manufacturer, is not guaranteed or endorsed by the publisher.

Advantages of publishing in Frontiers

OPEN ACCESS
Articles are free to read for greatest visibility and readership

FAST PUBLICATION
Around 90 days from submission to decision

HIGH QUALITY PEER-REVIEW
Rigorous, collaborative, and constructive peer-review

TRANSPARENT PEER-REVIEW
Editors and reviewers acknowledged by name on published articles

Frontiers
Avenue du Tribunal-Fédéral 34
1005 Lausanne | Switzerland

Visit us: www.frontiersin.org
Contact us: frontiersin.org/about/contact

REPRODUCIBILITY OF RESEARCH
Support open data and methods to enhance research reproducibility

DIGITAL PUBLISHING
Articles designed for optimal readership across devices

FOLLOW US
@frontiersin

IMPACT METRICS
Advanced article metrics track visibility across digital media

EXTENSIVE PROMOTION
Marketing and promotion of impactful research

LOOP RESEARCH NETWORK
Our network increases your article's readership